Localization of electromagnetic waves beyond Anderson : role of correlations, symmetries and topology

Luis Alberto Razo López

UNIVERSITÉ CÔTE D'AZUR | ÉCOLE DOCTORALE SCIENCES FONDAMENTALES ET APPLIQUÉES

THÈSE DE DOCTORAT

Localisation des ondes électromagnétiques au-delà d'Anderson : Rôle des corrélations, des symétries et de la topologie

Luis Alberto Razo López
Institut de Physique de Nice

Presentée en vue de l'obtention du grade de docteur en Physique d'Université Côte d'Azur

Dirigée par : Fabrice Mortessagne / Geoffroy Aubry

Soutenue le : 02 Avril 2024

Devant le jury, composé de :

Geoffroy Aubry,
Chargé de recherche CNRS,
INPHYNI, Université Côte d'Azur

Matthieu Davy,
Professeur,
IETR, Université de Rennes

Luis Froufe-Pérez,
Maître assistant (HDR),
Université de Fribourg

Arthur Goetschy,
Maître de conférences,
ESPCI, Paris

Vincent Josse,
Professeur,
Institut d'Optique, Palaiseau

Fabrice Mortessagne,
Professeur,
INPHYNI, Université Côte d'Azur

Sergey Skipetrov,
Directeur de recherche CNRS,
LPMMC, Université Grenoble-Alpes

Patrizia Vignolo,
Professeure,
INPHYNI, Université Côte d'Azur

CONAHCYT CONSEJO NACIONAL DE HUMANIDADES CIENCIAS Y TECNOLOGÍAS
UNIVERSITÉ CÔTE D'AZUR FRANCE 2030 Initiative d'Excellence
anr agence nationale de la recherche

Localisation des ondes électromagnétiques au-delà d'Anderson :
Rôle des corrélations, des symétries et de la topologie

Localization of electromagnetic waves beyond Anderson:
Role of correlations, symmetries and topology

Jury:

Présidente du jury
Patrizia Vignolo, *Professeure,* INPHYNI, Université Côte d'Azur

Rapporteurs
Matthieu Davy, *Professeur,* IETR, Université de Rennes
Luis Froufe-Pérez, *Maître assistant (HDR),* Université de Fribourg

Examinateurs
Arthur Goetschy, *Maître de conférences,* ESPCI, Paris
Vincent Josse, *Professeur,* Institut d'Optique, Palaiseau

Directeurs
Geoffroy Aubry, *Chargé de recherche CNRS,* INPHYNI, Université Côte d'Azur
Fabrice Mortessagne, *Professeur,* INPHYNI, Université Côte d'Azur

Invité
Sergey Skipetrov, *Directeur de recherche CNRS,* LPMMC, Université Grenoble-Alpes

Résumé

Au sens large, le terme de **localisation ondulatoire** fait référence à un phénomène où les ondes sont spatialement confinées dans de petites régions de l'espace sans la contrainte de barrières matérielles. Dans cette thèse, nous étudions (analytiquement, numériquement et expérimentalement) différents mécanismes physiques **collectifs** pour localiser spatialement, et donc pour contrôler **les ondes électromagnétiques**. En particulier, nous nous concentrons sur le rôle des potentiels **non corrélés** et **corrélés**, ainsi que sur des **effets topologiques** pour réaliser le confinement des ondes. Les études analytiques et numériques sont réalisées dans le cadre d'une approche récente de la modélisation de la **localisation d'Anderson** appelée **théorie du paysage de localisation**. D'autre part, des expériences sont réalisées à l'aide d'une plate-forme **micro-ondes** composée de petits cylindres diélectriques placés à l'intérieur d'une cavité constituée de deux plaques métalliques. La cavité met en œuvre un **système d'ondes propagatives**, où nous pouvons contrôler efficacement la permittivité locale au moyen des cylindres agissant comme des diffuseurs, ou comme un **système de de liaison forte** analogique, où, dans ce cas, les cylindres diélectriques jouent le rôle de résonateurs.

Dans un premier temps, nous étendons le champ d'application de l'approche du paysage de localisation à une large classe de systèmes de liaison forte unidimensionnels et bidimensionnels en présence d'un désordre non corrélé, où des fonctions propres localisées apparaissent en bord de bande. Nous démontrons comment la théorie du paysage de localisation est capable de prédire avec précision non seulement les emplacements, mais aussi les énergies des fonctions propres localisées dans les régimes de basse et de haute énergie. Ensuite, en utilisant notre cavité expérimentale comme système de propagation, nous réalisons des expériences de transport de micro-ondes dans des réseaux planaires bidimensionnels. Les expériences sont réalisées sur un réseau **désordonné** et sur une **spirale de Vogel apériodique** à partir de laquelle nous caractérisons les structures modales électromagnétiques dans l'espace réel. Nos résultats révèlent que les systèmes apériodiques possèdent une grande variété de modes à longue durée de vie – avec des décroissances spatiales gaussiennes, exponentielles et en loi de puissance – qui sont capables de survivre même dans un environnement tridimensionnel. Ceci est confirmé par différentes quantités de transport telles que la densité d'états, le temps de décroissance caractéristique et la conductance de Thouless qui sont également accessibles expérimentalement. À l'inverse, nous montrons que les états propres dans les milieux désordonnés traditionnels sont toujours limités à des décroissances radiales exponentielles avec d'importantes fuites dès que les systèmes ne sont plus bidimensionnels. Enfin, nous utilisons la configuration expérimentale de liaison forte pour étudier la propagation des **états hélicoïdaux** topologiques. En particulier, nous analysons expérimentalement un ensemble de structures en nid d'abeille construites à l'aide d'un réseau triangulaire avec une cellule unitaire hexagonale, qui sont caractérisées par l'invariant topologique Z_2. En accédant à la structure modale dans l'espace réel et à la densité d'états, nos résultats révèlent la possibilité d'ouvrir une bande interdite topologique, peuplée d'états de bord localisés en bordure de la structure. Nous démontrons la nature unidirectionelle de la propagation de ces **états de bord** hélicoïdaux contre-propagatifs.

Dans l'ensemble, nos résultats démontrent qu'il est possible de modéliser, de contrôler et de localiser les ondes électromagnétiques non seulement du point de vue d'Anderson, mais aussi au-delà. Grâce aux différents jalons que nous avons posés, nous ouvrons une voie vers l'hypothétique localisation d'Anderson des ondes électromagnétiques tridimensionnelles.

Mots clés : localisation ondulatoire, effets collectifs, ondes électromagnétiques, corrélations, effets topologiques, localisation d'Anderson, paysage de localisation, micro-ondes, ondes propagatives, liaison forte, systèmes désordonnés et apériodiques, spirale de Vogel, états hélicoïdaux, états de bord.

Abstract

In a broad sense, the term **wave localization** refers to a phenomenon where waves are spatially confined in small regions of the space without any bounding material barriers. In this Thesis, we investigate (analytically, numerically and experimentally) different physical **collective** mechanisms to spatially localize, and therefore, to control **electromagnetic waves**. Specifically, we focus on the role of **uncorrelated** and **correlated** potentials, as well as of **topological effects** to achieve wave confinement. Analytical and numerical studies are accomplished in the framework of a recent approach in the modeling of **Anderson localization** called **localization landscape theory**. On the other hand, experiments are performed using a **microwave** platform composed by small dielectric cylinders placed inside a cavity made of two metallic plates. The cavity implements a **propagative wave system**, where we can efficiently control the local permittivity by means of the cylinders acting as scatterers, or as an analogic **tight-binding system**, where, in this case, the dielectric cylinders play the role of resonators.

First, we extend the scope of the localization landscape approach to a wide class of one and two dimensional tight-binding systems in the presence of uncorrelated disorder, where localized eigenfunctions appear in both band-edges. We demonstrate how the landscape theory is able to predict accurately not only the locations, but also the energies of localized eigenfunctions in the low- and high-energy regimes. Later, by using our experimental cavity as a propagative system, we perform microwave transport experiments in two dimensional planar arrays. Experiments are carried out on a **disordered** lattice and on an **aperiodic Vogel spiral** from where we characterize the electromagnetic modal structures in real space. Our results reveal that aperiodic systems can carry a rich variety of long-lived modes—with Gaussian, exponential, and power law spatial decays—which are able to survive even in a three-dimensional environment. This is supported by different transport quantities such as the density of states, the characteristic decay time, and the Thouless conductance that are also experimentally accessible. On the contrary, we show that the eigenstates in traditional disordered media are always limited to exponential radial decays with leaking features beyond two-dimensions. Finally, we use the experimental tight-binding configuration to investigate the propagation of topological **helical states**. Particularly, we experimentally analyze a set of honeycomb-like structures built using a triangular lattice with a hexagonal unit cell, which are characterized by the Z_2 topological invariant. By recovering the modal structure in real space and the density of states, our results reveal the possibility to open a topological gap, dwelt by edge states that live in the border of the structure. We demonstrate the unidirectional counterpropagative features of such helical **edge states**.

Taken together, our results demonstrate that it is possible to model, control and localize electromagnetic waves not only within, but beyond Anderson's conception. Thanks to the crossroads we have taken, we have mapped out an itinerary that brings us closer to the main avenue leading perhaps to Anderson localization of three dimensional electromagnetic waves.

Keywords: wave localization, collective phenomena, electromagnetic waves, correlations, topological effects, Anderson localization, localization landscape, microwaves, propagative waves, tight-binding, disordered and aperiodic systems, Vogel spiral, helical states, edge states.

A la patria que me vio nacer,
A la patria que me ha acogido,
A mi familia,
A ella...

Acknowledgments

Antes que nada, flaca, fíjate que disparate,
estoy matando el tiempo antes que el tiempo me mate...
Sharif (Bendecido)

...y aquí estamos otra vez, posiblemente la última. He dejado pasar el tiempo luego de la defensa de esta tesís, primero, porque honestamente estaba muy cansado de escribir, y segundo, porque tengo la idea de que los "agradecimientos" y la "dedicatoria" de qualquier texto deben de hacerse con el corazón, y mi corazón no ha estado muy tranquilo por distintas razones. Diferentemente a lo que hice durante mi tesis de maestría, aquí voy a escribir en todos los idiomas que sean necesarios para que la gente aquí mencionada pueda entender mis palabras, sean estas cortas o largas, ya que, hay veces que la intención no basta. "Gracias a ese que hizo suya mi guerra" [1], estoy en deuda con todas las personas aquí mencionandas.

Como es típico en este tipo de textos, empezaré agradeciendo a mi familia más próxima, y aunque es usual comenzar por ellos, a lo largo de los años me he dado cuenta que mis sentimientos por ellos no son usuales. Iniciando por mis padres Miguel Mauricio Razo Jiménez y Leticia López Salas, que no sólo me han apoyado incodicionalmente en todos mis proyectos, sino que es por ellos, que soy quien soy. Han sido ellos, que con sus buenos consejos y buena educación me impulsaron en distintos momentos y es gracias a ellos que hoy este doctorado ha sido finalizado. En segundo lugar pero no menos importante, quiero agradecer a mis hermanos, Miguel Eduardo Razo López y Mauricio Alejandro Razo López, quienes han sido confidentes y amigos en momentos dificiles. Gracias a mi familia por todo su apoyo, por haber formado buenos valores, una buena moral, una buena ética y por estar ahí en cada decisión, sea buena o mala. Este logro no es sólo mío, sino de todos ustedes, de su esfuerzo y sudor.

I also would like to thanks to Sümeyra Seniha Baran for being next to me during a huge part of this travel. At this point of my life, it is still so hard to define what I want or where I'm going, but there is one stuff I'm sure and it is that I want to be next to you. Thanks for sharing the pureness of your heart, thanks for sharing your opinions, dreams and ideas, thanks for improving my life with your presence. Teşekkür ederim, seni çok seviyorum. "Acércate, que te quiero sentir, hoy te quiero decir: todo lo que me ofrece la vida sin ti es condena" [2]. I also would like to thank all the Baran and Şanlı families, thanks for receiving me in such kind and beautiful way.

Me gustaría ahora agradecer a Susana Plascencia Orozco por ser una de las personas que a logrado estar en los agradecimientos de cada una de mis tesis. Susanita, por mucho tiempo has sido mi mejor amiga y te agradezo el hecho de estar ahí en todo momento, te agradezco tus consejos y opiniones. Espero que la vida me tenga aún muchas aventuras contigo. Agradezco a Andrea Alejandra Arenales Franco, a Cecilia Calvario Hernandez y a Iris Carolina Valdez Achucarro por ser de mis amigas más cercanas y por estar ahí siempre que lo he necesitado. Gracias a Jesús Aldair Pantoja Gonzalez, a Jhony Ariel Herrera Mendoza y a Carlos Alberto López, por todo el apoyo y las buenas platicas, espero podamos compartir más proyectos juntos. Me gustaría también agradecer a Sabina Ascencio Ramirez, quien me demostro lo fácil que puede ser tirar el orgullo a un lado cuando las acciones son verdaderamente guiadas por corazón y las buenas intenciones. Agradezco a Francisco Zambrano por todas las aventuras que hemos tenido juntos, gracias por cada consejo y buena platica que hemos tenido ya sea estando en la montaña o en el mar. Espero que la vida nos de mas aventuras juntos y nos permita explorar muchos

[1] Suya mi guerra - La Raíz
[2] A la sombra de la sierra - La Raíz

nuevos lugares. I would finally like to thank to Junjie Lu, thanks for always being there with a smile and a bunch of nice energy.

Agradezco a todos mis compañeros y amigos que a lo largo de estos 12 años de física me han acompañado. Especialmente agradezo a Javier, Samantha, Pastor, Lupe, Nuñez, David, Juan, Christian, Paquito, Jordan, Misael, Irigamí quienes estuvieron conmigo en mis últimos años en México y que aún en la distancia me acompañan. Agradezco a Aurora, Carlos Peralta, Arturo, Rafael, Irma, Juan Pablo, Kaleb, Rodrigo, Nazareth, Kevin, Zack, Silvana, Isaac, Noel, Monica, Jorge, Santiago y Abraham por ser las personas con las que he crecido y que me han permitido aprender de ellas desde mi inicio en esto. A mis amigos personales que nada tienen que ver con la ciencia Oscar, Tico, Ezequiel, Juan, Hagel y Tote. Agradezco a todos los chicos que conocí en el camino y que siempre viviran en mi corazón. Gracias a Carmén Arnuncio, a Xavi, Irati, Ambrosio, Erik, Jose, Uranía, Virginia, Julio, Simone, Eli y Dani. Je voudrais aussi remercier tout les gens qui ont partagé les derniers années de ce doctorat avec moi, je remercie à David Paulovics, Mattis Raisner, FX, Pierre Vigot, Lucas Zanaglia, Léo Colliart, Marie Forest, Diana Neponoceno, Yassine Maalaoui, Mathis Cohen, Maria Blanco, Camielsa, Nicolas Brun, Jean-Pierre, Gasparito, David Medina et Klint. Je remercie aussi au gens du Riviera rugby club, especialment à Mathias Albert, Marsou, Alexandre Sorain, Banjamin Diegoni, Renan Warrick, Aurélien Crida, Arno Peduzzi, Arnoud, Bob, Valerian et le Pres. Gracias y mucho exito a todos.

Cette thèse n'aurait pas pu être réalisée sans l'aide des mes encadrants Fabrice Mortessagne et Geoffroy Aubry, merci pour être là, pas seulement comme mes supérieurs mais plutôt comme mes amis. J'espère on a toujours plein des études très intéressantes à comprendre ensemble. Je remercie a tous mes colaborateurs Marcel Filoche, Felipe Pinheiro, Sergey Skipetrov, Pierre Wulles, Romain Pierrat, Arthur Goetschy et Luis Foufre. También me gustaría agradecer a mis asesores anteriores José Antonio Méndez Bermúdez, Víctor Arturo Gopar Sánchez, Thomas Gorin, Rafael Alberto Méndez Sánchez y Víctor Domínguez, sin ustedes tampoco estaría aquí. Agradezco también a mis colaboradores en México, John Franco y Antonio Fernandez.

Finalmente agradezco a todos mis profesores que, durante estos 12 años, me han dado su tiempo y conocimiento. Agradezco a la Universidad de Guadalajara, donde comencé mis estudios. Al Instituto de Física "Luis Rivera Terrazas" y a la Benermerita Universidad Autonoma de Puebla, donde obtuve mi primer grado de maestría, así como a la Univeridad de Zaragoza y al ICTP por haberme acogido durante mis estudios. Je remercie aussi a l'Université Côte d'Azur oú j'ai fini mon deuxième master. Je voudrais remercier a l'Institut de Physique de Nice, l'École doctorale SFA, au CNRS et a l'ANR pour me donner l'opportunité de finir mes études de doctorat, ainsi que à Konstance Beck pour son soutien dans toutes mes démarches administratives. Finally, I gratefully acknowledge the financial support from CONAHCyT (Mexico), through Grant No. 775585, and from the French government, through the UCA$^{\text{JEDI}}$ Investments in the Future project managed by the National Research Agency (ANR) with the Reference No. ANR-15-IDEX-0001.

Contents

Introduction

The definition of an interesting problem
is that it cannot be solved by Random Matrix Theory.
Carlo Beenakker (Les Houches 2023)

Human beings can only perceive the outside world and understand nature through their senses. Sight, hearing and touch are capable of perceiving undulatory phenomena such as light, sound and vibration, respectively. When we observe the stars, hear a distant sound, or even if we have had the bad experience of feeling an earthquake, it is easy to assign to waves a propensity to spread out in space. However, this is not the whole picture.

The concept of *localization* was born far from the framework of wave systems, but emerges from the desire to understand metal-insulator transitions, where disorder in metallic materials halts the electronic conduction [1]. Nevertheless, since Anderson [2] proposed in 1985 that localization was a general wave phenomenon, and not inherent to the quantum nature of electrons, the physics community have made a huge effort to extend this concept to various wave systems. For instance, wave localization has been successfully measured for elastic waves [3–5], ultrasound [6], or optical fibers [7, 8]. But, what are we meaning by "wave localization"? As mentioned by Van Tiggelen [9], the exact definition seems not to be unique, so much so that he even preferred to define what localization is not. We can, however, attempt to delimit the concept. In the broadest sense, wave localization is a phenomenon characterized by the confinement of waves to small regions of space not bounded by any material barriers. Following this "definition", trapping a wave by simply surrounding it with a bunch of mirrors is not localization. We can add an ingredient, which plays an important role in this thesis, namely that wave localization is a consequence of the complex collective behavior of the whole system and not of the individual effect of its elements. In that way, a state in the gap of a semiconductor which have been created by local defects is not an example of what we call localization.

The Anderson localization for classical waves in uncorrelated random systems is generated by the constructive and destructive interferences, and it may happen for all kinds of waves [10]. Particularly, the possibility to confine electromagnetic waves in disordered media was early suggested by John [11], and it has been demonstrated in several 1D and 2D scattering experiments [7, 8, 12–16]. On the contrary, finding a convincing evidence for Anderson localization in the case of 3D electromagnetic systems has been a constant challenge for the community and the source of many controversies. Starting by the early claims by Wiersma et al. [17], and later by Störzer et al. [18] and Sperling et al. [19], all experimental works claiming the existence of 3D Anderson localization of light have been refuted [20, 21]. Why has the search for this phenomenon failed so far? As explained by Skipetrov and Page [10], one of the main reasons can be

the limits imposed by the nature itself, where the "relatively low" refractive indices of dielectric materials accessible in the experiments do not allow a sufficiently strong disorder. On the other hand, several theoretical works have also pointed out the role of near-field coupling between the scattering centers to open new transport channels, whose contribution become important at high densities [22–24]. Nevertheless, Yamilov et al. [25] have very recently reported numerical evidence of a localization transition in a 3D system using metallic spheres as scattering centers.

Undoubtedly, the question about the existence of Anderson localization of 3D electromagnetic waves is still an open problem. However, the unsuccessful search for light localization in the "Anderson way" has paved the way for the engineering of materials that go beyond the totally random scenario. In this sense, multiple authors have pointed out the role of partial order and correlated media to achieve localization of electromagnetic waves. The aim of this thesis is not to directly address the problem of Anderson localization of light in a 3D system, which has been shown to be still far from being fully understood, but to study analytically, numerically, and experimentally different physical and geometrical mechanisms that can lead to the confinement of electromagnetic waves, allowing to controlling them.

The first chapter of this thesis is intended as an introductory scan of the various concepts, models and theories that will be studied in greater detail throughout the manuscript. Particularly, we start by exploring the main concept of Anderson localization, as well as the theories to characterize it. Subsequently, we review the impact of correlated media to achieve wave confinement, and their ability to control wave transport. Finally, we establish the foundations and concepts of non-trivial topological systems and highlight the unconventional nature of the edge modes they possess.

The second chapter is devoted to present the experimental microwave platform and the different data analysis procedures that will be used in the subsequent chapters. We detail the different components of the setup, and specifically the building blocks of our experimental samples. Later, we show how several meaningful physical quantities such as the density of states, or the spatial shape of the eigenmodes can be extracted from the acquired data.

The third chapter is dedicated to analytically and numerically explore a recent powerful approach in the understanding of Anderson localization, namely the localization landscape [26]. We extent the localization landscape formalism to a wide class of 1D and 2D discrete materials in the presence of uncorrelated disorder. The different features of the approach are characterized, demonstrating the robustness of the proposed method. Additionally, we provide a theoretical analysis of the localization landscape and its possible applications to the Maxwell's equations and their corresponding scalar (polarized) forms. Part of the content of this Chapter forms the main body of Ref. [27].

In the fourth chapter, we report electromagnetic wave scattering experiments in a correlated disordered system and in an aperiodic lattice (Vogel spirals). For both systems, the localization phenomena is characterized by means of the eigenmodes features, showing how the specific structure of highly correlated media (Vogel spiral) can lead to localized modes that can survive even in a 3D space, in contrast to disordered lattices, whose localization features disappear in a 3D environment. The last part of the chapter is dedicated to illustrate the robustness of this new localization phenomenon with respect to the system size and the alteration of the lattice. The main results presented in this chapter have been published in Refs. [28] and [29].

Finally, in the fifth chapter we investigate the propagation of topological helical states and their impact on wave transport. Specifically, we experimentally analyze a set of honeycomb-like lattices built using triangular arrays with a hexagonal unit cell. By recovering the modal structure in real space and the density of states, our results reveal

the possibility to open a topological gap, dwelt by eigenstates confined in the edge of the structure. Finally, we demonstrate the unidirectional counterpropagative features of the helical modes that propagate around the boundary of the topological nontrivial material.

1

Physical mechanisms to localize electromagnetic waves

con una grieta en el cora, me llaman Doris Salcedo
estoy tan abajo, me queda lejos el cero
y estoy llenito de arena, como Madrid en la guerra
me sobran kilos de pena, me falta puto dinero...
Claudio Montana (La importancia de comer langosta)

Contents

This Chapter is dedicated to introduce the fundamental ideas, models, and concepts—about localization of electromagnetic waves—that will be used to further discussions along this thesis. Specifically, the Chapter is divided into three sections, each of which present a different physical mechanism to localize waves. The chapter is organized as follows: In Section 1.1, we unveil the impact of uncorrelated random disorder to halt wave transport. We start by introducing the main concepts of Anderson localization as well as of the different useful quantities and theories to distinguish it. We pay spatial attention to the case of localization of 3D light, for which so far there is no unequivocal proof of its existence. Later, we present a new deterministic approach namely the localization landscape theory. Section 1.2 is devoted to the study of localization via correlation in the potential. First, we provide an overview to classify distinct structured correlated media that are known to facilitate localization and at the same time admit different transport regimes. In the following, we reviewed the different studies performed using stealthy hyperuniform random systems, to finally introduce a specific type of aperiodic structure known as Vogel spirals. Finally, Section 1.3 meets the different important concepts about wave transport in nontrivial topological systems. Specifically, we focus in the emergence and impact of edge-states, a signature of the band structure of the dispersion relation in finite-size systems.

1.1 Localization via disorder

Before the advent of quantum mechanics, the conductivity σ in metallic materials was understood as the scattering of mobile electrons, interpreted as particles, by the immobile positive ions [30]. Although quantitatively relevant, the scattering lengths predicted by classical the Drude's theory differed strongly from the actual inter-atomic distances measured in experiments [31]. The emergence of quantum mechanics allowed then to understand that electrons are actually diffracted by the ions of the crystalline lattice and are just scattered by the impurities of the material, establishing a relationship between the conductivity and the imperfections of the system. Even though it had been identified fairly early that a high level of impurities could impair conduction, an article published in 1958 by Phillip W. Anderson has had a tremendous impact. In this work, Anderson proved that the presence of uncorrelated disorder in the crystalline lattice was able to completely halt electronic transport [1].

1.1.1 Introduction to Anderson localization

By using a tight-binding model with random on-site energies ν_i and random couplings $t_{i,j}$ (see Appendix A), Anderson [1] demonstrated that beyond a certain disorder value, the motion of the electrons completely stops: they are exponentially trapped in the system. For instance, Fig. 1.1 shows a minimalist diagram of a 1D tight-binding system in the $\hat{x}$-axis, sketching an exponentially localized eigenstate ψ that can be represented as

$$|\psi| \propto \mathrm{e}^{-|x-x_0|/\xi} + \text{fluctuations}, \tag{1.1}$$

where x_0 is the "center" of the mode, and ξ is the so-called localization length, which represents the decay length of the state inside the lattice.

Due to their spatial localization, the electrons cannot participate to the conduction, leading to a disorder-driven phase transition from metal to insulator. As it typically occurs in phase transitions, Anderson localization strongly depends on the dimensionality of the system. For instance, a couple of years after Anderson's first work was released, Mott and Twose [32] proved that all states in 1D random systems are actually localized. This result cannot be directly extended to higher dimension. In particular, in 3D it emerged

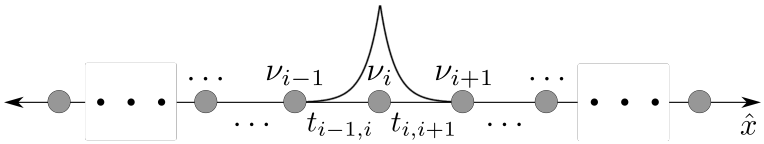

Figure 1.1: Simplified diagram of a tight-binding lattice with random on-site energies ν_i and random couplings $t_{i,j}$; a schematic representation of a localized eigenstate.

the "mobility edge" concept: a threshold that separates extended and localized modes, and therefore the metallic and the insulating regimes [33].

1.1.1.1 The Thouless conductance

Thouless and coworkers proposed to describe the phase transition between the metallic and the insulating regimes in a finite system by a single parameter g, now called the Thouless conductance, and defined as [34–37]

$$g = \frac{\delta\omega}{\Delta\omega}, \tag{1.2}$$

where $\delta\omega$ is the typical width of an eigenmode which is related to the sensitivity of the mode to the boundary, and $\Delta\omega$ is the mean level spacing between neighbouring modes in the frequency domain. If the modes are localized and not too close to the boundary, their spectral width is much smaller than the separation between them. Therefore, the value of the Thouless conductance drops down below the unity, and conductivity is suppressed [see Fig. 1.2(a)]. In contrast, non-localized modes reach and leak through the boundary, leading to large values of $\delta\omega$. Thus, the eigenmodes spectrally overlap allowing electronic Ohmic transport [see Fig. 1.2(b)]. Indeed, the Thouless conductance has become a key quantity in localization theory, and nowadays it is used as a fundamental criterion for Anderson localization in disordered systems, establishing that localization occurs for $g < 1$ [37, 38].

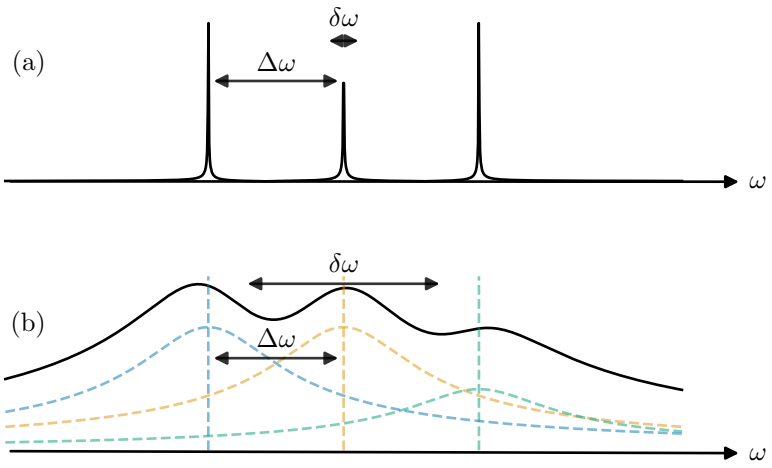

Figure 1.2: Simplified diagram of (a) isolated and (b) overlaping modes.

1.1.1.2 The Scaling localization theory

In 1979, the Thouless conductance was used to understand Anderson localization in higher dimensions by considering an hypercube of size L^D [39]. In this model, the metallic regime follows a macroscopic Ohmic conductor behaviour which is described by

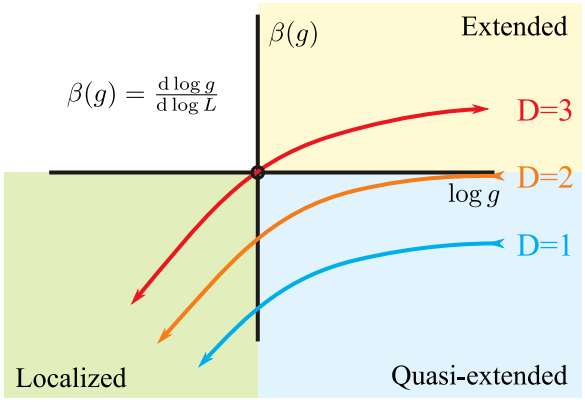

Figure 1.3: Scaling function $\beta(g)$ for D=1, 2, 3, showing the transition between different transport regimes. The sign of $\beta(g)$ indicates the direction of the flow: if β grows or decreases with respect to L. Image adapted from Ref. [42].

$g \propto \sigma L^{D-2}$. On the other hand, the exponential spatial localization in the isolating regime ($g \ll 1$) leads g to also fall off in an exponential way, that is $g = g_\xi \mathrm{e}^{-L/\xi}$, with g_ξ a dimensionless ratio depending only on the localization length ξ [39, 40]. Using these asymptotic forms of g, it was possible to develop a more sophisticated theory—*the scaling theory of localization*—for finite systems at higher dimensions. A scaling function was then defined as [39, 41],

$$\beta(g) = \frac{\mathrm{d}\log g}{\mathrm{d}\log L}, \tag{1.3}$$

where it was found that $\lim_{g\to\infty} \beta(g) = D - 2$ in the metallic regime and $\lim_{g\to 0} \beta(g) = \log g$ in the insulating regime. As depicted in Fig. 1.3, by taking into account these two asymptotic limits and the assumption that there is a continuous transition between them, the scaling function describes how the conductance scales with L, and settles the transition between different transport regimes at different dimensions.

The scaling theory of localization confirmed that in 1D, even a small amount of disorder is sufficient to localize a wavefunction, and established the same result for 2D lattices. Nevertheless, small 2D systems can still look as conductors in the quasi-extended regime, with all the states becoming completely localized when L increases. Opposite to those cases, in 3D there is a phase transition between a conducting phase (extended states) and an insulating phase (localized states) at a critical disorder, where the corresponding mobility edge has been completely characterized using the tight-binding formalism [43].

Anderson localization, a concept that originated in electronic transport, is based on the properties of matter waves. Since the emergence of physics of ultracold atoms gases, the manipulation of the latter are not restricted to the realm of condensed matter. Thus, localization has been observed with matter waves propagating in 1D or 3D disordered light potentials—laser speckles playing the role of impurities [44–48]. These observations have demonstrated that the central mechanism in the Anderson localization phenomenon is provided by the interference of matter waves multiply scattered by disorder. It can thus be naturally extended to all types of waves propagating in a disordered medium. For instance, inhomogeneous aluminum plates were used to give a classical picture of Anderson localization in elastic systems [3]. Later, localization in 3D aluminium beads clusters was reported using ultrasound waves [6]. And finally, Anderson localization has been successfully measured using 1D aluminum structured rods [4, 5].

1.1.2 Current debate on 3D light

Naturally, electromagnetic waves have been proposed several times as a good classical candidate to study Anderson localization [2, 11]. Starting from the early theoretical predictions [49, 50], localization of electromagnetic waves has been experimentally achieved in 1D and 2D photonic lattices [12–14], optical fibers [7, 8], as well as in 2D microwave cavities [15, 16] and even in quasi-2D biological media [51]. However, despite a significant experimental effort, studies claiming to have observed Anderson localization of light in 3D systems have all failed due to various experimental artifacts [21].

In 1997, Wiersma et al. [17] reported direct experimental evidence of Anderson localization with infrared light in strongly scattering semiconductor powders. These findings were firstly questioned by Scheffold et al. [52] two years later, and then finally refuted by their main authors [20], under the argument that the observed effects were not due to localization but the presence of absorption. Around the same time, Anderson localization was explored even in presence of optical absorption in thick wires, ruling out the possibility of 3D light localization in these samples [53].

New claimings about 3D electromagnetic localization were published in 2006 by Störzer et al. [18] and later in 2013 by Sperling et al. [19], presenting measurement of transport through bulk powders of TiO_2, where experiments were designed to be insensitive to absorption. However, such results were quickly questioned by Scheffold and Wiersma [54], who argued that non-linear effects—mainly inelastic scattering in the sample—could be easily confused with localization effects. Both works were finally refuted by Sperling et al. [21], demonstrating that previous data can be explained by a fluorescence process.

In recent years, numerous theoretical and numerical studies have led to significant progress towards a better understanding of Anderson localization of light. For instance, Skipetrov and Sokolov [22] reported the absence of light localization in 3D random ensembles of N immobile point dipoles [see inset in Fig. 1.4(a)]. The eigenvalues of the system are computed using the Green's matrix formalism [55] considering only the scalar or the vector character of light. Later, the authors extract the Thouless conductance as a function of the system size [Eq. (1.2)] and therefore the scaling function $\beta(g)$ [Eq. (1.3)]. As depicted in Fig. 1.4, Skipetrov and Sokolov [22] demonstrated that in the scalar case, it exists a change of sign of the scaling function $\beta(g)$, confirming an Anderson transition (see Fig. 1.3). However, no signature of Anderson localization has been observed in the vector case, where $\beta(g)$ never changes its sign.

Differently to 1D and 2D cases, 3D Anderson localization requires stronger disorder and higher dense media to go through the mobility edge. Consequently, near-field

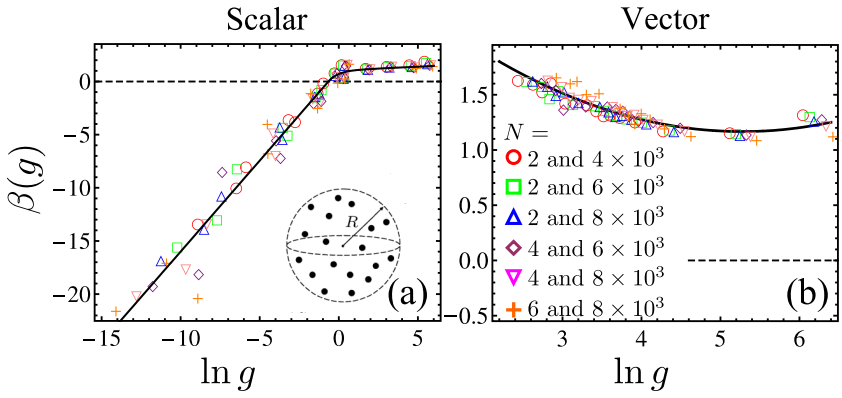

Figure 1.4: Scaling function $\beta(g)$ as a function of the Thouless number g in the (a) scalar and (b) vector models of light. Localization transition takes place for $\beta(g) < 1$. Different symbols are related with different densities. Figure adapted from Ref. [22].

coupling between the scatterers, which become important for high densities, seems to play an important role to prevent localization [10, 23]. A couple of years ago, van Tiggelen and Skipetrov [24] demonstrated that the interference between the longitudinal and transversal modes of the electromagnetic field is actually at the origin of new transport near-field channels. However, more recently Yamilov et al. [25] numerically showed the existence of a three dimensional localization transition of vector electromagnetic light using random packs of metallic spheres [see Fig. 1.5]. Remarkably, the same work denotes the absence of localization when considering high refractive index dielectrics. Localization of 3D electromagnetic waves have been achieved in dielectric system by adding certain correlation to the disordered pattern [56, 57]. These last works open a broad range of possibilities in the fundamental quest of Anderson localization of 3D light.

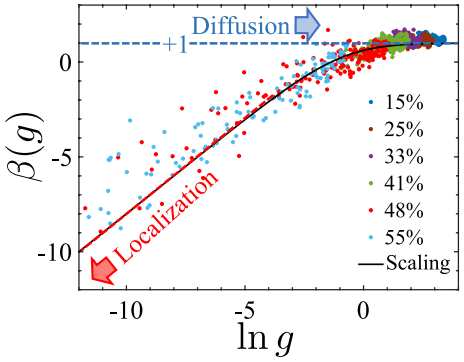

Figure 1.5: Scaling function $\beta(g)$ as a function of the Thouless number g for the vector model of light in 3D random metallic spheres arrangements. Localization transitions take place for $\beta(g) < 1$. Different symbols are related with different densities. Blue and red lines represent the diffusive and localized scaling behaviour $g \propto R$ and $g \propto \exp(-L/\xi)$, respectively. Figure adapted from Ref. [25].

1.1.3 The localization landscape

Among the different tools developed to study and understand Anderson localization, a new promising technique to investigate this phenomena (and many other wave effects) was proposed almost one decade ago [26]. This method is called the Localization landscape and is able to decode the information (such as to predict the position of the eigenfunctions and their energies) of a Hamiltonian without solving the eigenvalue problem. Additionally, in disordered systems, it allows the analysis sample by sample, avoiding a statistical approach. In this section, we follow the first theoretical works on the topic to illustrate the main properties of the localization landscape in continuous quantum systems.

1.1.3.1 The general definition

To present the localization landscape theory, a quantum particle of mass m in an Hermitian random potential V is considered. Here, the continuous Schrödinger equation for an eigenfunction ψ with eigenenergy E is written

$$\left(-\frac{\hbar^2}{2m}\Delta + V\right)\psi = E\psi \quad \text{in} \quad \Omega \quad \text{with} \quad \psi\Big|_{\partial\Omega} = 0, \tag{1.4}$$

where Ω is the domain, and Dirichlet boundary conditions have been considered, without loss of generality. For instance, Fig. 1.6(a) shows a random uniform potential between 0 and 1 for a one-dimensional quantum system of length L. The quantum modes corresponding to this potential are obtained by diagonalising Eq. (1.4). Fig. 1.6(c)

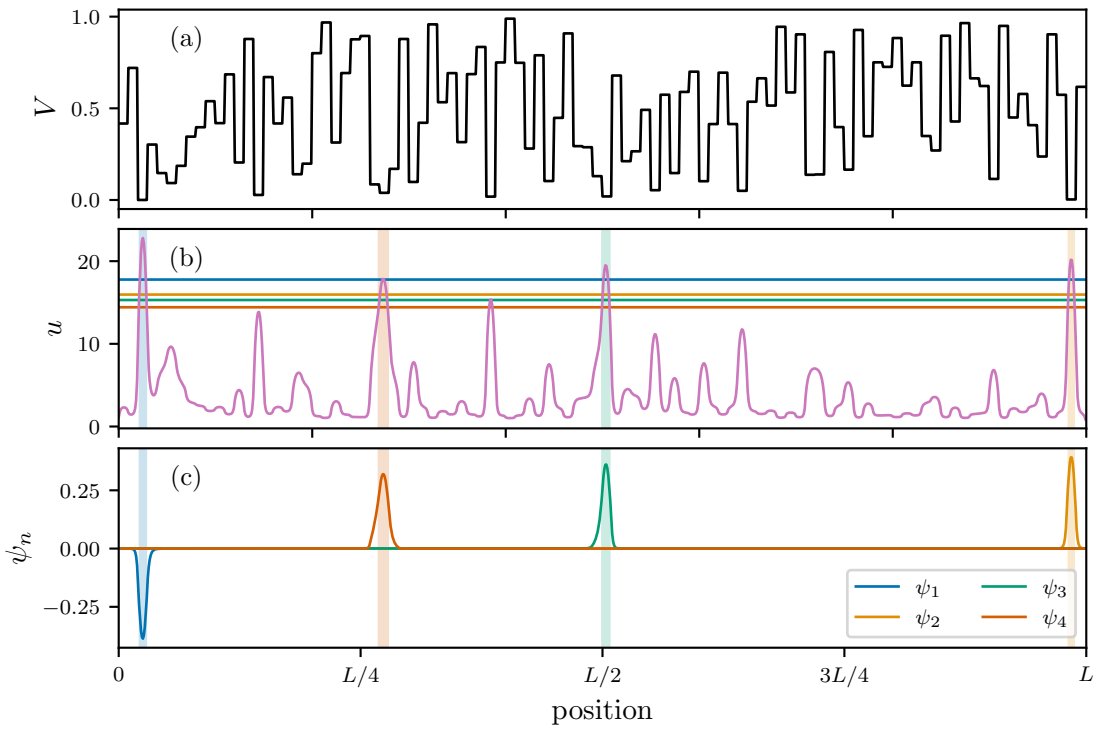

Figure 1.6: (a) Random potential V for a 1D system of length $L = 1000$ sites with Dirichlet boundary conditions. The value of the potential remains constant in intervals of 10 sites. Each random value is taken from a uniform random variable in the interval [0,1]. (b) Localization landscape u computed using Eq. (1.9) corresponding to the potential shown in (a). Horizontal color lines indicate the values $1/E$. (c) First four eigenfunctions ψ_n of lowest energies. States are characterized by energies: $E_1 = 0.0563$, $E_2 = 0.0627$, $E_3 = 0.0653$, and $E_4 = 0.0693$. Vertical colorful stripes indicate the localization subregions where $u > 1/E$ for each state.

depicts then the four eigenstates with lowest energies (with $\hbar^2/2m = 1$). Despite that the position of the states seems to be related with some of the minima of the potential V, no straightforward relations can be found either for the modes nor their energies. Therefore, we can briefly conclude that resolving the eigenvalue problem is an unavoidable condition to obtain any information about the behaviour of the particle in the potential.

Since the Laplacian Δ is an Hermitian operator, the hermiticity of $\mathcal{L} = -\Delta + V$ depends only on the hermiticity of the potential V. In this context, an eigenfunction $\psi(\mathbf{r})$ can be rewritten in terms of the resolvent $G(\mathbf{r}, \mathbf{r}')$ of $\mathcal{L}$, namely the Green's function

$$\begin{aligned} \psi(\mathbf{r}) &= \int_\Omega \psi(\mathbf{r}')\delta(\mathbf{r}' - \mathbf{r})\,\mathrm{d}\mathbf{r}' = \int_\Omega \psi(\mathbf{r}')\mathcal{L}_{\mathbf{r}'}G(\mathbf{r}, \mathbf{r}')\,\mathrm{d}\mathbf{r}'\,, \\ &= \int_\Omega G(\mathbf{r}, \mathbf{r}')\mathcal{L}_{\mathbf{r}'}\psi(\mathbf{r}')\,\mathrm{d}\mathbf{r}' = E\int_\Omega G(\mathbf{r}, \mathbf{r}')\psi(\mathbf{r}')\,\mathrm{d}\mathbf{r}'\,. \end{aligned} \tag{1.5}$$

with $\mathbf{r}$ and $\mathbf{r}' \in \Omega$. Then,

$$\begin{aligned} |\psi(\mathbf{r})| = |E|\left|\int_\Omega \psi(\mathbf{r}')G(\mathbf{r}, \mathbf{r}')\,\mathrm{d}\mathbf{r}'\right| &\leq |E|\int_\Omega \big|G(\mathbf{r}, \mathbf{r}')\big|\big|\psi(\mathbf{r}')\big|\,\mathrm{d}\mathbf{r}'\,, \\ &\leq |E|\,\sup_\Omega(|\psi|)\int_\Omega \big|G(\mathbf{r}, \mathbf{r}')\big|\,\mathrm{d}\mathbf{r}'\,, \end{aligned} \tag{1.6}$$

where $\sup_\Omega(|\psi|)$ is the maximum of the function ψ in Ω. Furthermore, the localization landscape can be formally defined as [26]

$$\boxed{u(\mathbf{r}) = \int_\Omega \big|G(\mathbf{r}, \mathbf{r}')\big|\,\mathrm{d}\mathbf{r}'\,.} \tag{1.7}$$

The choice of a real positive definite potential V leads to a positive definite $\mathcal{L}$, and consequently a real and non negative Green's functions. Ergo, the application of $\mathcal{L}$ over u produces

$$\mathcal{L}_{\mathbf{r}} u(\mathbf{r}) = \int_{\Omega} \mathcal{L}_{\mathbf{r}} G(\mathbf{r}, \mathbf{r}')\, \mathrm{d}\mathbf{r}', \tag{1.8}$$

$$\boxed{\mathcal{L}u = 1.} \tag{1.9}$$

As observed, this simple and elegant definition of the landscape [Eq. (1.9)] follows a differential equation given by the same operator $\mathcal{L}$ with the same boundary conditions of the original problem, but now equal to the unity. The localization landscape, plotted in Fig. 1.6(b) as the solution of Eq. (1.9) for the potential in Fig. 1.6(b), is a complex relief composed by peaks and valleys. On the contrary to what we observed for the potential, the position of the localized functions seem now to be related with the maxima of u.

Under the correct normalization of the eigenmodes [$\sup_{\Omega}(\psi) = 1$], the inequality (1.6) is written

$$|\psi| \leq Eu. \tag{1.10}$$

As u is independent of the eigenvalue problem, the eigenfunction ψ with energy E is constrained to be smaller than the landscape at its local minima. The normalization of the eigenstates also implies an effective constrain only for $uE < 1$. That means that the mode with energy E is restricted to live in the portion of the landscape where $u > 1/E$, i.e. the regions in which the inverse of the respective eigenenergy is smaller than the landscape. This natural condition defines the localization subregions of the domain Ω [26, 58, 59]. In Fig. 1.6(b), horizontal color lines are the values $1/E_n$ whose crossover with the landscape determines the localization subregions, highlighted by vertical colorful stripes in panels (b) and (c). It is clear that each eigenfunction dwells in the subregion regulated by the inequality $uE < 1$. As E increases, the space available for each mode increases too, explaining the delocalization of the states.

Undoubtedly, the localization landscape u is more appropriate to predict the position of the eigenstates, that cannot be guessed from the original potential V. This fact establishes the landscape as an useful tool that allows to save computation time without apparently precision losses. For instance, the landscape formalism has been already used to decode the pattern of hot spots of vibrations energy localization in proteins [60]. Lemut et al. [61] has extended the formalism to Dirac Fermions and non-Hermitian Hamiltonians via the Ostroski's comparison matrix [62, 63] and its definition in quantum graphs was firstly proposed some years ago by Harrell and Maltsev [64]. The first experimental demonstration of the LL theory was presented by Lefebvre et al. [65] with mechanical waves. In this case, the Shrödinger equation is replaced by the Kirchhoff-Love equation. By constructing the adapted $\mathcal{L}$ operator, Eq. (1.9) provides the analytical expression of the elastodynamic localization landscape. Using a thin clamped plate, the localization landscape is found to be proportional to the deformation of the plate under an uniform load. Thus, the authors obtained a direct measurement of the localization landscape, and compared it successfully to the theoretical prediction.

1.1.3.2 Localization landscape as a confining potential

Another interpretation of the localization landscape u can be found by considering the auxiliary function $\phi = \psi/u$ into the Shrödinger equation (1.4) [58]

$$\begin{aligned} \left(-\frac{\hbar^2}{2m}\Delta + V\right)(\phi u) &= E\phi u, \\ \left(-\frac{u\hbar^2}{2m}\Delta\phi - \frac{2\hbar^2}{2m}\nabla u \cdot \nabla\phi - \frac{\phi\hbar^2}{2m}\Delta u + V\phi u\right) &= E\phi u, \end{aligned} \tag{1.11}$$

where the third and fourth terms in the left-hand side are replaced by the definition (1.9). Thus

$$\left(-\frac{\hbar^2}{2m}\Delta\phi - \frac{2\hbar^2}{2m}\frac{\nabla u}{u}\cdot\nabla\phi + \frac{\phi}{u}\right) = E\phi, \tag{1.12}$$

$$-\frac{\hbar^2}{2m}\left[\frac{1}{u^2}\nabla\cdot\left(u^2\nabla\phi\right)\right] + W\phi = E\phi, \tag{1.13}$$

where $W \equiv 1/u$ has the dimension of an energy. Eq. (1.13) is a differential Schrödinger-type equation of the variable ϕ, and it is completely independent of the potential V. Nevertheless, the new potential term W has emerged, and plays the role of an "effective confining potential".

As the localization landscape, W is independent of the eigenvalue problem and its minima corresponds to the maxima of u. In other words, the localization subregions are now determined by the valleys of W and its crests act as barriers for the eigenfunctions of the original Hamiltonian. Thus, the localization subregions are now determined by the inequality $W < E$. For instance, Fig. 1.7(a) shows a comparison between both original and confining potentials, V and W. Note that W looks like a smoother version of V. Additionally, it has been proven that both differential operators in Eqs. (1.4) and (1.13) possess exactly the same spectrum [59, 66]. The horizontal brown line in Fig. 1.7(a) is the energy value corresponding to the 15th excited mode which is logarithmically depicted in Fig. 1.7(b). The linear drop of the state in logarithmic scale indicates the well know exponential decay of Anderson localized modes. All localization subregions are highlighted by vertical brown stripes in Fig. 1.7(b). Note that ψ_{15} drops exactly in the forbidden subregions $W > E_{15}$. The complete formalism of the localization landscape together with the confining potential has been already extended to many-body systems by Balasubramanian, Liao, and Galitski [67], and to real symmetric non-singular $\mathcal{M}$-matrices by Filoche, Mayboroda, and Tao [68].

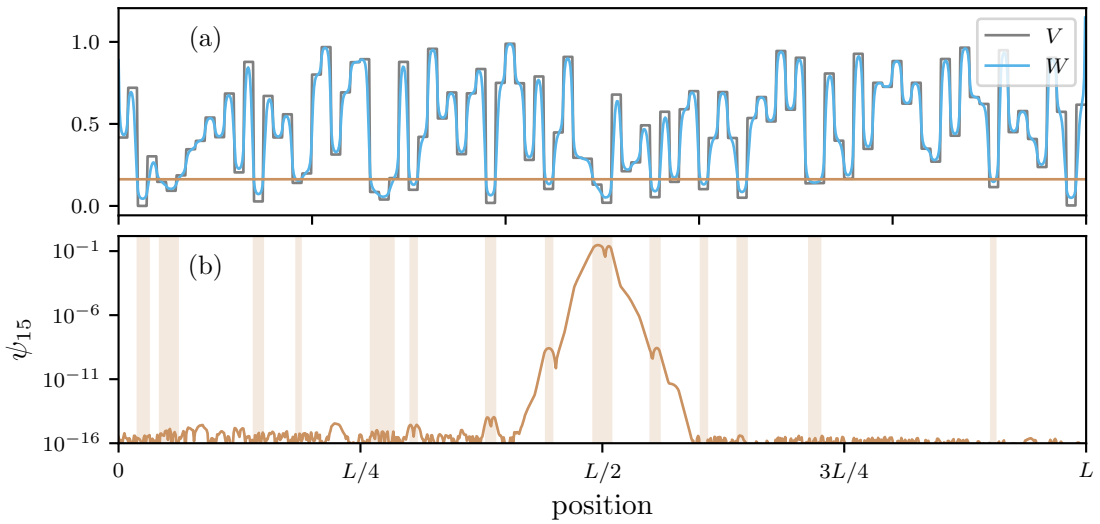

Figure 1.7: (a) Random potential V for a 1D system of length $L = 1000$ sites with Dirichlet boundary conditions (black). Effective confining potential W (indigo). The value of V remains constant in intervals of 10 sites and each random value is taken from a uniform random variable in the interval [0,1]. The horizontal brown line indicates the value $E_{15} = 0.1626$. (b) 15th eigenfunction ψ_{15}. The vertical colorful stripes indicate the localization subregions where $W < E_{15}$.

1.1.3.3 Prediction of the eigenvalues

As already shown, the localization landscape delimits the localization subregions allowing to extract the location of the eigemodes without solving the eigenvalue problem. To show another advantage of this powerful tool, we assume that the eigenfunction ψ_0 of the operator $\mathcal{L}$ is well localized and associated to a small eigenvalue [59]. As a consequence, ψ_0 is supported in a small subdomain Ω_0 where it is the fundamental Dirichlet eigenstate. We consider that in this subdomain Ω_0, the landscape can be approximated as the product of the fundamental mode ψ_0 and a constant c_0. To prove this last assumption, one can take Eq. (1.9) in the subdomain, and then expand the constant 1 in terms of the eigenfuntions

$$\mathcal{L}u = \sum_n c_n \psi_n. \tag{1.14}$$

Later, only the first term is kept and all others are dropped off

$$\begin{aligned} \mathcal{L}u \approx c_0\psi_0 = \frac{c_0\mathcal{L}\psi_0}{E}, \\ u \approx \frac{c_0\psi_0}{E}. \end{aligned} \tag{1.15}$$

By using the previous hypothesis together with the Rayleigh quotient [69], and the definition (1.9), the eigenvalue of the function ψ is written

$$\begin{aligned} E = \frac{\int_\Omega \psi_0 \mathcal{L}\psi_0 \,\mathrm{d}x}{\int_\Omega \psi_0^2 \,\mathrm{d}x} \approx \frac{\int_{\Omega_0} \psi_0 \mathcal{L}\psi_0 \,\mathrm{d}x}{\int_{\Omega_0} \psi_0^2 \,\mathrm{d}x}, \\ \approx \frac{\int_{\Omega_0} u\mathcal{L}u \,\mathrm{d}x}{\int_{\Omega_0} u^2 \,\mathrm{d}x} = \frac{\int_{\Omega_0} u \,\mathrm{d}x}{\int_{\Omega_0} u^2 \,\mathrm{d}x}. \end{aligned} \tag{1.16}$$

Finally, we assume now that u can be approximated by a quadratic bump-like function in Ω_0, that is

$$u \approx u_{\max}\left[1 - \sum^D \left(\frac{x_i}{a_i}\right)^2\right] \text{ where } \Omega_0 \approx \left\{\mathbf{r} \in \mathbb{R}^n | \sum^D \left(\frac{x_i}{a_i}\right)^2 \leq 1\right\}, \tag{1.17}$$

for a given set of constants a_i and D the dimension of the system. The eigenvalue is then written

$$E \approx W_{\min} \frac{\int_{\Omega_0}\left[1 - \sum^D \left(\frac{x_i}{a_i}\right)^2\right] \mathrm{d}\mathbf{r}}{\int_{\Omega_0}\left[1 - \sum^D \left(\frac{x_i}{a_i}\right)^2\right]^2 \mathrm{d}\mathbf{r}}, \tag{1.18}$$

where the integrals can be computed by performing the change of variable $x_i/a_i \to x_i'$ and then integrated in polar coordinates. We obtain

$$\begin{aligned} E \approx W_{\min} \frac{\int_0^1 \left(1 - r^2\right) r^{D-1} \,\mathrm{d}r}{\int_0^1 \left(1 - 2r^2 + r^4\right) r^{D-1} \,\mathrm{d}r}, \\ E \approx \left(1 + \frac{D}{4}\right) W_{\min}, \end{aligned} \tag{1.19}$$

which is completely independent of the values a_i. Eq. (1.19) is numerically demonstrated for 1D and 2D systems in Fig. 1.8, where the ratio $E/W_{\min}$ as a function of the state

number is shown. Random potentials made up of uniform numbers between 0 and 1 keep a constant value along linear intervals of 10 sites in 1D case, and in square areas of 5×5 sites in 2D. The corresponding lengths are (1D) $L = 4000$ sites and (2D) $L \times L = 100 \times 100$ sites. The proportional constants $(1 + D/4)$ in Eq. (1.19) are numerically extracted as $\langle E/W_{\text{min}} \rangle \approx 1.23 \pm 0.04$ and $\langle E/W_{\text{min}} \rangle \approx 1.51 \pm 0.04$ for a 1D and 2D systems, respectively. These results are in agreement with previous numerical findings in Ref. [59] and show another characteristic of the landscape method.

Recently, the localization landscape approach has been used to predict the eigenfunction and eigenenergies of confined states in semiconductor structures [70]. Previous predictions were also experimentally demonstrated and used to characterize the effect of compositional disorder in InGaN layers [71]. Finally, the method was successfully implemented to model the optical emission, and the carrier transport of LED heterostructures including the effects of disorder [72], or the light absorption in disordered semiconductor alloys [73].

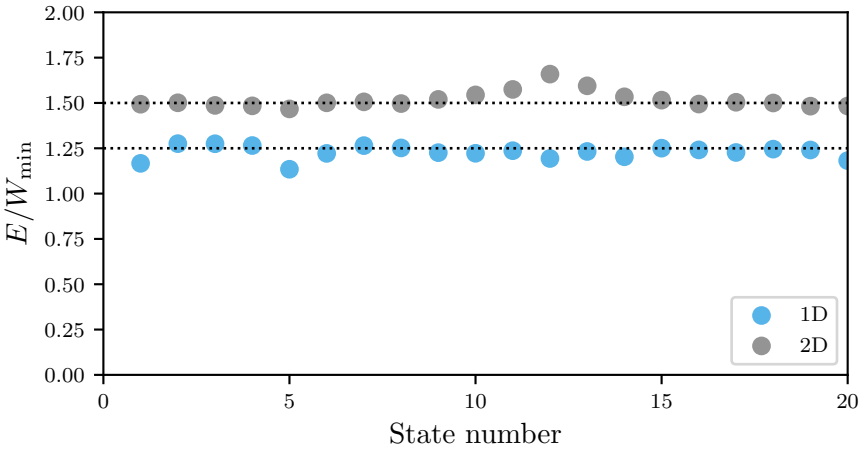

Figure 1.8: Ratio between the first 20 eigenvalues of disordered systems and the minima of their confining potential for a 1D (indigo) and 2D (gray) systems. Black dashed lines are the corresponding Eq. (1.19).

1.1.3.4 Positional limitations

As shown along this section, the landscape approach has proven to be an undisputed method to extract important information without dealing with the eigenvalue equation. The definition of the localization subregions together with the prediction of the energies establish a direct connection between W and each eigenfunction ψ. Nevertheless, a one to one correspondence between the rank of the eigenmodes and the minima of W is not always fulfilled. For instance, Fig. 1.9(a) and (b) present the confining potential and the first four states of a 2D disordered system, respectively. The minima of W and the eigenfunctions have been ranked and labeled, showing an ordering imprecision in the 3rd and 4th states even though their positions are correctly predicted. The break in the correspondence occurs when two of more eigenenergies are nearly equal, and analogously if two of more minima of W are almost the same.

Table 1.1 shows the actual values for both quantities, unveiling that the energies of the third and four states of (a) and (b) are slightly similar. However, the values of W_{min} are well separated from each other in this particular case.

Another problematic situation occurs when one basin contains two different minima. As illustrated in Figs. 1.9(c) and (d), the 1st and 3rd minima are contained by the same potential well in this case. Therefore, the 3rd minimum does not lead to a separate mode. The corresponding values of the energies and minima of W are included in Table 1.2. As we

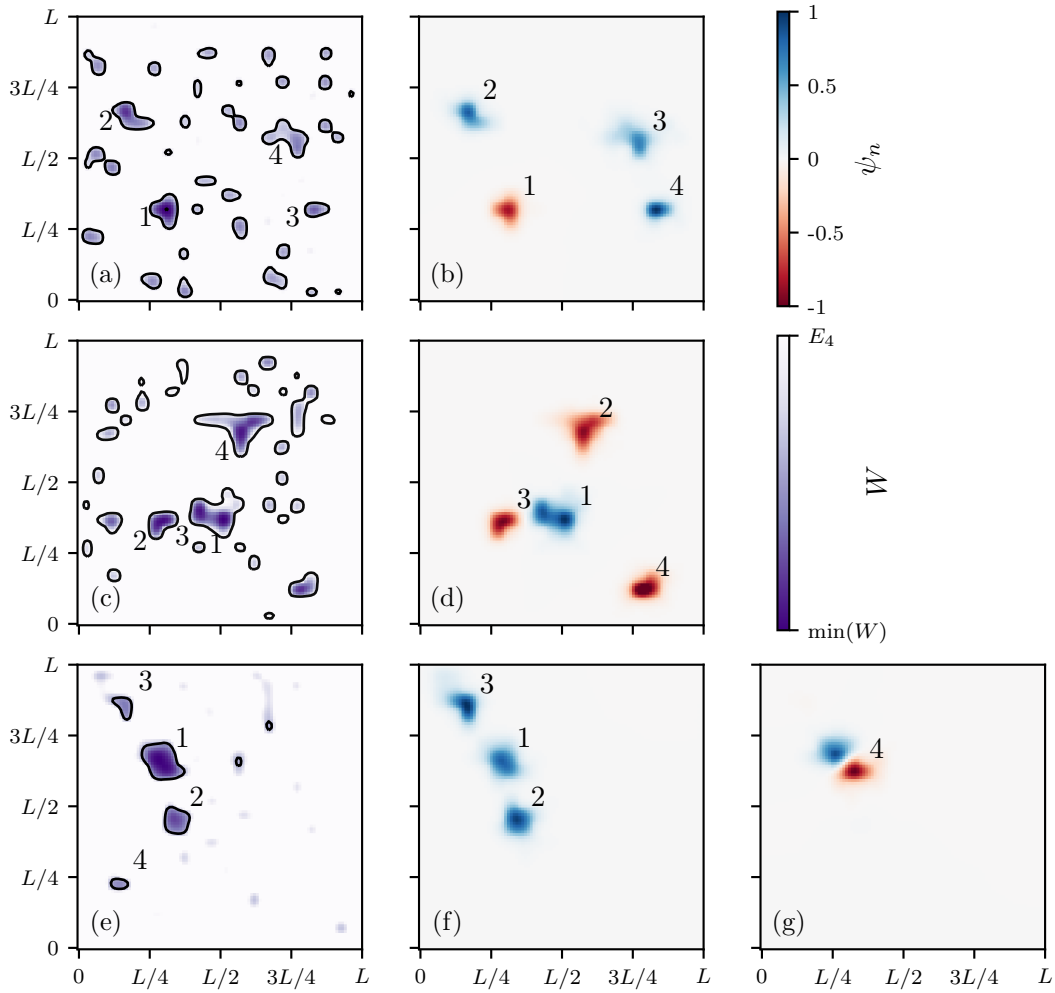

Figure 1.9: [(a), (c), and (e)] Effective confining potential W relative a the potential V (not shown). The potential V is different in each case. Each random potential V remains constant in squared areas of 5×5 sites in a 2D system of size $L \times L = 100$ sites with Dirichlet boundary conditions. Random values are taken from an uniform random variable in the interval [0,1]. Confining potentials are plotted considering a maximum threshold $W = E_4$. [(b), (d), (f) and (g)] First four eigenfunctions ψ_n with lowest energies corresponding to the confining potentials at left.

Table 1.1: Values of the effective potential at its first four minima, and first four eigenvalues for the eigenfunction shown in Figs. 1.9(a), and (b).

(a)

	1	2	3	4
$W_{\min}$	0.1240	0.1473	0.1663	0.1790
E	0.1927	0.2266	0.2548	0.2610

Table 1.2: Values of the effective potential at its first four minima, and first four eigenvalues for the eigenfunction shown in Figs. 1.9(c), and (d).

(c)

	1	2	3	4
$W_{\min}$	0.1331	0.1374	0.1400	0.1412
E	0.1970	0.2004	0.2030	0.2289

can observe, both the 1st and 3rd minima are not just close in position, but also in value. Additionally, the energies of the first three eigenfunctions are nearly equal, explaining the switching in the ordering of the 2nd and 3rd states.

The last situation appears when one wide potential well contains more that one eigenfunction. As the energy of the state defines the localization subregions, the probability to repopulate a given potential well increases for higher energies [26]. This fact is exemplified in Fig. 1.9(e), (f) and (g), presenting again the confining potential and the first four eigenmodes of a 2D disordered potential. Note that the 4th state is depicted alone in panel (g) to avoid the overlap with the 1st mode. In this example, the first three functions are well predicted by the minima of W, however the fourth one is placed again in the first basin, which is wider than others (see Ref. [59] for further details).

All these problems, together to the limitation imposed by total number of local minima of W, limit the prediction accuracy to the low energy part of the spectrum. However, the localization landscape has shown to be a tool able to obtain important information avoiding the diagonalization of the Hamiltonian, having remarkably good result at low energy. Because of that, the utility of all the landscape machinery has been broadly extended to different wave phenomena in physics. For instance, this theory has been also used to compute spectral function in cold atoms physics [74], and subsequently, to predict the mobility edge of 3D tight-binding systems [75]. Nevertheless, an electromagnetic landscape model is still missing. In Chapter 3, the localization landscape theory is directly applied to the Maxwell's equations with the aim to develop an electromagnetic landscape able to answer the devilish questions about localization of 3D light. The second section of the same Chapter 3 tackles the issue of the landscape for tight binding Hamiltonians for a wide class of 1- and 2D materials, where localization occurs at both low- and high-energy [43].

1.2 Localization via correlation in the potential

Along the road to find Anderson localization of 3D electromagnetic waves, different authors pointed out the importance of the spatial correlation of scatterers to prevent light transport [10, 22, 56, 57, 76–80]. Besides localization, heterogeneous correlated media have shown to be also characterized by distinct transport regimes such as diffusion or transparency depending on the frequency [81]. For instance, in 1899 Lord Rayleigh [82] explained that the blue color of the sky was given by the collective effect of the electromagnetic diffusive scattering by the atmosphere particles. Later, the transparency of the cornea for visible light [83–85], and the blue facial skin in male mandrills (*Mandrillus sphinx*) [86] were attributed to short-range correlation in the collagen fibers of the tissue [see Figs 1.10(a) and (b), respectively].

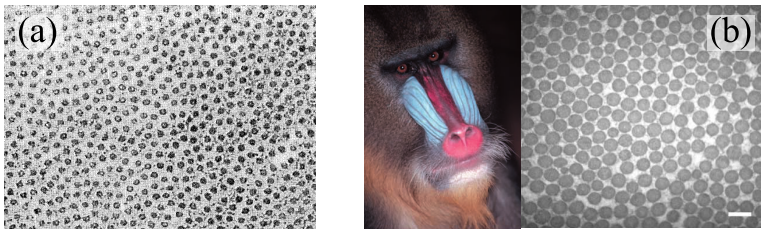

Figure 1.10: (a) Electron micrograph of the collagen fibrils of the cornea. Adapted from Ref. [83]. (b) Transmission electron micrographs of collagen arrays from structurally coloured Male mandrill facial skin. Adapted from Ref. [86].

1.2.1 Structural properties of correlated media

A full understanding and control of light transport in photonic media is crucial for the efficient design of optical structures. Controlling light transport in photonic materials involves the ability not only to understand but also to engineer the electromagnetic modes

that such systems can support. Given the rich structural variety that correlated disordered media can display, electromagnetic transport is affected in different ways depending on the specific correlations [87]. To describe then the correlation in random heterogeneous structures, we start by assuming a system composed by N particles with spatial positions $\mathbf{r}_i$ $(i = 1, \cdots, N)$ in a volume V. Therefore, the configuration of each particles can be statistically characterized by the normalized N-particle probability density function [88]

$$P_N(\mathbf{r}_1, \mathbf{r}_2, \ldots, \mathbf{r}_N)\mathrm{d}\mathbf{r}_1\mathrm{d}\mathbf{r}_2 \cdots \mathrm{d}\mathbf{r}_N, \tag{1.20}$$

which represents the probability of finding the center of particle i in the volume element $\mathrm{d}\mathbf{r}_i$ around $\mathbf{r}_i$. The exact form of $P_N(\cdot)$ depends on the specific interaction between the particles as well as their precise positions and shapes. Thus, for such huge ensembles of indistinguishable spherical particles, it is useful to define the probability of finding any subset of n particles in a volume element $\mathrm{d}\mathbf{r}^n$ as

$$\rho_n(\mathbf{r}^n) = \frac{N!}{(N-n)!}\int P_N(\mathbf{r}_1, \mathbf{r}_2, \ldots, \mathbf{r}_N)\mathrm{d}\mathbf{r}_{n+1}\mathrm{d}\mathbf{r}_{n+2} \cdots \mathrm{d}\mathbf{r}_N, \tag{1.21}$$

which is also called the *generic* n-particle probability density function. Note that the definition (1.21) is not normalized

$$\int \rho_n(\mathbf{r}^n)\mathrm{d}\mathbf{r}^n = \frac{N!}{(N-n)!}, \tag{1.22}$$

therefore, considering $n = 1$ leads to $\int \rho_1(\mathbf{r})\mathrm{d}\mathbf{r} = N$. In that way, assuming a statistically homogeneous isotropic distribution, ρ_1 corresponds to the total density $\rho_1 = \rho = N/V$ [89].

In this point, it is useful to show one interesting example. By considering the case of an uncorrelated non-interacting overlapping set of particles [see Fig. 1.11(a)], the probability function (1.20) is written as $P_N = 1/V^N$, and therefore, the probability (1.21) becomes [88]

$$\rho_n(\mathbf{r}^n) = \rho^n. \tag{1.23}$$

In this way, we define the n-correlation function as a measure of the particle correlation with respect to the completely random case [90]

$$g_n(\mathbf{r}^n) = \frac{\rho_n(\mathbf{r}^n)}{\rho^n}. \tag{1.24}$$

where $g_n(\mathbf{r}^n) = 1$ for a disordered uncorrelated system [see e.g. Fig. 1.11(b) for g_2].

It is important to define the pair correlation function

$$g_2(\mathbf{r}_{12}) = \frac{\rho_2(\mathbf{r}_{12})}{\rho^2}. \tag{1.25}$$

that for an isotropic system depends only on the distance between the two particles $g_2(\mathbf{r}_{12}) = g_2(r)$, and is therefore called the *radial distribution function*. The pair correlation function describes the conditional probability of finding one particle given the presence of another particle at the origin. Using Eq. (1.25), one can also define the total correlation function $h(\mathbf{r})$ as

$$h(\mathbf{r}) = g_2(\mathbf{r}) - 1, \tag{1.26}$$

which has the particularity to converge to zero in the non correlated case $h(r) \to 0$.

Another important quantity to understand correlations in wave physics is the *structure factor* $S(\mathbf{k})$, that describes how electromagnetic waves are scattered by the material as a function of the incident wave-vector $\mathbf{k}$ [88]. It is defined as

$$S(\mathbf{k}) = 1 + \rho\bar{h}(\mathbf{k}), \tag{1.27}$$

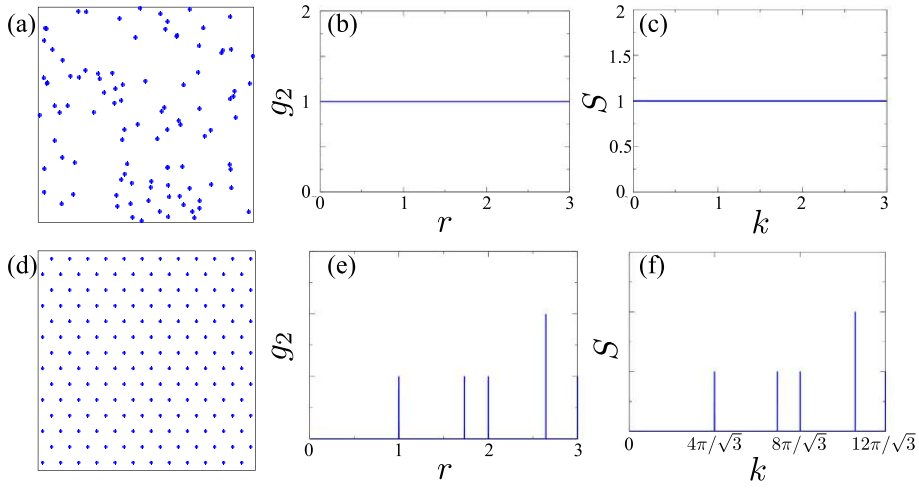

Figure 1.11: (a) Portion of an infinite uncorrelated point pattern. (b) Angular-averaged pair correlation function g_2 for the array in (a). (c) Angular-averaged structure factor S for the array in (a). (d) Portion of an infinite triangular lattice. (e) Angular-averaged pair correlation function g_2 for the array in (d). (f) Angular-averaged structure factor S for the array in (d). Adapted from Ref. [91].

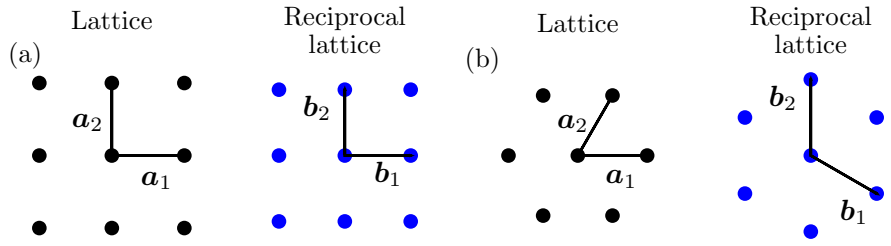

Figure 1.12: Lattice and reciprocal lattice for (a) a square and (b) a triangular arrays. Lattice vectors are denoted as $\mathbf{a}_i$ and the corresponding reciprocal lattice vectors as $\mathbf{b}_i$.

where $\bar{h}(\mathbf{k})$ is the Fourier transform of the total correlation function $h(\mathbf{r})$. Notably, for a completely random system, the structure factor is always equal to $S(k) = 1$ [see Fig. 1.11(c)]. This can be contrasted with the case of perfect ordered system, where the correlation function $g_2(\mathbf{r})$ is characterized by a series of Dirac peaks at $\mathbf{r} = \sum u_i \mathbf{a}_i$ with u_i integer and $\mathbf{a}_i$ a lattice vector [see Fig. 1.12]. Analogously the structure factor $S(\mathbf{k})$ shows Dirac peaks at $\mathbf{k} = \sum v_i \mathbf{b}_i$ where v_i is an integer and $\mathbf{b}_i$ a reciprocal lattice vector [92, 93] [see Fig. 1.11(d)-(f)].

1.2.1.1 Examples of disordered correlated structures

Among the variety of correlated point patterns, three particular examples are presented in Fig. 1.13(a), (b) and (c)[1]. First, Fig. 1.13 (a) shows an array of impenetrable particles of diameter a at a moderate density. This regime, is characterized by the absence of long-range correlation ($g_2 \to 1$ for $r \to \infty$). However, the impenetrability of the particles introduce correlations at short distances [see Fig. 1.13(d)] that increase with the particle density [90]. On the other hand, the structure factor goes from a flat behavior for low values of $k \sim 0$ to a sharp peak around $k \sim 2\pi$ which is followed by oscillations around $S \sim 1$. The short-range correlation in the system can be controlled by tuning the dimensionless *packing density* ϕ, going from an uncorrelated array at $\phi \to 0$ to a crystalline 2D triangular lattice at $\phi \to 0.72$ [99]. This kind of correlated disordered patterns has been found in

[1]Other kind of correlated arrays such as polycrystalline structures [94–96], or disordered fractal structures [97] are studied in Ref. [87]. The case of paracrystals is considered in Ref. [98].

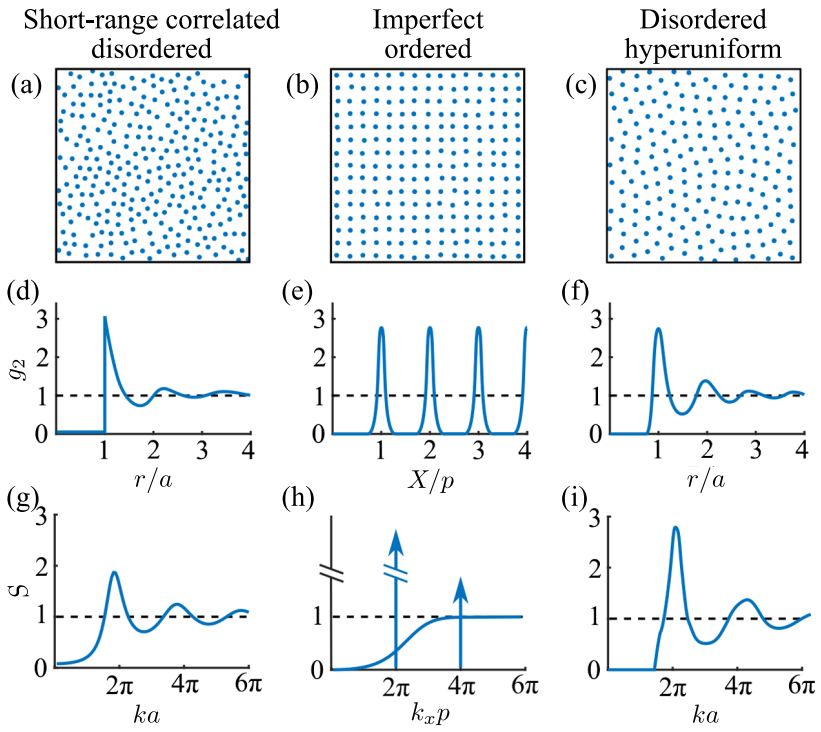

Figure 1.13: (a) Short-range correlated, (b) imperfect ordered, and (a) disordered hyperuniform point patterns. [(d), (e), and (f)] Angular-averaged pair correlation function g_2 for the array in [(a), (b), and (c)]. [(g), (h), and (i)] Angular-averaged structure factor S for the array in [(a), (b), and (c)]. Adapted from Ref. [87].

nature in bird feathers [100].

The second array presented in Fig. 1.13(b) is an imperfect ordered lattice. This array is generated using a regular system as basis, and then displacing randomly every single particle. In this case, the correlated function g_2 is characterized by the broadening of the Dirac peaks at $\mathbf{r} = \sum u_i \mathbf{a}_i$, which depend on the disordered amplitude [see Fig. 1.13 (e)] [87, 92, 93]. Additionally, even for moderate values of the disorder, long-range correlation survive. The corresponding structure factor is depicted in Fig. 1.13(h), showing Dirac peak of vanishing width and decreasing amplitude. Such peaks appear over a diffusive background with asymptotic values $S \to 1$ for large k and $S \to 0$ for $k \to 0$ [101].

Finally, Fig. 1.13(c) depicts an hyperuniform disordered lattice. Hyperuniform arrays were firstly defined by Torquato and Stillinger [89] in 2003. The authors analyzed the fluctuation in the number of particles $\sigma_N = \langle N^2 \rangle - \langle N \rangle^2$ contained by an hypersphere Ω of radius R. They compute σ_N in two different situations: a traditional uncorrelated system, where $\sigma_N \propto R^D$, and a regular array, where $\sigma_N \propto R^{D-1}$. Hyperuniform point patterns were then proposed as disordered point patterns whose particle fluctuation is slower than for usual disordered systems $\sigma_N \propto R^{D-1}$ [see Fig. 1.14]. Similarly to the short-range correlated array, hyperuniformity is characterized by the absence of long-range correlation in the moderate density limit ($g_2 \to 1$ for $r \to \infty$) [see Figs. 1.13(d) and (f)]. However, both cases are well-distinguishable by the structure factor, that goes to zero for certain values of the wave-number [$S(0 < k < k_{\max}) = 0$]. The hyperuniform point patterns are then defined by their structure factor [78, 102, 103]

$$\lim_{k \to 0} S(k) = 0. \tag{1.28}$$

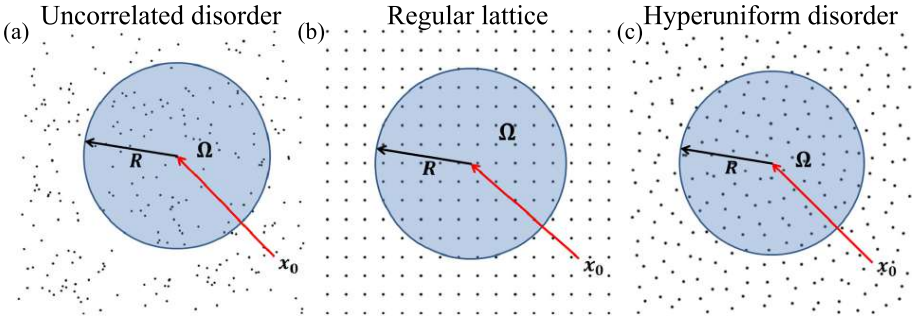

Figure 1.14: Simplified diagram of a circle Ω with radius R and centered in $\mathbf{x_0}$ for (a) an unicorrelated disordered system, (b) a regular array, and (c) a hyperuniform point pattern. Adapted from Ref. [91].

A particular class of hyperuniform disordered systems is obtained by tuning the structure factor [78, 99, 102, 103]

$$S(k) = 0, \qquad \text{for} \qquad k < k_{\max}, \tag{1.29}$$

leading frequency bands where the system remains transparent [104]. Given the transparency band, these peculiar hyperuniform arrays are also called as *stealthy* hyperuniform [102]. Then, it is possible to characterize stealthy hyperuniform point patterns via $k_{\max}$, that can be conveniently written in terms of a dimensionless parameter χ, also known as the degree of stealthiness [78]. Analogously to the short-range correlated systems with the packing density, the "randomness" of the hyperuniform lattices can be control by χ, where $\chi \to 0$ corresponds to totally random configuration [105] and $\chi \to 1$ to the crystalline case [99].

1.2.2 Electromagnetic waves in correlated structures

In 2009, the features of correlated media were numerically challenged by Florescu, Torquato, and Steinhardt [77], who demonstrated that photonic stealthy hyperuniform lattices can be designed to have a frequency band-gap for all polarization and in all directions. The opening of photonic bandgaps at certain frequencies in crystals are related to the scattering of propagating, extended electromagnetic waves from Bragg planes in periodic structures [93] that are not present in uncorrelated materials. Additionally, Florescu, Torquato, and Steinhardt [77] also showed the presence of Anderson localized modes in the band-edges.

The role of short-range and hyperuniform correlations in the formation of band-gaps was numerically studied in detail using 2D finite-size arrays of dielectric cylinders with periodic boundary conditions by Froufe-Pérez et al. [99] [see Figs. 1.15(a) and (c), respectively]. The authors demonstrated that by tuning the packing density in a short-range correlated point pattern ($\phi = 0.6$) or the stealthiness parameter in a hyperuniform system ($\chi = 0.5$), it is possible to match the peaks and oscillations of the pair correlation $g_2(r)$ and the structure factor $S(k)$ [see Figs. 1.15(e) and (f), respectively]. The existence of photonic band-gaps was analyzed by computing the normalized density of states [see Figs. 1.15(g)]. Remarkably, both correlated lattices present almost identical density of states, where the respective gap position and size correspond to the first peak of $S(k)$. Therefore, it is related to Bragg scattering at the isotropic Brillouin zone [99].

Besides gaps and localization, stealthy hyperuniform systems have demonstrated to be characterized by a richer transport diagram, including light diffusion and transparency. The complete phase diagram for hyperuniform disordered lattices as a function of the frequency ν and of the stealthiness parameter χ has been reported in

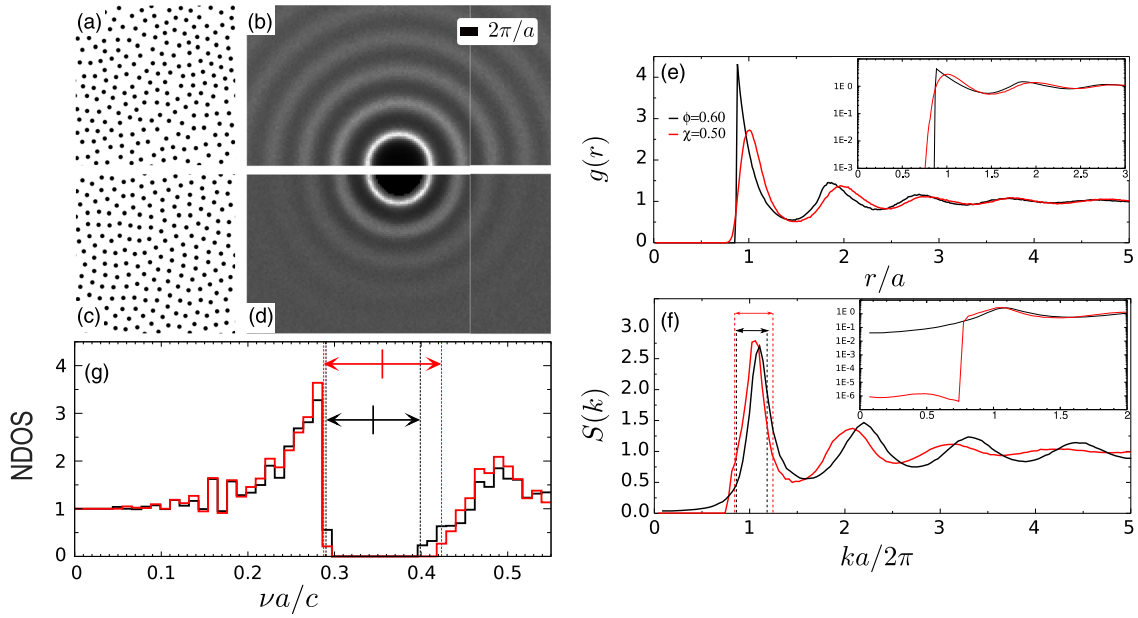

Figure 1.15: (a) Short-range correlated and (c) hyperuniform disordered point patterns. [(b) and (d)] Structure factor S corresponding to the array in [(a) and (c)]. (e) Angular-averaged pair correlation function g_2. (f) Angular-averaged structure factor S. (g) Normalized density of states. Black [red] lines in (e), (f), and (g) correspond to the short-range correlated [hyperuniform] point pattern. Adapted from Ref. [99].

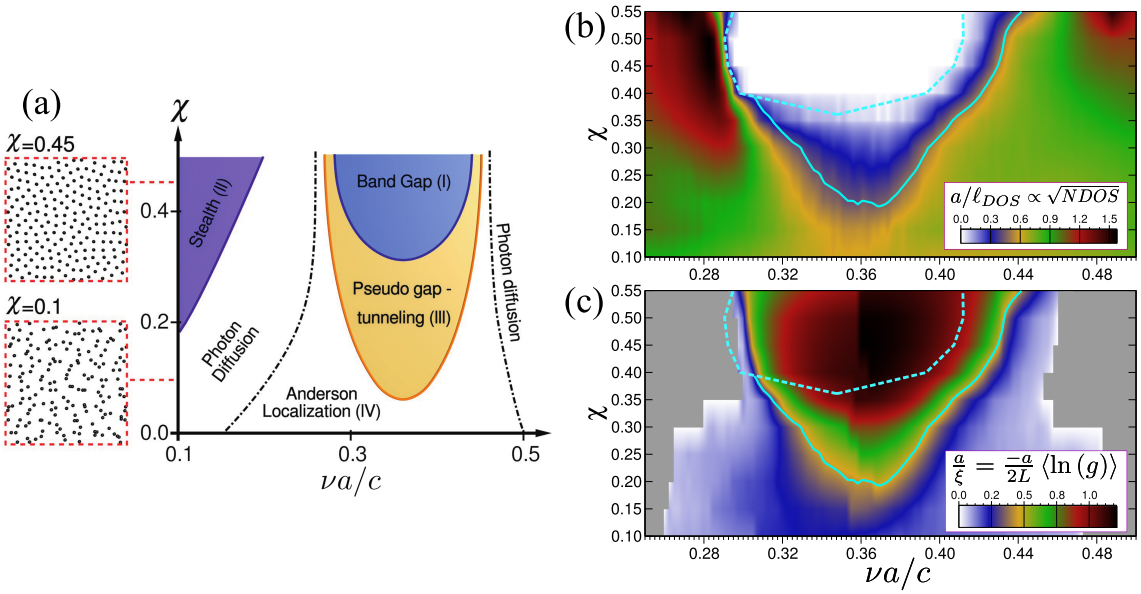

Figure 1.16: (a) Schematized transport phase diagram for 2D stealthy hyperuniform systems. (b) Normalized density of states and (b) Thouless conductance as a function of the stealthy parameter χ and the frequency ν. Adapted from Ref. [78].

Ref. [78]. Using a 2D dielectric hyperuniform array with periodic boundary conditions, Froufe-Pérez et al. [78] computed the normalized density of states and the Thouless conductance g [see Fig. 1.16]. Numerical results show the opening of a bandgap while increasing the stealthiness parameter ($\chi > 0.35$).

These numerical predictions have been experimentally demonstrated with microwaves by Aubry et al. [81]. Experiments were performed by placing different stealthy hyperuniform lattices consisting of dielectric cylinders into a cavity made of two metallic plates [see Fig. 1.17(a)]. Specifically, four different values of χ and a crystalline

triangular array were measured. Each lattice was mapped in frequency and space, allowing a full characterization of the system. To mimic a 2D situation, both conducting plates were put in contact with the faces of the dielectric cylinders. Additionally, to simulate open boundary conditions, the lattice was surrounded by absorbing foams [see Fig. 1.17(a)]. From the data acquisition, the authors were able to extract the number of states, and the Thouless conductance as a function of the frequency, as well as the spatial structure of the eigenstates. Experimental results demonstrate the existence of a photonic bandgap even for $\chi = 0.15$ [see Fig. 1.17(b)]. In addition, band edges are characterized by a sharp drop of the Thouless conductance, revealing the presence of localized states [see Fig. 1.17(c)]. This is confirmed by the eigenstates which denote the existance of multiple transport regimes for the same value of χ [see Fig. 1.17(d)]. Hyperuniform disordered systems have been also studied using optical nanocavities [106, 107].

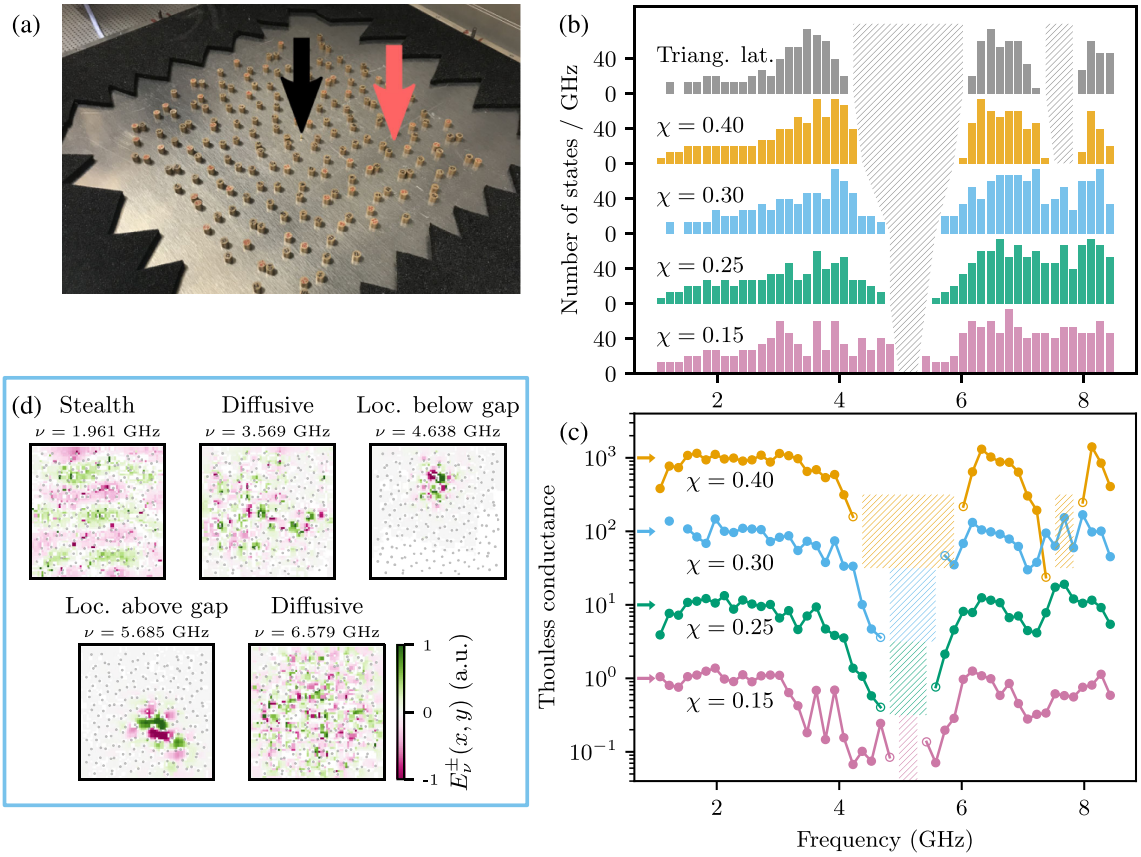

Figure 1.17: (a) Experimental 2D microwave setup. (b) Number of states carried by the system and (c) Thouless conductance as function of the frequency and the stealthiness. (d) Eigenmode spatial structure for $\chi = 0.3$. Adapted from Ref. [81].

1.2.3 Aperiodic materials

As an alternative to periodic or disordered photonic structures, aperiodic materials designed by means of deterministic mathematical rules have emerged as a novel material platform for photonic devices [108–111]. These structures exhibit unique optical properties that exist neither in periodic nor in disordered photonic media, such as fractal transmission spectra [112–114] and subdiffusive transport [114]. Additionally, they have also demonstrated to support spatial localization [115–118]. From a technological point of view, these unusual optical properties have fostered the development of functionalities that cannot be found in conventional periodic or disordered structures, including

applications in lasing [119], optical sensing [120–122], photo-detection [123], and optical imaging [124].

Among various classes of deterministic aperiodic photonic media[2], Vogel spiral arrays single out for their versatility and the possibility to tailor their structural order [126–128] and light-matter interactions [129, 130]. Before becoming relevant in physics, the structure of Vogel spirals was identified to characterize the growing pattern of several plants [see e.g. Fig. 1.18], becoming an object of study for botanists, biologists and mathematicians [131–135]. In 1837, the brothers Louis and Auguste Bravais [131] showed that the geometrical problem of *phyllotaxis*—related to spatial arrangement of leaves, seeds, florets etc. on growing plants—has a correspondence with the Fibonacci sequences, where the number of spiral arms turning in the clockwise and anti-clockwise senses were always given by two subsequent numbers of a Fibonacci series [136]. However, it was until 1978 when a full model to generate the spiral pattern has been proposed by Vogel [137].

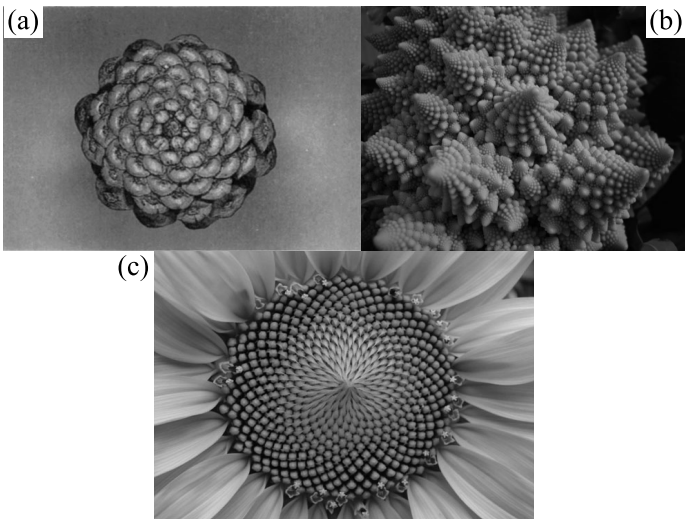

Figure 1.18: The double spiral pattern of phyllotaxis in (a) a pine cone, (b) the florets of a Romanesco cauliflower and, (c) a sunflower head. Adapted from Ref. [136].

1.2.3.1 Wave transport in Vogel spirals

Vogel spirals are usually defined in polar coordinates (r, θ) as [137]

$$\begin{aligned} r_i &= a_0\sqrt{i}, \\ \theta_i &= i\alpha, \end{aligned} \tag{1.30}$$

with $i = 1, 2, \ldots,$ a_0 a positive constant called the scaling factor and α an irrational number known as the divergence angle that sets the aperture between two consecutive points [108]. The divergence angle (in radians) is usually defined as $\alpha = 2\pi/\xi^2$ [138, 139], where the value of ξ allows to control the structure and symmetries of the spiral [140]. Particularly, it has been observed that the sunflower head is well represented by choosing ξ equals the golden number: $\xi = (1 + \sqrt{5})/2$, which is approximated to the ratio between any consecutive numbers of any Fibonacci series [136]. As a result, $\alpha/(2\pi)$ is irrational $\alpha \approx 2.4$ and the Vogel spiral is characterized by the absence of rotational and translational symmetries [141]. This peculiar structure is also know as *Golden-Angle* spiral or "sunflower spiral.

[2]Other aperiodic structures such as Fibonacci chains [113, 115, 116], Halton-Sobol [114], Thue-Morse [117] or Rudin-Shapiro sequences [118] are presented in Ref. [125]

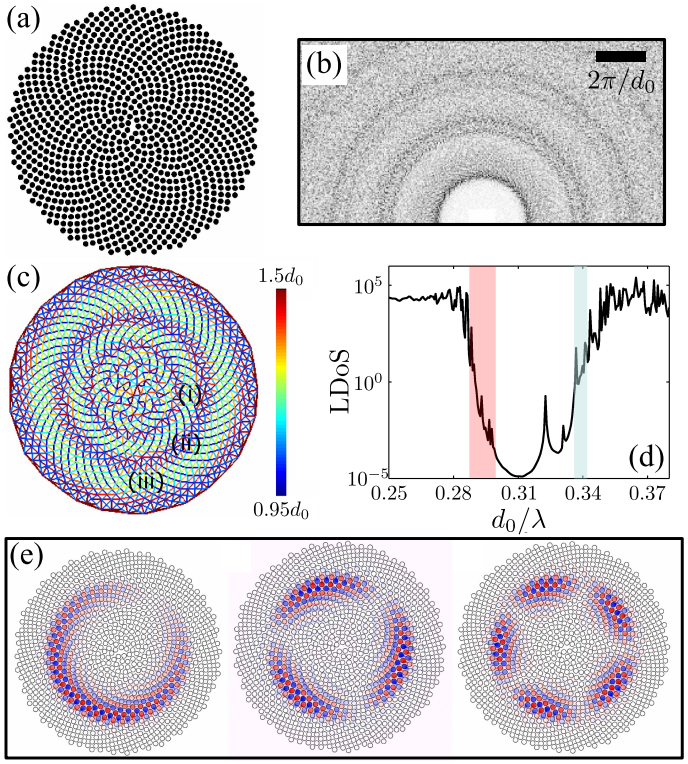

Figure 1.19: (a) Golden-angle spiral array with $N = 1000$. (b) Structure factor S corresponding to the array in (a). (c) Map of distances between neighbouring holes of the lattice shown in (a). (d) Local density of states calculated in the center of the spiral as a function of the normalized frequency d_0/λ. (e) Spatial distribution of the eigenmodes in the band edge. Adapted from Ref. [138].

The impact of the specific spatial structure of Vogel spirals in wave localization was numerically analyzed using 2D golden-angle spiral arrays of air holes hosted in dielectric media by Liew et al. [138]. Figs. 1.19(a) and (b) present a golden spiral characterized by $N = 1000$ holes and its corresponding structure factor $S(\mathbf{k})$. Similar to the structure factors obtained for the short-range and the stealthy hyperuniform disordered systems [see Figs. 1.15(b) and (d)], $S(\mathbf{k})$ is composed of concentric rings that correspond to the dominant frequencies of the structure. The map of the distances between neighbouring sites is plotted in Fig. 1.19(c), where each pair of holes is connected by a color segment and d_0 is the average distance. Fig. 1.19(c) reveals a structure of rings with alternated statistically homogeneous distances.

To investigate the existence of the bandgaps, Liew et al. [138] computed the Local density of states at the center of the spiral. As depicted in Fig. 1.19(d), a reduction in the number of states is observed for $d_0/\lambda \approx 0.31$. Around to the bandgap, several peaks revealed the existence of band edge modes that are plotted in Fig. 1.19(e). Remarkably, different eigenstate are confined within the rings previously identified in Fig. 1.19(c). According to Liew et al. [138], the local standing wave pattern of the modes indicate light confinement perpendicular to the arms of the spiral via Bragg scattering in the holes. On the contrary to extended modes in periodic lattices, the inhomogeneous spacing distribution between neighbouring holes leads to light localization in Vogel spiral.

In contrast to theoretical predictions in uncorrelated random media by Skipetrov and Sokolov [22], in 2019, Sgrignuoli et al. [141] numerically showed the absence of 3D electromagnetic transport using Vogel spiral planar arrays made of punctual dipoles embedded in a full 3D space. Using the Green's matrix formalism [55] to compute the eigenstates of the system [see Fig. 1.20(b)] and the Thouless conductance g as functions of the frequency ω [see Fig. 1.20(a)], it was demonstrated that localized modes

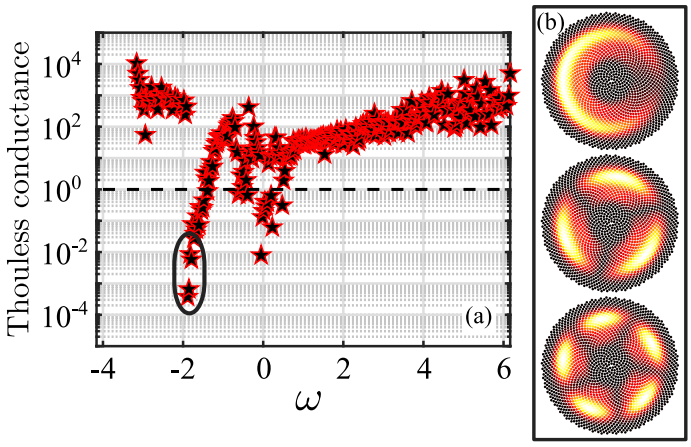

Figure 1.20: (a) Thouless conductance in a planar golden-angle spiral embedded in a 3D space. (b) Spatial distribution of the eigenmodes associated to lowest Thouless values in a golden-angle spiral. Adapted from Ref. [141].

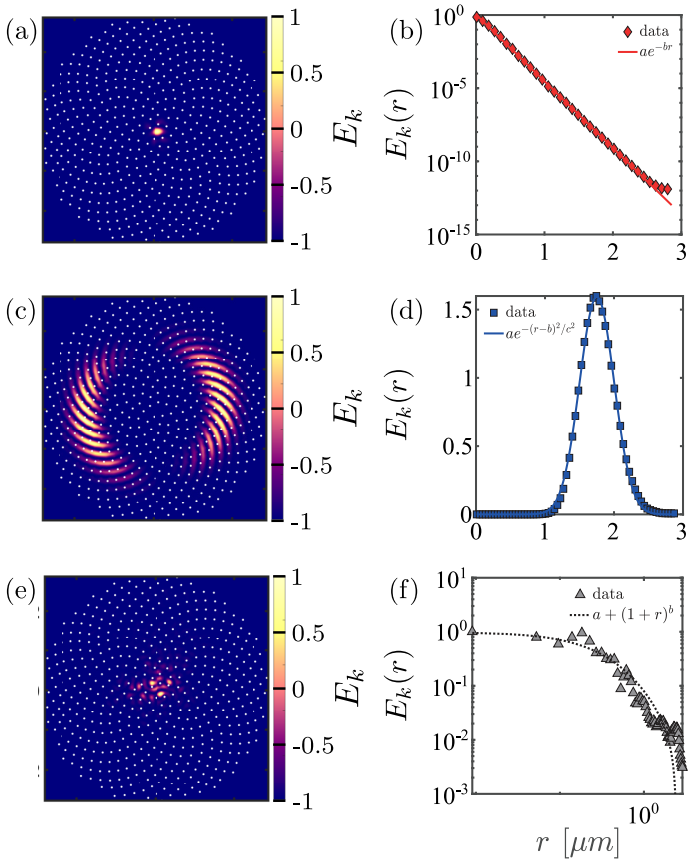

Figure 1.21: Spatial distribution and angular-averaged radial decay of characteristic eigenmodes with [(a) and (b)] exponential, [(c) and (d)] Gaussian, and [(e) and (f)] power-law decays found in a golden-angle spiral. Adapted from Ref. [142].

previously identified by Liew et al. [138] are associated to small g-values when considering the full vector nature of the electromagnetic field. Remarkably, the field is not only confined in the plane, but its leakage in the out-of-plane direction is equivalent to the one in the spiral boundaries.

More recently, it has been theoretically demonstrated that aperiodic Vogel spiral arrays display a rich spectrum of long-lived and spatially localized eigenmodes with distinctive spatial decay forms. By solving the Green's matrix, Prado et al. [142]

numerically reconstructed the spatial distribution of the eigenstates. The radial decay of each mode is computed by performing an azimuthal average operation [see Fig. 1.21]. On the contrary to traditional disordered systems, where all eigemodes are always expected to decay exponentially, Vogel spirals present three distinct localized decay natures namely (a) exponential, (c) Gaussian, and (e) power law. Additionally, it was shown that Gaussian are characterized by the smallest Thouless conductance values.

In Chapter 4, we experimentally demonstrate that these characteristic types of electromagnetic modes coexist in Vogel spirals, and that this unique electromagnetic modal structure leads to unusual wave transport phenomena. By conducting microwave transport experiments in Vogel spiral arrays of cylinders with high dielectric permittivity, we unveil the consequences of this peculiar modal structure on wave transport and localization. Particularly, we show that the presence of long-lived quasimodes with exponential, power law and Gaussian spatial decays is at the origin of a very slow decay of the electromagnetic energy that propagates throughout the arrays. Furthermore, we experimentally prove that these localized modes satisfy the Thouless criterion for Anderson localization in random systems, despite the fact that the propagation medium is not disordered, and that the modes are not necessarily exponentially localized in space. Moreover, we demonstrate the robustness of these long-lived modes against the change in the dimensionality of the cavity, beyond the 2D limit, preserving their spatial profiles and quality factors even when the homogeneity of the electric field in the z-direction is broken.

1.3 Localization via topology

Up to now, we have discussed two different mechanisms to localize electromagnetic waves. In both cases, the collective effects of disorder or correlations trap the waves in the bulk of the system, halting the transport. In this last section, we present a completely different physical realm. In this world, wave transport is provided by localized states on the edges of systems that are insulating in the bulk. This novel and remarkable property is what makes *topological insulators* so attractive. Subtly, this edge conduction is not due to interface-specific physics, but is based on the topological characteristics of bulk wave functions. A topological insulator is therefore an electronic material whose bulk features correspond to a conventional insulator, i.e. it possesses gaps separating energy bands, but in some specific cases these gaps can be filled by conducting edge states [143]. The objective of this section is to present the physics of topological insulators in a nutshell, focusing on their ability to localize electromagnetic waves while allowing conduction.

The story of topological insulators started in 1980 with the discovering of the *quantum Hall effect* [144], characterized by the quantization of the Hall conductance [145] in the presence of strong magnetic fields and low temperatures. In the years following the first observation of the quantum Hall effect, the phenomenon was modelled in the now renowned TKNN article [146], where the authors, in the framework of a 2D electron gas in a periodic potential, were able to prove analytically the quantization of the conductance. The picture became clearer in 1983, when Barry Simon linked Thouless' results with the topology of the electronic bands in momentum space [147]. By reinterpreting the recent concept of the Berry curvature [148], Simon demonstrated that the positions of the plateaus in the Hall conductance correspond to the values of a topological invariant of the system, namely the Chern number [149]. The latter which is given by the integral of the Berry curvature of a band is basically related to the dephasing of the band's wavefunctions across the Brillouin zone. Topological insulators are classified according to their topological invariants. For instance in the case of the Chern number, $C = 0$ defines a trivial insulator behavior, and a non-vanishing $C \neq 0$ a nontrivial topological insulator, also known as Chern insulator.

1.3.1 Edge states and Time-reversal symmetry

The topological invariant of a given material is strongly related with the conducting edge states through the *bulk-edge correspondence*, which is a general phenomenon of topologically nontrivial structures [150, 151]. As demonstrated by Qi, Wu, and Zhang [152], the topological order in the bulk of a system with non-vanishing Chern number always leads to spatially localized states whose energies occupy the energy band gap of the bulk. Such states are confined in the edge of the nontrivial material, and their number is equal to the Chern invariant. Frequently, the edge states, also known as anomalous edge states, are observed at the interface between two materials with different topological invariants. Nevertheless, the boundary of a nontrivial topological sample with the topologically trivial vacuum ensures the existence of such states at the edge [153].

The most important ingredient to obtain a topological insulator is the breaking of the time-reversal symmetry. For instance, in 1988 Haldane [154] considered a tight-binding honeycomb lattice with complex second nearest-neighbour coupling [see Fig. 1.22(a) and Appendix A]. The complex second nearest-neighbour hoppings break the time-reversal symmetry of the system and open a topological nontrivial gap, leading to non-vanishing Chern numbers [see Figs. 1.22(c) and (d)]. The Haldane model [154] is also characterized by a particular set of edge modes, namely the *chiral states*. Such modes display chiral properties in the sense that they propagate unidirectionally along the sample boundary. Given the absence of counterpropagative states, chiral states are immune to backscattering. The band structure of a ribbon following the Haldane model is presented in Fig. 1.22(b), where the chiral modes are represented by the blue and red lines.

A new type of topological insulator conserving the time-reversal symmetry, known as Z_2 topological insulator, was proposed in 2005. As demonstrated by Kane and Mele [155], it is possible to consider two identical Chern insulators each of which with an opposite spin, therefore having individual non-vanishing Chern invariants C_{up} and C_{down}. Since the spins are opposite to each other, the total time reversal symmetry is preserved and the total Chern number $C_{\text{up}} + C_{\text{down}}$ is zero. In addition, if the spins remain uncoupled and independent, each Chern insulator has the same number of edge states but in opposite propagating direction, namely helical states [155]. Therefore, according to the Kramers' theorem, at least one pair of topological edge states are preserved as long as the time-reversal symmetry holds [153]. To characterize this topological insulator, the new topological invariant Z_2 was defined as $C_{\text{up}}\text{mod } 2 (= C_{\text{down}}\text{mod } 2)$,

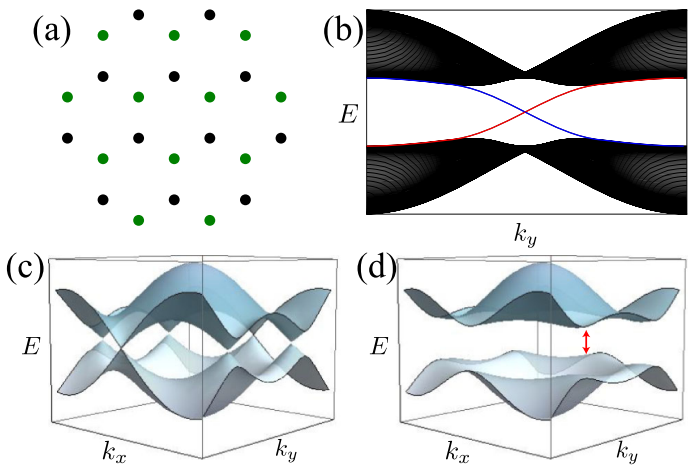

Figure 1.22: (a) Honeycomb lattice. (b) Typical band structure with edges modes for the Haldane model when the topological gap is open. Red and blue lines indicate the edges states. (c) Bulk band structure of the honeycomb lattice with nearest-neighbour hopping only. (d) Typical bulk band structure of the Haldane model in the presence of second-neighbour complex hopping. Adapted from Ref. [153].

taking the values: 0 for a trivial system, and 1 for a nontrivial system [143, 153, 155].

1.3.2 Z_2 photonic crystal

Almost one decade ago, Wu and Hu [156] proposed a new perspective to design a Z_2 photonic insulator using a conventional crystal. They observed that a honeycomb lattice can be seen as a regular triangular structure with lattice parameter a_0, where each site becomes the center of a regular hexagonal cluster of variable radius R [see Fig. 1.23(a)]. In this way, by considering a tight binding approach (see Appendix A), it is possible to separate an inner-cell coupling t_0 and an outer-cell coupling t_1, both depending on the value of R, and where the classical honeycomb lattice is recovered for $t_0 = t_1$. In the honeycomb limit ($t_0 = t_1$, and $a_0/R = 3$), considering the hexagonal cluster as a primitive cell folds the Brillouin zone, removing the degenerated Dirac point at K, and producing a new doubly degenerated point at Γ [see Figs. 1.23(c) and (d)].

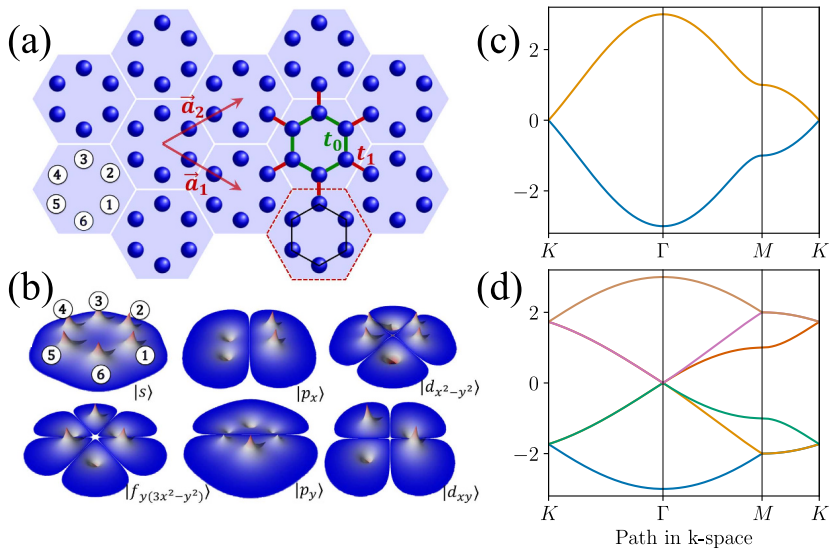

Figure 1.23: (a) Honeycomb lattice constructed from a triangular lattice with hexagonal clusters. (b) Emergent orbitals in the hexagonal artificial cell. (c) Band structure of the honeycomb lattice (with two sites per primitive cell). (d) Band structure of the honeycomb lattice with six sites per primitive cell. Adapted from Ref. [157].

1.3.2.1 Topological order

To understand all the consequences in the choice of the hexagonal unit cell, one can start by solving the Hamiltonian $\hat{H}_0$ of a individual cell in the perfect honeycomb case [157]

$$\hat{H}_0 = t_0 \begin{pmatrix} 0 & 1 & 0 & 0 & 0 & 1 \\ 1 & 0 & 1 & 0 & 0 & 0 \\ 0 & 1 & 0 & 1 & 0 & 0 \\ 0 & 0 & 1 & 0 & 1 & 0 \\ 0 & 0 & 0 & 1 & 0 & 1 \\ 1 & 0 & 0 & 0 & 1 & 0 \end{pmatrix}, \tag{1.31}$$

where $t_0(=t_1)$ is the coupling between any two consecutive sites. The eigenstates of $\hat{H}_0$ are then given by

$$\begin{aligned}
|s\rangle &= \begin{bmatrix}1 & 1 & 1 & 1 & 1 & 1\end{bmatrix}, \\
|p_x\rangle &= \begin{bmatrix}1 & 1 & 0 & -1 & -1 & 0\end{bmatrix}, \\
|p_y\rangle &= \begin{bmatrix}1 & -1 & -2 & -1 & 1 & 2\end{bmatrix}, \\
\left|d_{x^2+y^2}\right\rangle &= \begin{bmatrix}1 & 1 & -2 & 1 & 1 & -2\end{bmatrix}, \\
|d_{xy}\rangle &= \begin{bmatrix}1 & -1 & 0 & 1 & -1 & 0\end{bmatrix}, \\
\left|f_{y(2x^2-y^2)}\right\rangle &= \begin{bmatrix}1 & -1 & 1 & -1 & 1 & -1\end{bmatrix},
\end{aligned} \tag{1.32}$$

with energies $2t_0$, t_0, t_0, $-t_0$, $-t_0$ and $-2t_0$, respectively [see Fig. 1.23(b)]. It is worth noting that the lattice is an element of the C_6 cyclic group [158], where the pair of degenerated states $\{|p_x\rangle, |p_y\rangle\}$ and $\{\left|d_{x^2+y^2}\right\rangle, |d_{xy}\rangle\}$ are the basis functions of an irreducible representation [156]. According to Wu and Hu [157], it is then possible to define the wavefunctions

$$|p_\pm\rangle = \frac{1}{\sqrt{2}}\left(|p_x\rangle \pm \mathrm{i}\,|p_y\rangle\right), \qquad \text{and} \qquad |d_\pm\rangle = \frac{1}{\sqrt{2}}\left(\left|d_{x^2+y^2}\right\rangle \pm \mathrm{i}\,|d_{xy}\rangle\right), \tag{1.33}$$

together with the operator $\mathcal{T} = \mathcal{U}\mathcal{K}$, where $\mathcal{K}$ is the complex conjugate operator, $\mathcal{U} = \mathrm{i}\sigma_z$ is a unitary operator, and σ_z is the Pauli matrix. In this case, $\mathcal{U}$ is obtained from the matrix representation of the $\pi/3$ rotation in each irreducible basis. Therefore, $\mathcal{T}$ can be taken as a pseudo time-reversal operator, with the orbital angular momentum playing the role of the pseudospin [157, 159]. In consequence, the system shares the same physics as the Z_2 topological insulator presented in the previous section. As mentioned by Wu and Hu [157], the pseudospin is directly related to the chiral current density of the hexagonal cell. Thus, by evaluating the current density along the cell, it is possible to obtain the anticlockwise and clockwise circulation currents that are associated to the two pseudospin [see Fig. 1.24(a) and (b)].

It is important to note that any values of R preserves the C_6 rotational symmetry, which is at the origin of the time-reversal symmetry. Thus, to exhibit the topological behaviour of the system, Wu and Hu [157] compute the dispersion relation of the systems for three values of the outer-cell coupling t_1 [see Fig. 1.24(c)-(e)]. Note that the choice of $t_1 \neq t_0$ opens a photonic band gap at the Γ point. For each value of t_1, they project the wavefunctions onto the orbitals of the unitary hexagonal cell, showing that for $t_1 \leq t_0$, the valence bands behave like the d orbitals and the conduction bands as p orbitals. By increasing the value of $t_1 > t_0$, they observe that the bottom (valence) bands now exhibit a p character while the top (conduction) bands behave like the d orbital: a band inversion takes place by increasing the outer-cell coupling, indicating the nontrivial topological behavior [160].

1.3.2.2 Chern invariant and edge states

One of the more important points investigated by Wu and Hu [156] is the evaluation of the Z_2 invariants for the two pseudopsin channels. The authors report that in the case of $t_1 \leq t_0$, the Chern invariant for each band is zero, showing a trivial behaviour. On the contrary, for values of the coupling $t_1 > t_0$, the Chern numbers for the pseudospin-up and -down channels are $C_\pm = \pm 1$. Finally, the robustness of the edge states was analyzed by considering a semi-infinite ribbon with nontrivial topology in contact with a trivial topological structure. Fig. 1.25(a) shows the band structure of the ribbon where the red lines indicate the double degenerated edge states. The spatial map of the edge current associated with the edge states is depicted in Fig. 1.25(b), denoting the spatial

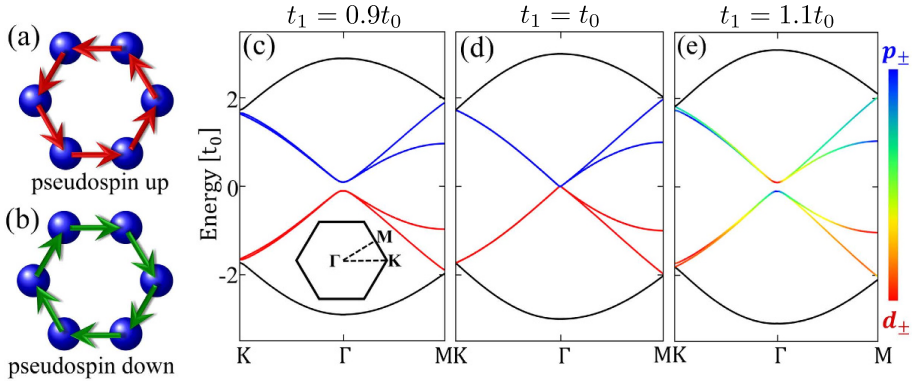

Figure 1.24: Current density in (a) the pseudospin-up channel ($|p_+\rangle$ and $|d_+\rangle$) and (b) the pseudospin-down channel ($|p_-\rangle$ and $|d_-\rangle$). Dispersion relation for the system in Fig. 1.23(a), considering (c) $t_1 = 0.9t_0$, (d) $t_1 = t_0$, and (e) $t_1 = 0.9t_0$ Taken from Ref.[157].

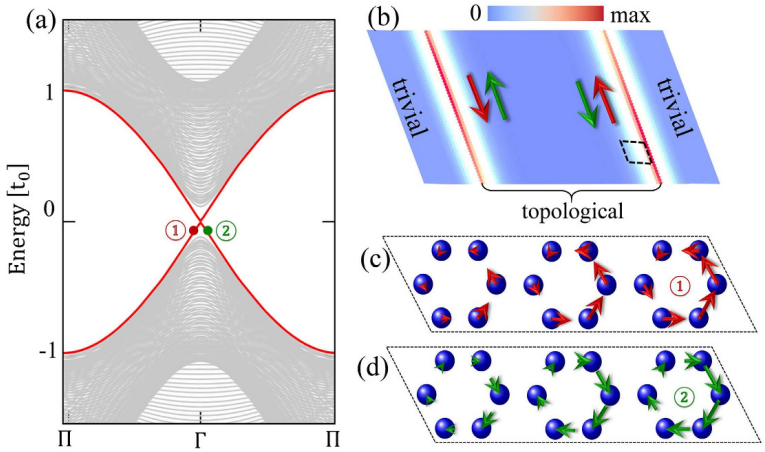

Figure 1.25: (a) Band dispersion of a nontrivial topological ribbon ($t_1 = 1.1t_0$) cladded in both sides by trivial topological structures ($t_1 = 0.9t_1$). (b) Spatial distribution of the gap states associated with the red lines in (a). Space distributions of the current densities corresponding to the (c) red and (d) green points in (a). The excess currents are indicated by red and green arrows. Taken from Ref.[157].

localization of the states in the boundary between both structures. The authors also investigated the edge current distribution [Fig. 1.25(c) and (d)], finding that the edge states are unambiguously associated with the pseudospin channels.

Note that at the interface between two structures, the C_6 symmetry is substituted by a C_2 rotational symmetry, and therefore the time-reversal symmetry is not conserved. As a result, a mini gap opens at the Γ point due to the coupling between the two pseudospin channels. However, Wu and Hu [156] demonstrated that the symmetry and topology holds for moderate deformations.

In Chapter 5, we experimentally investigate the existence and impact of helical edge-states using the Wu-Hu model of honeycomb lattices previously presented. By performing microwave transport experiments in honeycomb arrays of cylinders with high dielectric permittivity, we explore the evolution of the topological nontrivial regime as well as the edge-states as a function of R. Particularly, we demonstrate the unidirectional counterpropagative features of the helical modes that propagate around the boundary of the topological nontrivial material. Moreover, we experimentally explore the robustness of the modes with respect to the abrupt breaking of the crystalline structure (i.e. the C_6 rotational symmetry).

1.4 Lecture guide for the rest of the manuscript

Throughout this Chapter, we have discussed three different physical mechanisms to control and localize electromagnetic waves. We started by introducing the so-called Anderson localization phenomenon, which is characterized by a complete halt of wave transport due to presence of uncorrelated impurities in the materials. We have paid special attention to a recent approach known as the localization landscape that has become an efficient tool in the understanding of Anderson localization. Chapter 3 then reports how the localization landscape can be successfully extended to a broad class of 1D and 2D tight binding materials, where spatially localized modes exist at both band edges. We have also pointed out the fact that Anderson localization is a general wave phenomenon which can be found in different kinds of wave systems, however up to this moment, there is no unequivocal evidence of its existence for 3D electromagnetic waves[3]. To this concern, in Chapter 3, we also explore the applicability of the localization landscape theory on the Maxwell's equations.

The second part of this Chapter is dedicated to the analysis of wave scattering in heterogeneous correlated media. Over the years, structured correlated systems have demonstrated to not only improve localization effects but also to support different transport regimes such as diffusion or transparency. We start by focusing on the so-called stealthy hyperuniform disorder, which has demonstrated to be an excellent platform to control wave transport. As an alternative to disordered system, we introduce the notions of aperiodicy and, in particular, of Vogel spirals, which have recently been shown to be able to localize light even in 3D. Chapter 4 is then dedicated to report experimental findings of wave transport—localization—through Vogel spirals.

Finally, the last section of the current Chapter has introduced the different notions about wave transport in nontrivial topological systems. We have shown how Berry-phase-related attributes of wavefunctions in a band induced by a periodic lattice lead, among other effects, to the emergence of "anomalous" edge states. In addition, we discussed the importance of breaking or preserving of the time-reversal symmetry in the presence and robustness of these edges-modes. In Chapter 5, we experimentally demonstrate the existence of topological helical edge-states protected by the time-reversal symmetry in dielectric microwave samples.

[3]Numerical simulations have highlighted Anderson localization in a metallic random overlapping spheres ensemble, but the Authors show that this regime can not be obtained in a similar dielectric system [25].

2

Experimental setup and data analysis tools

Quiero morir siendo esclavo
de los principios,
no de los hombres
Emiliano Zapata

Contents

The objective of this Chapter is to present the experimental setup and the different data analysis procedures that will be used in the subsequent Chapters. It is organized as follows: in Section 2.1, we show the different elements that compose the experimental platform. An analytical description of the electromagnetic cavity is provided. The electromagnetic field in the cavity is injected by antennas with different shape that allow to control the polarization of the field. Section 2.2 is devoted to illustrate the versatility of the dielectric cylinders which are the building blocks of our experimental samples. The behaviour of the dielectric in the presence of different polarization of the field is detailed. Later, in Section 2.3 the different sources of incertitude in our experiments are characterized. Finally, Section 2.4 is dedicated to introduce all the different algorithms to analyze the experimental data. We show how the Density of States and the spatial shape of the eigenmodes are computed, and how to reconstruct the evolution of a short temporal pulse through the sample.

2.1 The experimental platform

All our experiments are conducted using a quasi-two-dimensional cavity made up of two parallel aluminum plates separated by a distance h. The top plate is suspended thanks to a horizontal metallic arm, which in turn is attached to a motorized XY-stage (Newport IMS600C and Newport ESP301), thus the top plate is completely movable in the $\hat{x} - \hat{y}$ plane and the cavity is completely open in both, $\hat{x}$ and $\hat{y}$ directions. The XY-stage provides a 200 nm precision in each direction and it is supported by a hydraulic lift that allows to control the height of the top plate h with a 0.5 mm precision. Fig. 2.1 shows an image of the mechanic part of the experimental platform.

Electromagnetic waves are induced and measured using one or two antennas that penetrate into the cavity through two holes drilled in the center of the bottom and top plates, respectively (the particularities of the antenna will be properly introduced in the following sections). The antennas are connected to a two-ports Vector Network Analyzer (VNA, Rohde & Schwarz ZVA 24) via two shielded flexible coaxial cables (Flexco

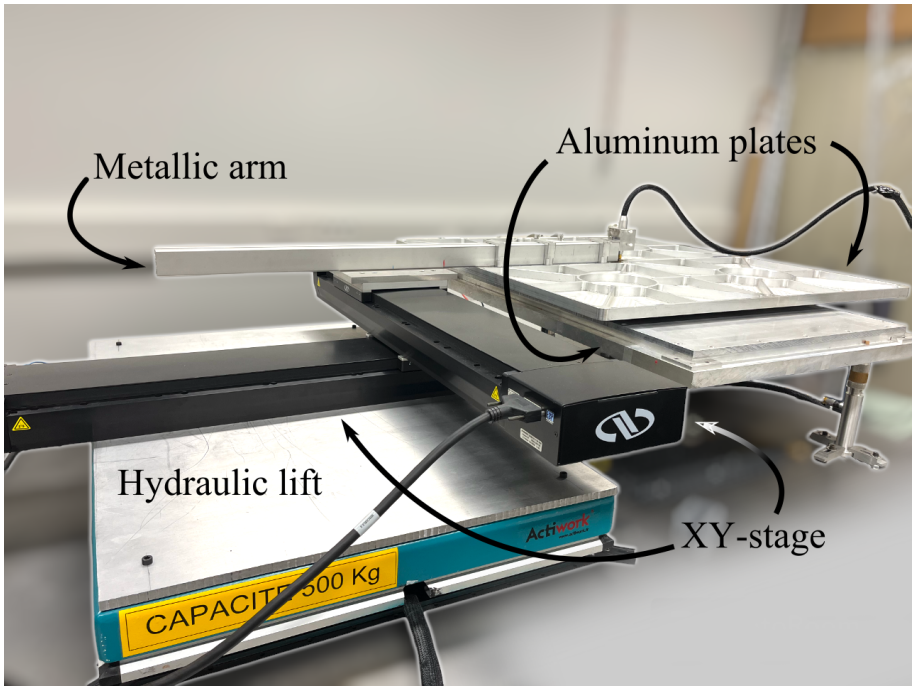

Figure 2.1: Image of the actual mechanic part of the experimental platform.

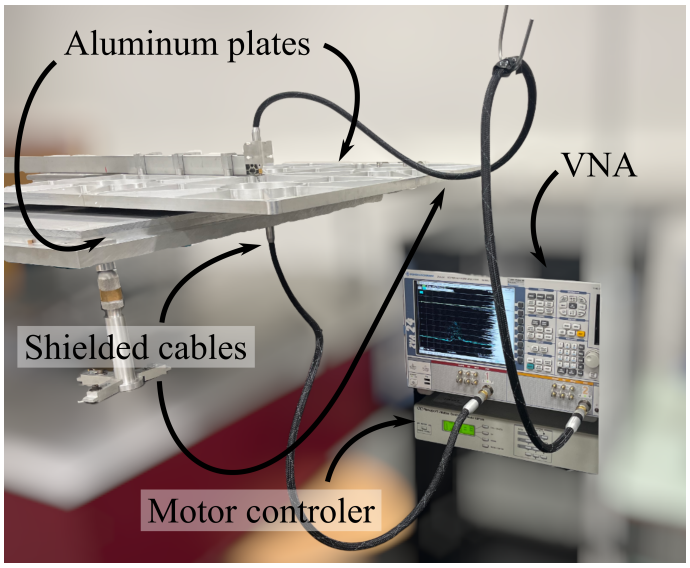

Figure 2.2: Image of the actual microwave experimental setup.

NTC195-50R49). The VNA operates in a frequency range going from 10 MHz to 24 GHz corresponding to wavelengths in vacuum from 1.25 cm to 29 m. The field inside the cavity is injected and extracted by the VNA via the antennas and the coaxial cables. Fig. 2.2 shows a image of the microwave part of the experimental setup.

Note that up to this point, the signal registered by the VNA also includes the response of the propagating waves inside the cables. Nevertheless, the cable contribution can be easily removed thanks to a well standardized calibration method. To carry out this process, a set of precision mechanical standards (Rhode & Schwarz ZN-Z235) is connected to the end of the cables and then a measurement protocol is followed by the VNA. Finally, by comparing the actual measurements with the well-known answer of each standard (provided by the manufacturer), the VNA can automatically correct future measurements.

As the VNA measures modifications in amplitude and phase of a reference signal, it provides the 2×2 complex Scattering Matrix S defined as

$$\begin{pmatrix} S_{11} & S_{12} \\ S_{21} & S_{22} \end{pmatrix} \begin{pmatrix} V_{\text{in}}^1 \\ V_{\text{in}}^2 \end{pmatrix} = \begin{pmatrix} V_{\text{out}}^1 \\ V_{\text{out}}^2 \end{pmatrix}, \tag{2.1}$$

where V_{in}^1 and V_{in}^2 are the input signals injected to the emitting antennas and V_{out}^1 and V_{out}^2 the signals registered by the measuring antennas. Considering only the incoming wave from the antenna (1), Eq. (2.1) reads

$$V_{\text{in}}^1 S_{11} = V_{\text{out}}^1, \qquad V_{\text{in}}^1 S_{21} = V_{\text{out}}^2, \tag{2.2}$$

where S_{11} and S_{21} are therefore known as the reflection amplitude of the antenna (1) and transmission amplitude from the antenna (2) to the antenna (1), respectively. Similarly, by choosing $V_{\text{in}}^1 = 0$, we obtain S_{22} as the reflection amplitude of the antenna (2) and S_{21} as the transmission amplitude form the antenna (1) to the antenna (2). Finally, the transmission and reflection coefficients are defined as the square of the respective amplitudes [161].

Our experiments are normally performed using two antennas, where the antenna (2) is located at the center of the bottom plate and the antenna (1) is attached to the movable top plate, allowing to map the signal in the $\hat{x} - \hat{y}$ plane. Specifically, we measure the reflection in the movable top antenna (S_{11}), as well as its transmission to the fixed bottom antenna (S_{21}).

2.1.1 Modes in the cavity

To describe the modes supported by the empty cavity, we start by considering the Maxwell's equations without sources in a non-magnetic medium [162]

$$\begin{aligned} \nabla \times \mathbf{E}(\mathbf{r},t) &= -\partial_t \mathbf{B}(\mathbf{r},t), & \nabla \cdot \mathbf{D}(\mathbf{r},t) &= 0, \\ \nabla \times \mathbf{B}(\mathbf{r},t) &= \mu_0 \partial_t \mathbf{D}(\mathbf{r},t), & \nabla \cdot \mathbf{B}(\mathbf{r},t) &= 0, \end{aligned} \tag{2.3}$$

where $\mathbf{E}(\mathbf{r},t)$ is the electric field, $\mathbf{B}(\mathbf{r},t)$ is the magnetic field, $\mathbf{D}(\mathbf{r},t) = \epsilon_0 \mathbf{E}(\mathbf{r},t)$ is the so-called displacement vector, and μ_0 and ϵ_0 are the magnetic permeability and the dielectric permittivity of the air ($\sim$vacuum), respectively. Given the presence of the conducting plates, the electric and magnetic fields also satisfy the boundary conditions

$$[\hat{\mathbf{n}} \times \mathbf{E}(\mathbf{r},t)]\Big|_{z=0 \text{ and } z=h} = 0, \qquad [\hat{\mathbf{n}} \cdot \mathbf{B}(\mathbf{r},t)]\Big|_{z=0 \text{ and } z=h} = 0, \tag{2.4}$$

with $\hat{\mathbf{n}} (= \pm \hat{z})$ the unit normal vectors to the planes of each plate.

Assuming a harmonic monochromatic time dependence with frequency ω [$\mathbf{E}(\mathbf{r},t) = \mathbf{E}(\mathbf{r})\mathrm{e}^{-\mathrm{i}\omega t}$ and $\mathbf{B}(\mathbf{r},t) = \mathbf{B}(\mathbf{r})\mathrm{e}^{-\mathrm{i}\omega t}$], the Maxwell's equations (2.3) read

$$\begin{aligned} \nabla \times \mathbf{E}(\mathbf{r}) &= \mathrm{i}\omega \mathbf{B}(\mathbf{r}), & \nabla \cdot \mathbf{E}(\mathbf{r}) &= 0, \\ \nabla \times \mathbf{B}(\mathbf{r}) &= -\mathrm{i}\mu_0 \epsilon_0 \omega \mathbf{E}(\mathbf{r}), & \nabla \cdot \mathbf{B}(\mathbf{r}) &= 0. \end{aligned} \tag{2.5}$$

The substitution of the Maxwell-Faraday equation into the Ampère-Maxwell equation [left hand side Eqs. in (2.5)] and vice versa allows to obtain independent equations for the electric and magnetic field, respectively. That is

$$\nabla \times \nabla \times \mathbf{E}(\mathbf{r}) = \frac{\omega^2}{\mathrm{c}_0^2}\mathbf{E}(\mathbf{r}), \qquad \nabla \times \nabla \times \mathbf{B}(\mathbf{r}) = \frac{\omega^2}{\mathrm{c}_0^2}\mathbf{B}(\mathbf{r}), \tag{2.6}$$

where, $\mathrm{c}_0 = 1/\sqrt{\mu_0 \epsilon_0}$ is the speed of light in the vacuum and $k = \omega/\mathrm{c}_0$ the wave number. Next, by using the Gauss' law [right hand side Eqs. in (2.5)], Eqs. (2.6) read

$$\Delta \mathbf{E}(\mathbf{r}) = -\frac{\omega^2}{\mathrm{c}_0^2}\mathbf{E}(\mathbf{r}), \qquad \Delta \mathbf{B}(\mathbf{r}) = -\frac{\omega^2}{\mathrm{c}_0^2}\mathbf{B}(\mathbf{r}). \tag{2.7}$$

Given the cylindrical symmetry of the system and the presence of the conductor plates, all components of each field can be expressed as product of independent functions of the individual cylindrical variables (ρ, ϕ, z)

$$A_{\hat{\imath}} = P_{A,\hat{\imath}}(\rho)\Phi_{A,\hat{\imath}}(\phi)Z_{A,\hat{\imath}}(z), \tag{2.8}$$

with $A = \{E, B\}$ and $\hat{\imath} = \{\hat{\rho}, \hat{\phi}, \hat{z}\}$. Additionally for both fields, the Gauss' law [right hand side Eqs. in (2.5)] can be written as

$$\nabla_{\hat{\rho},\hat{\phi}} \cdot \mathbf{E}_{\hat{\rho},\hat{\phi}}(\mathbf{r}) = -\partial_z E_{\hat{z}}(\mathbf{r}), \qquad \nabla_{\hat{\rho},\hat{\phi}} \cdot \mathbf{B}_{\hat{\rho},\hat{\phi}}(\mathbf{r}) = -\partial_z B_{\hat{z}}(\mathbf{r}), \tag{2.9}$$

where $\nabla = \nabla_{\hat{\rho},\hat{\phi}} + \hat{z}\partial_z$. Eqs. (2.9) together with Eq. (2.8), allows to rewrite the boundary conditions [Eq. (2.4)] as follows

$$\left.\begin{aligned} Z_{E,\hat{\rho}}(z)\Big|_{z=0 \text{ and } z=h} &= Z_{E,\hat{\phi}}(z)\Big|_{z=0 \text{ and } z=h} \\ \partial_z Z_{E,\hat{z}}(z)\Big|_{z=0 \text{ and } z=h} &= Z_{B,\hat{z}}(z)\Big|_{z=0 \text{ and } z=h} \end{aligned}\right\} = 0. \tag{2.10}$$

Since the boundary conditions on $E_{\hat{z}}(\mathbf{r})$ and $B_{\hat{z}}(\mathbf{r})$ are different, the corresponding eigenfrequencies and eigenstates are different too. Therefore, we can divide the electromagnetic field into two different categories [162]:

Transverse magnetic (TM) waves, $B_{\hat{z}}(\mathbf{r}) = 0$ with boundary conditions

$$\partial_z E_{\hat{z}}(\mathbf{r})\Big|_{z=0 \text{ and } z=h} = 0. \tag{2.11}$$

Transverse electric (TE) waves, $E_{\hat{z}}(\mathbf{r}) = 0$ with boundary conditions

$$B_{\hat{z}}(\mathbf{r})\Big|_{z=0 \text{ and } z=h} = 0. \tag{2.12}$$

To solve the two Helmholtz equations (2.7), we use the continuous rotational symmetry along the $\hat{\phi}$-axis that allows to express the angular dependence as $\Phi(\phi) = \mathrm{e}^{\mathrm{i}\alpha\phi}$ where α is an integer. On the other hand, the solution for the z-dependent function can be written as standing waves $a\cos(k_z z) + b\sin(k_z z)$, with a and b constants and k_z the wave number in the $\hat{z}$-direction. Therefore, by applying the boundary conditions for each polarization [TM in (2.11) and TE in (2.12)], the $\hat{z}$-component $A_{\hat{z}}$ of the two fields is given by [162]

$$\text{TM waves} \quad \rightarrow \quad E_{\hat{z}}(\mathbf{r}) = P_{E,\hat{z}}(\rho)\mathrm{e}^{\mathrm{i}\alpha\phi}\cos\left(\frac{j\pi z}{h}\right) \qquad (j = 0, 1, \dots), \tag{2.13}$$

$$\text{TE waves} \quad \rightarrow \quad B_{\hat{z}}(\mathbf{r}) = P_{B,\hat{z}}(\rho)\mathrm{e}^{\mathrm{i}\alpha\phi}\sin\left(\frac{j\pi z}{h}\right) \qquad (j = 1, 2, \dots), \tag{2.14}$$

where $k_z = j\pi/h$. In addition, the differential equation of $P_{A,\hat{z}}(\rho)$ becomes

$$\rho^2\frac{\mathrm{d}^2 P_{A,\hat{z}}(\rho)}{\mathrm{d}\rho^2} + \rho\frac{\mathrm{d}P_{A,\hat{z}}(\rho)}{\mathrm{d}\rho} + \left[q\rho^2 - \alpha^2\right]P_{A,\hat{z}}(\rho) = 0, \tag{2.15}$$

with $q = \sqrt{k^2 - k_z^2}$ and the condition of having a non-divergent function at $\rho = 0$ and $\rho \to \infty$, leading to

$$\text{TM waves} \quad \rightarrow \quad E_{\hat{z}}(\mathbf{r}) = E_0 J_\alpha(q\rho)\mathrm{e}^{\mathrm{i}\alpha\phi}\cos\left(\frac{j\pi z}{h}\right) \qquad (j = 0, 1, \dots), \tag{2.16}$$

$$\text{TE waves} \quad \rightarrow \quad B_{\hat{z}}(\mathbf{r}) = B_0 J_\alpha(q\rho)\mathrm{e}^{\mathrm{i}\alpha\phi}\sin\left(\frac{j\pi z}{h}\right) \qquad (j = 1, 2, \dots), \tag{2.17}$$

where J_α is the Bessel function, and E_0 (B_0) a constant.

Note that the condition $(k^2 - k_z^2) \geq 0$ gives the cutoff frequencies of the propagating modes in the cavity as

$$\nu_{j,\mathrm{cut}} = j\frac{\mathrm{c}_0}{2h}. \tag{2.18}$$

with j a strictly positive integer [Eqs. (2.16) and (2.17)]. For instance, Fig. 2.3 shows the amplitude of $Z_{A,\hat{z}}(z)$ [see Eq. (2.8)] with respect to the mode index j for $j = 0, 1, 2$. As can be observed, below the cutoff frequency of the first transverse mode [$\nu < \nu_{1,\mathrm{cut}}(h)$], the amplitude of the field is homogeneous in the $\hat{z}$-direction. Thus, for TM waves in this frequency regime, the cavity can be seen as a 2D system and 3D effects are expected for frequencies above the cutoff. Additionally, the fundamental transverse mode TM_0 has a cutoff frequency $\nu_{\mathrm{cut}} = 0$, therefore TM waves propagates at any frequency. In contrast, TE waves are not able to propagate at low frequency $\nu < \nu_{1,\mathrm{cut}}(h)$, i.e., waves are always evanescent beneath this limit.

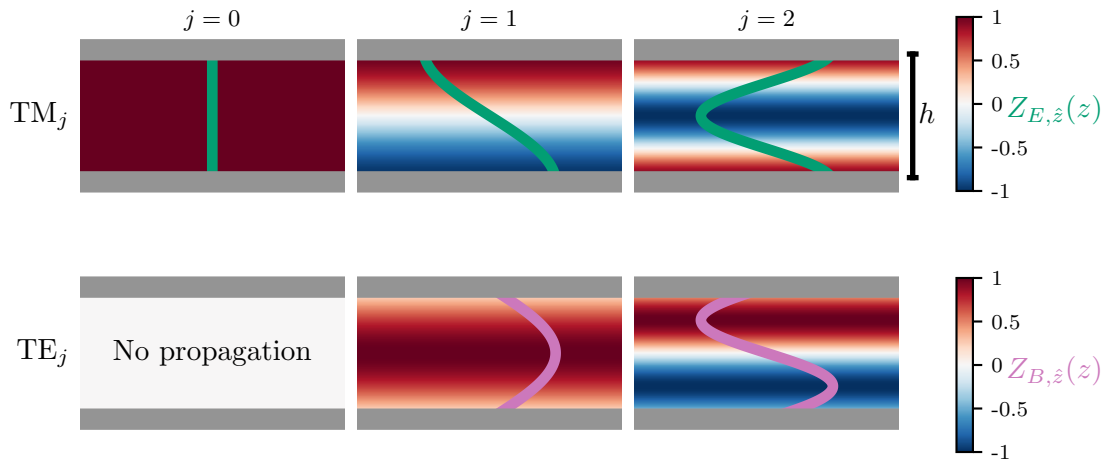

Figure 2.3: Intensity of $Z_{A,\hat{z}}(z)$ with respect to the number of mode j for TM and TE waves, respectively.

2.1.2 Microwave antennas

TM or TE wave polarizations can be selectively excited in our experimental setup via the specific geometry of the antenna used, which shapes its radiation pattern. For instance, Fig. 2.4(a) depicts the diagram of a straight antenna whose radiated electric field is mostly parallel to its longitudinal axis ($\hat{z}$-axis). Additionally, the corresponding magnetic field rotates around the longitudinal axis and, as a consequence, its $\hat{z}$-component is always zero ($B_{\hat{z}} = 0$). Thus, this kind of antennas fulfil the spatial conditions to excite/measure a electromagnetic field with TM polarization. An image of the actual antenna used in our experiment can be seen in Fig. 2.4(c) labeled with the number 3.

A different result can be obtain by considering an antenna with a distinct geometry. In the case shown in Fig. 2.4(b), the shape of a straight antenna is modified by folding the conductor into a loop in the $\hat{\rho} - \hat{\phi}$ plane. Then, the circuit is closed by welding the

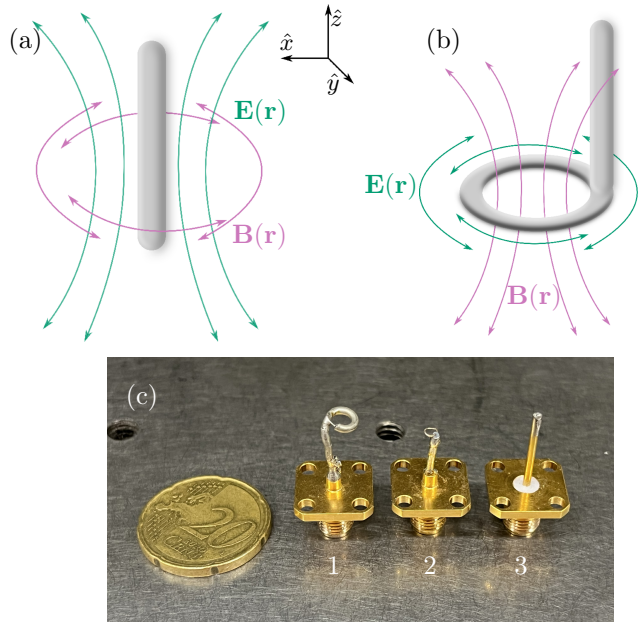

Figure 2.4: Diagram of the electric and magnetic field radiated by a (a) straight antenna and a (b) loop antenna. (c) Image showing the actual loop and straight antennas used in our experiments.

conductor's end with its inner part. The corresponding electric field of this new loop antenna follows the loop geometry having a $\hat{z}$-component equal to zero $E_{\hat{z}} = 0$. The sinusoidal electrical current in the loop induces a magnetic field perpendicular to the $\hat{\rho} - \hat{\phi}$ plane and proportional to the electric field ($B_{\hat{z}} \propto E_{\hat{\phi}}$). On the contrary to the straight antenna, loop antennas fulfil the spatial conditions to excite/measure electromagnetic waves with TE polarization. Two different loop antennas used in our setup are shown in Fig. 2.4(c) labeled as 1 and 2. Note that the polarized patterns radiated by the straight and loop antennas are incompatible with each other.

Typical loop antennas used in our experiments have a loop diameter of 2 and 5.5 mm, being in between the wavelengths range of the sinusoidal signal generated by the VNA. As a result, loop antennas exhibit measurable resonances produced by standing waves inside them. The effect of such undesirable resonances is experimentally avoided by tuning the usable frequency window for each antenna. In practice, the small loop antenna (loop diameter= 2 mm) displays a flat usable frequency interval (7 GHz, 10 GHz). On the other hand, the big loop antenna (loop diameter= 5.5 mm) works perfectly in the range (5 GHz, 8 GHz).

2.2 Dielectric cylinders

The flexibility of our experimental setup in mainly due to the fact that we can locally modify the permittivity of the microwave cavity by means of the dielectric cylinders. These ceramic cylinders are 5 mm height, 3 mm radius and are made of TiZrNbZnO (Exxelia Temex manufacturer serie E6000). They are characterized by a high relative permittivity $\epsilon_c = 45$, no magnetic properties (relative permeability $\mu_c = 1$, therefore $n_c = \sqrt{\mu_c \epsilon_c} \approx 7$) and a large quality factor of $Q \approx 8000$ (@ 5 GHz). Fig. 2.5 shows an image of an actual dielectric cylinder used in our experiments.

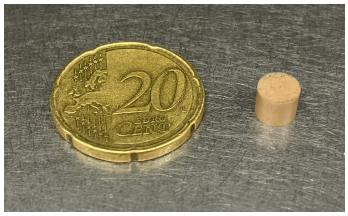

Figure 2.5: Image showing the actual dielectric cylinder.

The dielectric cylinders are precisely placed over the bottom plate by dropping them through a metallic tube. In order to use the motorized XY-stage to indicate the positions, the top plate is removed and replaced by a tube. In Fig. 2.6 we show a image of the cylindrical metallic tube used in the experimental setup to place the dielectrics.

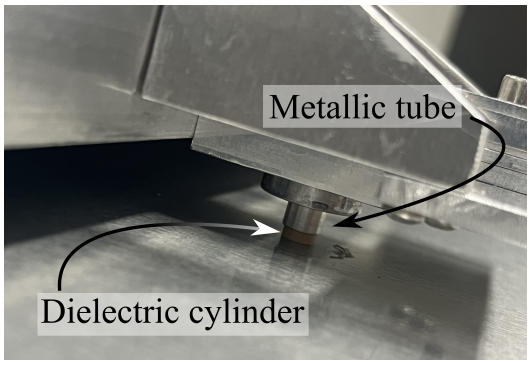

Figure 2.6: Image of the metallic tube used to place the cylinders.

2.2.1 Individual cylinder resonances

To predict the resonances of an isolated cylinder, we solve the Maxwell's equations (2.3) with the boundary conditions (2.4). We use cylindrical coordinates (ρ, θ, z) where the displacement vector is then written as

$$\mathbf{D}(\mathbf{r}) = \epsilon(\rho)\mathbf{E}(\mathbf{r}), \tag{2.19}$$

with $\epsilon(\rho) = [\epsilon_0 + (\epsilon_c - \epsilon_0)\Xi(r_c - \rho)]$, $\Xi(\rho)$ the Heaviside function and r_c the radius of the cylinder. Note that in writing Eq. (2.19), we have also assumed that both conducting plates are in contact with the cylinder.

We consider a sinusoidal monochromatic time dependence for both fields [$\mathbf{E}(\mathbf{r}, t) = \mathbf{E}(\mathbf{r})\mathrm{e}^{-\mathrm{i}\omega t}$ and $\mathbf{B}(\mathbf{r}, t) = \mathbf{B}(\mathbf{r})\mathrm{e}^{-\mathrm{i}\omega t}$, see Eq. (2.5)]. The individual Maxwell's equation solutions inside and outside the cylinder are matched following the continuity conditions at the interface between the dielectric and the air. This results in tangential continuity conditions of the electric and magnetic fields

$$[\hat{\mathbf{n}} \times (\mathbf{E}_D - \mathbf{E}_A)]\Big|_{\rho=r_c} = 0, \qquad [\hat{\mathbf{n}} \times (\mathbf{B}_D - \mathbf{B}_A)]\Big|_{\rho=r_c} = 0, \tag{2.20}$$

and the continuity of the normal components of the displacement vector and the magnetic field

$$[\hat{\mathbf{n}} \cdot (\mathbf{D}_D - \mathbf{D}_A)]\Big|_{\rho=r_c} = 0, \qquad [\hat{\mathbf{n}} \cdot (\mathbf{B}_D - \mathbf{B}_A)]\Big|_{\rho=r_c} = 0. \tag{2.21}$$

with the index D (A) denoting the dielectric (air).

Helmholtz equations now reads

$$\Delta\mathbf{E}(\mathbf{r}) = -k^2(\rho)\mathbf{E}(\mathbf{r}), \qquad \Delta\mathbf{B}(\mathbf{r}) = -k^2(\rho)\mathbf{B}(\mathbf{r}), \tag{2.22}$$

where $k(\rho) = \omega/\mathrm{c}(\rho)$ is the wave number and $\mathrm{c}(\rho) = 1/\sqrt{\mu_0\epsilon(\rho)}$ is the wave velocity. Given the cylindrical symmetry of the system and the presence of the conducting plates, the process presented in Section 2.1.1 is followed step by step to obtain

$$\text{TM mode} \quad \rightarrow \quad E_{\hat{z}} = E_0\mathrm{e}^{\mathrm{i}\alpha\theta}\cos\left(\frac{j\pi z}{h}\right)\begin{cases} J_\alpha(q_D\rho) & \rho < r_c \\ aH_\alpha^{(1)}(q_A\rho) & \rho > r_c \end{cases} \quad (j = 0, 1, 2, \dots) \tag{2.23}$$

$$\text{TE mode} \quad \rightarrow \quad B_{\hat{z}} = B_0\mathrm{e}^{\mathrm{i}\alpha\theta}\sin\left(\frac{j\pi z}{h}\right)\begin{cases} J_\alpha(q_D\rho) & \rho < r_c \\ aH_\alpha^{(1)}(q_A\rho) & \rho > r_c \end{cases} \quad (j = 1, 2, 3, \dots) \tag{2.24}$$

with $q_D = \sqrt{k_c^2 - k_z^2}$, $q_A = \sqrt{k^2 - k_z^2}$, $H_\alpha^{(1)}$ the Hankel function and $a = J_\alpha(q_D r_c)/H_\alpha^{(1)}(q_A r_c)$. Here, $k_c = \omega n_c/\mathrm{c}_0$ and $k = \omega/\mathrm{c}_0$ are the wave numbers inside and outside the cylinder, respectively, and similarly to propagating modes in the empty cavity, the constraints $k_c > k_z$ and $k > k_z$ provide the frequency limits for non-evanescent waves in the dielectric and in the air, respectively. Therefore, according to the polarization of the waves emitted by the antenna, our experimental system presents different features that can be classified into two categories as detailed in the following sections.

2.2.1.1 Transverse magnetic (TM) polarization

The TM polarization is characterized by propagating waves at any frequency in both media (inside and outside the cylinder). However, given the difference in the refractive

index, the cylinders remain an obstacle that scatter the incident wave in all directions, leading to Mie scattering.

The scattering efficiency of the individual Mie resonances supported by a 2D cylinder can be computed using cylindrical harmonic expansion [163]. In this case, we consider a incident plane wave with wave number k scattering on the cylinder. Thus, the scattered electric and magnetic fields are given by [40, 163]

$$\mathbf{E}_s = -\sum_{\alpha=1}^{\infty} E_\alpha \left(\mathrm{i}a_\alpha \mathbf{M}_\alpha + b_\alpha \mathbf{N}_\alpha\right), \qquad \mathbf{H}_s = \frac{\mathrm{i}k}{\omega}\sum_{\alpha=1}^{\infty} E_\alpha \left(b_\alpha \mathbf{M}_\alpha + \mathrm{i}a_\alpha \mathbf{N}_\alpha\right). \tag{2.25}$$

where $\mathbf{M}_\alpha$ and $\mathbf{N}_\alpha$ are called the *cylindrical vector harmonics* and are defined by

$$\mathbf{N}_\alpha = \frac{\nabla_{\hat{\rho},\hat{\phi}} \times \mathbf{M}_\alpha}{k}, \qquad \mathbf{M}_\alpha = \nabla_{\hat{\rho},\hat{\phi}} \times (\hat{z}\chi_\alpha), \quad \text{and} \quad \nabla^2_{\hat{\rho},\hat{\phi}}\chi + k^2\chi = 0, \tag{2.26}$$

with χ known the as *generating function*. Since, χ is the solution of a 2D scalar cylindrical wave equation, it can be written as $\chi_\alpha = P_\alpha(k\rho)\mathrm{e}^{\mathrm{i}\alpha\phi}$, with $P_\alpha(k\rho)$ the solution of a Bessel differential equation. It is worth noting that $\mathbf{M}_\alpha$ lies in the $\hat{\rho}-\hat{\phi}$ plane, while $\mathbf{N}_\alpha$ is out of the plane. Finally, using the continuity relations at the cylinder surface, the coefficients a_α and b_α are computed as

$$a_\alpha = 0, \qquad b_\alpha = \frac{J_\alpha(n_c x)J'_\alpha(x) - n_c J'_\alpha(n_c x)J_\alpha(x)}{J_\alpha(n_c x)H^{(1)\prime}_\alpha(x) - n_c J'_\alpha(n_c x)H^{(1)}_\alpha(x)}, \tag{2.27}$$

where $x = kr_c$ is the wave number normalized by the radius of the cylinder. Given the initial TM polarization of the fields, the coefficients a_α are always zero since they are associated with an in-plane electric field and the $\hat{z}$-component of the magnetic field. The normalized scattering efficiency in 2D is then defined as

$$Q_{\mathrm{sca}} = \frac{2}{x}\left[|a_0|^2 + |b_0|^2 + 2\sum_{\alpha=1}^{\infty}\left(|a_\alpha|^2 + |b_\alpha|^2\right)\right]. \tag{2.28}$$

Fig. 2.7(a) displays the scattering efficiency as a function of the frequency for a infinite 2D cylinder with the radius and refractive index of our experimental dielectrics. As it can be observed, up to 15 GHz, six different resonances driven by the presence of cylinder are well visible. To mimic as closely as possible a purely 2D situation with our experimental setup, we need to impose the cavity to be in contact with the bottom and top faces of the cylinder (in practice $h = 5$ mm), and restrict the frequency range below the cutoff the first TM mode [$\nu_{\mathrm{cut}}(h = 5\text{ mm}) \approx 30$ GHz], as previously implemented by Aubry et al. [81]. This is not the case for the experiments presented here, where the height of the top plates is always > 5 mm. As shown by Reisner [164], increasing the air gap between the cylinder and the top plate shifts the Mie resonant frequencies in a non-monotonic way, this shift being different for each resonance. Additionally, breaking the symmetry in the $\hat{z}$-axis, also breaks the dichotomy between TM and TE modes, leading to new hybrid modes. The latter exhibits simultaneously $E_{\hat{z}}$ and $B_{\hat{z}}$ components of the electromagnetic field. Consequently a polarized antenna will not be able to collect all the energy stored in a hybrid mode, leading to fictitious losses. For example, a straight antennas is not sensitive to the $B_{\hat{z}}$ component.

As an example, we plot the electric field's $\hat{z}$-component ($E_{\hat{z}}$) scattered by a cylinder in our experimental cavity with $h = 13$ mm [$\nu_{\mathrm{cut}} \approx 11.53$ GHz] in Fig. 2.7(b). The reflected field is measured by a straight antenna at a distance $d \approx 11.31$ mm from the center of the cylinder, where the measured signal shows four different peaks below the 2D cutoff. However, by going through the cutoff frequency, the complexity of the signal highly

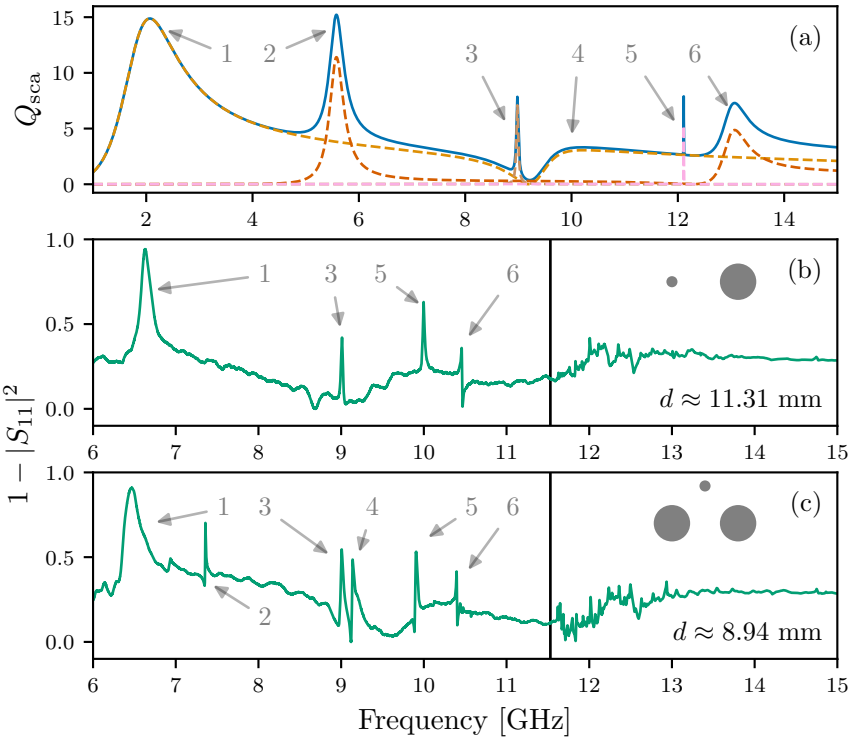

Figure 2.7: (a) Scattering efficiency for a 2D cylinder of radius 3 mm and refractive index $= \sqrt{45}$ (continuous blue line). Dashed lines represent the individual Mie resonances. Reflected scattered field (S_{11}) by (b) one and (c) two cylindrical dielectrics in a cavity characterized by $h = 13$ mm. The straight antenna is placed at distances (b) $d \approx 11.31$ mm and (c) $d \approx 8.94$ mm from the center of the cylinders. Cylinders in (c) are separated by a distance of 8 mm. A minimalist sketch of the array (cylinders-antenna) is represented by grey circles in (c) and (d). Vertical lines in (b) and (c) represent the cutoff frequency $\nu_{\text{cut}} \approx 11.53$ GHz.

increases. Despite that the break in the dichotomy between the TM and TE polarization prevents a one-by-one correspondence between the peaks in Figs. 2.7(a) and (b) [164], a big similitude is observed.

The effect of adding a second cylinder into the cavity can be seen in Fig. 2.7(c), where the scattered electric field is measured at a distance $d \approx 8.94$ mm from the center of both cylinders, which are separated by a distance of 8 mm. Below the 2D limit, three of the four peaks in Fig. 2.7(b) (labeled as 1, 3 and 6) appear almost at the same frequency (6.5, 10 and 10.5 GHz) with similar widths. Additionally, another two peaks have emerged at ~ 7.4 GHz and ~ 9.1 GHz. As for a single cylinder, the complexity of the scattered pattern strongly increases over the cutoff frequency. Chapter 4 is devoted to study the electric field given by the effect of the collective multiple scattering after adding several cylinders into the cavity.

2.2.1.2 Transversal electric (TE) polarization

Differently to TM polarization, TE waves lead to two different configurations. For high frequencies $\nu > c_0/(2h)$, the electromagnetic field can propagate everywhere and scattering processes equivalent to those described in the TM situation occurs. However, given the magnetic field inhomogeneity in the $\hat{z}$-axis for the lowest propagative mode [see Fig. 2.3], the perfect 2D limit stays unreachable when considering the presence of the conducting plates.

Contrary to the propagating modes, the frequency interval $c_0/(2n_c h) < \nu < c_0/(2h)$ is characterized by waves that can freely propagate inside the dielectric medium but still

exhibiting an evanescent behavior in the air. As a result, the electromagnetic field is confined in the cylinder leading to sharp well-isolated resonances. As the scattering resonances in the previous section, the increasing of the distance between the plates also shifts non-monotonically the TE resonance frequencies. However, Reisner [164] also shows that, at least for the fundamental TE eigenstate ($\alpha = 0$), the polarization symmetry holds, i.e. there is no hybridization with the TM modes even at $h = 16$ mm. While working in these polarization, we will restrict our research to this fundamental TE state (see, e.g., Chapter 5), further informations about higher modes are provided in Ref. [164].

In this particular frequency regime $[\mathrm{c}_0/(2n_c h), \mathrm{c}_0/(2h)]$, the magnetic field [Eq. (2.24)] can be properly written around the fundamental TE mode ($\alpha = 0$) with frequency ν_0 as

$$B_{\hat{z}} = B_0 \sin\left(\frac{\pi z}{h}\right) \begin{cases} J_0(q_D \rho) & \rho < r_0 \\ a K_0(\gamma_A \rho) & \rho > r_0 \end{cases} \tag{2.29}$$

where K_α is the modified Bessel function, and $a = J_0\left(q_D r_c\right) / K_0\left(\gamma_A r_c\right)$, with $q_D = \sqrt{\left(\frac{2\pi\nu_0 n_c}{\mathrm{c}_0}\right)^2 - \left(\frac{\pi}{h}\right)^2}$, and $\gamma_A = \sqrt{\left(\frac{\pi}{h}\right)^2 - \left(\frac{2\pi\nu_0}{\mathrm{c}_0}\right)^2}$. In order to model the situation in which there is an air gap over the cylinder, we assume that the solution of the wave equation can still be expressed as the product of functions of the individual variables. The z-dependency is then represented by $F(z)$, fulfiling the boundary conditions $F(0) = F(h) = 0$ with $h > 5$ mm and q_{eff} defined via the function $F(z)$ [165]. Given the lacking of symmetry in the $\hat{z}$-axis, we suppose that the field inside the cylinder can excite several evanescent modes in the air with wave numbers $\gamma_{m,\mathrm{eff}} = \sqrt{\left(\frac{m\pi}{h}\right)^2 - \left(\frac{2\pi\nu_0}{\mathrm{c}_0}\right)^2}$, leading to

$$B_{\hat{z}} \approx B_0 \begin{cases} F(z) J_0(q_{\mathrm{eff}} \rho) & \rho < r_c \\ \sum_m c_m \sin\left(\frac{m\pi z}{h}\right) K_0(\gamma_{m,\mathrm{eff}} \rho) & \rho > r_c \end{cases} \tag{2.30}$$

where c_m are constants determined by the continuity conditions. Eq. (2.30) is finally rewritten by including the z-dependency in the coefficient $c'_m = c_m \sin\left(\frac{m\pi z_0}{h}\right)/F(z_0)$ as

$$B_{\hat{z}} \approx B'_0 \Psi(\rho) = B'_0 \begin{cases} J_0(q_{\mathrm{eff}} \rho) & \rho < r_c \\ \sum_m c'_m K_0(\gamma_{m,\mathrm{eff}} \rho) & \rho > r_c \end{cases} \tag{2.31}$$

where the loop antenna is sitting at a height z_0 and $B'_0 = 1$ is a constant.

Eq. (2.31) can be experimentally challenged using a loop antenna. For instance, Fig. 2.8(a) depicts the $\hat{z}$-component of the magnetic field ($B_{\hat{z}}$) reflected by one cylinder in a cavity characterized by $h = 13$ mm, where the center of the antenna's loop is aligned with the center of the dielectric. A sharp peak indicates the isolated TE resonance of the cylinder, whose parameters (complex amplitude A_0, frequency ν_0 and width $\delta\nu_0$) can be obtained by fitting a Lorentzian function [see black line in Fig. 2.8(a)]

$$L(\nu) = \frac{A_0}{\nu - \nu_0 + \mathrm{i}\delta\nu_0}. \tag{2.32}$$

This analysis is then repeated along the $\hat{\rho}$-axis to extract the amplitude of the field as a function of the position. A comparison between Eq. (2.31) and the actual experimental data is depicted in Fig. 2.8(b) where a good agreement is observed.

Suppose now a system with two identical cylinders characterized by a bare resonant frequency ν_0 and separated by a distance d of the order of r_c, where one of the dielectrics is excited by a magnetic field with frequency $\nu \approx \nu_0$. Since the evanescent field that leaks out from the excited cylinder is able to excite the resonant mode of the second dielectric,

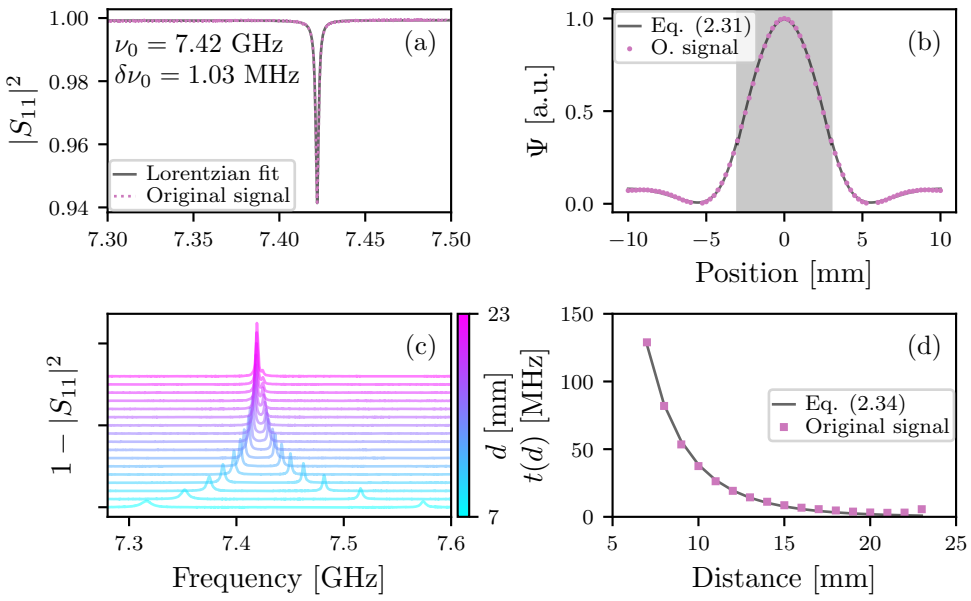

Figure 2.8: (a) Reflected magnetic field (S_{11}) by one cylinder in a cavity characterized by $h = 13$ mm (pink dotted line). A fit of Eq. (2.32), which allows to find the resonance parameters is represented by the black solid line. (b) Experimental radial function $\Psi(\rho)$ in a cavity with $h = 13$ mm (pink dots). A fit of Eq. (2.31) is represented by the black solid line and allows to find $q_{\text{eff}} = 0.61$ mm^{-1} with $m = 4$. The grey stripe represents the size occupied by the cylinder. (c) Reflected magnetic field (S_{11}) by two cylinders separated by a distance d in a cavity characterized by $h = 13$ mm. The exciting antenna is placed at a distant 8 mm from one of the cylinders (resonators). (d) Resonance splitting as a function of the distance between two resonators. A fit of Eq. (2.34) is represented by the black solid line and allows to find $\kappa = 43.58$ MHz and $\gamma_1 = 0.12$ mm^{-1}.

the cylinders can couple each other leading to a symmetric frequency splitting $\Delta\nu_0(d)$ [see e.g. Fig. 2.8(c)]. Our experimental system of coupled dielectrics can be then described by the Tight-Binding formalism (see Appendix A), where each resonant cylinder represents a site. The associated Hamiltonian matrix [see Eq. (A.4)] for two cylinders is written as

$$H(d) = \begin{pmatrix} \nu_0 & t(d) \\ t(d) & \nu_0 \end{pmatrix}, \tag{2.33}$$

with the coupling $t(d)$ determined by evaluating the superposition of the evanescent fields in between the cylinders as [164, 166]

$$t(d) = \frac{\Delta\nu_0}{2} \approx \kappa K_0\left(\gamma_1 \frac{d}{2}\right)\left[K_2\left(\gamma_1 \frac{d}{2}\right) + K_0\left(\gamma_1 \frac{d}{2}\right)\right], \tag{2.34}$$

where κ and γ_1 are constants.

Fig. 2.8(c) depicts the $\hat{z}$-component of the magnetic field reflected by two coupled cylinders (resonators) as a function of the distance between their centers d. The actual experimental data is fitted by a sum of two Lorentzian functions [see Eq. (2.32)] allowing to extract the frequency splitting $\Delta\nu_0$ as a function of the distance d [see Fig. 2.8(d)]. A comparison between the experimental coupling parameter (pink squares) and the theoretical prediction [Eq. (2.34), solid black line] can be seen in Fig. 2.8(d), where a good agreement is observed.

By adding several resonators into our cavity, our system becomes an experimental emulator of tight-binding lattices. In Chapter 5 we use our electromagnetic tight-binding simulator to explore the paradigmatic features of topological systems.

2.3 Experimental incertitudes

In the last sections, we presented the details of the experimental platform used all along this thesis. As previously mentioned, the presence of the top and bottom plates, as well as the distance between them, play an important role on the behaviour of the cylinders that constitute our lattices. Moreover, the influence of the metallic plates has to be properly taken into account. For instance, the lack of parallelism between the plates breaks the homogeneity of the boundary conditions along the $\hat{z}$-axis, modifying locally the behaviour of certain cylinders. Fortunately, this issue can be corrected by measuring and adjusting in multiple locations the height of the top plate. In that way, prior any data acquisition, both plates are aligned with a precision < 1 mm. Similarly, we adjust the motorized XY-stage to ensure a perpendicular movement in the plane.

Besides the issues due to the metallic plates and the XY-stage, other important experimental incertitudes are linked to the dielectric cylinders themselves. Indeed, we use sets of ceramics belonging to the same series, which are not completely identical and have slightly different resonant frequencies. To overcome this issue one can use the cylinders as resonators and characterize them by their individual TE resonant frequency. Afterwards, measurements are performed by preparing our samples using the set of cylinders with the most similar features. However, the resonant frequency of each resonator can also be affected by the quality of the contact with the metallic bottom plate. Given that our experimental cavity is never completely free of imperfections or dust, and that the placement of the cylinders is carried out just by dropping them through the metallic tube (see Fig. 2.6), it always exists an inhomogeneous air layer between the plate and the dielectric. As a consequence, in each replacement of same resonator, there is a random variation in its resonant frequency. This issue is quantified in Fig. 2.9(a) where the magnetic field reflected by a single cylinder, which has been replaced ten times at the same position over the metallic plate, is depicted. As we can observe, the standard deviation of the resonant frequencies σ_{ν_0} is of the same order of the typical width of the Lorentzian $\langle \delta\nu_0 \rangle$. To correct this problem, the bottom plate is covered by a self-adhesive thin plastic film ensuring an uniform poor electrical contact with the cylinders. The previous replacing experiment is repeated under the new conditions [see Fig. 2.9(b)], reducing drastically the random variation of the eigenfrequencies.

As previously mentioned, the placement of the cylinders is performed by drooping them through a metallic tube (see Fig. 2.6). To allow the cylinders to pass through the tube, the internal radius of the tube is slightly larger than the radius of the cylinders, giving rise to another incertitude. To quantify the quality of the resonator spatial placing,

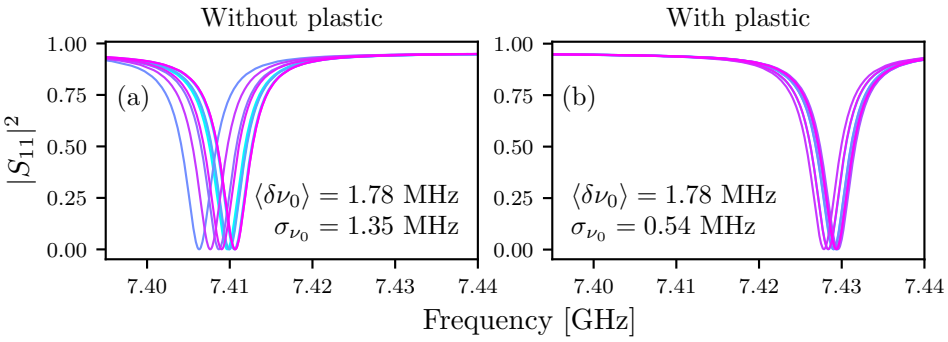

Figure 2.9: Reflected magnetic field (S_{11}) by one cylinder in a cavity characterized by $h = 13$ mm (a) without and (b) with the thin insulating plastic film.

the same cylinder is replaced 25 times by setting the guide at the same position. In each replacement, the resonator is spatially scanned around its first TE mode [see Fig. 2.8(b)] to precisely locate its center. Fig. 2.10 shows then the center spatial position of the cylinder, in both directions Δ_x and Δ_y after each replacement. Despite that there exist a random variation (Δ_x, Δ_y) of the cylinder center, the corresponding standard deviations are always smaller than 0.08 mm in each direction, proving the high precision of our experimental setup.

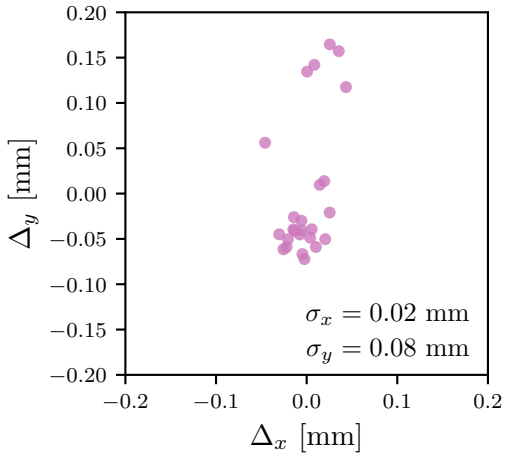

Figure 2.10: Center position of a single resonator in a cavity characterized by $h = 13$ mm. Each point represent the position of eigenfunctions center when the cylinder is replaced at the same position.

2.4 Data analysis

As it can be inferred in Section 2.2, the $\hat{z}$-components of the electric and magnetic fields can be related to the wave-functions ψ of the system *cavity-cylinders*. At each position, it is then possible to write $E_{\hat{z}}(\mathbf{r}) \propto \psi(\mathbf{r})$ and $B_{\hat{z}}(\mathbf{r}) \propto \psi(\mathbf{r})$ for the TM and TE polarization, respectively. For instance, the features of one or two well isolated resonances corresponding to the fundamental TE mode can be extracted by simply fitting a sum of Lorentzian functions [Eq.(2.32)]. However, by increasing the number of cylinders in the system, the complexity of the signal increases too, leading to the impossibility to identify and characterize all the Lorentzian peaks in the signal. In this Section, we introduce different algorithms and tools that will be used all along this work to analyze the experimental data.

2.4.1 The Breit-Wigner decomposition

We start by assuming that the system *cavity-cylinders* can be modelled as a closed system characterized by the Hamiltonian $\hat{H}$ with discrete spectrum $\{\nu_n\}$ and corresponding eigenstates $\{\psi_n(\mathbf{r})\}$. To transform our closed system into a scattering one, we attach to the cavity N weakly coupled antennas with coupling strength σ_i $(i = 1, 2, \ldots, N)$. Finally, computing the scattering properties of the effective Hamiltonian ($\hat{H}$ + antennas) allows to relate the elements of the scattering matrix (see Section 2.1) with the features of the eigenmodes of the system *cavity-cylinders* as [167]

$$S_{ij}(\nu) = \delta_{ij} - \mathrm{i}\sqrt{\sigma_i \sigma_j} \sum_k \frac{\psi_k(\mathbf{r}_i)\psi_k^*(\mathbf{r}_j)}{\nu^2 - \nu_k^2 + \mathrm{i}\Gamma_k^2}, \tag{2.35}$$

where δ_{ij} is the Kroneker delta and Γ is related with the width of the states. Eq. (2.35) is known as the Breit-Wigner decomposition of the scattering matrix, and despite it is defined for N open channels (antennas), our system is physically restricted to $N = 2$. Therefore, the vectors $\mathbf{r}_{i,j}$ indicate the position of the antennas in our experimental cavity.

2.4.2 The Harmonic Inversion

According to the Breit-Wigner decomposition of the S-matrix [Eq. (2.35)], the transmission and reflection signals can be viewed as the superposition of complex resonances, each of which being represented by a Lorentzian function, i.e., by four parameters: the frequency ν_k, the width $\delta\nu_k$, and the complex amplitude A_k. Due to the specific use we will make of it, we will concentrate here only on the complex resonance sum decomposition of the transmission signal S_{21}. In the case of our microwave cavity with weakly coupled antennas, the latter can be written for any given measurement position as [167]

$$S_{21}(\nu) = -\mathrm{i}\sqrt{\sigma_i\sigma_j}\sum_k \frac{\psi_k(\mathbf{r}_i)\psi_k^*(\mathbf{r}_j)}{\nu^2 - \nu_k^2 + 2\mathrm{i}\nu_k\delta\nu_k}. \tag{2.36}$$

Then, for frequencies close to $\nu_k(\approx \nu)$, we have

$$S_{21}(\nu) = -\mathrm{i}\sum_k \frac{A_k}{\nu - \nu_k + \mathrm{i}\delta\nu_k}, \tag{2.37}$$

where we have assumed constant antenna couplings $\sigma_1(\sigma_2)$ throughout the whole frequency range, thus $A_k = \sqrt{\sigma_1\sigma_2}\psi_k(\mathbf{r}_2)\psi_k^*(\mathbf{r}_1)/(2\nu_k)$.

Given the huge amount of unknown parameters, the extraction of the resonances from the raw signal is not a trivial task. Here, we use a powerful tool known as *harmonic inversion* to obtain all the resonances parameters of a complex signal. This method was first introduced by Wall and Neuhauser [168], and then improved by Mandelshtam and Taylor [169, 170]. To apply the harmonic inversion to our experimental signals, we start by choosing a filter $g(\nu)$ defined as

$$g(\nu) = \begin{cases} 1 & \text{for} \quad \nu \in [\nu_0 - \Delta\nu, \nu_0 + \Delta\nu], \\ 0 & \text{everywhere else}, \end{cases} \tag{2.38}$$

where the filtered transmitted signal $S'_{12}(\nu) = S_{12}(\nu) \times g(\nu) = -\mathrm{i}\sum_{k=1}^{K}\frac{A_k}{\nu-\nu_k+\mathrm{i}\delta\nu_k}$ is expected to have around $K \sim 50 - 200$ resonances inside the interval $[\nu_0 - \Delta\nu, \nu_0 + \Delta\nu]$. Then, the filtered signal is Fourier transformed to the "time" domain to obtain a band-limited signal

$$C(t) = \frac{1}{2\pi}\int_{\nu_0-\Delta\nu}^{\nu_0+\Delta\nu} S'_{12}(\nu)\mathrm{e}^{-\mathrm{i}(\nu-\nu_0)t}\mathrm{d}\nu = \sum_{k=1}^{K} A_k\mathrm{e}^{-\mathrm{i}(\nu_k-\mathrm{i}\delta\nu_k-\nu_0)t}, \tag{2.39}$$

with $\nu_k \in [\nu_0 - \Delta\nu, \nu_0 + \Delta\nu]$. Additionally, the introduction of ν_0 into the exponential shifts the signal by $-\nu_0$ in the "frequency" domain and relocates it around 0, decreasing the phase oscillations of the band-limited signal $C(t)$. Finally, Eq. (2.39) can be discretized in a $2K$ equidistant grid with time step $\tau = \pi/\Delta\nu$

$$c_j = C(t = j\tau) = \sum_{k=1}^{K} A_k\mathrm{e}^{-\mathrm{i}(\nu_k-\mathrm{i}\delta\nu_k-\nu_0)j\tau}, \qquad j \in [0, 2K-1], \tag{2.40}$$

reducing the problem of finding the resonances to the resolution of a set of $2K$ nonlinear equations

$$c_j = \sum_{k=1}^{K} A_k z_k^j, \qquad j \in [0, 2K-1], \tag{2.41}$$

where $z_k = \mathrm{e}^{-\mathrm{i}(\nu_k - \mathrm{i}\delta\nu_k - \nu_0)\tau}$.

The strategy to solve Eq. (2.41) is to convert the system of nonlinear equations into a linear algebra problem. We start by expressing K of its elements in a matrix representation

$$\begin{aligned} \begin{pmatrix} c_{j+1} \\ \vdots \\ c_{j+K} \end{pmatrix} &= \begin{pmatrix} z_1^{j+1} & \cdots & z_K^{j+1} \\ \vdots & & \vdots \\ z_1^{j+K} & \cdots & z_K^{j+K} \end{pmatrix} \begin{pmatrix} A_1 \\ \vdots \\ A_K \end{pmatrix} \\ \longrightarrow \begin{pmatrix} z_1^{j+1} & \cdots & z_K^{j+1} \\ \vdots & & \vdots \\ z_1^{j+K} & \cdots & z_K^{j+K} \end{pmatrix}^{-1} \begin{pmatrix} c_{j+1} \\ \vdots \\ c_{j+K} \end{pmatrix} &= \begin{pmatrix} A_1 \\ \vdots \\ A_K \end{pmatrix}, \end{aligned} \tag{2.42}$$

then, we replace Eq. (2.42) into Eq. (2.41) to get

$$c_j = \begin{pmatrix} z_1^j \cdots z_K^j \end{pmatrix} \begin{pmatrix} z_1^{j+1} & \cdots & z_K^{j+1} \\ \vdots & & \vdots \\ z_1^{j+K} & \cdots & z_K^{j+K} \end{pmatrix}^{-1} \begin{pmatrix} c_{j+1} \\ \vdots \\ c_{j+K} \end{pmatrix} = \sum_{k=1}^{K} a_k c_{j+k}, \tag{2.43}$$

where, we observe that every signal point c_j can be computed from a linear combination of the next K points, and is determined by the coefficients a_k with $k = 1, \ldots, K$. Now, by substituting Eq. (2.41) into both sides of Eq. (2.43), we obtain

$$\sum_{k=1}^{K} A_k z_k^j = \sum_{k=1}^{K} \sum_{l=1}^{K} a_l A_k z_k^{j+l} \longrightarrow \sum_{k=1}^{K} \left[\sum_{l=1}^{K} a_l z_k^{j+l} - z_k^j \right] A_k = 0, \tag{2.44}$$

which is satisfied for an arbitrary set of amplitudes A_k. Thus, the values $z_k = \mathrm{e}^{-\mathrm{i}(\nu_k - \mathrm{i}\delta\nu_k - \nu_0)\tau}$ are given as the zeros of the polynomial

$$\sum_{l=0}^{K} a_l z^l = 0 \quad \text{with} \quad a_0 = 1, \tag{2.45}$$

and finding them represents the only nonlinear step of the method. The roots of a polynomial can be found by the diagonalization of the Hessenberg matrix

$$\mathbf{A} = \begin{pmatrix} -\frac{a_{K-1}}{a_K} & -\frac{a_{K-2}}{a_K} & \cdots & -\frac{a_1}{a_K} & -\frac{a_0}{a_K} \\ 1 & 0 & \cdots & 0 & 0 \\ 0 & 1 & \cdots & 0 & 0 \\ \vdots & \vdots & & \vdots & \vdots \\ 0 & 0 & \cdots & 1 & 0 \end{pmatrix}, \tag{2.46}$$

which is highly robust for finding the zeros of a high degree polynomial. As a last step, the values of z_k are substituted in Eq. (2.41) to compute the values of the amplitude A_k.

To summarize, the four parameters of each of the resonances that make up the signal are given by (i) the solutions of the set of linear equations (2.43), for a_k; (ii) the diagonalization of the matrix (2.46), for the frequencies $\nu_k = \nu_0 - \mathrm{Im}\{\ln z_k\}/\tau$ and the widths $\delta\nu_k = -\mathrm{Re}\{\ln z_k\}/\tau$; (iii) the solution of the non linear system of equations (2.41), for the amplitude A_k.

To exemplify the use of the Harmonic inversion method, Fig. 2.11(a) shows the intensity of the experimental transmitted signal $|S_{21}|^2$ in a Golden Angle spiral (this system is studied in detail in Chapter 4). Vertical dash-dotted lines indicate the limits of one chosen window (7.95 GHz to 8.55 GHz). The complex nature of the signal is presented in Fig. 2.11(b), and (c) (purple lines) by means of the amplitude $|S_{21}|$ and phase $\arg\{S_{21}\}$;

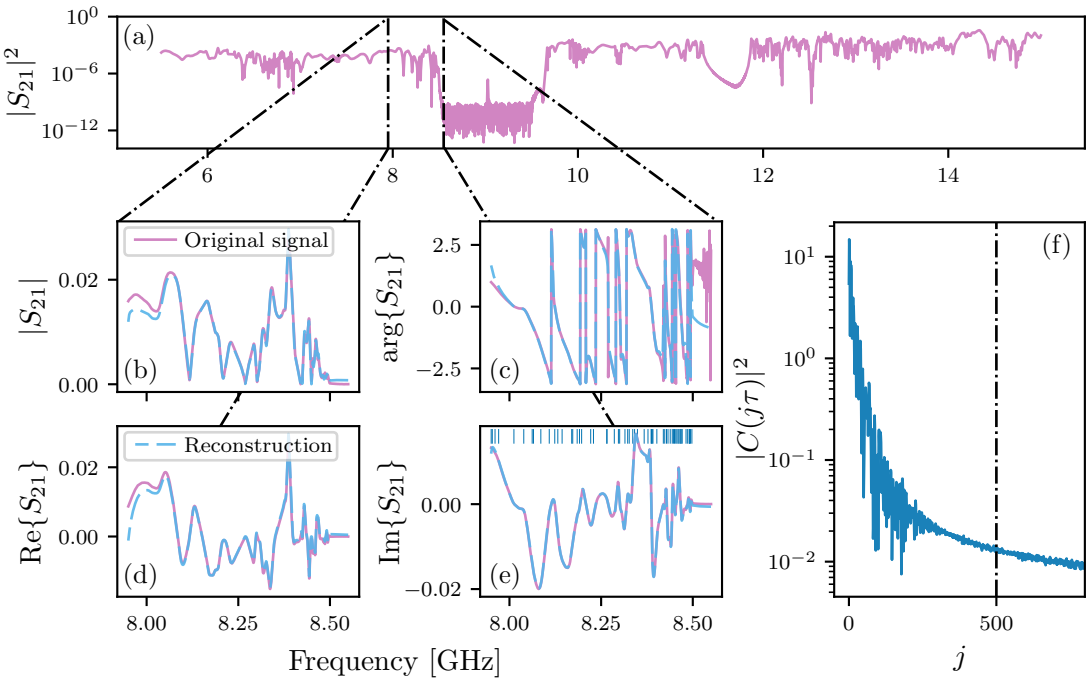

Figure 2.11: (a) Transmitted intensity $|S_{12}(\nu)|^2$ for the golden-angle spiral. Black dash-dotted lines indicate the frequency interval considered in this example ($7.95 \leq \nu \leq 8.55$). (b) Amplitude $|S_{12}(\nu)|$, (c) phase $\arg\{S_{12}(\nu)\}$, (d) real part $\mathrm{Re}\{S_{12}(\nu)\}$ and (e) imaginary part $\mathrm{Im}\{S_{12}(\nu)\}$ of the complex filtered signal shown in (a). Purple continuous line represents the original signal while indigo dashed lines are Eq. (2.37) evaluated for the resonances obtained by the harmonic inversion. Blue vertical lines in (e) display the frequencies ν_k recovered by the harmonic inversion method. (f) Intensity of the band-limited signal $|C(j\tau)|^2$ corresponding to the Fourier transform of the filtered signal shown in (b), (c), (d) and (e). The black dash-dotted line indicates the value $2K = 500$ considered in this example.

or in Fig. 2.11(d), and (e) by the real $\mathrm{Re}\{S_{21}\}$, and imaginary parts $\mathrm{Im}\{S_{21}\}$ of the filtered signal shown in Figure 2.11(a). As expected up to this point, no guess about the resonances that compose the signal can be done from the raw measurement. During the harmonic inversion method, the complex spectrum is Fourier transformed to obtain the band-limited signal whose intensity is plotted in Fig. 2.11(f). $|C(j\tau)|$ is characterized by sharp peaks for small values of j, up to a certain limit ($j \sim 250$ in this case). Such peaks disappear and the signal falls below the level of noise. We use twice the value of this transition to set the value of $2K$ needed in Eq. (2.40). Note that this value is different for each case. The choice of K sets exactly the number of resonances that will be found by the algorithm.

To ensure the robustness of the result, three different criteria are used to discriminate spurious resonances recovered by the harmonic inversion. As a first criterion, the non linear system (2.41) is solved twice, once by considering $j = 0, \ldots, 2K-1$ and, then with $j = 1, \ldots, 2K$. Later, both results are compared, and the resonances depending on the choice of j, or out of the limits of the filter, are discarded. The second discrimination is carried out by considering that all resonances whose amplitude $|A_k| < 10^{-8}$ GHz are the result of the noise in the original signal, and are also discarded. Finally, only resonances with sufficient resonance depth/height are taken into account. To do this, we compare the amplitude A_k versus the width $\delta\nu_k$ of the resonance. Numerically we chose $|A_k|/\delta\nu_k > 10^{-4}$. The result of the harmonic inversion after filtering with the three discriminating criteria is shown in Fig. 2.11(b), (c), (d), and (e), where a reconstruction of the corresponding complex signal is represented by the dashed indigo line. A good agreement between the original signal and its reconstruction is observed. In this case, a total of 61 resonances were found in

this interval, and their frequencies ν_k are plotted in Fig. 2.11(e) where each vertical blue line represents a resonance. Note that having all parameters of a resonance also allows to estimate the strength of its energy confinement via the quality factor Q_k as

$$Q_k = \nu_k / \delta\nu_k. \tag{2.47}$$

2.4.3 The clustering

In all cases studied in this thesis (see Chapters 4 and 5), the transmitted signal is measured in numerous positions thanks to the movable antenna (see Section 2.1, pp. 34). Once we are able to find the parameters of the resonances that compose one complex signal (for example Fig. 2.11), the harmonic inversion can be applied individually over all measured spatial locations. Each resonance k extracted using the harmonic inversion procedure is therefore associated with a position on the map (x_k, y_k) and can then be represented in a 6-dimensional space. An example of the resulting data is shown in Fig. 2.12 for the same Golden-angle spiral, where resonance density maps (from dark blue to yellow) are depicted. In Fig. 2.12, the spatial positions (a) x_k and (b) y_k as well as (c) the phases $\arg\{A_k\}$, (d) the widths $\delta\nu_k$ and (e) the amplitudes $|A_k|$ of each resonance extracted by the harmonic inversion are plotted as a function of the frequencies ν_k in a short frequency window ($8.42 \leq \nu_k \leq 8.52$). As a result of the high point density in certain regions, different structures made up of clusters emerge. Such clusters are directly related with the eigenmodes of the system and their correct identification and delimitation was previously used to find the number of states carried by the system [81] [which is proportional to the density of states (DoS)].

All resonances belonging to the same cluster should ideally posses the same frequency. Due to the presence of the measurement antenna, the resonance frequencies extracted at a given spatial position are affected differently and slightly shifted according to the electromagnetic field intensity at that point [171]. By allowing the mobile antenna to penetrate only slightly into the cavity, in practice 3 mm, this effect is reduced, but still present [167]. Additionally to the presence of the antenna, small local variations in the cavity height also modify the resonant frequencies. To reduce this effect, the distance between plates is measured at different positions ensuring a variation < 1 mm. The combination of these two effects explains the dispersion of the Lorentzian parameter values observed in Fig. 2.12.

For the identification of all data points belonging to a certain cluster [see e.g. Fig. 2.12], a density-based algorithm [172] is implemented. Specifically, we use a slightly modified version of the C-DBSCAN algorithm [81], firstly proposed by Ruiz, Spiliopoulou, and Menasalvas [172]. C-DBSCAN identifies point neighbourhoods in a D-dimensional metric space and requires no a priori knowledge of the shape, number of points or data distribution of the cluster. In our case, the metric space can be freely chosen as (x, y, ν), $(x, y, \nu, \delta\nu)$, $(x, y, \nu, \ln|A|)$, or $(x, y, \nu, \delta\nu, \ln|A|)$ in order to obtain the best clustering results at the desired frequency. In addition, each cluster must satisfy the constraint of not containing two points with the same (x, y) coordinates. The procedure is highly efficient, but cannot be fully automated. The main difficulties are of two kinds: (*i*) when the amplitude of the resonances is of the order of noise, the harmonic inversion procedure fails; (*ii*) when two or more clusters interpenetrate too densely, preventing their identification. The clustering process can also be carried out by manually choosing the points belonging to a cluster. However, in this way it is impossible to meet the condition of having only one point per position.

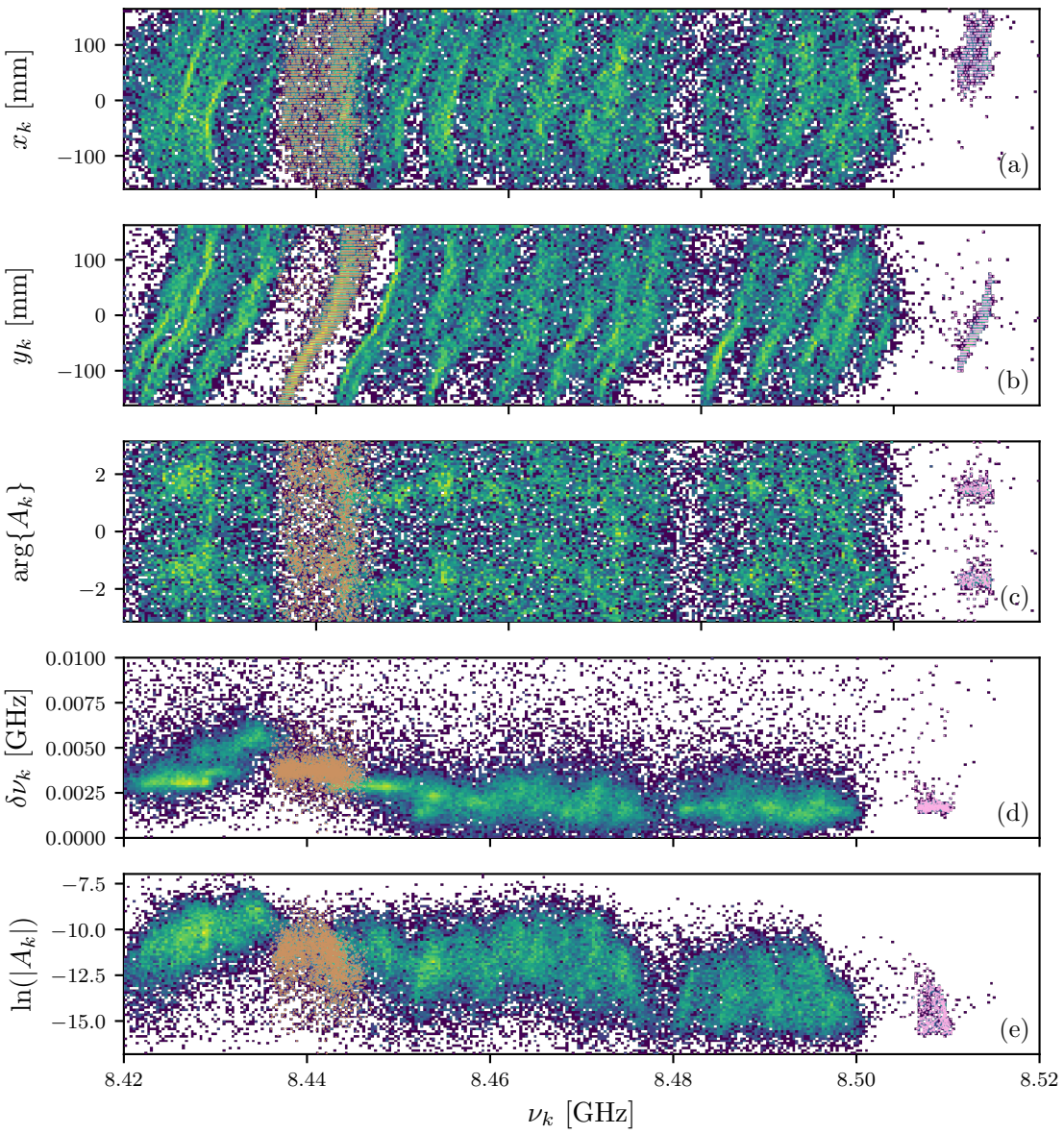

Figure 2.12: Spatial positions (a) x_k and (b) y_k, (c) phases $\arg\{A_k\}$, (d) widths $\delta\nu_k$ and (e) logarithm of the amplitudes $|A_k|$ as a function of the frequencies ν_k extracted by the harmonic inversion. Density plots allow the identification of modes and regions with high-density of resonances. Brown and pink dots show two different examples of clusters.

2.4.4 Reconstruction of the modes

After selecting a given cluster [see, e.g., brown dots in Fig 2.13(a) for the same Golden-angle spiral], a phase rotation is applied on the complex amplitudes $D_k = \mathrm{e}^{\mathrm{i}\alpha} A_k$ such that their real and imaginary parts become independent variables $\langle \mathrm{Re}\{D_k\}\,\mathrm{Im}\{D_k\}\rangle = 0$ [173]. We have

$$\begin{aligned} \mathrm{Re}\{D_k\} &= \mathrm{Re}\{A_k\}\cos\alpha - \mathrm{Im}\{A_k\}\sin\alpha, \\ \mathrm{Im}\{D_k\} &= \mathrm{Im}\{A_k\}\cos\alpha + \mathrm{Re}\{A_k\}\sin\alpha, \end{aligned} \tag{2.48}$$

$$\left\langle \mathrm{Re}\{A_k\}\,\mathrm{Im}\{A_k\}\cos 2\alpha + \frac{1}{2}\left(\mathrm{Re}\{A_k\}^2 - \mathrm{Im}\{A_k\}^2\right)\sin 2\alpha \right\rangle = 0 \tag{2.49}$$

$$\tan 2\alpha = -\frac{2\,\langle \mathrm{Re}\{A_k\}\,\mathrm{Im}\{A_k\}\rangle}{\langle \mathrm{Re}\{A_k\}\rangle^2 - \langle \mathrm{Im}\{A_k\}\rangle^2}. \tag{2.50}$$

Fig. 2.13(b) illustrates the effect of rotation in the complex plane when applying Eq. (2.50). The existence of a phase reference allows to represent the complex mode through its signed amplitude

$$E_k = |D_k| \mathrm{sgn}\left[\mathrm{Re}\left(D_k\right)\right] . \tag{2.51}$$

The spatial modal structure [Eq. (2.51)] of the cluster shown in Fig. 2.13(a) and (b) is then reconstructed in Fig. 2.13(c).

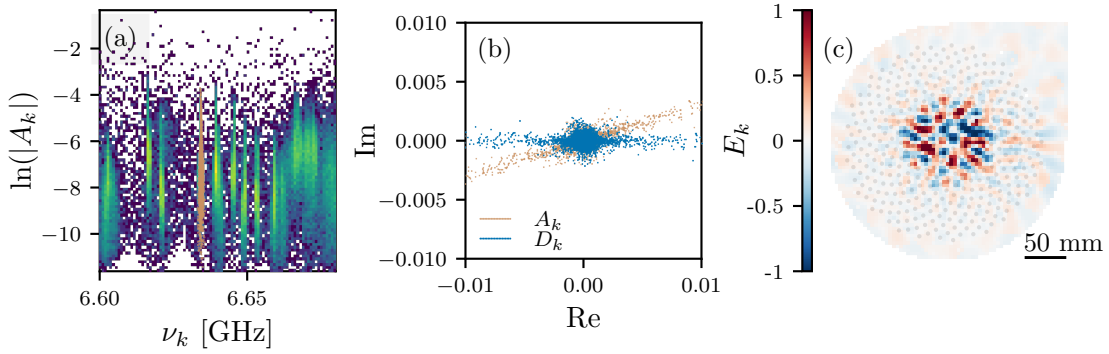

Figure 2.13: (a) Density plot of the amplitudes $|A_k|$ as a function of the frequencies ν_k, extracted via the harmonic inversion. Brown dots represent one selected cluster. (b) Real and imaginary parts of the complex amplitudes A_k (brown dots) and D_k (blue dots) [see Eq. (2.48)]. The amplitude A_k is directly extracted from (a) while D_k is its corresponding phase rotated amplitude. (c) Spatial structure of the cluster shown in (a) after the rotation.

2.4.4.1 The Spatial Autocorrelation Function

The ability to recover the spatial distribution of states can lead to wonder about the specific shape of the radial decay (see Chapter 4 for a detailed analysis). For instance, Anderson localized modes are characterized by an exponential radial decay with respect to the "*center*" of the state. However, it is precisely the lack of a preferred center in disordered systems, and consequently in their eigenmodes that prevents the unambiguous determination of the radial decay of the state amplitude. In this case, the most suitable quantity for correctly study the decay law of those modes is given by the spatial autocorrelation [16], with the property of being centered at the origin. In 2D, the spatial autocorrelation function is defined as

$$\mathrm{Cor}(E_k)(x', y') = \int_{-\infty}^{\infty}\int_{-\infty}^{\infty} E_k^*(x, y) E_k(x + x', y + y')\, \mathrm{d}x\, \mathrm{d}y\, . \tag{2.52}$$

where the Wiener-Khinchin theorem allows to reinterpret Eq. (2.52) in terms of the Fourier transform of the complex amplitude E_k as

$$\mathrm{Cor}(E_k) = \left|\mathcal{F}^{-1}\left\{\left|\mathcal{F}\left\{E_k\right\}\right|^2\right\}\right| . \tag{2.53}$$

For instance, Fig. 2.14(a) shows an eigenmode found in a 2D disordered system (this point pattern is studied in detail in Chapter 4). As mentioned before, the state lacks of a well defined center, however its autocorrelation function $\mathrm{Cor}(E_k)$ [see Fig. 2.14(b)] is peaked by definition at the origin of the reference system. The radial decay function of the mode can then be computed using the spatial autocorrelation [see Fig. 2.14(c)], here $r' = \sqrt{x'^2 + y'^2}$ is the radial coordinate of the autocorrelation space, and (x', y') the

corresponding Cartesian coordinates. Note that in the particular case of an exponential function, Eq. (2.53) allows us to prove that

$$\mathrm{Cor}(E_k) \propto \mathrm{e}^{-r'/\xi_{\mathrm{loc}}}, \tag{2.54}$$

where ξ_{loc} is the localization length which can thus be extracted from the experimental data.

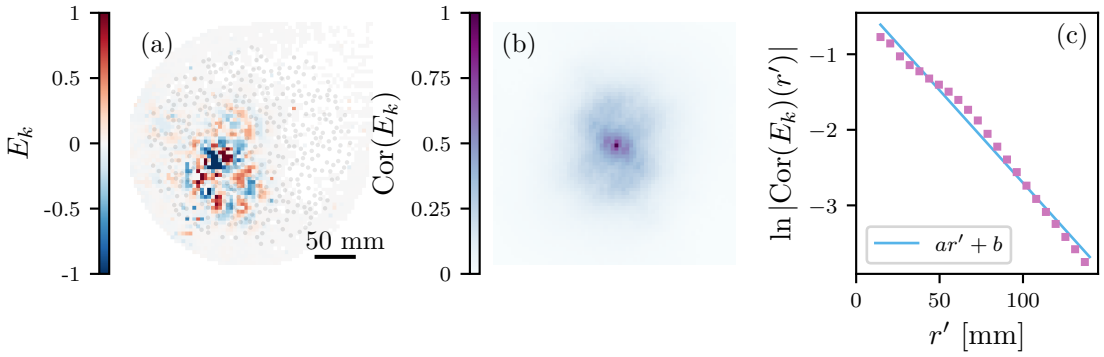

Figure 2.14: (a) Spatial modal structure, (b) spatial autocorrelation function, and (c) radial profile of the spatial autocorrelation of a mode found in a disordered system. The amplitude map (a) is normalized such that $\max(|E_k|) = 1$. Radial decay (purple dots) is obtained by performing an angular average operation in the autocorrelation space (r' is measured from the well defined autocorrelation center).

2.4.5 Simulating a temporal pulse

Dynamical electromagnetic transport properties can be probed by measuring the temporal evolution of a pulse in the system. Despite that the continuous signal injected by the VNA is inadequate to develop this task, time-domain analysis is still possible indirectly by the Fourier transform of the measured signals. At a given position $\mathbf{r}$, the propagating signal driven by a certain superposition of modes can be obtained by Fourier transforming the original complex transmission signal as

$$S_{21}^{f_0,\Delta\omega}(\mathbf{r},t) = \mathcal{F}\left\{S_{21}(\mathbf{r},\nu) \times F^{f_0,\Delta\omega}(\nu)\right\}, \tag{2.55}$$

where $\mathcal{F}\{\cdot\}$ represents the Fourier-transform and $F^{f_0,\Delta\omega}(\nu)$ a band-pass filter of bandwidth $\Delta\omega$ centered around f_0. The time-domain transmitted signal $S_{21}^{f_0,\Delta\omega}(\mathbf{r},t)$ directly depends on the shape of the band-pass filter. To avoid windowing effects on the Fourier-transform, we use two different filters in this thesis: a Gaussian filter and a Hanning filter.

Figures 2.15(a) and (c) shows the two different filters in the frequency domain. The respective Fourier transform of the filters correspond to the time-domain excitation induced into the system [see Figures 2.15(b) and (d)]. Note that even though the two filters seem to be quite similar, their characteristic bandwidths are different. Despite that more than 95% of the area of the Gaussian filter is in the interval $[f_0 - 2\Delta, f_0 + 2\Delta]$, it is also characterized by infinite long tails. On the contrary, the Hanning filter is zero for all values out of the interval $[f_0 - \Delta/2, f_0 + \Delta/2]$. Temporal analysis by Fourier transforming the transmission signals using a Gaussian filter has been previously used to identify the different transport regimes in 2D stealthy hyperuniform disordered systems [81].

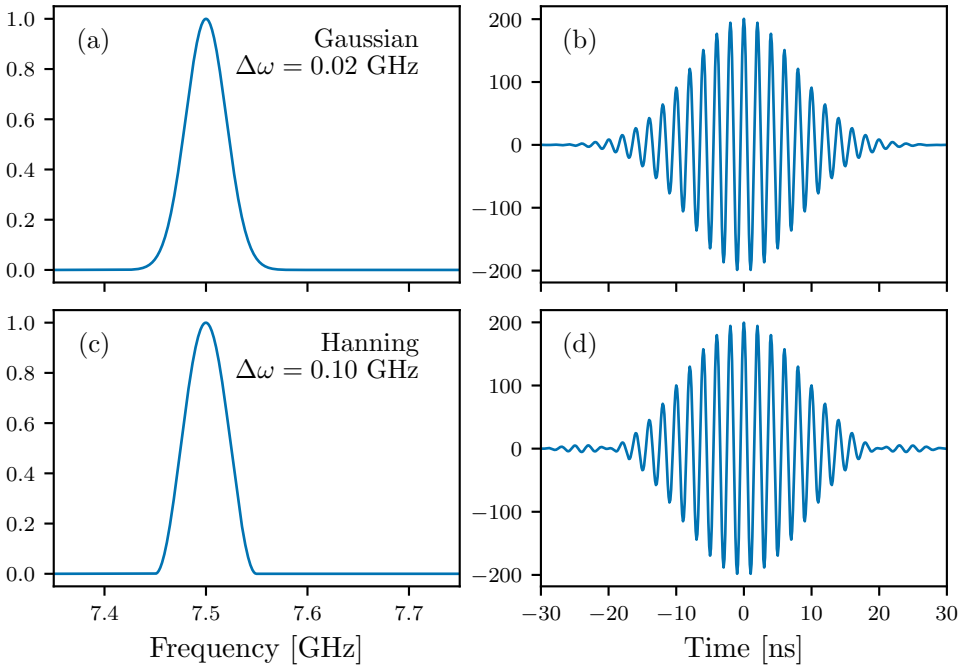

Figure 2.15: (a) Gaussian band-pass filter characterized by $f_0 = 7.5$ GHz and $\Delta\Omega = 0.02$ GHz. (b) Gaussian temporal pulse corresponding to the filter in (a). (c) Hanning band-pass filter characterized by $f_0 = 7.5$ GHz and $\Delta\Omega = 0.1$ GHz. (d) Hanning temporal pulse corresponding to the filter in (c).

2.4.6 The experimental Density of States

As the harmonic inversion and clustering techniques (see Sections 2.4.2 and 2.4.3) are unable to extract all the resonances within the entire frequency domain, we have to deal with an incomplete set of resonances, and thus cannot build correctly the density of states. Yet this quantity is of crucial interest to identify different transport regimes [79]. Fortunately, due to its connection with the singularities of the Green's function, the Local Density of States (LDoS) at position $\mathbf{r}$ is written as [174]

$$\begin{aligned} \mathrm{LDoS}(\mathbf{r},\nu) &= \sum_k \left|\psi_k(\mathbf{r})^2\right| \delta(\nu^2-\nu_k^2), \\ &= \frac{1}{\pi}\sum_k \frac{|\psi_k(\mathbf{r})|^2\Gamma_k^2}{(\nu^2-\nu_k^2)^2+\Gamma_k^4}, \\ &= -\frac{1}{\pi}\,\mathrm{Im}\{G(\mathbf{r},\nu)\}, \end{aligned} \tag{2.56}$$

where

$$G(\mathbf{r},\nu) = \sum_k \frac{|\psi_k(\mathbf{r})|^2}{\nu^2-\nu_k^2+\mathrm{i}\Gamma_k^2}. \tag{2.57}$$

Similarly, using once again the Breit-Wigner decomposition [Eq. (2.35)] [167] and assuming a constant antenna coupling σ in the complete frequency range, any reflection term of the scattering matrix at position $\mathbf{r}$ is written

$$S_{ii}(\mathbf{r},\nu) = 1 - \mathrm{i}\sigma \sum_k \frac{|\psi_k(\mathbf{r})|^2}{\nu^2-\nu_k^2+\mathrm{i}\Gamma_k^2}, \tag{2.58}$$

Straightforwardly, considering Eq. (2.56) and the real part of Eq. (2.58) leads to [113]

$$\mathrm{LDoS}(\mathbf{r},\nu) = \frac{1}{\pi\sigma}\left[1 - \mathrm{Re}\{S_{ii}(\mathbf{r},\nu)\}\right], \tag{2.59}$$

where the prefactor $1/(\pi\sigma)$ can be neglected by renormalizing (rescaling) the wavefunctions ψ_k [164]. Finally, the density of states (DoS) can be obtained by averaging the LDoS over all measured positions

$$\mathrm{DoS}(\nu) = \langle \mathrm{LDoS}(\mathbf{r},\nu)\rangle_{\text{all positions}} = 1 - \langle \mathrm{Re}\{S_{ii}(\mathbf{r},\nu)\}\rangle_{\text{all positions}}\,. \tag{2.60}$$

Note that the LDoS reconstruction via the scattering matrix does not rely on the perfect knowledge of all individual resonances.

As previously explained in Section 2.1, before each measurement session, the VNA is recalibrated to correct the phase and amplitude modulation of propagating waves inside the cables. However, the effects of the antennas and the surrounding near- and far-fields coming from the aluminium plates are still present. To solve this, two different methods are implemented depending on the polarization of the electromagnetic field and both are explained in the following Sections.

2.4.6.1 Baseline calibration (TE polarization)

For TE polarization and frequencies below the TE_1 cutoff limit (tight-binding type systems), the far-field contribution can be neglected. Thus, the ideal reflection spectrum of the system in a position $\mathbf{r}$ can be assumed to be $S(\mathbf{r},\nu)$, while the antenna and near-field modulations at the same point can be represented as $m(\mathbf{r},\nu)$ [164], leading to a measured signal

$$S_{ii}(\mathbf{r},\nu) = m(\mathbf{r},\nu)S(\mathbf{r},\nu)m(\mathbf{r},\nu) = m^2(\mathbf{r},\nu)S(\mathbf{r},\nu). \tag{2.61}$$

Then, by expecting the empty cavity to be characterized by $S^{\text{empty}}(\mathbf{r},\nu) = 1$, the modulation can be obtained as $S_{ii}^{\text{empty}}(\mathbf{r},\nu) = m^2(\mathbf{r},\nu)$. Consequently, the reflection spectrum is corrected by simply measuring the empty cavity at the same positions and then computing the complex ratio

$$S(\mathbf{r},\nu) = S_{ii}(\mathbf{r},\nu)/S_{ii}^{\text{empty}}(\mathbf{r},\nu). \tag{2.62}$$

For instance, Fig. 2.16 depicts the complex reflected spectrum S_{11} in a certain position of a honeycomb array in the tight-binding approximation (this system is studied in detail in Chapter 5). As it can be observed for the amplitude [see Fig. 2.16(a)], the introduction of the empty cavity modulation effectively removes the oscillating background phase, resulting an almost flat baseline. On the other hand, Figs. 2.16(c) and (d) reveal that the real and imaginary parts of the signal are in fact carried by an envelope which has been identified to be related with the effective length of the antenna [164].

2.4.6.2 Weakly coupled antennas regime (TM polarization)

Differently to the previous situation, the presence of propagating modes in the cavity (TM_0 or higher order, as well as TE_1 or higher order) promotes far-field reflections where the preceding model leads to inconsistencies (for example negative values of the LDoS). Nevertheless, thanks to the fact that the antennas are weakly coupled, one can approximate the LDoS in Eq. (2.59) and remove the global frequency factor at the same time [164]. We have

$$|S_{ii}(\mathbf{r},\nu)|^2 = 1 - 2\sigma\sum_k \frac{|\psi_k(\mathbf{r})|^2 {\delta\nu_k}^2}{(\nu^2-\nu_k^2)^2+\Gamma_k^4} + \sigma^2\sum_{k,k'}\left(\frac{|\psi_k(\mathbf{r})|^2}{\nu^2-\nu_k^2+\Gamma_k^2}\times\frac{|\psi_{k'}(\mathbf{r})|^2}{\nu^2-\nu_{k'}^2+\Gamma_{k'}^2}\right), \tag{2.63}$$

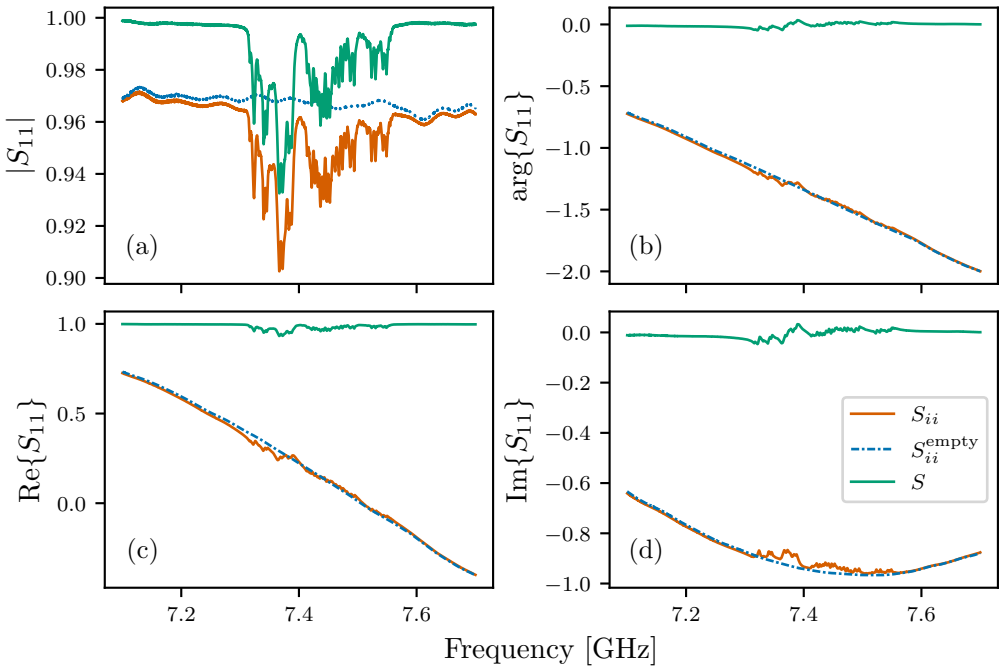

Figure 2.16: Reflected signal S_{11} for a honeycomb-like structure. The original signal, the empty cavity signal, and the complex ratio [Eq. (2.62)] are represented by orange, blue and green lines, respectively. (a) Amplitude $|S_{11}(\nu)|$, (b) phase $\arg\{S_{11}(\nu)\}$, (c) real part $\mathrm{Re}\{S_{11}(\nu)\}$, and (d) imaginary part $\mathrm{Im}\{S_{11}(\nu)\}$ of the complex measured signal.

where consider $\sigma^2 \ll 1$ leads to

$$1 - |S_{ii}(\mathbf{r},\nu)|^2 \approx 2\sigma \sum_k \frac{|\psi_k(\mathbf{r})|^2 \Gamma_k^2}{(\nu^2 - \nu_k^2)^2 + \Gamma_k^4}. \tag{2.64}$$

Finally, Eq. (2.64) allows to write Eq. (2.59) as

$$\mathrm{LDoS}(\mathbf{r},\nu) \approx \frac{1}{2\pi\sigma}\left[1 - |S_{ii}(\mathbf{r},\nu)|^2\right], \tag{2.65}$$

where the prefactor $1/(2\pi\sigma)$ can be once again neglected by renormalizing (rescaling) the wavefunctions ψ_k.

3

The localization landscape for tight-binding Hamiltonians

Madre le dijo: "Todos somos hijos de la luz,
el mundo es tuyo, haz con él lo que te plazca,
pero nunca olvides que le debes mostrar gratitud
y preservar su luz para el próximo que nazca..."
Sharif (Serlo todo)

Contents

As mentioned in Section 1.1.3, the aim of this Chapter is to extend the localization landscape theory to electromagnetic systems, and therefore to develop an approach applicable to our experimental setup introduced in Chapter 2. The Chapter is organized as follows: Section 3.1 provides a theoretical analysis of the localization landscape applicability onto the vector Maxwell's equations and the corresponding TM and TE polarizations. Later, in Section 3.2 the localization landscape approach is successfully extended to a broad class of 1D and 2D tight-binding lattices where localization appears in the two band-edges. The low-energy part of the spectrum is described by a discrete extension of the localization landscape in continuous systems. Meanwhile for the high-energy part of the spectrum, there are proposed two different procedures depending on the symmetries of the energy band. Part of the content of this Chapter forms the main body of Ref. [27].

3.1 Classical electromagnetic waves

We start by considering a linear, frequency-independent non-magnetic medium with random permittivity $\epsilon(\mathbf{r})$. For a system without sources, the Maxwell-Faraday and the Ampère-Maxwell equations are respectively written [162]

$$\nabla \times \mathbf{E}(\mathbf{r},t) = -\partial_t \mathbf{B}(\mathbf{r},t), \tag{3.1}$$

$$\frac{1}{\mu_0}\nabla \times \mathbf{B}(\mathbf{r},t) = \partial_t \mathbf{D}(\mathbf{r},t), \tag{3.2}$$

where $\mathbf{B}(\mathbf{r},t)$ is the magnetic field and $\mathbf{E}(\mathbf{r},t)$ the electric field. Additionally, the displacement vector $\mathbf{D}(\mathbf{r},t)$ is related to the electric field and the random permittivity by

$$\mathbf{D}(\mathbf{r},t) = \epsilon_0 \epsilon(\mathbf{r})\mathbf{E}(\mathbf{r},t), \tag{3.3}$$

with μ_0 and ϵ_0 the permeability and the permittivity of the vacuum, respectively.

A Shrödinger-like equation independent of the magnetic field can be obtained by computing the curl of Eq. (3.1) and then substituting Eq. (3.2) and Eq. (3.3) into it

$$\nabla \times [\nabla \times \mathbf{E}(\mathbf{r},t)] = -\frac{\epsilon(\mathbf{r})}{\mathrm{c}_0^2}\partial_t^2 \mathbf{E}(\mathbf{r},t), \tag{3.4}$$

where, $\mathrm{c}_0 = 1/\sqrt{\mu_0\epsilon_0}$ is the speed of light in the vacuum. Identically, the magnetic field equation can be obtained by substituting Eq. (3.3) into Eq. (3.2) and then computing the curl

$$\nabla \times \left[\frac{\mathrm{c}_0^2}{\epsilon(\mathbf{r})}\nabla \times \mathbf{B}(\mathbf{r},t)\right] = \partial_t \nabla \times \mathbf{E}(\mathbf{r},t). \tag{3.5}$$

The subsequent substitution of Eq. (3.1) leads to

$$\nabla \times \left[\frac{\mathrm{c}_0^2}{\epsilon(\mathbf{r},t)}\nabla \times \mathbf{B}(\mathbf{r})\right] = -\partial_t^2 \mathbf{B}(\mathbf{r},\mathbf{t}). \tag{3.6}$$

Finally, one can remove the time-dependence by considering monochromatic fields $\mathbf{E}(\mathbf{r},t) = \mathbf{E}(\mathbf{r})\mathrm{e}^{-\mathrm{i}\omega t}$ [$\mathbf{B}(\mathbf{r},t) = \mathbf{B}(\mathbf{r})\mathrm{e}^{-\mathrm{i}\omega t}$] in Eq. (3.4) [Eq. (3.6)]. We have

$$\boxed{\frac{1}{\epsilon(\mathbf{r})}\nabla \times [\nabla \times \mathbf{E}(\mathbf{r})] = \frac{\omega^2}{\mathrm{c}_0^2}\mathbf{E}(\mathbf{r}),} \tag{3.7}$$

$$\boxed{\nabla \times \left\{\frac{1}{\epsilon(\mathbf{r})}[\nabla \times \mathbf{B}(\mathbf{r})]\right\} = \frac{\omega^2}{\mathrm{c}_0^2}\mathbf{B}(\mathbf{r}).} \tag{3.8}$$

The main mathematical difference between the Schrödinger equation (1.4) and both Eqs. (3.7) and (3.8) is the vector character of the electromagnetic fields. This fact increases the number of field components to calculate, and as a consequence, the complexity of the problem. In addition, the role of both disordered terms V [in Eq. (1.4)] and $\epsilon(\mathbf{r})$ [in Eqs. (3.7) and (3.8)] is completely different. While electromagnetic equations present a disordered term as part of the differential operator, in Eq. (1.4) the potential V is simply summed to the Laplacian term.

Despite Eqs. (3.7) and (3.8) have both a vector character, they remain different from each other. For instance, whilst the magnetic operator is Hermitian, the electric one lacks this property. Therefore the eigenfunctions $\mathbf{E}(\mathbf{r})$ could not construct an orthogonal basis. One can write the differential magnetic operator in Eq. (3.8) as

$$\nabla \times \left\{ \frac{1}{\epsilon(\mathbf{r})} \left[\nabla \times\right] \right\} = \nabla \frac{1}{\epsilon(\mathbf{r})} \times \left[\nabla \times\right] + \frac{1}{\epsilon(\mathbf{r})} \nabla \times \left[\nabla \times\right], \tag{3.9}$$

whose second term is equal to the operator of Eq. (3.7).

3.1.1 The electric field

The first step to correctly construct a valid localization landscape for the electric field is to find a Hermitian operator. To do that, the change of variable $\mathbf{F}(\mathbf{r}) = \sqrt{\epsilon(\mathbf{r})}\mathbf{E}(\mathbf{r})$ is proposed [175]. Then, by substituting into Eq. (3.7) we obtain

$$\frac{1}{\sqrt{\epsilon(\mathbf{r})}} \nabla \times \left[\nabla \times \frac{\mathbf{F}(\mathbf{r})}{\sqrt{\epsilon(\mathbf{r})}} \right] = \frac{\omega^2}{\mathrm{c}_0^2} \mathbf{F}(\mathbf{r}), \tag{3.10}$$

where the operator $\frac{1}{\sqrt{\epsilon(\mathbf{r})}} \nabla \times \left[\nabla \times \frac{1}{\sqrt{\epsilon(\mathbf{r})}} \right]$ is Hermitian and the eigenvalues ω^2/c_0^2 are real positive numbers. Additionally, the functions $\mathbf{F}_m$ construct an orthogonal basis with the conditions

$$\int_\Omega \mathbf{F}_m(\mathbf{r}) \cdot \mathbf{F}_n(\mathbf{r}) \, \mathrm{d}\mathbf{r} = \int_\Omega \epsilon(\mathbf{r}) \mathbf{E}_m(\mathbf{r}) \cdot \mathbf{E}_n(\mathbf{r}) \, \mathrm{d}\mathbf{r} = \delta_{n,m}. \tag{3.11}$$

However, Eq. (3.10) is a vector differential equation whose spatial components are coupled. Unfortunately, to the best of our knowledge, no vector landscape has been previously defined, pushing this problem out of the scope of this work. Even so, by imposing some suitable spatial conditions, the differential equation (3.7) presents symmetries that allow to investigate the scalar character of the electric field.

3.1.2 TM polarization

To reduce the vector electromagnetic field into a scalar one, we restrict $\mathbf{E}(\mathbf{r})$ to be normal to the $\hat{x} - \hat{y}$ plane. This condition is known as transversal-magnetic (TM) polarization and it can be directly studied in our experimental setup (see Section 2.1.1). By chosen the electric field as $\mathbf{E}(\mathbf{r}) = E(x, y)\hat{z}$, Eq. (3.7) becomes

$$-\frac{1}{\epsilon(\mathbf{r})} \Delta_{\hat{x},\hat{y}} E(x, y) = \frac{\omega^2}{\mathrm{c}_0^2} E(x, y), \tag{3.12}$$

with $-\frac{1}{\epsilon(\mathbf{r})}\Delta$ known to be non Hermitian and $\Delta_{\hat{x},\hat{y}} = \hat{x}\partial_x + \hat{y}\partial_y$. Once again, the hermiticity of the operator can be recovered by introducing a scalar version of the previous change of variable $F(x, y) = \sqrt{\epsilon(\mathbf{r})}E(x, y)$. The final equation whose differential operator is Hermitian reads as follows

$$-\frac{1}{\sqrt{\epsilon(\mathbf{r})}} \Delta_{\hat{x},\hat{y}} \left[\frac{F(x, y)}{\sqrt{\epsilon(\mathbf{r})}} \right] = \frac{\omega^2}{\mathrm{c}_0^2} F(x, y). \tag{3.13}$$

Thus, it allows us to define a scalar landscape function u_e as

$$\Delta_{\hat{x},\hat{y}}\left[\frac{u_e}{\sqrt{\epsilon(\mathbf{r})}}\right] = -\sqrt{\epsilon(\mathbf{r})}. \tag{3.14}$$

where the localization subregions are determined by

$$u_e > \mathrm{c}_0^2/\omega^2. \tag{3.15}$$

The efficiency of the approach can be tested by solving numerically Eqs. (3.13) and (3.14), and then recovering the electric field functions. Fig. 3.1 displays (a) a 1D random permittivity, (b) the localization landscape associated to it, computed according to Eq. (3.14), (c) the eigenfunctions F_n of Eq. (3.13), and (d) the electric field functions E_n recovered from F_n and ϵ. Note that despite the randomness of ϵ, the localization landscape shows a structure similar to the one calculated in the case of a system whose permittivity is constant. As a result, localization subregions are extended over the whole domain, leading to delocalized eigenfunctions F_n. Similarly to the localization landscape, the states F_n follow the permittivity structure on well extended envelopes. The reconstructions of the electric modes removes this permittivity dependence revealing the actual shape of the envelopes. As for F_n, the states E_n are completely delocalized and they correspond to box modes in a homogeneous material. Therefore, the random permittivity behaves as an effective medium where the smallest-frequency modes are not localized.

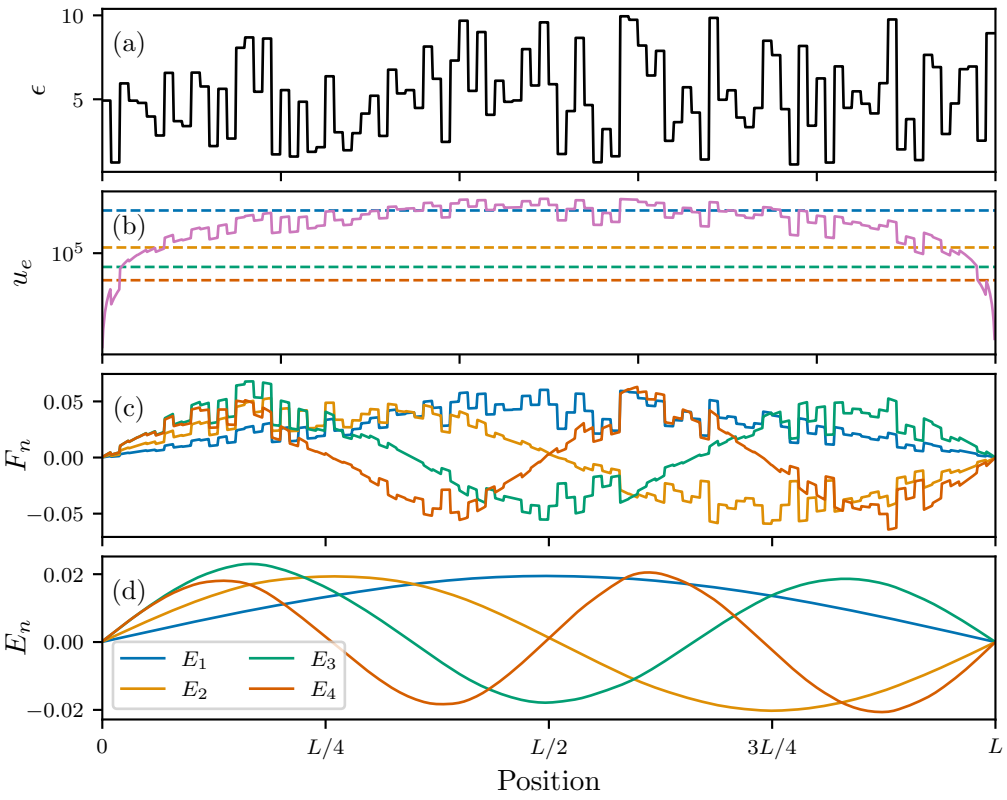

Figure 3.1: (a) Random permittivity ϵ for a one-dimensional system of $L = 1000$ sites with Dirichlet boundary conditions. The value of the permittivity is constant in intervals of 10 sites, in which each value is taken from a uniform random variable between 1 and 10. (b) Electric localization landscape u_e computed from Eq. (3.14). Horizontal color dashed lines indicate the values c_0^2/ω^2 for the four first eigenstates. (c) Four eigenfunctions F_n of lowest frequencies. (d) Four eigenfunctions E_n relative to F_n in panel (c). States are characterized by frequencies: $\omega_1 = 406$ kHz, $\omega_2 = 846$ kHz, $\omega_3 = 1.245$ MHz, and $\omega_4 = 1.622$ MHz.

3.1.3 The magnetic field

In contrast with the electric field case, the operator applied to the magnetic field $\nabla \times \left[\frac{1}{\epsilon(\mathbf{r})}\nabla\times\right]$ is directly Hermitian. However, the spatial components of the field are also coupled in this case, preventing the definition of a localization landscape. Thus, we proceed to impose suitable spatial conditions to transform Eq. (3.8) into a scalar equation.

3.1.4 TE polarization

Similarly to what was shown for the electric field, we now restrict the magnetic field $\mathbf{B}(\mathbf{r})$ to be normal to the $\hat{x}-\hat{y}$ plane. This polarization is known as transversal-electric (TE) polarization and as discussed in Section 2.2.1.2, can be also studied in our experimental setup for sufficiently high frequencies or large distances between plates. The magnetic field is then expressed as $\mathbf{B}(\mathbf{r}) = B(x,y)\hat{z}$, leading to

$$-\nabla_{x,y}\cdot\left[\frac{1}{\epsilon(\mathbf{r})}\nabla_{x,y}B(x,y)\right] = \frac{\omega^2}{\mathrm{c}_0^2}B(x,y), \tag{3.16}$$

where $-\nabla\cdot\left[\frac{1}{\epsilon(\mathbf{r})}\nabla\right]$ is Hermitian. Subsequently, the magnetic localization landscape is expressed as

$$-\nabla_{x,y}\cdot\left[\frac{1}{\epsilon(\mathbf{r})}\nabla_{x,y}u_b\right] = 1, \tag{3.17}$$

with localization subregions determined by

$$u_b > \mathrm{c}_0^2/\omega^2. \tag{3.18}$$

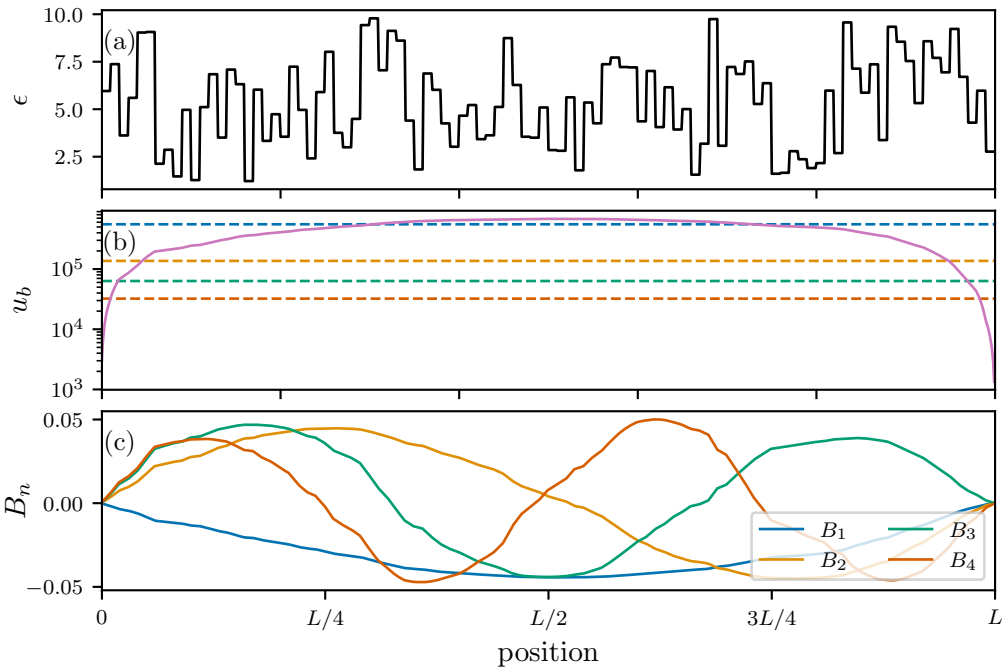

Figure 3.2: (a) Random permittivity ϵ for a one-dimensional system of $L = 1000$ sites with Dirichlet boundary conditions. The value of the permittivity remains constant in intervals of 10 sites, in which each value is taken from a uniform random variable between 1 and 10. (b) Localization landscape u_b computed from Eq. (3.17). Horizontal color dashed lines indicate the values c_0^2/ω^2 for the four lowest eigenenergies. (c) Four lowest frequency eigenfunctions B_n. States are characterized by frequencies: $\omega_1 = 403$ kHz, $\omega_2 = 811$ kHz, $\omega_3 = 1.192$ MHz, and $\omega_4 = 1.669$ MHz.

Given the similarity between Eqs. (3.14) and (3.17), an analogous behavior can be expected. As previously, Eqs. (3.16) and (3.17) are solved numerically for the 1D disordered permittivity shown in Fig. 3.2(a). Similarly to the TM polarization example, the magnetic localization landscape [see Fig. 3.2(b)] remains extended along the whole domain. As a consequence the localization subregions cover most of the space, leading to extended delocalized magnetic eigenfunctions [see Fig. 3.2(c)]. As for the electric case, the lowest frequency states are not affected by the random permittivity.

3.1.5 Localization at high frequencies

The origin of the delocalization of electromagnetic waves at low frequency can be understood from the definition of the localization subregions [Eqs. (3.15) and (3.18)], where for $\omega \to 0$, the localization subregion goes to infinity. Nevertheless, electromagnetic localization can be still achieved at higher frequency. To illustrate this, Fig. 3.3 displays the four states with highest eigenfrequency for (a) TM and (b) TE polatizations. Unfortunately, the current localization landscape approach for continuous systems is still incapable to make predictions for states far away from the lowest bandedge. Therefore, defining a localization landscape in the most general electromagnetic case as well as in the two scalar simplifications, settled by TM and TE polarization, remains open.

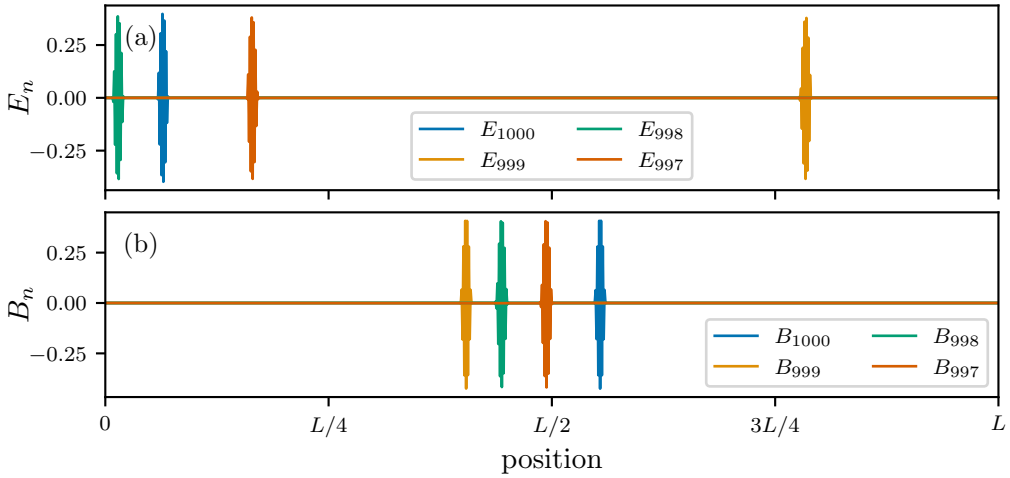

Figure 3.3: (a) Four electric eigenmodes E_n with large frequencies: $\omega_{996} = 546$ MHz, $\omega_{997} = 547$ MHz, $\omega_{998} = 548$ MHz, and $\omega_{999} = 562$ MHz; (b) Four eigenmodes B_n with largest frequencies: $\omega_{996} = 555$ MHz, $\omega_{997} = 561$ MHz, $\omega_{998} = 563$ MHz, and $\omega_{999} = 566$ MHz.

3.2 Tight-binding lattices

As shown in the Section 2.2, the field induced by loop antennas (TE polarization) together with the presence of both aluminum plates allows our experimental setup to mimic a tight-binding system (see Appendix A). This fact opens a new possibility to develop a suitable localization landscape for our experimental setup. A general tight-binding Hamiltonian $\hat{H}$ is defined as

$$\hat{H} = \sum_n V_n a_n^\dagger a_n - \sum_{n,m} t_{nm} \left(a_n^\dagger a_m + \text{h.c.} \right). \tag{3.19}$$

where V_n is the on-site potential at position n, t_{nm} is the energy of the coupling between the sites n and m, and $a_n^\dagger$ (a_n) is the creation (annihilation) operator of a particle in the

site n. Additionally, the second sum is carried out only over the nearest neighbours of n, which usually are the closest ones. In such discrete systems, the eigenvalue problem is reduced to the solution of a set of linear equations. From Eq. (3.19), we can write

$$-\sum_{m\in\langle n\rangle} t_{nm}\psi_m + V_n\psi_n = E\psi_n, \tag{3.20}$$

where $\boldsymbol{\psi} \equiv (\psi_n)_{n\in[1,N]}$ is the wave function defined on the sites of the lattice (labeled from 1 to N), and $\langle n\rangle$ indicates the ensemble of nearest neighbours of site n. In the following, we assume that $t_{nm} = 1$, thus setting the energy unit. In the same way, for the on-site energies we have $V_n = V_{\max}\nu_n$, where ν_n is an i.i.d random variable with uniform law in $[-0.5, 0.5]$, and $V_{\max}$ being therefore the disorder strength.

3.2.1 The two sets of localized states

Let us start our study by presenting results on the honeycomb lattice. Figs. 3.4(a) and 3.4(b) show this lattice and its celebrated dispersion relation in the tight-binding approximation, respectively[1]. We solve the set of equations defined in Eq. (3.20) on the honeycomb lattice, with the on-site potential depicted in Fig. 3.4(c) and $V_{\max} = 3$. In Fig. 3.4(d) are displayed the first four eigenstates which, as expected for a random potential, exhibit a finite spatial extension typical of Anderson-localized modes, which in turn can be contrasted with the extended electromagnetic states studied in the previous section. At the other end of the spectrum, Fig. 3.4(e) illustrates a feature that has no continuous counterpart: the existence of high-energy localized modes (the last four eigenstates are displayed in the example). This phenomenon is well known for instance in the case of 3D Anderson localization on a cubic lattice at low disorder strength, in which the spectrum of the Hamiltonian is symmetric in the range $[-6 - V_{\max}/2; 6 + V_{\max}/2]$ and exhibits a transition (the *mobility edge*) between localized and delocalized states at both ends [43].

In the following, we show how to build the two discrete localization landscapes which accurately predict the location of the localized modes near the two band edges (low and high energy), as well as their energies, without solving Eq. (3.20). We then generalize this method to a wide class of 2D lattices.

3.2.2 The discrete localization landscapes

Previously, Lyra, Mayboroda, and Filoche [176] have studied a 1D linear chain with nearest-neighbour coupling and have shown that positions of the localized modes are given by two different localization landscape. The low energy landscape is straightforwardly obtained by solving the analog of Eq. (1.9) in the discrete setting, i.e.,

$$\hat{H}\boldsymbol{u} = \mathbf{1}, \tag{3.21}$$

with $\boldsymbol{u} \equiv (u_n)_{n\in[1,N]}$, $\mathbf{1}$ a vector filled with 1 and fulfilling the same boundary conditions than the eigenvalue problem. Another localization landscape, called the *dual localization landscape*, gives the position of the envelope of the highly oscillating, high-energy, wave functions. The existence of the two discrete localization landscapes have been also extrapolated to 2D square arrays [177, 178]. More recently, Wang and Zhang [179] have proven mathematically that, in any dimension, the reciprocals of these discrete landscapes act indeed as effective confining potentials in a tight-binding system at both low- and high-energy regimes, respectively. Nevertheless, a complete generalization for

[1]The band calculations shown in this work are calculated using the PythTB Python package by S. Coh and D. Vanderbilt

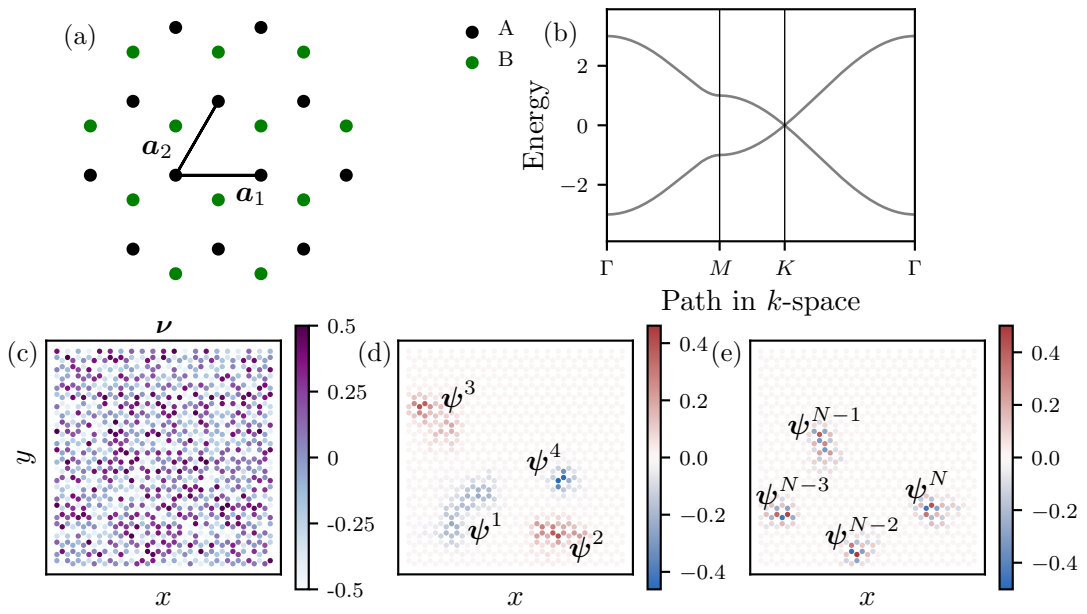

Figure 3.4: (a) The honeycomb lattice. (b) Band structure of the honeycomb lattice. (c) Plot of the random potential $V_n/V_{\max} = \nu_n$. (d) Eigenmodes with the four lowest eigenvalues of a honeycomb lattices with on-site disorder, $N = 964$ sites and $V_{\max} = 3$. (e) Eigenmodes with the four highest eigenvalues of Eq. (3.20).

non-squared 2D materials [180] (see also Ref. [181] and the related collection of papers), where some of the results cannot be directly anticipated, is still missing.

Figure 3.5(a) shows the reciprocal of the localization landscape, $1/\boldsymbol{u} \equiv (1/u_n)_{n\in[1,N]}$ computed on the honeycomb lattice with the on-site disorder depicted in Fig. 3.4(c). Note that a shift $\hat{H} \to \hat{H} + V_{\text{shift}}$, with $V_{\text{shift}} = 3 + V_{\max}/2$, has been performed in (3.21) to ensure a positive definite Hamiltonian. As already observed for continuous systems, the role of effective confining potential played by $1/\boldsymbol{u}$ is revealed through its basins, labelled following their depth in Fig. 3.5(a). Indeed, one can observe the correspondence between the deepest wells of $1/\boldsymbol{u}$ and the positions of the first eigenmodes plotted in Fig. 3.5(b). As analyzed in the Section 1.1.3.4 as well as by Arnold et al. [59] for the continuous setting, two almost-equal eigenvalues can lead to a different ordering in the values of the minima of $1/\boldsymbol{u}$, thus inducing a mismatch in the correspondence. This effect, which does not affect the ability of the landscape to predict the position of localized modes, is visible in

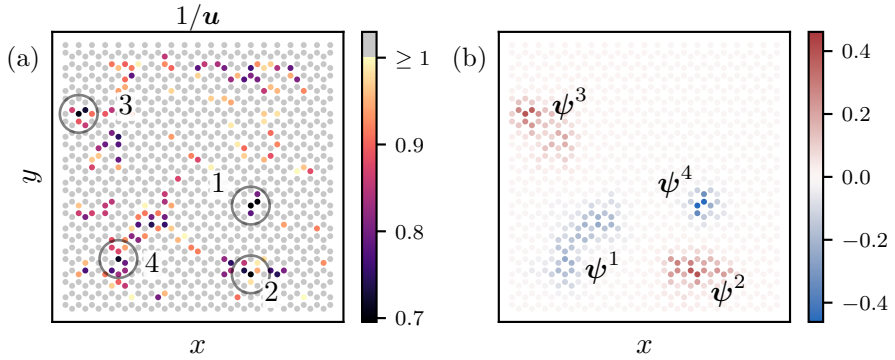

Figure 3.5: (a) Inverse of the localization landscape calculated for the system as in Fig. 3.4 (c) where the four lowest minima are numbered. (b) Eigenmodes with the four lowest eigenvalues of a honeycomb lattices with on-site disorder, $N = 964$ sites and $V_{\max} = 3$.

Fig. 3.5(a) and (b) with the first and fourth eigenstates and minima, and is analyzed in detail for these discrete settings in Section 3.2.5.

3.2.3 High-energy landscape for symmetrical DoS

On the other hand, the high-energy situation is much more intricate. The symmetry of the honeycomb lattice allows us a straightforward derivation of the landscape governing the high-energy localized states, namely the dual localization landscape. Indeed, the tight-binding Hamiltonian (3.19) can be decomposed into $\hat{H} = \hat{H}_0 + \hat{V}$, where $\hat{H}_0$ stands for the uniform honeycomb lattice with zero on-site energy, and $\hat{V}$ accounts for the disordered on-site potential. The unperturbed part of the Hamiltonian displays the usual chiral symmetry for a bipartite lattice, $\Sigma_z \hat{H}_0 \Sigma_z = -\hat{H}_0$, where the Pauli-like matrix Σ_z acts on the sublattice degree of freedom: it keeps the amplitudes on the A sites fixed but inverts those on the B sites ($\Sigma_z = P_A - P_B$, the difference between the respective projectors on the two sub-lattices). Due to the *diagonal* nature of the disordered potential, the complete Hamiltonian obeys the symmetry $\Sigma_z \left(\hat{H}_0 + \hat{V}\right) \Sigma_z = -\left(\hat{H}_0 - \hat{V}\right)$. The latter property is exemplified in Fig. 3.6: unlike the DoS of the uniform lattice, the DoS of a given realization of the disordered system is not symmetric with respect to the origin, but the DoS obtained by inverting the sign of all on-site energies is the exact symmetric of the original situation.

Let us call $\boldsymbol{\phi} \equiv (\phi_n)_{n\in[1,N]}$ the eigenstates of the inverted Hamiltonian ordered by increasing eigenvalues. The low-energy states of the inverted Hamiltonian now correspond to the high-energy states of the original Hamiltonian through $\boldsymbol{\phi} = \Sigma_z \boldsymbol{\psi}$. Since the high-energy eigenstates oscillate with a period equal to the nearest-neighbour distance, the new low-energy states appear as "demodulated" versions of their high-energy counterparts, see Fig. 3.7(b) and (c). We can now therefore use the localization landscape for the inverted system, but with $\boldsymbol{u}^\star$ being now the solution to $\hat{H}^\star \boldsymbol{u}^\star = \mathbf{1}$ with

$$(\hat{H}^\star \boldsymbol{\phi})_n = -\sum_{m\in\langle n\rangle} \phi_m + (V_{\text{shift}} - V_n)\,\phi_n. \tag{3.22}$$

In the example of Fig. 3.7(a), one can clearly see how the deepest wells (which are different from the low-energy wells) pinpoint the locations of the localized states.

As discussed in Section 1.1.3.3, the localization landscape also provides accurate estimates of the localized eigenvalues in the continuous setting [59]. However, the generalization of the simple Eq. (1.19) to tight-binding Hamiltonians has never been studied beyond the simple cubic lattice, nor its extension to the higher part of the spectrum. We plot on Fig. 3.8(a) [resp. 3.8(b)] the lowest [resp. highest] eigenvalues of Eq. (3.20) versus the local minimum values of the effective potential $1/\boldsymbol{u}$ [resp. $1/\boldsymbol{u}^\star$] at

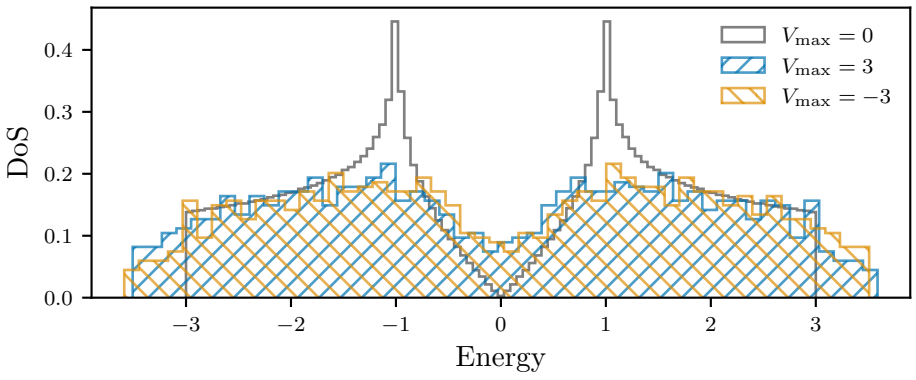

Figure 3.6: Density of state of the honeycomb lattice without and with disorder [see Fig. 3.4(c)].

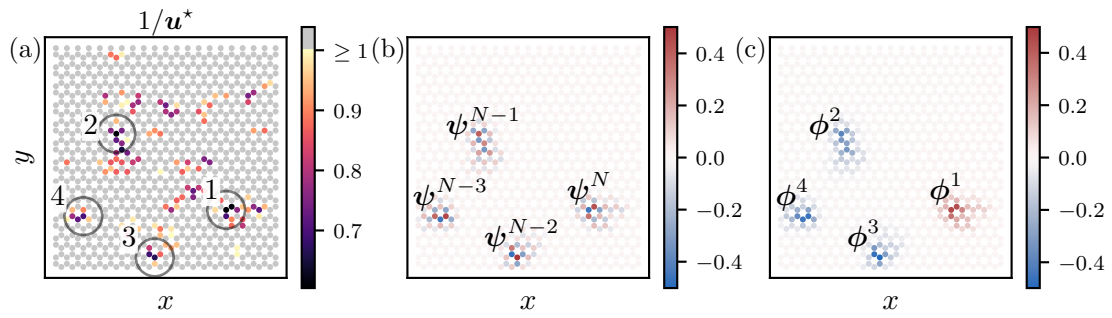

Figure 3.7: (a) Inverse of the dual landscape. (b) Eigenmodes with the four highest eigenvalues of Eq. (3.20) considering the potential depicted in Fig. 3.4(c). (c) Eigenmodes with the four lowest eigenvalues of the inverted Hamiltonian.

the position of localized eigenstates for a honeycomb lattice with $N = 2135$ sites and for a given disorder $V_{\max} = 3$. Each scatter plots corresponds to 100 realizations of the disordered potential. In both cases, a direct proportionality is clearly observed for the lowest part of the plots, with Pearson coefficients of the linear regression close to 0.99. Note also that in order to obtain this proportionality (which is more than a simple linear dependency), one has to choose V_{shift} so that the shifted potential has a minimum value close to zero, being $V_{\text{shift}} = 3 + V_{\max}/2$ in the two, localization and dual localization landscapes, cases. These observations indicate that the discrete low-energy localization landscape performs as well as its continuous analog in predicting energy and spatial distribution of localized modes without resolving an eigenvalue equation. Moreover, the high-energy dual landscape also exhibits the same properties.

From Fig. 3.8(a), and (b), one can also observe that the quality of the linear proportionality can be affected by the number of eigenvalues and minima of the confining potential considered during the analysis. In Figs. 3.8(c) and (d), we plot the Pearson coefficient ρ of the linear regression as a function of the number of minima taken to compute the slope considering different values of $V_{\max}$ for the same 100 honeycomb lattice realizations. We see that whatever the disorder, the maximum correlation is always obtained when we chose the $\sim$ 3% of states with the lowest (or highest) eigenvalues. However, both cases present values larger than 0.84 even for the 10% of states. The linear regression stops evolving and shows a flat behavior when the number of mimina considered in the analysis exceeds the actual number of minima of the potential.

Beyond the honeycomb lattice, this spectrum inversion strategy can be deployed for others lattices with symmetric band structure. In Table 3.1, we list the set of the different lattices studied, together to the symmetry of their DoS. Note that the energy shift needed to avoid negative eigenvalues V_{shift} is also different for each lattice. Since the disordered term is given as $V_n = V_{\max}\nu_n$ with ν_n an i.i.d. random variable with uniform law in $[-0.5, 0.5]$, the energy shift for the localization landscape is defined as $V_{\text{shift}} = -\min(\mathcal{E}) + V_{\max}/2$ where $\mathcal{E}$ is the energy of the system *without* disorder at *zero* on-site energy. On the other hand, in the case of the dual localization landscape, we use $V_{\text{shift}} = \max(\mathcal{E}) + V_{\max}/2$. All considered values for different lattices are also shown in Table 3.1. We have to point out that for the 1D chain with 2$^{\text{nd}}$ neighbours coupling, the energy is given by

$$\mathcal{E} = -2\left[t_1 \cos\left(k_x a\right) + t_2 \cos\left(2k_x a\right)\right], \tag{3.23}$$

where the corresponding $k_{\max}$ is the solution of the transcendental equation

$$t_1 \sin\left(k_x a\right) = -2t_2 \sin\left(2k_x a\right). \tag{3.24}$$

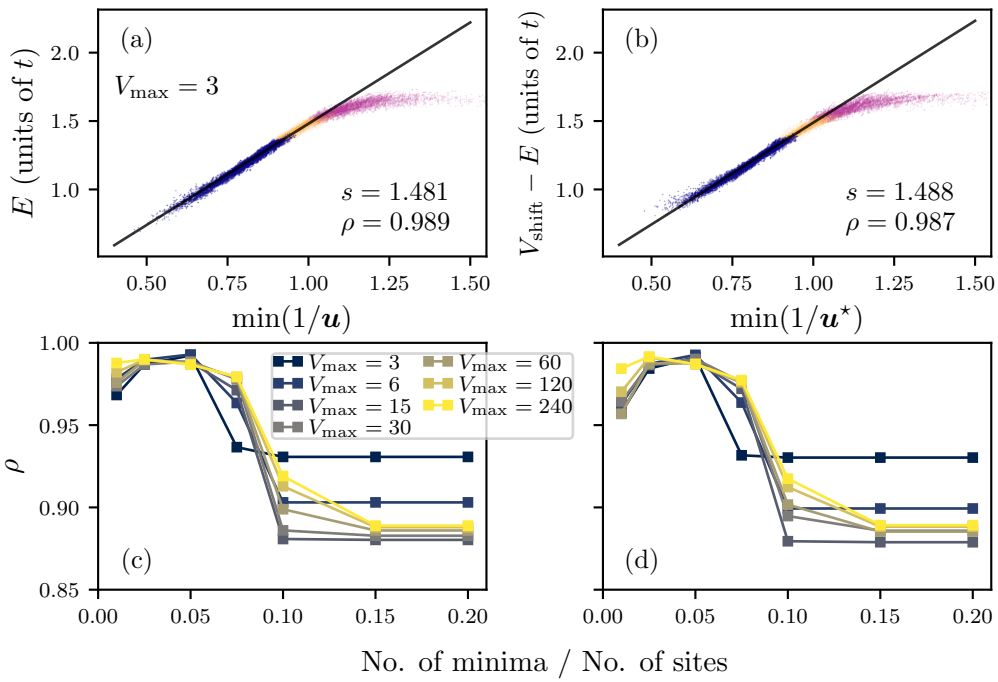

Figure 3.8: (a) Proportionality between $\min(1/\boldsymbol{u})$ and E for the lowest energies. The blue dots correspond to the 3% states of lowest energy for 100 different configurations, the orange dots to the 3-5%, and the purple dots to the 5-7%, respectively. The black line corresponds to a linear fit of the pink dots, the slope s and the Pearson coefficient ρ being given in the frame. (b) Proportionality between $\min(1/\boldsymbol{u}^\star)$ and $(V_{\text{shift}} - E)$ for the highest energies. Similar plot to (a), but for the states of highest energy. [(c) and (d)] Pearson correlation coefficient as a function of number of minima taken into account for the honeycomb lattice with different strengths of disorder $V_{\max}$. (c) The landscape prediction. (d) The dual landscape prediction using the symmetry of the band structure. The linear regression quality do not evolve when the number of minima considered is larger than the actual number of minima of $1/\boldsymbol{u}$ ($1/\boldsymbol{u}^\star$).

For this lattice, values shown in Table 3.1 correspond to the particular case $t_2 = t_1/\sqrt{8}$.

To quantify the strength of the disorder unequivocally for different lattices, the parameter $V_{\max}$ is not the best suited. Indeed, for a given value of $V_{\max}$, the relative weight of the potential term in (3.20) compared to the kinetic term depends on the connectivity of the discrete Laplacian $\sum_m(\psi_m - \psi_n)$. The number of edges of the graph on which this operator is relying is given by the number of nearest-neighbour couplings, which itself depends on the elementary motif of each given lattice. Therefore, we will use

Table 3.1: DoS symmetry for the different lattices studied. Smallest and largest eigenvalues of the tight binding Hamiltonian without on-site potential and with $V_{\text{shift}} = 0$. The couplings are all $t = 1$, except for 1D dimer chain and the 1D chain with 2^{nd} neighbour coupling cases where they are explicitly written.

Lattice	DOS Sym?	$-\min(\mathcal{E})$	$\max(\mathcal{E})$
1D chain	y	2	2
1D dimer chain	y	$t_1 + t_2$	$t_1 + t_2$
1D chain with 2^{nd} neighbour coupling	n	$2\,(t_1 + t_2)$	$\sqrt{2}t_1$
Square	y	4	4
Lieb	y	$\sqrt{8}$	$\sqrt{8}$
tts	n	5	3
hexagonal	n	6	3
Honeycomb	y	3	3
Kagome	n	4	2

a less contingent quantity, namely the inverse participation ratio (IPR) defined for a given eigenvector $\boldsymbol{\psi}^{(j)}$ as

$$\mathrm{IPR}_j = \sum_n \left|\psi_n^{(j)}\right|^2 / \left(\sum_n \left|\psi_n^{(j)}\right|^2\right)^2 . \tag{3.25}$$

The IPR is a conventional quantity used to measure the localization of a state. Specifically, it measures the number of sites in the lattice that contribute significantly to a mode by means of two asymptotic values

$$\mathrm{IPR} \to \begin{cases} 0 & \text{for a maximally extended states} \\ 1 & \text{for a maximally localized states} \end{cases} \tag{3.26}$$

In Fig. 3.9, we plot 2D histograms showing the eigenstates density in the eigenvalues-IPR plane for two values of $V_{\max}$ in the honeycomb and hexagonal lattices. We clearly see the more localized states for higher disorder, and the asymmetry of the density of states for the hexagonal lattices.

The proportionality between the energies and the inverse of the localization landscape (dual localization landscape) minima can be then obtained for a large variety of "canonical" lattices (1D: chain, dimer chain, chain with second-neighbour coupling; 2D: square, honeycomb, Lieb, hexagonal, Kagome, tts [182]) and in a wide range of strength disorder. In Figure 3.10 we consider the first (a) and last (b) 3% of the eigenstates to compute the slopes, that are plotted versus the mean IPR corresponding to the same 3% of the eigenstates.

With one noticeable exception for the Lieb lattice, the values of the slope s appear to evolve continuously between $s = 1 + D/4$ and $s = 1$, both for the lowest and the highest eigenvalues [see Fig. 3.10(a) and 3.10(b)]. Moreover, all the curves bunch into two smooth master curves, one for each space dimension. In the weak disorder limit, i.e. $\langle \mathrm{IPR} \rangle \to 0$,

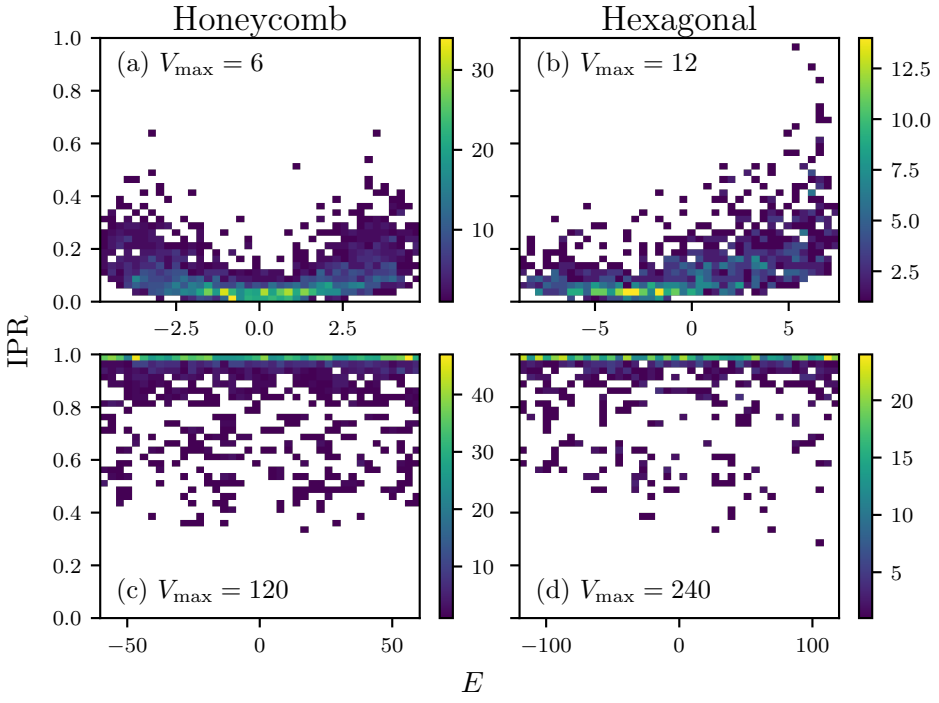

Figure 3.9: 2D histogram showing how the eigenvalues and the IPR are distributed at [(a) and (b)] low- and [(c) and (d)] high-disordered strength.

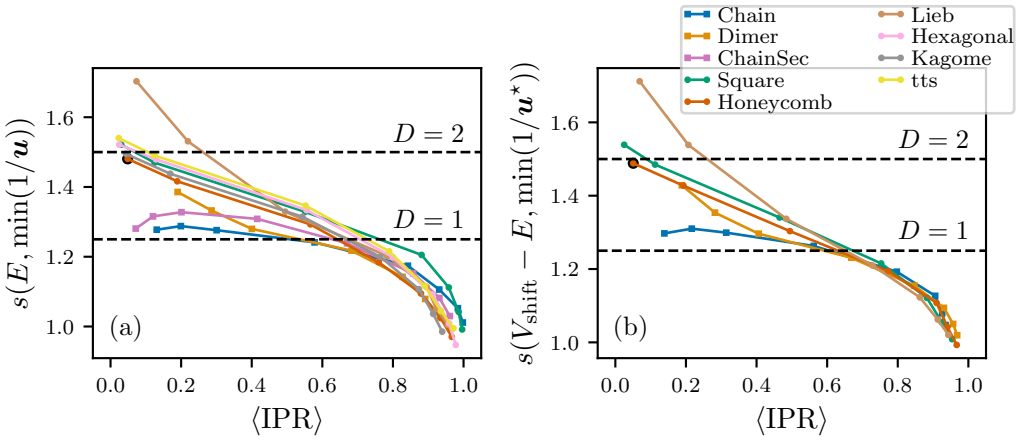

Figure 3.10: (a) Slope s for the low-energy states, for different lattices in 1D (squares) and 2D (circles). Each symbol corresponds to a disorder strength $V_{\max}$, but instead of reporting $V_{\max}$ on the horizontal axis, we chose to use the average value of the IPR which is a better comparison parameter across different lattices. The dashed horizontal lines show the limits expected in the continuous case from Eq. (1.19). (b) Similar plot to (a) for the highest-energy states in the DoS symmetric case. The black circle corresponds to the cases displayed in Fig. 3.8.

that is to say when the influence of the disordered potential is small compared to the Laplacian term, localized eigenfunctions and localization subregions are well distributed along a large number of sites, fulfilling the assumption that the localization landscape (dual localization landscape) is approximated by a quadratic bump-like function. As a consequence, one can reasonably expect that the continuous result of Eq. (1.19) still holds for both the lowest and the highest part of the spectrum. This is indeed observed: the slopes fall on the $(1+D/4)$ limit for $\langle \text{IPR} \rangle \to 0$. In the other limit case, when the disorder is so strong that an eigenstate is localized on a single site ($\langle \text{IPR} \rangle \to 1$), the localization landscape (dual localization landscape) is essentially supported locally on the same site. Since the eigenstate and the localization landscape are locally proportional, Eq. (3.21) at the only site n supporting the wave function therefore becomes $Hu_n = 1 \approx Eu_n$, hence $E \approx 1/u_n$ and a slope $s \simeq 1$ is expected.

The definition and the properties of the low-energy localization landscape are valid for any lattice, in any dimension, and are not restricted to nearest-neighbour coupling. We simulated thoroughly many different "canonical" lattices, for which details are provided in Table 3.2. For each lattice, we computed 100 different disordered configurations. The construction of the high-energy dual landscape, however, used explicitly in this example the chiral symmetry of the honeycomb lattice, i.e. the central symmetry of its DOS.

Table 3.2: Summary of the simulations

Lattice	♯ of sites N	Disorder calculated $V_{\max}$
1D chain	1001	1, 2, 4, 10, 20, 40, 80, 160
1D dimer chain ($t_2 = t_1/2$)	2001	1, 2, 4, 10, 20, 40, 80, 160
1D chain with 2$^{\text{nd}}$ neighbour coupling	1001	1, 2, 4, 10, 20, 40, 80, 160
Square	961	4, 8, 20, 40, 80, 160, 320
Lieb	2821	$\frac{8}{3}$, $\frac{16}{3}$, $\frac{40}{3}$, $\frac{80}{3}$, $\frac{160}{3}$, $\frac{320}{3}$, $\frac{640}{3}$
tts	3661	5, 10, 25, 50, 100, 200, 400
Hexagonal	1068	6, 12, 30, 60, 120, 240, 480
Honeycomb	2135	3, 6, 15, 30, 60, 120, 240
Kagome	3185	4, 8, 20, 40, 80, 160, 320

3.2.4 High-energy landscape for non symmetrical DoS

We will show now that when the chiral symmetry property cannot be used, there remains a general procedure which consists in "demodulating" Eq. (3.20) around a local maximum of the dispersion relation. This procedure can be applied to any lattice, leading to a dual localization landscape that relies on the specific band structure of the given system. To illustrate this, we now focus on the hexagonal lattice [Fig. 3.11(a)] whose dispersion relation is not symmetric [Fig. 3.11(c)]. In Fig. 3.11(d), we display the states corresponding to the 4 highest eigenvalues. Similarly to what was observed for the honeycomb lattice [Fig. 3.4(e)], we first note that the high-energy eigenstates are spatially localized and oscillate with a period equal to the nearest-neighbour distance. The objective of the "demodulation" process is, therefore, to find localization landscape for the envelopes of the height-energy states. To remove the rapidly oscillating part of the high-energy eigenstates, let us assume that $\mathbf{k}_{\max}$ is a wave vector at which the dispersion relation $E(\mathbf{k})$ of the Hamiltonian without potential exhibits a local maximum. Thus, the dispersion relation can be written locally as

$$E(\mathbf{k}) = E(\mathbf{k}_{\max}) - \frac{1}{2}(\mathbf{k}_{\max} - \mathbf{k})^\top \mathcal{A}\,(\mathbf{k}_{\max} - \mathbf{k}) + \mathrm{O}\left(\|\mathbf{k} - \mathbf{k}_{\max}\|^2\right), \tag{3.27}$$

where $\mathcal{A}$ is a definite positive 2-by-2 matrix whose eigenvalues are the inverse of the effective masses in both directions. One can then write any eigenfunction $\boldsymbol{\psi}$ of the full Hamiltonian (i.e., including the potential V_n) as

$$\boldsymbol{\psi} = \mathrm{e}^{\mathrm{i}\mathbf{k}_{\max}\cdot\mathbf{r}}\boldsymbol{\phi}, \tag{3.28}$$

where $\boldsymbol{\phi}$ is an envelope function satisfying the following equation

$$-\sum_{m\in\langle n\rangle} \mathrm{e}^{\mathrm{i}\mathbf{k}_{\max}\cdot(\mathbf{r}_m - \mathbf{r}_n)}\phi_m + V_n\phi_n = E\phi_n, \tag{3.29}$$

with E being the energy of $\boldsymbol{\psi}$. The local maximum of the dispersion relation $E(\mathbf{k}_{\max})$ implies that

$$\sum_{m\in\langle n\rangle} \mathbf{r}_m\,\mathrm{e}^{\mathrm{i}\mathbf{k}_{\max}\cdot\mathbf{r}_m} = \mathbf{0}, \tag{3.30}$$

where the sum is taken over all interacting neighbours of the site n located at $\mathbf{r}_n = \mathbf{0}$. Thus, a new Hamiltonian $\hat{H}^\star_{\mathbf{k}_{\max}}$ can be defined by

$$(\hat{H}^\star_{\mathbf{k}_{\max}}\boldsymbol{\phi})_n = E(\mathbf{k}_{\max}) + \sum_{m\in\langle n\rangle} \mathrm{e}^{\mathrm{i}\mathbf{k}_{\max}\cdot(\mathbf{r}_m - \mathbf{r}_n)}\phi_m - V_n\phi_n. \tag{3.31}$$

with energies given by

$$E^*(\mathbf{k}) = \langle\boldsymbol{\phi}|\hat{H}^\star_{\mathbf{k}_{\max}}|\boldsymbol{\phi}\rangle = \frac{1}{2}\mathbf{k}^\top\mathcal{A}\,\mathbf{k} - \frac{V_{\max}}{2} + \mathrm{O}\left(\|\mathbf{k}\|^2\right). \tag{3.32}$$

Therefore, the localization landscape approach can be applied to this new Hamiltonian after shifting the energies by $V_{\max}/2$.

In the case of the hexagonal lattice without disorder, the highest eigenvalues are located at the vertices K of the *first* Brillouin zone [Fig. 3.11(b) and 3.11(c)]. The corresponding wave vectors are then $\mathbf{k}_{\max} = \left\{\pm\frac{4\pi}{3a}\hat{x}, \pm\left(\frac{2\pi}{3a}\hat{x} + \frac{2\pi}{\sqrt{3}a}\hat{y}\right), \pm\left(\frac{2\pi}{3a}\hat{x} - \frac{2\pi}{\sqrt{3}a}\hat{y}\right)\right\}$. By injecting any of these $\mathbf{k}_{\max}$ into equation (3.28), and lately into equation (3.20), the "demodulated" equation for the envelopes $\boldsymbol{\phi}$ is obtained. For instance, if $\mathbf{k}_{\max} = \frac{4\pi}{3a}\hat{x}$, the envelope equation reads

$$\begin{aligned}\mathrm{e}^{\mathrm{i}\frac{4\pi}{3}}\phi_{n+\mathbf{a}_1} + \mathrm{e}^{-\mathrm{i}\frac{4\pi}{3}}\phi_{n-\mathbf{a}_1} + \mathrm{e}^{\mathrm{i}\frac{2\pi}{3}}\phi_{n+\mathbf{a}_2} + \mathrm{e}^{-\mathrm{i}\frac{2\pi}{3}}\phi_{n-\mathbf{a}_2} \\ +\mathrm{e}^{\mathrm{i}\frac{2\pi}{3}}\phi_{n+\mathbf{a}_1-\mathbf{a}_2} + \mathrm{e}^{-\mathrm{i}\frac{2\pi}{3}}\phi_{n-\mathbf{a}_1+\mathbf{a}_2} - V_{\max}\nu_n\phi_n = -E\phi_n,\end{aligned} \tag{3.33}$$

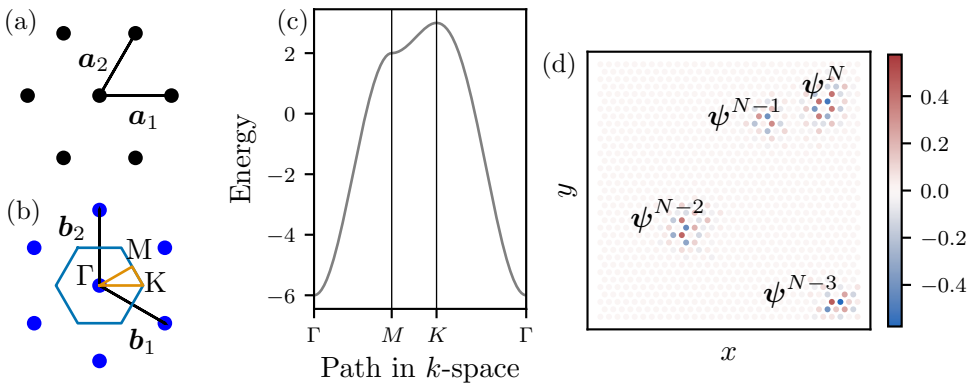

Figure 3.11: (a) Hexagonal lattice and (b) reciprocal lattice with the first Brillouin zone and the high symmetry points. (c) Dispersion relation of the Hexagonal lattice. (d) Four states with the highest eigenvalues of a hexagonal lattice with on-site disorder, $N = 1068$ and $V_{\max} = 6$.

where, the notation $n + \mathbf{a}$ denotes the site reached from site n by a translation of a lattice vector $\mathbf{a}$ [see Fig. 3.11(a) for the definition of $\mathbf{a}_1$ and $\mathbf{a}_2$]. Note that considering another of the $\mathbf{k}_{\max}$ values leads to same Eq. (3.33) or its complex conjugate. Even though the complex character of Eq. (3.33), its eigenvalues are all real and are precisely the eigenvalues of the original problem (3.20). Additionally, the band structure is successfully inverted by changing the signs of both the couplings and the on-site energies as confirmed by the DoS displayed in Fig. 3.12.

The left-hand side of Eq. (3.33) can be written as a complex Hermitian operator that becomes positive-definite by adding the appropriate energy shift $V_{\text{shift}} = \max(\mathcal{E}) + V_{\max}/2$ (see Table 3.1) [183], leading to the definition of $\hat{H}^{\star}_{\mathbf{k}_{\max}}$ of which $\boldsymbol{\phi}$ is an eigenfunction

$$\hat{H}^{\star}_{\mathbf{k}_{\max}} \boldsymbol{\phi} = (V_{\text{shift}} - E)\boldsymbol{\phi}. \tag{3.34}$$

A purely real localization landscape was derived from a complex Hamiltonian via the Ostrowski comparison matrix in the context of Dirac fermions by Lemut et al. [61]. However, in our case, the comparison matrix removes all phases related to the demodulation process, spoiling the recovery of the envelope functions and their energies. We then compute the dual landscape $\boldsymbol{u}^{\star}$ associated to the envelopes as

$$\hat{H}^{\star}_{\mathbf{k}_{\max}} \boldsymbol{u}^{\star} = \mathbf{1}, \tag{3.35}$$

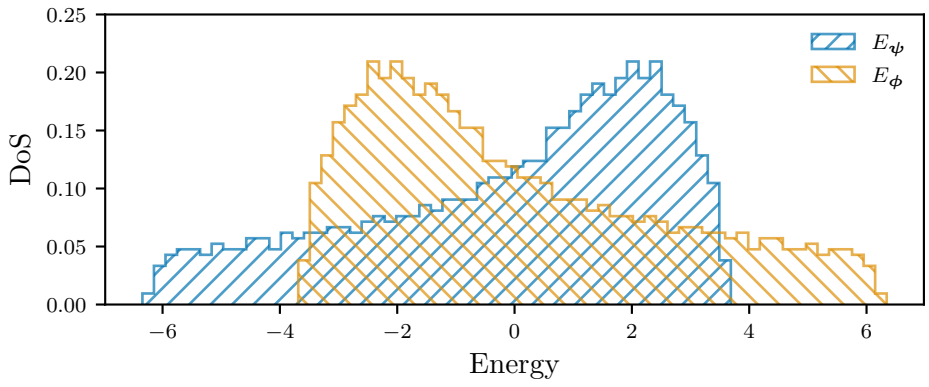

Figure 3.12: Density of states of the hexagonal lattice with disorder for the original [Eq. (3.20)] and the demodulated [Eq. (3.33)] equations and $V_{\max} = 6$.

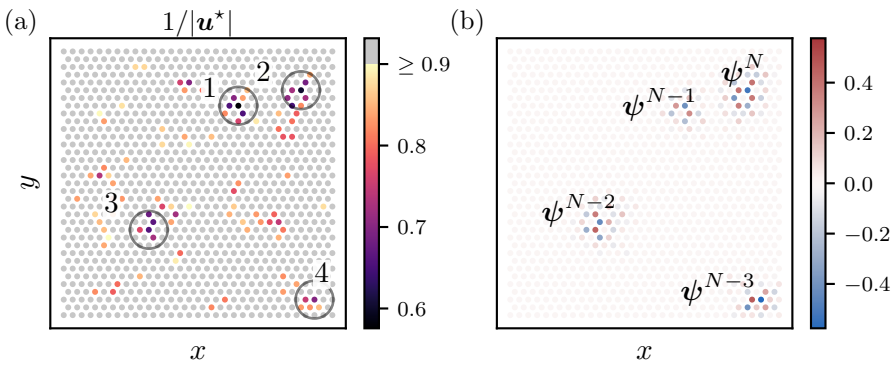

Figure 3.13: (a) Effective potential where the four deepest minima are labelled. (b) Four states with the highest eigenvalues of a hexagonal lattice with on-site disorder, $N = 1068$, and $V_{\max} = 6$.

to obtain a complex confining potential $1/\boldsymbol{u}^\star$ or, depending on $\mathbf{k}_{\max}$, its complex conjugate. Next, we plot the absolute value of $1/\boldsymbol{u}^\star$ in Fig. 3.13(a), where the comparison between the deepest wells of $1/|\boldsymbol{u}^\star| \equiv (1/|u_n^\star|)_{n\in[1,N]}$ and the locations of the aforementioned localized high-energy states [see Fig. 3.13(b)] clearly shows a direct match between the two sets. A detailed analysis of the correspondence between both quantities is performed in Section 3.2.5 for the two methods to compute the dual localization landscape.

As in the symmetric case, the proportionality between the minima of $1/|\boldsymbol{u}^\star|$ in the basins and the actual energies holds and can be studied for a broad class of 2D lattices. In Table. 3.3, we list the different lattices studied here with their band properties. Note that for most of the lattices with more than one band, looking for the maximum of the dispersion relation in the first Brillouin zone leads to $k_{\max}a = 0$, resulting in a "null demodulation" process. The appropriate $\mathbf{k}_{\max}$ vectors shown in Table 3.3 are then given by the maxima of the neighbouring cells in the reciprocal space: $\pm\mathbf{b}_1$, $\pm\mathbf{b}_2$ and $\pm(\mathbf{b_1} + \mathbf{b_2})$ [see Fig. 3.11(b) for the definition of $\mathbf{b}_1$ and $\mathbf{b}_2$ in the case of the hexagonal lattice]. With the exception of the 1D chain with 2$^{\text{nd}}$ neighbour coupling, $\mathbf{k}_{\max}$ never depends on the coupling details. For this specific case, the coupling values are also indicated in Table 3.3.

Fig. 3.14 is similar Fig. 3.10(b), except that all calculations are done using the explicit demodulation technique, explaining the increment in the number of studied lattices when the constraint on the symmetry of the DoS is lifted. In this case, we have performed extensive simulations on 9 types of lattices (3 1D and 6 2D) for various disorder strengths, all exhibiting Pearson coefficients larger than 0.96 and even larger than 0.98 in most cases (see Section 3.2.5). Particularly for the 1D chain, and the Square and Lieb lattices, the demodulation method conduces to the same real Hamiltonian found by symmetrical

Table 3.3: High energy wave vector for the different lattices studied.

Lattice	Bravais lattice	♯ of bands	$k_{\max}a$
1D chain	1D	1	$\pm\pi$
1D dimer chain	1D	2	$\pm 2\pi$
1D chain with 2$^{\text{nd}}$ neighb. coup. ($t_2 = t_1/\sqrt{8}$)	1D	1	$\pm\frac{3\pi}{4}$
Square	sql	1	M $(\pm\pi, \pm\pi)$
Lieb	sql	3	$(\pm 2\pi, \pm 2\pi)$ (flat band in the middle)
tts	sql	4	$(\pm 2\pi, \pm 2\pi)$
hexagonal	hxl	1	K $\left(\pm\frac{4\pi}{3}, 0\right)$, $\pm\left(\frac{2\pi}{3}, \frac{2\pi}{\sqrt{3}}\right)$, $\pm\left(\frac{2\pi}{3}, -\frac{2\pi}{\sqrt{3}}\right)$
Honeycomb	hxl	2	$\left(0, \pm\frac{4\pi}{\sqrt{3}}\right)$, $\pm\left(2\pi, \frac{2\pi}{\sqrt{3}}\right)$, $\pm\left(2\pi, -\frac{2\pi}{\sqrt{3}}\right)$
Kagome	hxl	3	flat band

arguments, and therefore the proportionality s follows the same master curves plotted in Fig. 3.10(b). However, for the 1D dimer and the Honeycomb lattice, s is significantly lower than in the symmetrical case. Note for instance, that both, the Hexagonal and Honeycomb, curves follows the same behavior. For the Kagome lattice, the flat band in the top of the dispersion relation spoils the detection of $\mathbf{k}_{\max}$, as indicated in Table 3.3. Therefore, results in Fig. 3.14 were obtained via the maxima of the second band as $\mathbf{k}_{\max} = \left\{(\pm\frac{8\pi}{3}, 0)\,,\ \pm\left(\frac{4\pi}{3}, \frac{4\pi}{\sqrt{3}}\right),\ \pm\left(\frac{4\pi}{3}, -\frac{4\pi}{\sqrt{3}}\right)\right\}$.

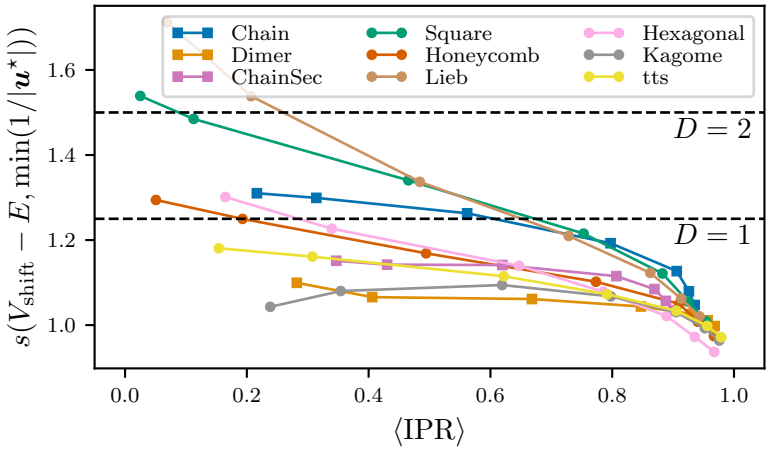

Figure 3.14: Proportionality factor between $V_{\text{shift}} - E$ and the minima of $1/|\boldsymbol{u}^\star|$ for the different 1D (squares) and 2D (circles) lattices studied. The linear fits are done on states with the 3% highest energy. The dashed horizontal lines show the limit expected using the approximate form Eq. (1.19). Each symbol correspond to a disorder strength. The results are plotted as a function of the mean IPR calculated over the 3% states found for a given disorder strength.

3.2.5 Accuracy of the predictions

Along this section, we have shown how to compute the localization landscape and the dual localization landscape for discrete systems in a broad class of 2D lattices. In the case of the dual landscape, two different methods that can be applied even beyond 2D have been developed according to the symmetry of the DoS. In this section, we quantify the quality of the predictions for the energies and the location of the localized eigenfunctions performed by each landscape.

To quantitatively test the efficiency of the tight-binding localization landscape and the dual localization landscape to pinpoint the position of localized modes, we start calculating the distances between the position n of the maximum of an eigenstate $\max \boldsymbol{\psi}^N$, and the positions m of all the wells of the effective potential $1/\boldsymbol{u}$. Then, by minimizing the distances, we identify the rank of the containing well of a given mode. For instance, Fig. (3.15) shows this correspondence for the dual localization landscape depicted in Fig. (3.13), where the 2$^{\text{nd}}$, 1$^{\text{st}}$ and 3$^{\text{rd}}$ wells contain $\boldsymbol{\psi}^N$, $\boldsymbol{\psi}^{N-1}$ and $\boldsymbol{\psi}^{N-2}$, respectively.

Previous analysis is systematically repeated for the 100 realizations of the Honeycomb and Hexagonal lattices in a situation of weak [Fig. 3.16(a), (c), (e), and (g)] and strong disorder [Fig. 3.16(b), (d), (f), and (h)]. In the high-energy case, the computations are done using the symmetry of the band structure for the honeycomb lattice [Figs. 3.16(e) and (f)], and the explicit demodulation for the hexagonal lattice [Figs. 3.16(g) and (h)]. Note that sharp diagonals indicate a good performance of both landscapes.

At strong disorder, all confining potentials are able to predict the location of the lowest- (highest-)energy states with more of 95% precision. This percentage is slightly

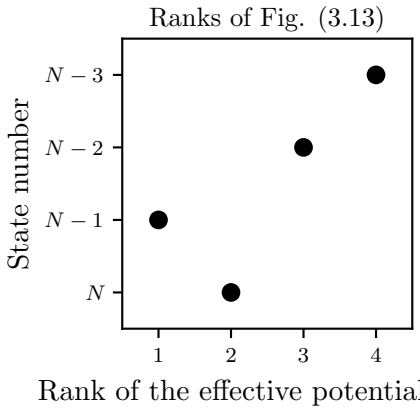

Figure 3.15: Correspondence between the maxima of the dual landscape and the eigestate position for the example in Fig. 3.13.

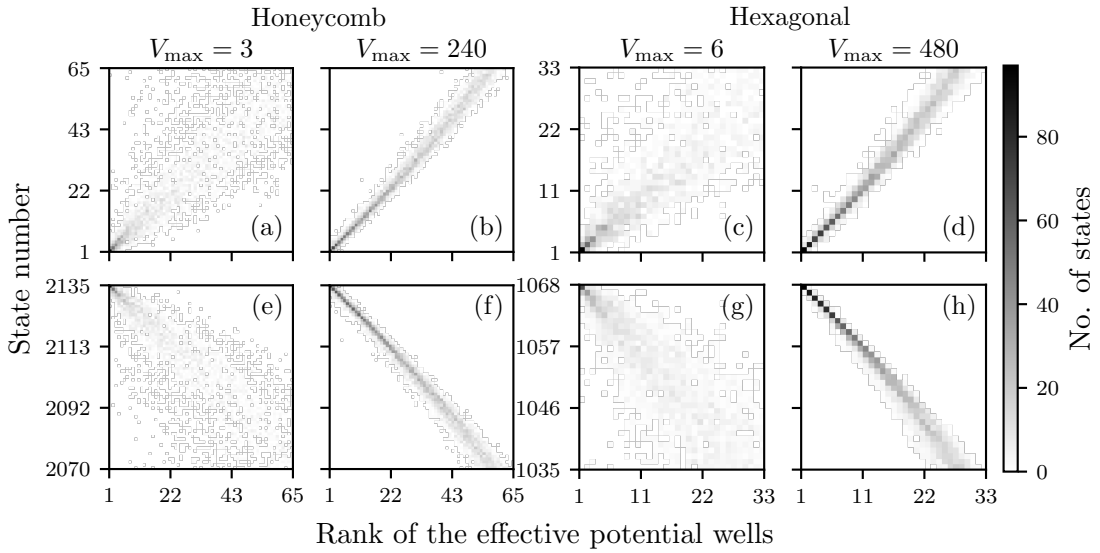

Figure 3.16: Number of states whose position match [(a)-(d)] with the maxima of the landscape and [(e)-(h)] with the maxima of the dual landscape. We consider the 3% of the states for each lattice with the weakest and strongest disorders shown in Table 3.2 ($V_{\max} = 3$ and $V_{\max} = 240$ for the Honeycomb lattice and $V_{\max} = 6$ and $V_{\max} = 480$ for the Hexagonal lattice) and 100 disorder configurations.

slower in the case of weak disorder ($\sim 85\%$), where the correspondence spreads faster from the diagonal. In this regime, the potential wells are wider and thus can be repopulated easily, additionally the probability of having eigenstates with similar energies also increases (see Section 1.1.3.4). Notably, both methods to compute the dual localization landscape present similar features.

We shown in Figure 3.17(a) and (b) the Pearson coefficient ρ inherent to s in Figs. 3.10. Figure 3.17(c) in equivalent to its both superior panels but it corresponds to Fig. 3.14. Numerical results demonstrate that in every case considered in this work, the eigenvalues and the minima of the effective potential are highly correlated, presenting Pearson coefficients between 0.96 and 1 even for the Kagome lattice whose $\mathbf{k}_{\max}$ cannot be properly defined. Despite the symmetric and demodulation dual localization landscapes provide different s values for the Honeycomb and Dimer lattices, Figure 3.17 proves that the corresponding Pearson coefficient are almost identical in both cases.

Finally, the energy predictions also allow to compute the Integrated Density of States (IDoS) —also known as the counting function— near the band edges. Figure 3.18 depicts

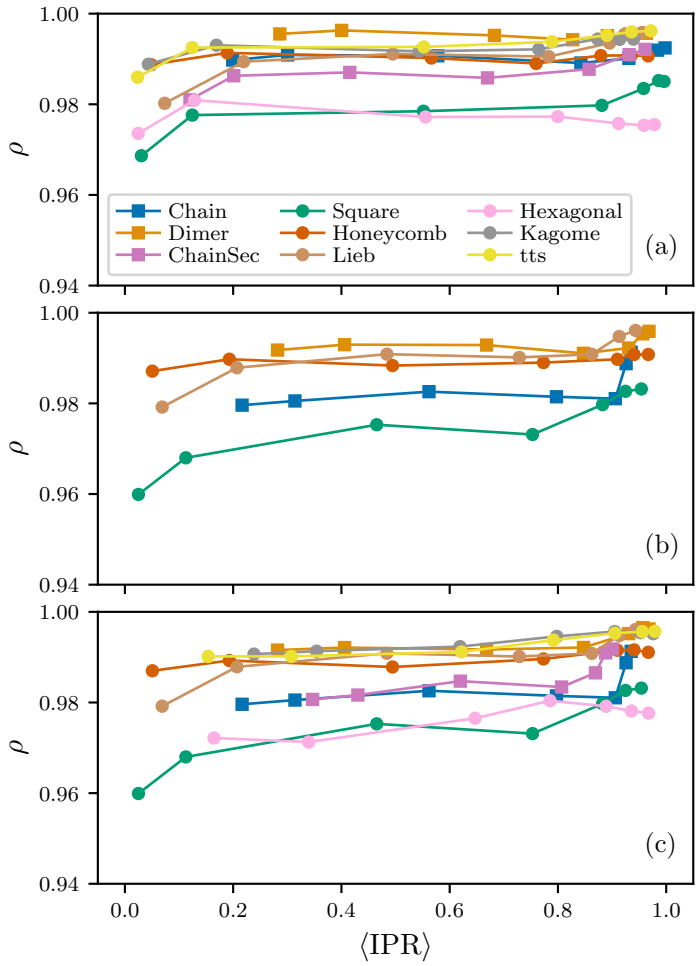

Figure 3.17: Pearson correlation coefficient as a function of the ⟨IPR⟩ corresponding to the data plotted in Figs. 3.10 and Fig. 3.14. (a) The landscape prediction. (b) The dual landscape prediction for the symmetric lattices using the symmetry of the DoS property. (c) The dual landscape prediction for all the lattices using the explicit demodulation.

the IDoS for the Honeycomb and Hexagonal lattices with a strong on-site disorder ($V_{\max} = 240$ and $V_{\max} = 480$ for the Honeycomb an Hexagonal lattice, respectively). Blue lines correspond to the solution of Eq. (3.20) while orange lines are the minima of both confining and dual confining potentials. We can see that for the two lattices and in both range of energy, the localization landscape and dual localization landscape provide a good estimate of the IDoS.

3.3 Conclusions

Born a decade ago, the localization landscape theory has proven its remarkable efficiency to bring in a more accessible form the information contained in a Hamiltonian [184]. In this chapter, we started by analysing the applicability of this powerful theory to wave scattering in disordered electromagnetic media. Even though localization has been already demonstrated experimentally in those systems in 1D or 2D, the discussion about the existence of a vector localization landscape is still open. In this chapter, solutions for electromagnetic fields have been found by solving the scalar differential equations corresponding to TM and TE polarizations where localization is just achieved at frequencies much longer than those in the lower band edge, therefore the

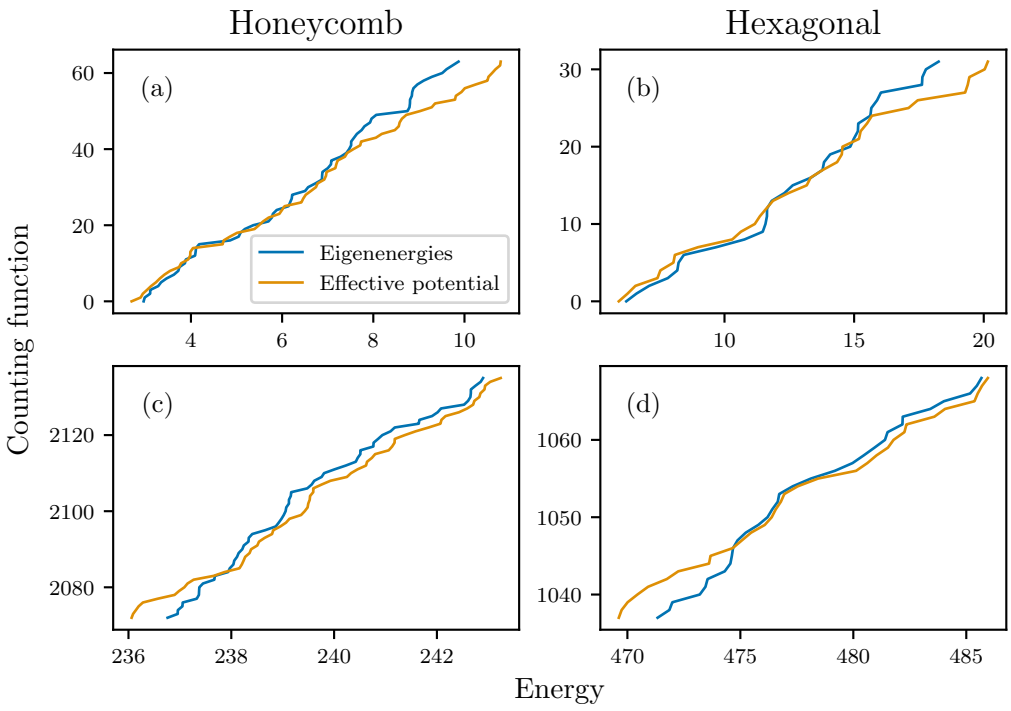

Figure 3.18: The counting function computed by [(a) and (b)] the confining potential, and by [(c) and (d)] the dual confining potential. We consider the 3% of the states for each lattice. Here, the strongest disorder was chosen ($V_{\max} = 240$ and $V_{\max} = 480$ for the Honeycomb an Hexagonal lattice, respectively).

respective localization landscape is incapable to predict the behavior of such high-frequency localized states. This can be contrasted with discrete systems described by a tight-binding Hamiltonians, where localization appears in both band edges. The second part of this chapter successfully extends the localization landscape scope to discrete systems with a focus on 2D lattices. The low-energy part of the spectrum is described by a discrete extension of the effective confining potential defined for continuous systems. It bears the same efficiency than its continuous counterpart in predicting the localization regions and the corresponding energies, hence the density of states [185]. More challenging is the construction of the *dual* confining potential that acts on the upper part of the spectrum. When the lattice is characterized by chiral symmetry, like the honeycomb lattice, the high-energy theory is directly deduced from the low one. When this symmetry is not present, we have proposed a general procedure to build the dual localization landscape. Our method is efficient, robust and very general but not yet completely universal. It has yet to be completely extended to situations like the one encountered with the Kagome lattice. In this case, the DoS is not symmetric, and the high energy states lie on a flat band: the definition of $\mathbf{k}_{\max}$ remains a challenge. Finally, it is also worth noting that interesting properties appear in the center of the band for many of the new 2D materials. Although this energy range doesn't fall directly into the frame of our approach, we were able to pinpoint the localization regions in this case thanks to an approach inspired by the $\mathcal{L}^2$-landscape method [186]. This last one is able to give information about the localization subregions, but predictions about the eigenenergies, IDoS, etc. are still missing despite of its efficient numerical implementation [187]. In Appendix B, an algorithm that allows the energy extraction from the $\mathcal{L}^2$-landscape is introduced. Unfortunately, this algorithm does not improve the calculation time needed to solve Eq. (3.20), therefore predicting the eigenenergies and the IDoS by this new landscape must be the topic of future investigations.

4

Strong localization in Vogel Spirals

...para contarte,
que quisiera ser un perro y oliscarte,
vivir como animal que no se altera,
tumbado al sol lamiéndose la breva,
sin la necesidad de preguntarse
si vengativos Dioses nos condenaran,
si por Tutatis el cielo sobre nuestras cabezas caerá...
Extremoduro (La ley innata: la realidad)

Contents

As mentioned in Section 1.2.3, this Chapter is devoted to the study of electromagnetic wave scattering through dielectric lattices displaying either aperiodicity or disorder. The Chapter is organized as follows: Section 4.1 starts by detailing the experimental procedure, together with the definition of the two dielectric arrays used as scattering media. We then describe the data analysis technicalities that allow to retrieve the individual eigenmodes and the transport quantities in both cases. In Section 4.2, we present the results in the traditional disordered system: they demonstrate that all eigenstates show a consistent exponential radial behaviour, as well as the loss of Anderson localization when the dimension of the cavity from 2D to 3D. Finally, in Section 4.3, we disclose a new type of wave localization driven by the particular correlations of Vogel spirals that survives this 2D/3D transition. The confined eigenmodes are then classified, showing either power-law, exponential or Gaussian radial decays, and high quality factors, leading to slow energy decays. The last part of this section is dedicated to the full characterization of this new localization phenomenon, where the robustness of the states is tested with respect to the size of the Vogel spiral, and the partial destruction of it. The main results presented in this Chapter have been published in [28] and [29].

4.1 Experimental setup and analysis details

We investigate two different lattice structures, both comprised of N identical dielectric cylinders made of TiZrNbZnO ceramics (see Section 2.2). One type of lattice features aperiodicity, as the cylinders are arranged in a Vogel spiral. The second type exhibits positional disorder. Cylinder arrays are placed into the cavity introduced in Section 2.1 (see Fig. 2.2) and the electromagnetic field is induced and measured by two straight antennas placed at (1) the center of the movable top plate, and (2) on the bottom plate. The antenna (2) defines the origin of the reference system $(x, y) = (0, 0)$. As discussed in Section 2.1.2, straight antennas induce a TM polarization, where the corresponding electric field is homogeneous in the $\hat{z}$-direction below the frequency $\nu_{\text{cut}} = \mathrm{c}_0/(2h)$, with c_0 the speed of light in air and h the distance between both plates (see Section 2.1.1). Therefore, by going beyond this frequency, the cavity cannot be seen as a 2D anymore. We also studied a regular lattice in an analog way and the results are presented in Appendix C.

4.1.1 The Golden-Angle spiral array

Positions in a Vogel spiral array are defined in terms of polar coordinates (r, θ) as [137]

$$\begin{aligned} r_i &= a_0\sqrt{i}, \\ \theta_i &= i\alpha, \end{aligned} \tag{4.1}$$

where $i = 1, 2, \ldots$ is an integer, the *scaling factor* a_0 is a positive constant that sets the particle separation, and the *divergence angle* α determines the constant aperture between successive points [125]. One of the possible definitions for the angle α is a function of an irrational number ξ, as $\alpha = 2\pi\,[1 - \mathrm{frac}(\xi)]$ where $\mathrm{frac}(\xi)$ is the fractional part of ξ [114, 142]. With $\alpha/(2\pi)$ irrational, Vogel spirals are characterized by the absence of rotational and translational symmetries. Here, we study the *Golden-Angle* Vogel spiral, also known as "sunflower spiral" which is obtained when ξ equals the golden number: $\xi = (1+\sqrt{5})/2$, resulting in $\alpha \approx 2.4$ (137.5°), also known as the "golden angle". Experimentally, we implement a golden-angle spiral made up of $N = 390$ cylinders, and a scaling factor $a_0 = 6.93$ mm, leading to a radius $R_0 = 140$ mm with a planar 2D density $\rho \approx 0.65$ cm^{-2}. The sketch of the golden-angle spiral map used to place the cylinders as well as a picture of the real systems is shown in Fig. 4.1(a) and (b), respectively.

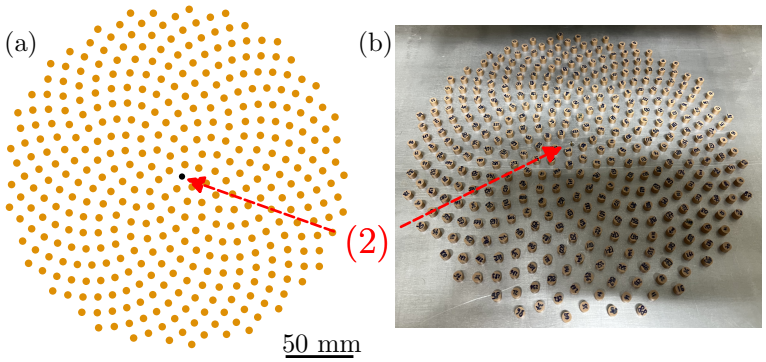

Figure 4.1: (a) Golden-angle spiral array consisting of $N = 390$ cylinder created with $a_0 = 6.93$ mm and $\xi = (1+\sqrt{5})/2$. The black dot indicates the position of the fixed antenna (2), which determines the origin of the reference system. (b) Image of the 2D golden-angle spiral array of dielectric cylinders. The top plate has been removed to reveal the details of the sample.

4.1.2 The disordered array

The disordered array is composed by allocating N hard disks according to the algorithm developed in [99]. The latest is basically an isochoric Monte Carlo simulation of hard disks of radius R in a square surface of area A with periodic boundary conditions. At a given time, the center positions of the N disks generate a pattern of points, with a packing density $\phi = N\pi R^2/A$. To get the disordered array, an initial random configuration is compressed up to the target density and then relaxed to reach equilibrium. As mentioned by Froufe-Pérez et al. [99], an equilibration time set at 10^4 Monte Carlo sweeps is sufficient to equilibrate the sample. The lattice used in our experiments consists of $N = 497$ disks of radius $R = 3.25$ mm (the dielectric cylinder radius + the metallic tube thickness, see Section 2.2) confined in a square box of side 140 mm, leading to the packing density $\phi = 0.2199$ and to the same 2D density than the golden-angle spiral $\rho \approx 0.65$ cm^{-2}. For comparison with the golden-angle spiral, only the sites enclosed within a circular area of radius 140 mm are selected, resulting in a disordered lattice of $N = 388$ sites, as shown in Fig. 4.2.

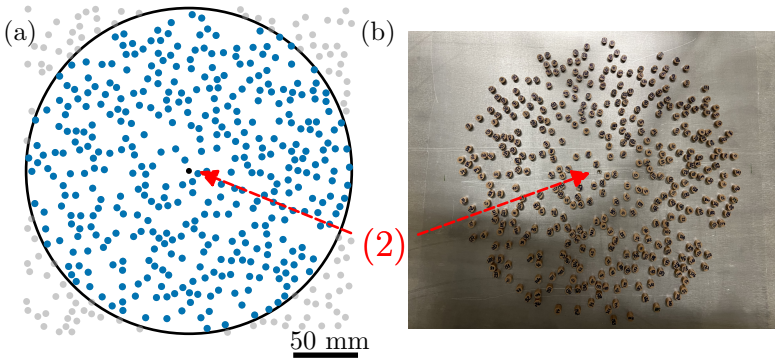

Figure 4.2: (a) Disordered array consisting of $N = 497$ hard disks created by the software in [99] with $\phi = 0.2199$ (blue and gray dots). The circle of radius 140 mm encloses $N = 388$ sites (blue dots). The black dot indicates the position of the fixed antenna (2), which determines the origin of the reference system. (b) Image of the 2D disordered array of dielectric cylinders. The top plate has been removed to reveal the details of the sample.

4.1.3 Experimental and data analysis performance

Our experiments are carried out by considering three different values of h (13 mm, 15 mm and 17 mm) in the frequency range $[5.5\,\text{GHz}, 15\,\text{GHz}]$ with a frequency step of 250 kHz, corresponding to wavelengths in the range $[20\text{ mm}, 54\text{ mm}]$. It is worth noting that the cavity cannot be viewed as purely 2D over the whole range: a transition to a three-dimensional regime occurs—the higher the cavity height, the lower the transition frequency in the air [$\nu_{\text{cut}}(h = 13\text{ mm}) \approx 11.53$ GHz, $\nu_{\text{cut}}(h = 15\text{ mm}) \approx 9.99$ GHz, and $\nu_{\text{cut}}(h = 17\text{ mm}) \approx 8.81$ GHz].

Using the movable antenna (1), a disk of radius 160 mm centered at the origin is mapped over a 5×5 mm^2 square grid. Additionally, the electric field outside the lattice is measured on sites belonging to the upper right corner of a square of size 165 mm enclosing the disk [see Fig. 4.3(a)]. The final measured map contains 3675 points and is shown in Fig. 4.3(a), where the golden [blue] circle delineates the golden spiral [disordered system], whose geometrical center is located at $(x, y) = (-5\text{ mm}, 0)$ [$(x, y) = (0, 0)$], and the grey points represents the measured positions. Note that the geometrical center of the Vogel spiral has been shifted to avoid the collision between the central antenna and the scatterers.

At each position (x, y), both complex reflected and transmitted signals are registered [$S_{11}(\nu)$ and $S_{21}(\nu)$, respectively] by the VNA. Examples of the intensity of both measured signals, $|S_{11}|^2$ (purple line) and $|S_{11}|^2$ (orange line), are presented in Fig. 4.3(b) and (c) for the golden-angle spiral and the disordered system, respectively. Both panels show measurements taken at a given distance $d \approx 106$ mm between the antennas [red dot in Fig. 4.3(a)] for a distance between plates $h = 13$ mm. The weak coupling regime between the antenna and the field explains the low transmission values observed in both panels.

As shown in Section 2.4.6, up to an inversion, the reflected signals in Figs. 4.3(b) and (c) can be reinterpreted as the local density of states at different positions for the two lattices. Consequently, in Fig. 4.3(b), the frequency regions with values of the reflection close to 1 (and vanishing transmission values) indicate the presence of band gaps. In particular, two frequency windows with these characteristics are identified around ~ 9 GHz and ~ 11 GHz for the golden spiral case. In comparison, a unique and smaller gap is observed for the disordered array around ~ 9 GHz [see Fig. 4.3(c)]. Outside of these gaps, the transmitted signal is a superposition of peaks which are related to the resonances of the system.

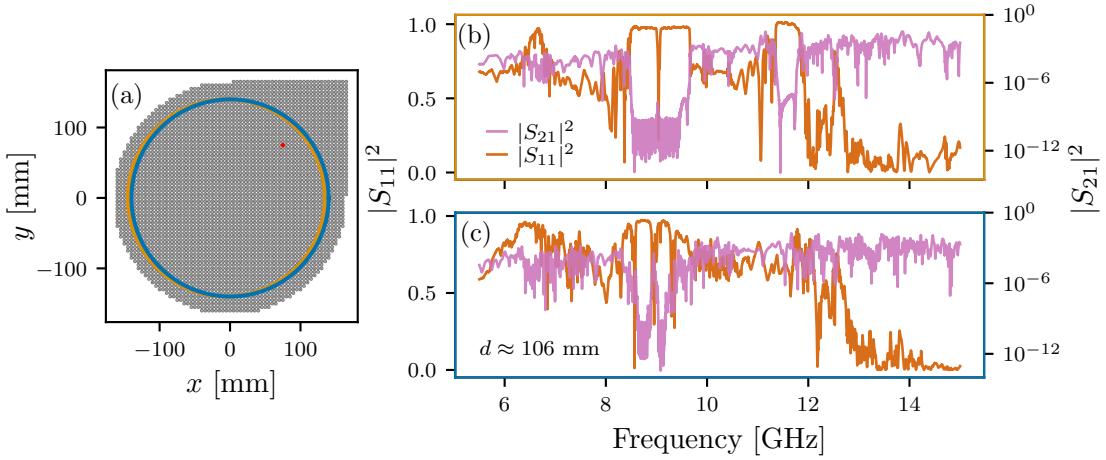

Figure 4.3: (a) The experimental map used to scan the cavity (gray dots). Golden (blue) circle delineates the golden-angle spiral (disordered system). Reflected $|S_{11}(\nu)|^2$ (orange line) and transmitted coefficients $|S_{12}(\nu)|^2$ (purple line) for (b) the golden-spiral spiral and (c) the disordered system at a distance $d \approx 106$ mm from the origin ($x = 75$ mm, $y = 75$ mm). The red dot in (a) indicates the measurement position corresponding to signals in (b) and (c).

The posterior analysis of the transmitted signal is conducted using the harmonic inversion/clustering methods (see Sections 2.4.2 and 2.4.3). To apply the harmonic inversion to our experimental data, the complex spectrum at each position is first divided into 19 frequency intervals, each one with a bandwidth of 0.6 GHz, overlapping each other by 0.05 GHz to avoid the interval of interest of being spoiled by spurious resonances generated by the filtering of the signal. Similar to the example shown in Section 2.4.2, the value of $2K$ used to feed the harmonic inversion algorithm is determined from the band-limited time signal as twice the value of the transition between the sharp peaks and the noise for each frequency window. After recovering the parameters of the resonances, the amplitudes of the same resonance measured at all positions are clustered to reveal the map of the electric field amplitude $E_k(x, y)$ of each eigenmode of the system [81]. In addition to the mode analysis, the dynamics around certain states is studied by Fourier-transforming the transmitted signal filtered by a bandpass Gaussian filter $F^{f_0,\Delta\omega}$ with $\Delta\omega = 0.01$ GHz (see Section 2.4.5).

$$S_{21}^{f_0,\Delta\omega}(\mathbf{r}, t) = \mathcal{F}\left\{S_{21}(\mathbf{r}, \nu) \times F^{f_0,\Delta\omega}(\nu)\right\}, \tag{4.2}$$

The systematic repetition over all measured points allows to compute the total energy carried by a given superposition of modes as

$$E^{f_0,\Delta\omega}(t) = \sum_{\text{all positions}} \left|S_{21}^{f_0,\Delta\omega}(\mathbf{r}, t)\right|^2. \tag{4.3}$$

In the following sections, we present a detailed analysis of the wave propagation through both structures: the disordered array and the golden-angle spiral. Besides the modal analysis, results from the harmonic inversion together with the energy dynamics and the density of states (DoS) are studied to provide an overview of the transport characteristics in different frequency regions. Particularly, the energy in the system is mapped via 472 Gaussian band-pass filter uniformly distributed in the frequency interval $[5.54\text{ GHz}, 14.96\text{ GHz}]$ with $\Delta\omega = 0.01$ GHz. On the other hand, the density of states is directly computed from the measured reflected signal as DoS $\simeq \left[1 - \left\langle |S_{ii}(\mathbf{r}, \nu)|^2 \right\rangle\right]$ (see Section 2.4.6).

4.2 Conductance through Anderson modes (disordered systems)

We start our analysis by studying the modal structure in the traditional disordered system. Figs. 4.4[(a)-(o)] present fifteen modes with frequencies in the interval [$\sim$ 6.6 GHz,$\sim$ 10.9 GHz] extracted via the harmonic inversion/clustering algorithms at different heights h (see details in Sections 2.4.2 and 2.4.3). Specifically, Figs. 4.4 depicts states found for $h = 13$ mm [(a), (d), (g), (j), and (m)], $h = 15$ mm [(b), (e), (h), (k), and (n)], and $h = 17$ mm [(c), (f), (i), (l), and (o)]. Given the lack of a geometrical center in disordered structures, radial decay functions can only be computed through the *Spatial Autocorrelation* introduced in Section 2.4.4.1, and are presented in Figs. 4.4(p), (q), and (r). As expected for a disordered system, this analysis always leads to exponential radial decays no matter the spatial extension, frequency, position of the center, or the amplitude distribution with respect to the center of the mode. The localization lengths ξ_{loc} can then be extracted by fitting $\text{Cor}(E_\nu) \propto \exp(-r'/\xi_{\text{loc}})$ and are shown together with the quality factors of the modes in Table 4.1.

The localization length indicates the spatial extension of an exponentially localized mode allowing to define a criterion to determine if the states are ($\xi_{\text{loc}} \lesssim R_0$) or not

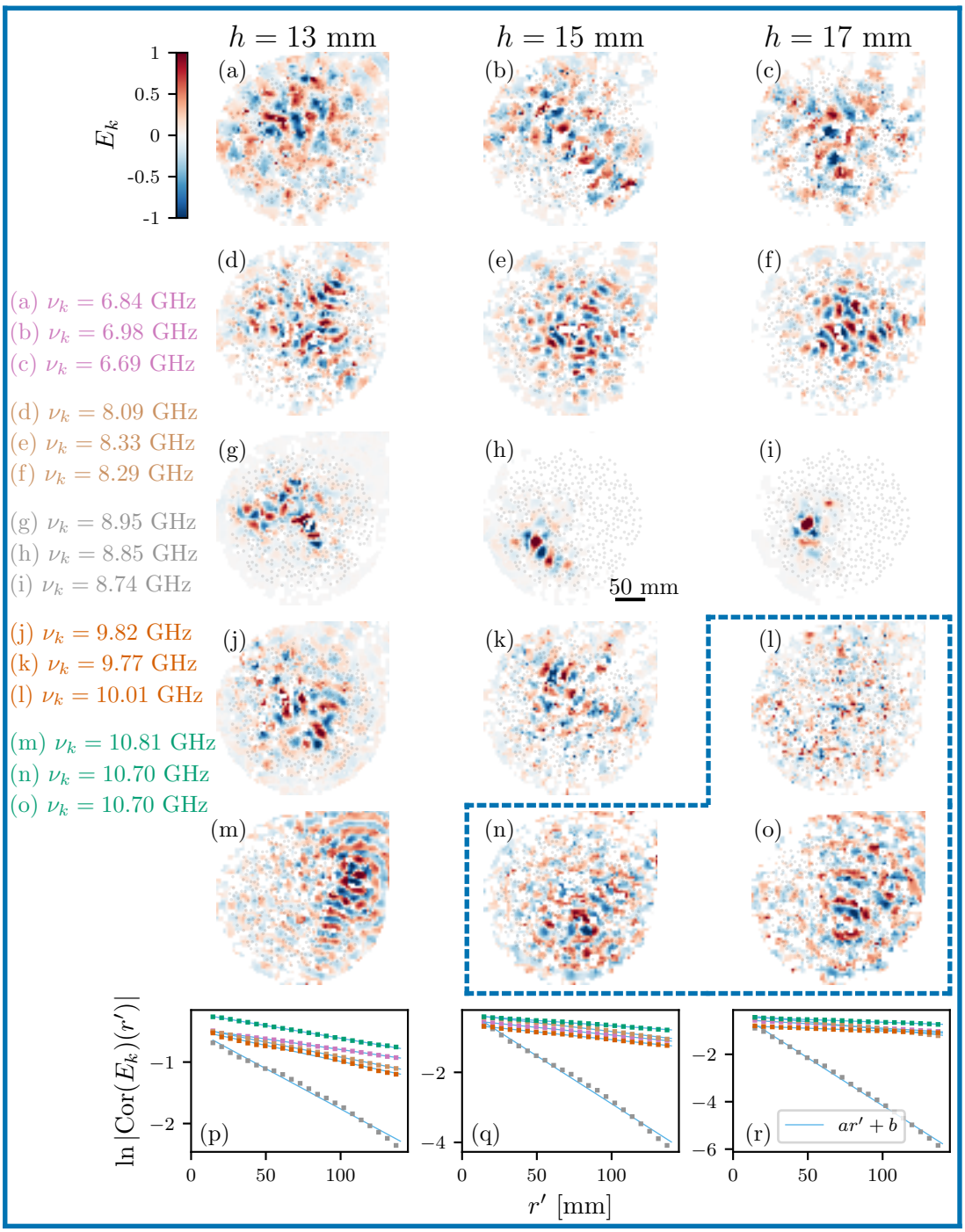

Figure 4.4: [(a)-(o)] Spatial modal structure, and [(p)-(r)] radial profile of the spatial autocorrelation field (not shown) of representative modes found in the same disordered system. Amplitude maps are normalized such that $\max(|E_k|) = 1$. The blue dotted box contains the states with frequencies beyond the 2D limit. Radial decays are obtained by performing an angular average in the autocorrelation space (r' is measured from the well defined autocorrelation center). The corresponding localization lengths ξ_{loc} and quality factors Q_k are shown in Table 4.1.

($\xi_{\mathrm{loc}} > R_0$) confined inside the structure. Our results reveal the presence of well-confined states ($\xi_{\mathrm{loc}} \sim 50$ mm) with high quality factors ($Q_k \sim 3500$) around $\nu \sim 8.8$ GHz [see Figs. 4.4(g), (h) and (i)]. Notably, the modes characterized by $\xi_{\mathrm{loc}} < R_0$ are placed below the 3D transition, where the system is purely 2D. At lower frequencies ($\nu_k \lesssim 8.4$ GHz), the eigenmodes are characterized by $\xi_{\mathrm{loc}} \sim 200$ mm. They therefore reach the boundaries

Table 4.1: Localization lengths ξ_{loc}, and quality factors Q_k of each state in Fig. 4.4.

	h [mm]	ν_k [GHz]	ξ_{loc} [mm]	Q
(a)	13	6.84	291	1813.22
(b)	15	6.98	231	1222.43
(c)	17	6.69	264	1284.87
(d)	13	8.09	205	639.61
(e)	15	8.33	207	1368.58
(f)	17	8.29	165	1117.12
(g)	13	8.95	81	3980.98
(h)	15	8.85	40	2541.99
(i)	17	8.74	28	4512.35
(j)	13	9.82	195	3596.37
(k)	15	9.77	227	3029.09
(l)	17	10.01	435	2541.23
(m)	13	10.81	240	2434.86
(n)	15	10.70	337	2671.44
(o)	17	10.70	448	2398.99

of the structure and subsequently leak, giving rise to poor quality factors. Remarkably, this behaviour is robust against the change of h.

The fourth and fifth rows of Fig. 4.4 present modes with frequencies around $\nu \sim 10$ GHz and $\nu \sim 10.7$ GHz, respectively. A huge increase in the amount of noise generated by the mixture of states is observed compared to the states shown in the first three rows. Both rows display a steady increase of the localization length ξ_{loc} and a reduction of the quality factors as a function of the frequency and the distance h. Note that at $\nu \sim 10$ GHz only the mode at $h = 13$ mm [Fig. 4.4(j)] can be considered quasi-localized ($\xi_{\text{loc}} = 196$ mm) while the others can easily reach the structure's boundaries and leak. Unfortunately, for higher frequencies, the large modal overlap regime (mean mode spacing much smaller than the modal width) makes the eigenstate reconstruction impossible.

4.2.1 Energy dynamics

Besides the quality factor, the evolution of the energy confined inside the system and carried by a subset of states can be studied by means of Eq. (4.3). For instance, Fig. 4.5(a) displays the energy as a function of the time in three different frequency ranges centered around the frequency of the modes with smallest ξ_{loc} shown in Fig. 4.4 [(g), (h), and (i)] and with $\Delta\omega = 0.1$ GHz. In addition, the corresponding temporal Gaussian pulse is shown in Fig. 4.5(b). Within these frequency intervals, the presence of modes with high quality factors leads to very slow energy dynamics in all cases. However, a decrease of the total confined energy with respect to h is also observed.

Assuming an exponential decay of the energy with respect to the time, $E(t) \sim \exp(-t/t_0)$, one can fit a characteristic decay time t_0 that is closely related to the average width of the modes contributing to the transport $\langle \delta\nu_k \rangle \sim 1/t_0$. Note that this analysis always considers a subset of states whose frequency is in between the band-pass filter, therefore it is not directly comparable with the individual values of Q_k shown in Table 4.1. Nevertheless, by knowing the quality factor of all modes inside the filter, the characteristic time can still be computed for a given frequency band $\Delta\omega$ as $t_0 \sim \langle Q_k/\nu_k \rangle_{\Delta\omega}$. In this example, the slowest dynamics occurs for $h = 17$ mm, followed by $h = 15$ mm and $h = 13$ mm.

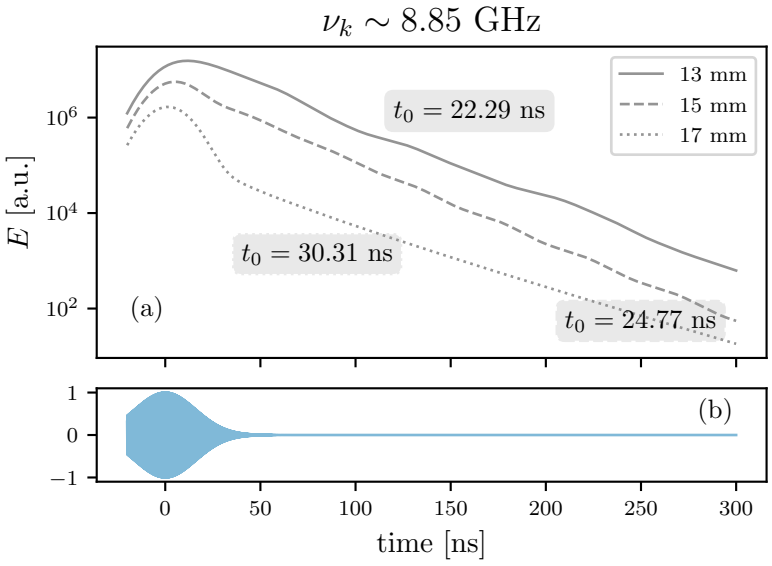

Figure 4.5: (a) Evolution of the energy as function of time for three different frequency centers f_0 and $\Delta\omega = 0.01$ GHz. Specifically, $f_0 = 8.96$ GHz for $h = 13$ mm, $f_0 = 8.84$ GHz for $h = 15$ mm and $f_0 = 8.74$ GHz for $h = 17$ mm.

4.2.2 Absence of electromagnetic localization in 3D disordered systems

We now use the results of harmonic inversion, together with the energy dynamics and the density of states, to unravel the global consequences of the 2D/3D transition in a disordered system. This is achieved by changing the distance between the top and bottom plates. In Figs. 4.6(a), (b), and (c), Q_k is plotted as a function of ν_k for the disordered array in the cases $h = 13$ mm, $h = 15$ mm, and $h = 17$ mm, respectively. Blue arrows are added to indicate the frequency of the states of Fig. 4.4. As performed in the previous section, the temporal evolution of the energy is used to recover the characteristic decay time t_0 as a function of the frequency and of h [see Fig. 4.6(d)]. The corresponding density of states are also depicted in Figs. 4.4(e). Finally, using the two previously introduced quantities (DoS and t_0), the average Thouless conductance (see Section 1.1.1.1) is experimentally extracted as

$$\langle g \rangle_{\Delta f} = \frac{\langle \delta\nu_k \rangle_{\Delta f}}{\langle \Delta\nu_k \rangle_{\Delta f}} \sim \frac{\langle \mathrm{DoS} \rangle_{\Delta f}}{t_0 \Delta f}, \tag{4.4}$$

where $\langle \cdot \rangle_{\Delta f}$ defines the average over the frequency interval Δf [see Fig. 4.6(f)]. Remember that the Thouless criterion establishes that Anderson localization occurs for $g < 1$ [36–38].

Figs. 4.6(a), (b), (c) and (d) reveal a huge similarity between t_0 and the density of Q_k. Here, t_0-regions associated with frequency windows containing well-confined exponential modes are characterized by high peaks whose maximum values are of the order of 40 ns, whilst t_0-valleys correspond to short-lived, not spatially localized states. Note that no band gap can be clearly observed in the density of states for any h in the whole frequency range.

At low frequency ($\nu < 8.8$ GHz) and for all values of h, Figs. 4.6(a), (b), and (c) show three bumps of the quality factor Q_k of the resonances, going from values close to zero when $\nu \sim 5.5$ GHz, to reach a first maximum near $\nu \approx 6.5$ GHz and then decrease to minimum values at $\nu \approx 7.1$ GHz. The second bump has a local maximum at $\nu \approx 7.5$ GHz where $Q_k \sim 3000$, and lately, Q_k values go near zero at $\nu \approx 8$ GHz to reach the new local maxima at $\nu \sim 8.7$ GHz. Likewise, the DoS curves in this frequency range ($\nu < 8.7$ GHz) are quite similar to each other being only differentiated by their intensity. Since this

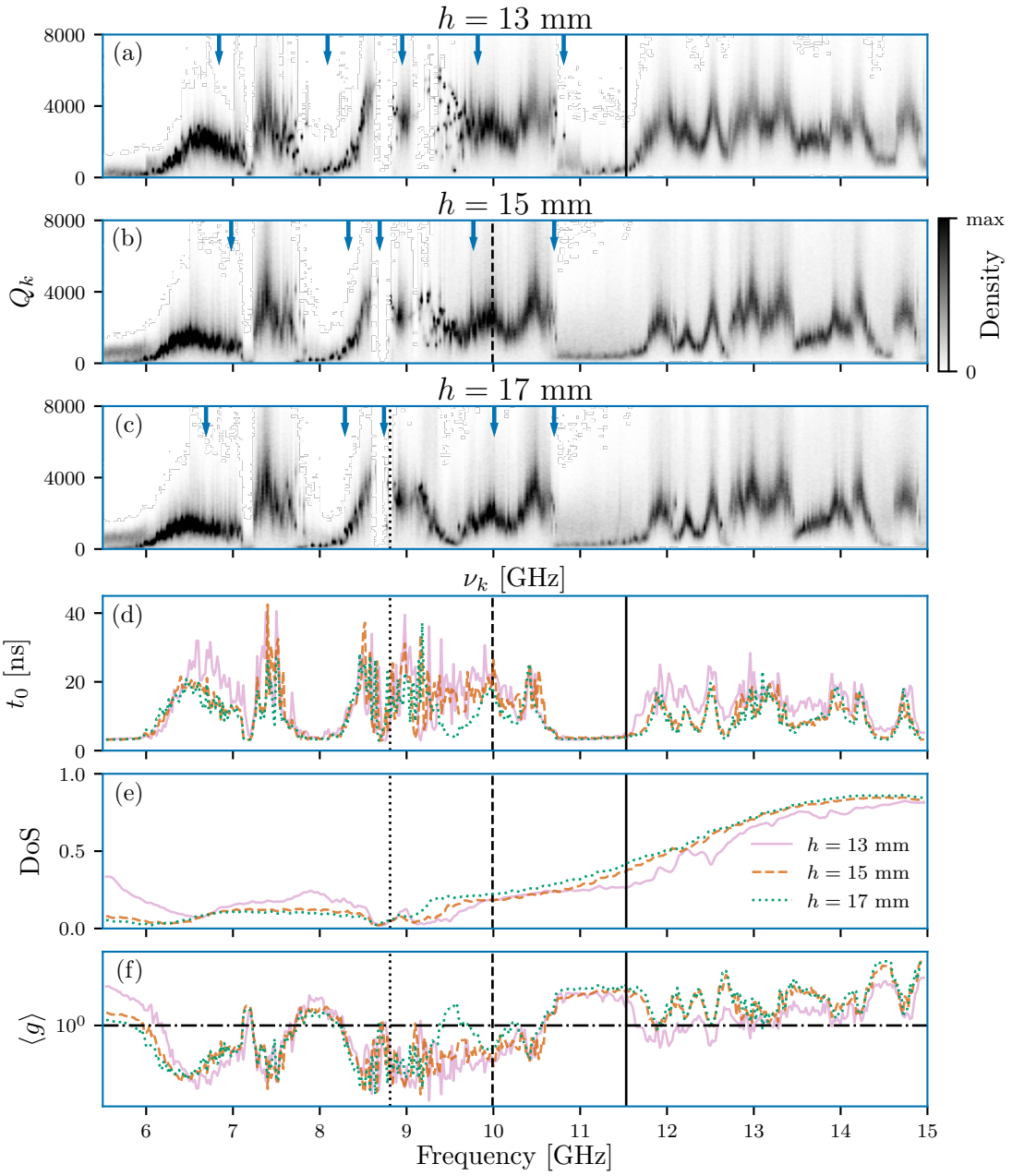

Figure 4.6: Density plots of the quality factors Q_k as a function of the resonant frequencies ν_k extracted via the harmonic inversion with a distance between plates (a) $h = 13$ mm, (b) $h = 15$ mm, and (c) $h = 17$ mm for the disordered system. Arrows indicate the frequencies of the states presented in Fig. 4.4. (d) Characteristic decay time t_0 as a function of the frequency. The total frequency range has been mapped by 472 frequency filters spaced by $\Delta f = 0.02$ GHz with $\Delta\omega = 0.01$ GHz. (e) Experimental DoS as a function of the frequency. (f) Experimental Thouless conductance $\langle g \rangle$ as a function of the frequency. The dash-dotted line indicates $\langle g \rangle = 1$. Black vertical lines indicate the cut-off frequency ν_{cut}.

frequency region always lies below the estimated 2D/3D threshold, the difference in the signal intensity simply reflects the variation in the antenna coupling with the height. Particularly, a reduction in the number of states carried by the system can be seen at $\nu_k \approx 6.5$ GHz and $\nu_k \approx 8.7$ GHz. A detailed analysis of the characteristic time t_0 also reveals a slight difference with respect to the height h. The largest values are obtained for $h = 13$ mm, while smaller and identical for $h = 15$ mm and $h = 17$ mm, for both bumps. Differences with respect to h in the density of states and t_0 compensate each other resulting in almost indistinguishable values of $\langle g \rangle$, which shows a fast decay of around one order of

magnitude near $\nu \approx 6.5$ GHz followed by a sudden increase at $\nu \approx 7.1$ GHz. A second and a third dropping are observed at $\nu \approx 7.5$ GHz and $\nu \approx 8.7$ GHz with maximum at $\nu \approx 8$ GHz. Leaking modes shown in the first and second rows of Fig. 4.4 [(a)-(f)] belong to the first [6.2 GHz, 7 GHz] and third bumps [8 GHz, 8.5 GHz] of the quality factor, respectively. Similarly localized states in Fig. 4.4(g)-(i)] are associated to the last local maxima of Q_k in this regime ($\nu \sim 8.8$ GHz).

By going through $\nu_{\text{cut}}(h = 17$ mm), the impact of the dimensionality of the cavity is firstly illustrated at $\nu \sim 9.1$ GHz, where well-spaced eigenmodes with high quality factors ($Q_k \sim 5000$) are found at $h = 13$ mm, while new states with lower quality factors ($Q_k \sim 3000$) emerge for $h = 15$ mm and $h = 17$ mm. In addition, a huge reduction of Q_k is specially observed at $h = 17$ mm with $Q_k \to 0$ at $\nu \sim 9.6$ GHz [see Fig. 4.6(c)]. This is also confirmed by t_0 where a similar behavior is observed in the cases at $h = 15$ mm and $h = 17$ mm in the interval [$\nu \sim 8.9$ GHz, $\nu \sim 9.3$ GHz], followed by a drop at $\nu \sim 9.6$ GHz for $h = 17$ mm. On the other hand, the density of states curves display an increment of the number of modes with respect to h at $\nu \sim 9.2$ GHz ($h = 17$ mm) and $\nu \sim 9.6$ GHz ($h = 15$ mm). The emergence of these peaks as a function of the cavity height is due to the appearance of 3D states which can arise above the cutoff frequency. The cutoff frequencies plotted as black lines in Fig. 4.6 are calculated for an empty cavity, i.e., with an effective refractive index of $n = 1$. The presence of the high-refractive index scatterers in the cavity increases the value of the effective refractive index, and thus decreases the cutoff frequencies explaining the shift of the increment for $h = 15$ mm. The increment in the number of states for $h = 17$ mm together with the reduction of the characteristics decay time t_0 leads to a sudden increase of $\langle g \rangle$ at $\nu \approx 9.6$ GHz. The extended exponential modes shown in the fourth row of Fig. 4.4 [(j)-(i)] correspond to this interval ($\nu \sim 10$ GHz).

For the rest of the measured frequency band (10 GHz $< \nu <$ 15 GHz) and for all values of h, the number of states in the system shows a continuous increment. However, the highest intensity is now found for the curve corresponding to $h = 17$ mm, followed by the case $h = 15$ mm. The expected difference in the intensity of the signal given the height of the cavity is compensated by the new 3D emerging states. In this frequency range, the quality factors present similar behaviours for all h, firstly with values between 1000 and 4000 until dropping to zero at $\nu \sim 10.7$ GHz. At highest energies ($\nu > 11.5$ GHz), an increment in the quality factors from zero to ~ 2000 is noticeable for all values of h. The biggest increment occurs for $h = 13$ mm, and is smaller for the other two heights. This is confirmed by t_0 where the case $h = 13$ mm always presents the highest values in all the interval. In consequence, the Thouless conductance is smaller for $h = 13$ mm, taking values around 1, while other two heights are always > 1. Unfortunately, given the high density of clusters in this region ($\nu > 11$ GHz), single mode cannot be clearly distinguished and separated, hindering their reconstruction with our current tools. Nevertheless, the last row of Fig. 4.4 [(m)-(o)] shows modes around $\nu \sim 10.7$ GHz.

4.3 A new type of localization (in aperiodic systems)

In the previous section, we have shown that even though localization can be achieved in our setup via a disordered array, well-confined modes are truly restricted to 2D geometries. Similarly to the previous section, we study here the modal structure and transport properties of waves in a golden-angle spiral lattice. In order to present all similitudes and differences with respect to the disordered system, we focus first on the case $h = 13$ mm. Figure 4.7 shows the spatial modal structure of three characteristic eigenstates found in the same experimental golden-angle spiral and their corresponding radial decay. Specifically, power-law, exponential, and Gaussian radial decays have been identified by minimizing the sum of the squared residuals.

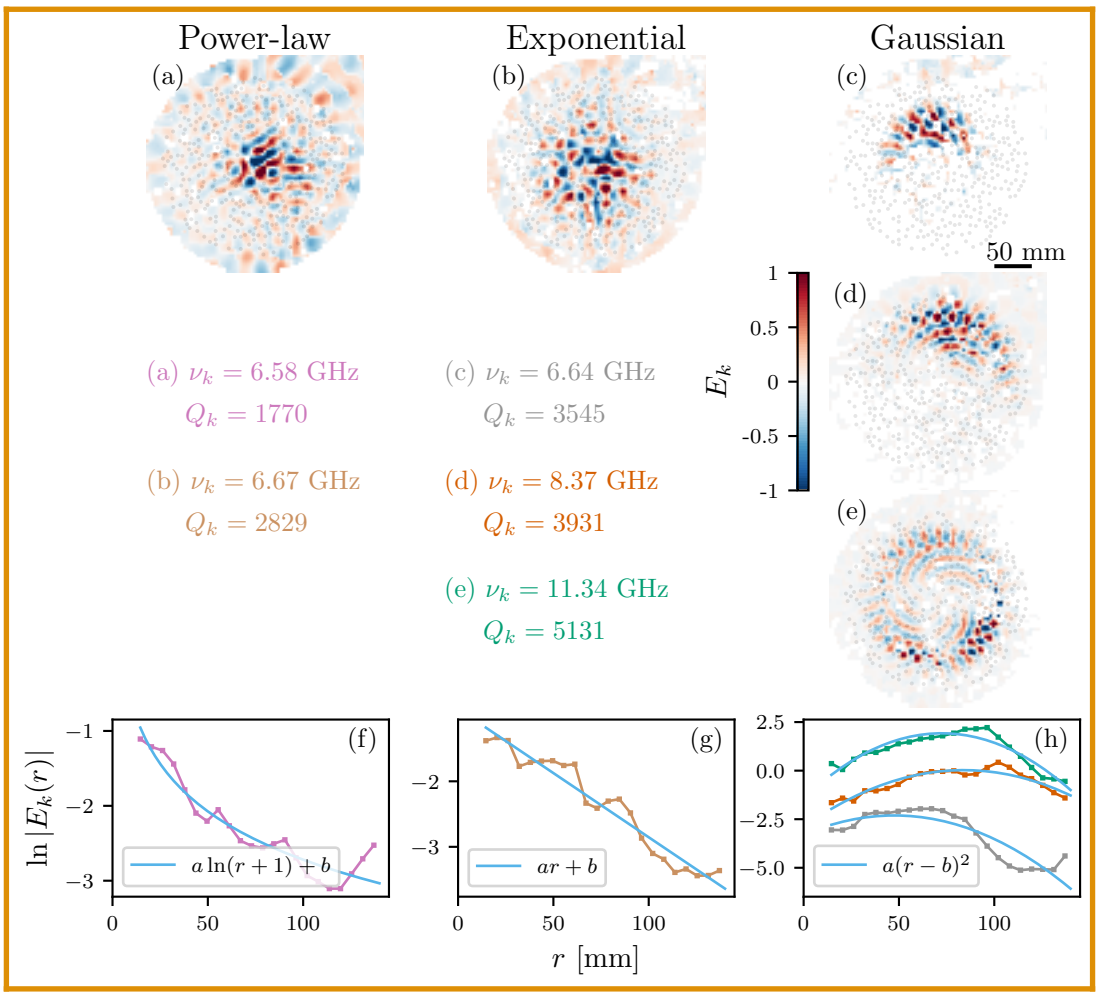

Figure 4.7: Spatial modal structure and radial profile of representative eigenmodes with characteristic [(a) and (f)] power law, [(b) and (g)] exponential, and [(c), (d), (e) and (h)] Gaussian decay. Amplitude maps are normalized such that $\max(|E_\nu|) = 1$. Radial decays (colorfull dots) are obtained by performing an azimuthal average operation where $r = \sqrt{(x+5)^2 + y^2}$, i.e., r is measured from the geometrical center of the spiral and expressed in mm. Different radial decays are discriminated by minimizing the sum of squared residuals.

Our experimental results demonstrate that Vogel spirals support a rich variety of long-lived modes that exhibit different spatial extent and radial decay profiles, hence confirming recent theoretical predictions [142]. This can be contrasted to disordered samples, where (Anderson) localized states are always characterized by an exponential radial decay (see Fig. 4.4). The analyzed long-lived modes found experimentally in this golden-angle spiral sample are distributed in three frequency windows around $\nu \sim 6.6$ GHz (exponential, power-law and Gaussian modes), $\nu \sim 8.3$ GHz and $\nu \sim 11.2$ GHz (Gaussian modes) and are characterized by high quality factors $Q_k = \nu_k/\delta\nu_k$, i.e., low energy-loss ratios. Remarkably, quality factors are of the same order or even larger that those found in the disordered array ($Q_k \sim 5000$). It should be noted that, up to this point, all long-lived modes shown have been found below the 2D cutoff frequency in air ($\nu_{\text{cut}} \approx 11.5$ GHz), so the electromagnetic field is confined in the plane of the array.

4.3.1 2D/3D transition in Vogel spirals

In order to study the effect of the 3D cavity geometry on the golden-angle spiral states, the previous data analysis for transport quantities (of Section 4.2.2) is repeated. We plot the density of Q_k, the characteristic decay time t_0, the DoS, and the average Thouless conductance $\langle g \rangle$ in Fig. 4.8.

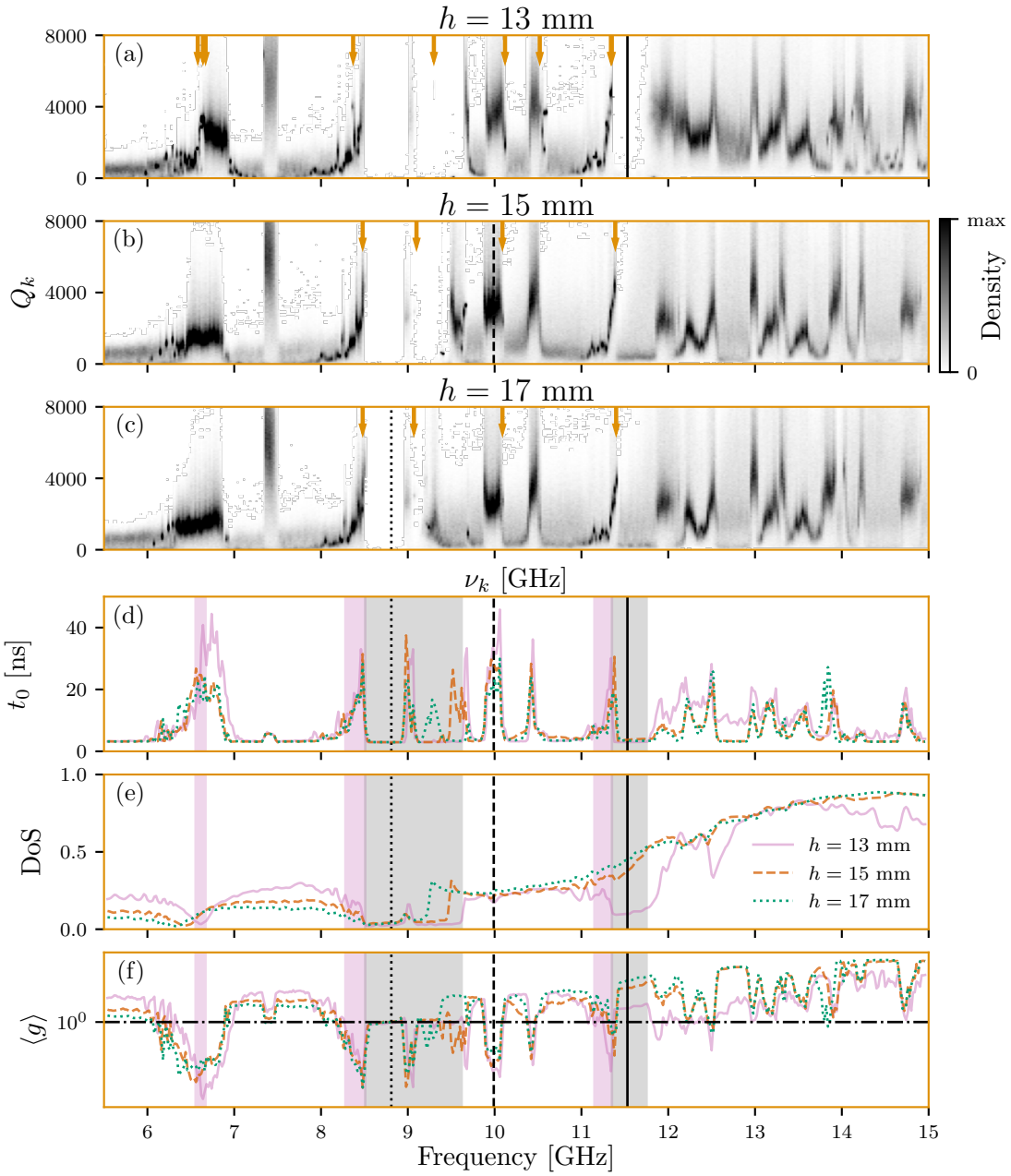

Figure 4.8: Density plots of the quality factors Q_k as a function of the resonant frequencies ν_k extracted via the harmonic inversion with a distance between plates (a) $h = 13$ mm, (b) $h = 15$ mm, and (c) $h = 17$ mm for the golden-angle spiral. Arrows indicate the frequencies of the states presented in Figs. 4.7, 4.9, 4.10 and 4.11. (d) Characteristic decay time t_0 as a function of the frequency. The total frequency range has been mapped by 472 frequency filters spaced by $\Delta f = 0.02$ GHz with $\Delta\omega = 0.01$ GHz. (e) Experimental DoS as a function of the frequency. (f) Experimental Thouless conductance $\langle g \rangle$ as a function of the frequency. The dash-dotted line indicates $\langle g \rangle = 1$. Frequency windows with the analyzed long-lived states (exponential, power-law or Gaussian) or band gaps for the $h = 13$ mm case have been highlighted (violet or grey stripes, respectively). Black vertical lines indicate the cut-off frequency ν_{cut}.

As previously discussed for the disordered array, similarities between the density of Q_k [see Figs. 4.8(a)-(c)] and the characteristic time t_0 [see Fig. 4.8(d)] are observed. Here, t_0-regions corresponding to frequency windows containing exponential, power-law or Gaussian states (pink stripes) are always characterized by high peaks whose maximum values are of the order of those found in disordered systems ($t_0 \sim 40$ ns), while t_0-valleys correspond to short-lived, not spatially localized states or even band gaps.

The existence of band gaps is investigated via the density of states in Fig. 4.8(e), where in contrary to the disordered lattice case, two long flat valleys are identified as band gaps (and highlighted by two grey stripes) for the case $h = 13$ mm. Note that a huge reduction in the number of states is still visible for the disordered system in the frequency region corresponding to the first band gap (8.5 GHz $< \nu <$ 9.1 GHz), and highly confined states belong here (see Figs. 4.4 and 4.6).

It is worth noting that the presence and the width of the band gaps in the golden-angle spiral depends on h. For the first gap (8.5 GHz $< \nu <$ 9.1 GHz), when increasing the height of the cavity, the upper band edge is pushed toward lower frequencies and particularly, in the $h = 17$ mm case, the second half of the band gap almost completely vanishes. As mentioned before, cutoff frequencies plotted as black lines are calculated for an empty cavity, i.e., with an effective refractive index of $n = 1$. Nevertheless, the presence of the high-refractive index scatterers increases the effective refractive index of the cavity, therefore decreasing the cutoff frequencies, and explaining the shifts between the vertical lines and the upper band edges of the first band gaps, specially in the case $h = 15$ mm. Opening the cavity also leads to the emergence of peaks in t_0 and the density of Q_k around $\nu \sim 9.5$ GHz [see Fig. 4.8(a)-(d)], where a monotone decrease of both quantities is recognized with respect to h, giving way to a small negative bump of $\langle g \rangle$. Another consequence is the suppression the second band gap (11.5 GHz $< \nu <$ 12 GHz), which, for $h = 15$ mm and $h = 17$ mm is populated by resonances with low quality factor $Q_k \to 0$ [see Figs. 4.8(a)-(c)] that are attributed to the appearance of new 3D states. These new leaky modes which appear at frequencies much higher than the cut-off frequencies are clearly modes that exist only beyond 2D. Unfortunately, given the large modal overlap regime the reconstruction of the modes is impossible.

4.3.1.1 Spiral defect modes extraction

The peaks at the center of the first gap (8.5 GHz $< \nu <$ 9.1 GHz) are a signature of the lattice's defect modes that are caused by slight scatterers imperfections, i.e. their position depends on the specific location of certain cylinders. For a given golden-angle spiral realization, these peaks stay unchanged when increasing the height of the cavity, keeping similar quality factors and characteristic times for all different values of h ($Q_k \sim 3000$ and $t_0 \sim 30$ ns, respectively). Subsequently, a sharp drop can be observed in the mean Thouless conductance ($\langle g \rangle \sim 10^{-1}$). Fig. 4.9[(a)-(c)] show the reconstruction of the amplitude of three localized defect modes with frequencies $\nu_k \approx 9.2$ GHz for different values of h. Such modes are characterized by the fact that they are supported by a small quantity of cylinders (< 10), and, on the contrary to the states previously studied in those structures (see Fig. 4.7), they are not centered at the center of the spiral. Thus, the radial decay of the correlated fields is computed by angular averaging around the well-defined origin of the spatial autocorrelation (not shown). The corresponding radial decays are plotted in Figs. 4.9[(d)-(f)], showing an almost exponential law in all cases. Instead of the narrow defect peaks observed in the golden-angle spiral ($\nu \sim 9.1$ GHz), the disordered case displays a distributed set of small peaks throughout the same region (8.5 GHz $< \nu <$ 9.7 GHz).

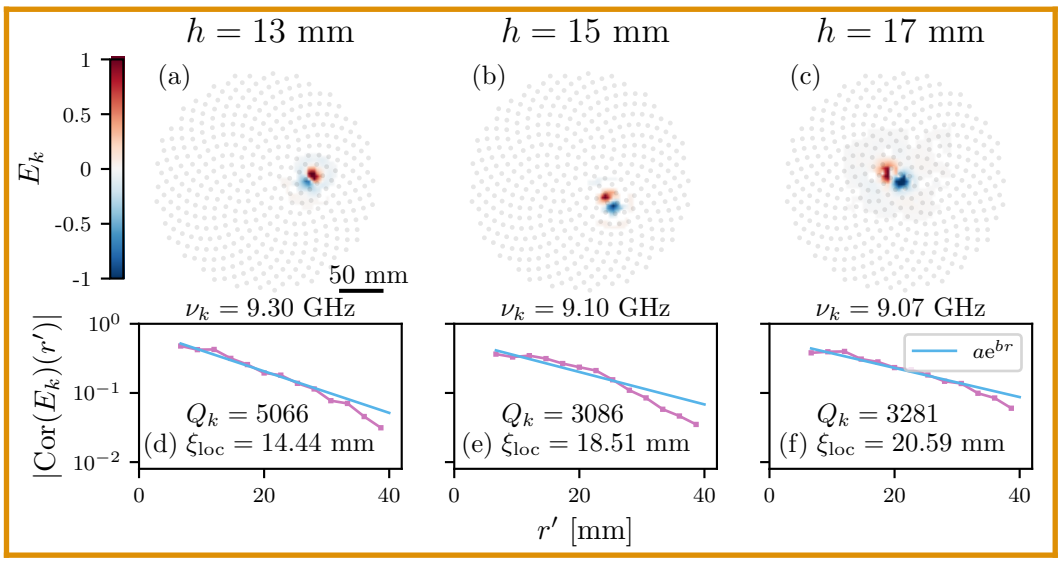

Figure 4.9: Spatial modal structure, and radial profile of the field spatial autocorrelation (not shown) of representative defect eigenmodes in the golden-angle spiral for [(a) and (d)] $h = 13$ mm, [(b) and (e)] $h = 15$ mm, and [(c) and (f)] $h = 17$ mm. Amplitude maps are normalized such that $\max(|E_k|) = 1$. All modal structures are just supported by a few dielectric cylinders. Radial decays (pink dots) are obtained by performing an angular average in the autocorrelation space (r' is measured from the well defined autocorrelation center).

4.3.1.2 Localized Gaussian modes

For $h = 13$ mm, the lower band edges of the two gaps ($\nu \sim 8.3$ GHz and $\nu \sim 11.2$ GHz) are exclusively populated by Gaussian states (see Section 1.2.3.1) characterised by huge quality factors ($Q_k \sim 5000$) and large characteristic decay times ($t_0 \sim 32$ ns) (see Figs. 4.7 and 4.8). Remarkably, the transport analysis reveals certain robustness to the 2D/3D transition. For instance, the density of Q_k and t_0 present identical behaviours with respect to h in both frequency windows. As a consequence, $\langle g \rangle$ still drops by around one order of magnitude, despite the disappearance of the second band gap because of the presence of 3D leaking states.

The presence of long-lived modes previously predicted by the analysis of the density of Q, t_0 and $\langle g \rangle$ is verified by the harmonic inversion/clustering methods. In Fig. 4.10, the spatial structure of six representative Gaussian states populating the band gap edges of the same golden-angle spiral are shown for a cavity characterized by [(a) and (g)] $h = 13$ mm, [(b) and (h)] $h = 15$ mm, and [(c) and (i)] $h = 17$ mm. High quality factors ($Q_k \sim 5000$) confirm the existence of long-lived modes even in the case where the 2D confinement of the electromagnetic field cannot be attributed anymore to the geometry of the cavity. Notably, the mode's shape, frequency, quality factor, and radial decay function remain almost invariant even beyond the 2D threshold, proving the robustness of Gaussian long-lived modes in Vogel spirals against the situation in which the electric field is inhomogeneous in the $\hat{z}$-direction [see Fig. 4.10(g), (h) and (i)].

It was shown that confined Gaussian band edge states result from Bragg scattering in the arms of the spiral given the homogeneity distribution of spacing between neighbouring cylinders [138]. The existence of such modes is attributed to the specific correlations of the cylinder positions in the structure and is predicted to take place for $\rho c_0^2/\nu^2 > 3.5$ ($\nu < 12.9$ GHz in our experimental spiral) [141]. In addition, Figs. 4.8(f) and 4.10 experimentally demonstrate that non-random systems can fulfil the Thouless criterion for Anderson localization, originally conceived to characterize localization in

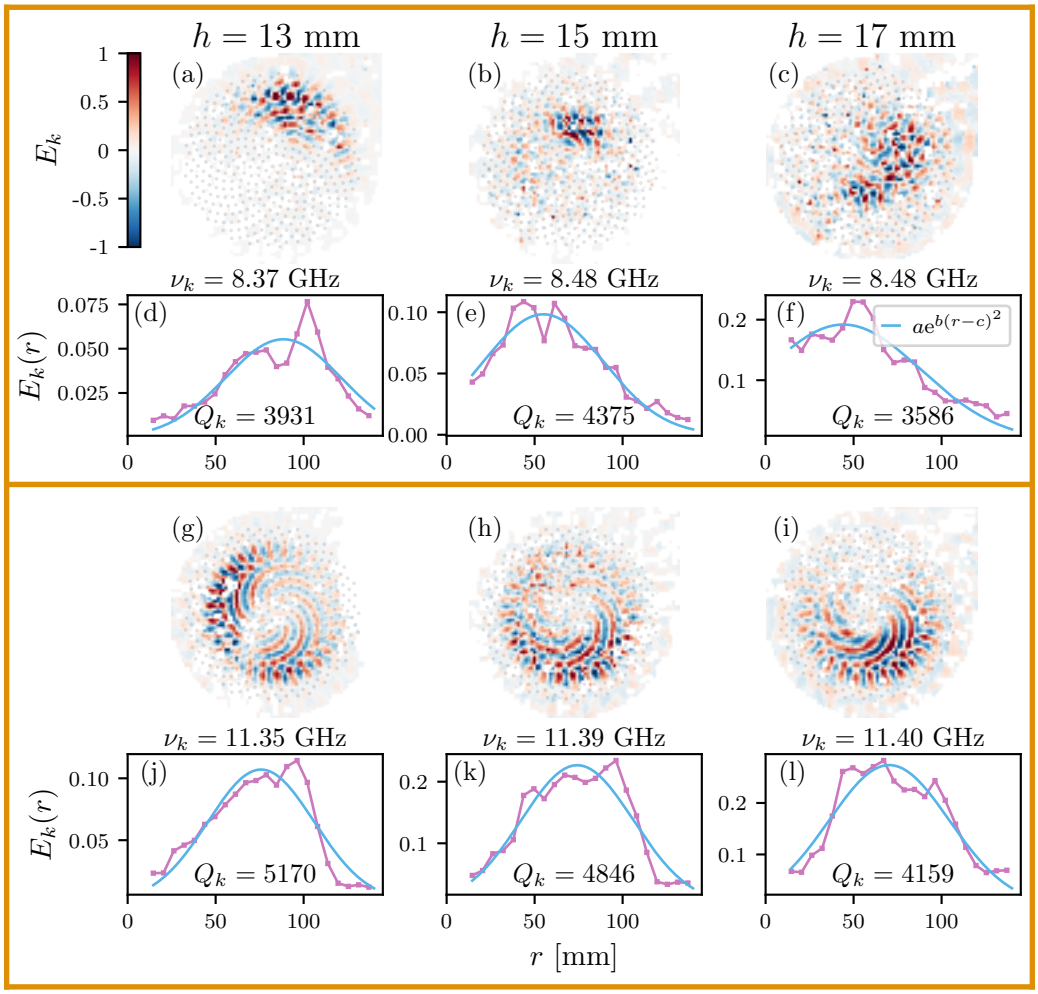

Figure 4.10: Spatial modal structure and radial profile of representative Gaussian eigenmodes for [(a), (d), (g) and (j)] $h = 13$ mm, [(b), (e), (h) and (k)] $h = 15$ mm, and [(c), (f), (i) and (l)] $h = 17$ mm. Amplitude maps are normalized such that $\max(|E_k|) = 1$. Radial decays (pink dots) are obtained by performing an angle averaging where $r = \sqrt{(x+5)^2 + y^2}$ is measured from the center of the spiral and expressed in mm.

disordered structures, confirming theoretical predictions [141]. Our findings confirm that not only eigenmodes characterized by an exponential spatial decay can satisfy the Thouless condition, as it occurs for disordered systems, but also other modes with different spatial decay forms, such as Gaussian and power-law decays. This result demonstrates experimentally the unique modal structure that aperiodic Vogel spirals support, leading to unusual properties of wave transport and localization.

4.3.1.3 Transport in other frequency regimes

For frequencies below the lowest band edge ($\nu < 8.1$ GHz), $Q_k - \nu_k$ maps shows quality factors close to zero over the whole interval except for two frequency windows (see Fig. 4.8). The first interesting interval (6 GHz, 7 GHz) is characterized by a huge decrease of the DoS, and large decay times ($t_0 \sim 30$ ns), giving rise to a drop of the Thouless conductance. Both, the density of Q_k and t_0 also show a monotonic decrease of the bump, together with its widening with respect to h. The localized modes in Figs. 4.7(a)-(c) are found in this frequency window. The second frequency range ($\nu_k \sim 7.4$ GHz) is noted by its huge quality factors ($Q_k \sim 6000$). Nevertheless, the poor characteristic decay times t_0 and a completely flat DoS curve leads to a flat Thouless conductance ($\langle g \rangle > 1$). Additionally,

no confined modes are detected by the harmonic inversion/clustering algorithm in this frequency band. Note that in all this frequency window (5.5 GHz $< \nu <$ 8.1 GHz), all the density of states curves present a similar behavior, being just differentiated by their intensity [see Fig. 4.8(e)]. As mentioned before, this difference is explained by the coupling of the antenna to the electromagnetic field.

In Fig. 4.8, the first band gap is followed by a long frequency region (9.6 GHz $< \nu <$ 11 GHz) with states characterized by low quality factors ($Q_k \to 0$, apart from two bands located around 10 GHz and 10.4 GHz), illustrating a very high loss rate. Note that all DoS curves computed for the three different height keep a constant value all along this interval. As explained previously, this tendency is related to the 3D emerging states that compensate the decrease of the coupling between the antenna and the cavity. The $Q_k - \nu_k$ maps also show two stripes with higher quality factors ($Q_k \sim 2000$) located around $\nu \sim 10.1$ GHz and $\nu \sim 10.4$ GHz that are also robust to the dimensional change. In these two stripes, high characteristic times ($t_0 \sim 35$ ns) promote the drooping of the Thouless conductance, indicating the existence of long-live states. Figs. 4.11[(a)-(c)] present the spatial reconstruction of three representatives modes found at $\nu \sim 10.1$ GHz when $h = 13$ mm, $h = 15$ mm and $h = 17$ mm, respectively. On the other hand, at $\nu \sim 10.4$ GHz our harmonic inversion and clustering algorithms are just able to recover a few states for $h = 13$ mm [see Fig 4.11(d)]. The spatial distributions of states are centered around "defects", instead of the center of the spiral, but in contrary to the modes populating the middle of the first band gap, their spatial extensions occupy the whole measured space. The analysis of the corresponding spatial autocorrelation functions (not shown) leads to radial decay functions that are neither power-law, exponential, nor

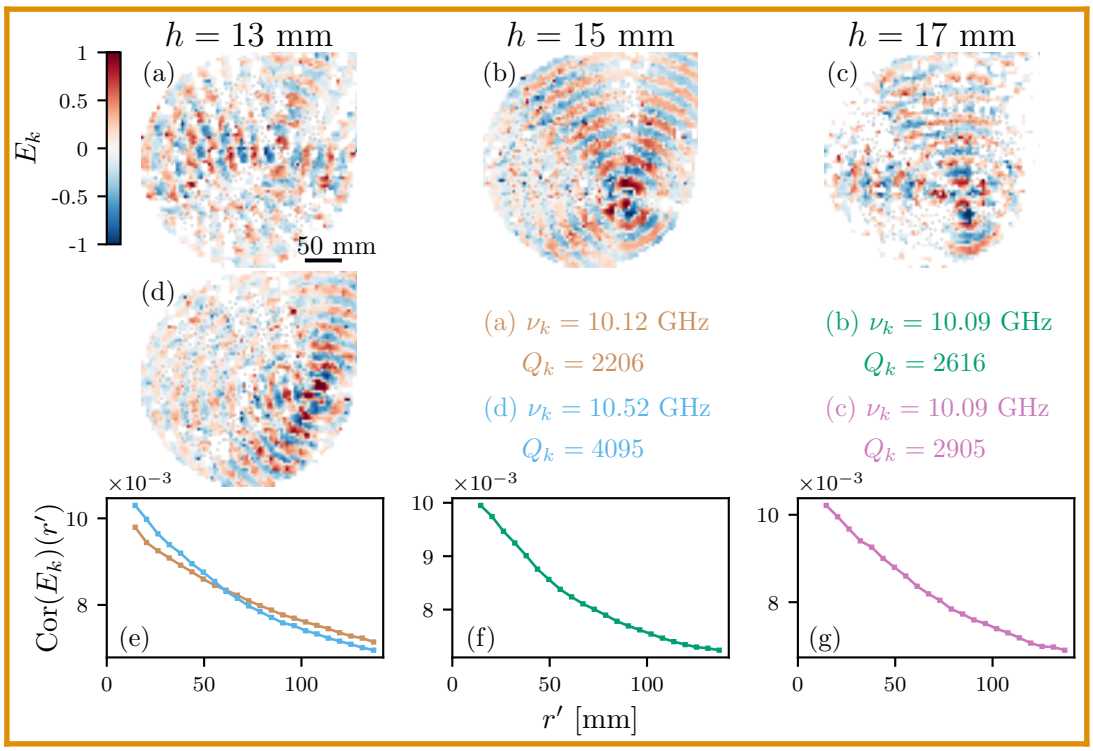

Figure 4.11: [(a)-(d)] Spatial modal structure, and [(e)-(g)] radial profile of the spatial autocorrelation field (not shown) of representative eigenmodes found in the same golden-angle spiral on the 10.1 GHz and 10.4 GHz high-Q bands (see Fig. 4.8). Amplitude maps are normalized such that $\max(|E_k|) = 1$. Radial decays are obtained by performing an angular average in the autocorrelation space (r' is measured from the well defined autocorrelation center).

Gaussian [see Fig. 4.11(e)-(g)]. Given the robustness of these states to the distance between plates, their insensitivity to a complete reconstruction of the spiral with the same sequence of cylinders, and their high quality factors, we think that their nature is related to the imperfections of the cylinders (in size or in dielectric permeability).

Finally, in the frequency region where the three system are 3D ($\nu > 12$ GHz), a sequence of bumps with quality factors $0 < Q_k < 3000$ are recovered by the harmonic inversion. Similarly, the characteristic time is made of valleys and peaks with poor values ($t_0 \sim 15$ ns), that together with the highly populated density of states curves result into high Thouless conductance values ($\langle g \rangle > 1$). Unfortunately, in these 3D situations, the modal overlap obliterates the DoS details, thus making eigenstate reconstruction impossible.

4.3.2 Scaling analysis

The existence of modes with different radial decay behavior in the same system (Vogel spirals) means that these distinct classes of states have different sensitivity to the sample boundaries. As a result, we expect the transport quantities measured in regions where these modes exist to have different evolution when the size of the system is varied. To investigate how the transport quantities as well as the modes are affected by the boundaries of the spiral, the experiment is repeated for 12 different configurations, and for each of them, the number N of cylinders in the array is reduced according to $N = 390 - 34 \times i$ ($i = 0, 1, \cdots, 11$), respectively, as depicted in Fig. 4.12. All samples are characterized by the same scaling factor $a_0 = 6.93$ mm and their centers are always located at $(x, y) = (-5 \text{ mm}, 0)$ where the central antenna (2) sets the origin $(x, y) = (0, 0)$. The distance between plates is fixed as $h = 13$ mm.

In contrast with the measurements presented in the previous sections, we focus here on just two frequency intervals, with $h = 13$ mm. The first one includes various eigenstates with diverse radial decays: exponential, power-law and Gaussian [6.0 GHz,

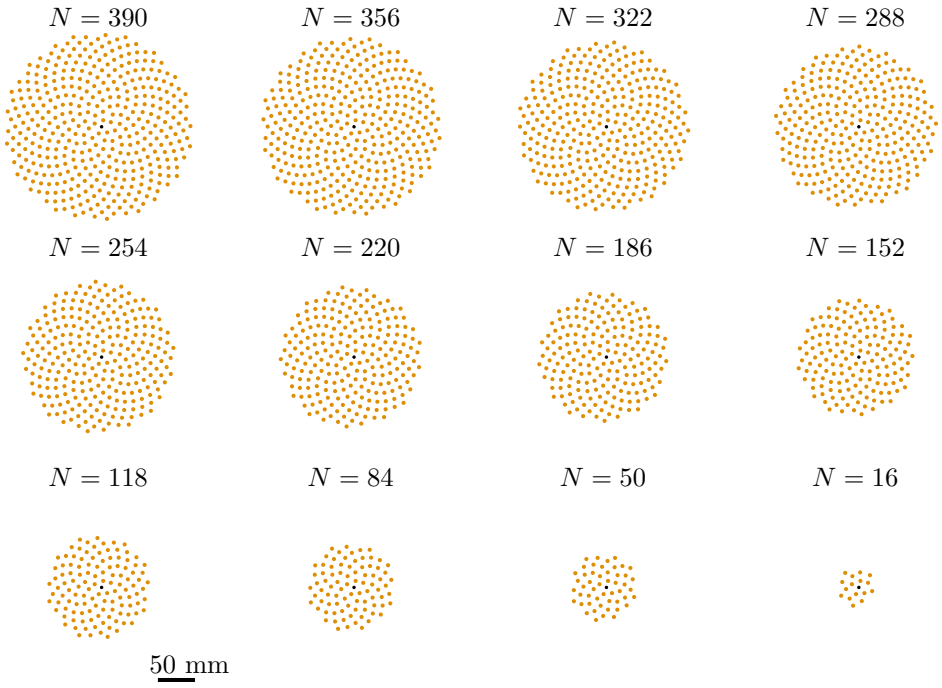

Figure 4.12: Golden-angle spiral arrays consisting of N cylinders created with $a_0 = 6.93$ mm and $\xi = (1 + \sqrt{5})/2$. The black dot sets the position of the fixed antenna (2) with respect to the cylinder pattern.

7.0 GHz] (see Fig. 4.7). The second one contains the Gaussian modes robust to the 2D/3D transition [10.5 GHz, 11.5 GHz] (see Fig. 4.10). The cavity is once again mapped with the 3675 positions shown in Fig. 4.3(a), and both, the reflected and transmitted signals are measured. Subsequently, the data analysis is carried out analogously to preceding experiments (see Section 4.1.3).

The spatial structure of three different eigenmodes with characteristic (a) power-law, (b) exponential, and (c) Gaussian decays found by the harmonic inversion/clustering methods are shown in Fig. 4.13. Note that below a certain threshold N [(a) $N \simeq 84$, (b) $N \simeq 186$, (c) $N \simeq 288$], the number of resonances recovered by the harmonic inversion is found to be insufficient to form a cluster and subsequently to reveal the spatial structure of the modes. Here the leaking of the wave out of the spiral is due to the absence of certain cylinders needed to support the long-lived modes. For example, the power-law and exponential modes [see Fig. 4.13(a) and (b), respectively] cannot be recovered by our analysis whenever the typical system size becomes smaller than the noticeable modal size when $N \simeq 84$ and $N \simeq 186$, respectively. At higher frequency, Gaussian modes are found to have larger sizes, and are therefore more sensitive to changes in the system boundaries, then they only exist for large systems $N \geq 288$.

In Fig. 4.14, we show as a function of the number of cylinders and frequency, [(a) and (e)] the mean quality factor $\langle Q \rangle_{f_0}$, where $\langle \cdot \rangle_{f_0}$ represents the average over a frequency interval $[f_0 - \Delta\omega, f_0 + \Delta\omega]$, [(b) and (f)] the characteristic decay time t_0, [(c) and (g)] the normalized density of states, and [(d) and (h)] the average Thouless conductance $\langle g \rangle$ in two frequency windows containing the analyzed long-lived modes (from 6.0 to 7.0 GHz and from 10.5 to 11.5 GHz) for $h = 13$ mm. Around ~ 6.6 GHz, Fig. 4.14(a), (b) and (d) show that the localization signatures earlier analyzed (high values of t_0 and $\langle Q \rangle$, and $\langle g \rangle < 1$) remain unperturbed even for lattices with a reduced number of cylinders $N \simeq 84$, while Fig. 4.12(c) shows that the density of states start to lose its structure and becomes

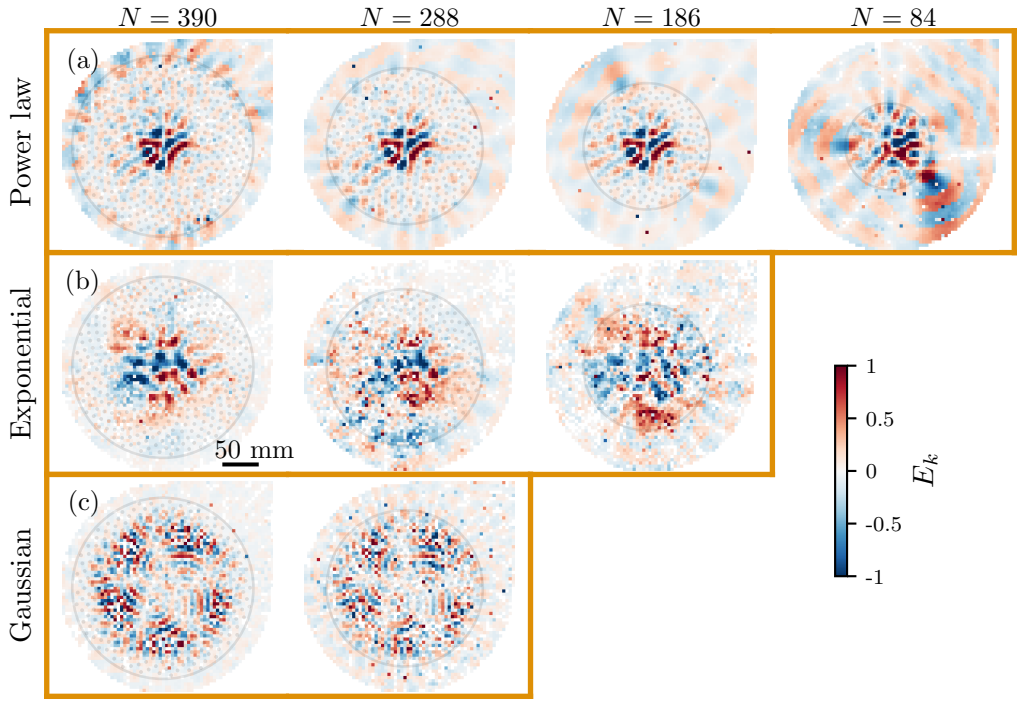

Figure 4.13: Spatial modal structure as a function of the number of cylinders of modes with (a) power-law ($\nu = 6.586$ GHz), (b) exponential ($\nu = 6.646$ GHz), and (c) Gaussian ($\nu = 11.357$ GHz) radial decay. The grey circles show the boundary of the samples.

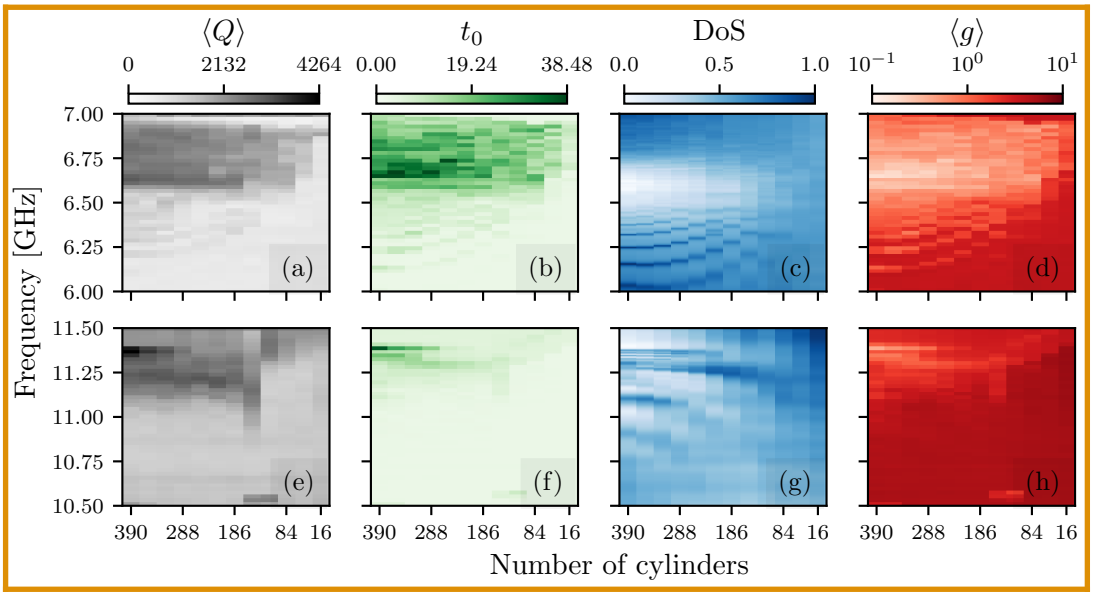

Figure 4.14: [(a) and (e)] Mean quality factor $\langle Q \rangle_{f_0}$ computed via the harmonic inversion. [(b) and (f)] Characteristic decay time t_0 as a function of the frequency and of the number of cylinders. The total frequency range has been mapped by 47 frequency filters spaced by $\Delta f = 0.02$ GHz with $\Delta\omega = 0.01$ GHz. [(c) and (g)] Experimental normalized density of states (DoS). [(d) and (h)] Experimental Thouless conductance $\langle g \rangle$.

flat below $N \simeq 152$. This is in agreement with the smallest system size able to support power-law and exponential states found in Fig. 4.13(a) and (b). Note that the localization signature coincides with the drop in the density of states, confirming the absence of a band gap in this frequency region. At high frequencies ($\nu \sim 11.3$ GHz), the same localization features are observed to disappear around $N \simeq 288$. This value of N also determines a critical size above which Gaussian modes can exist [see Fig. 4.13(c)]. Despite the fast decrease of high t_0 and $\langle Q \rangle$ values with respect to N, the DoS remains unperturbed even for smaller systems ($N \simeq 186$), where the band gap starts to be populated by leaky states [see Figs. 4.6(f) and (g)].

4.3.3 Robustness of localization to spatial modification of the lattice

Now that the existence of long-lived modes in Vogel Spirals has been proven to be robust to the 2D/3D dimensional transition (see Section 4.3.1), we can follow the same methodology used to perform the scaling analysis (see Section 4.3.2) to analyze the variation of the same transport quantities ($\langle Q \rangle$, t_0, DoS and $\langle g \rangle$), as well as the eigenmodes of the system with respect to different "alterations" of the structure. Specifically, we study the effect of either dislocations, scars or spatial disorder in the lattice.

Firstly, to investigate the consequences of dislocations in the system, the golden-angle spiral experiment is repeated for 6 different configurations, each of them being characterized by $390 - M$ cylinders, respectively. Differently to the scaling experiments, the cylinders are removed randomly as depicted in Fig. 4.15(a). Then, the effect of opening scars in the system is examined by repeating 5 times the experiment, now considering different golden-angle spiral arrays whose number of cylinders is given by $390 - 13 \times S$. To remove the cylinders, a preferred angle is chosen randomly in the interval $[0, 2\pi]$, then 13 random cylinders are discarded in order to create a path from the origin to the edge of the spiral as shown in Fig. 4.15(b). Finally, positional disorder

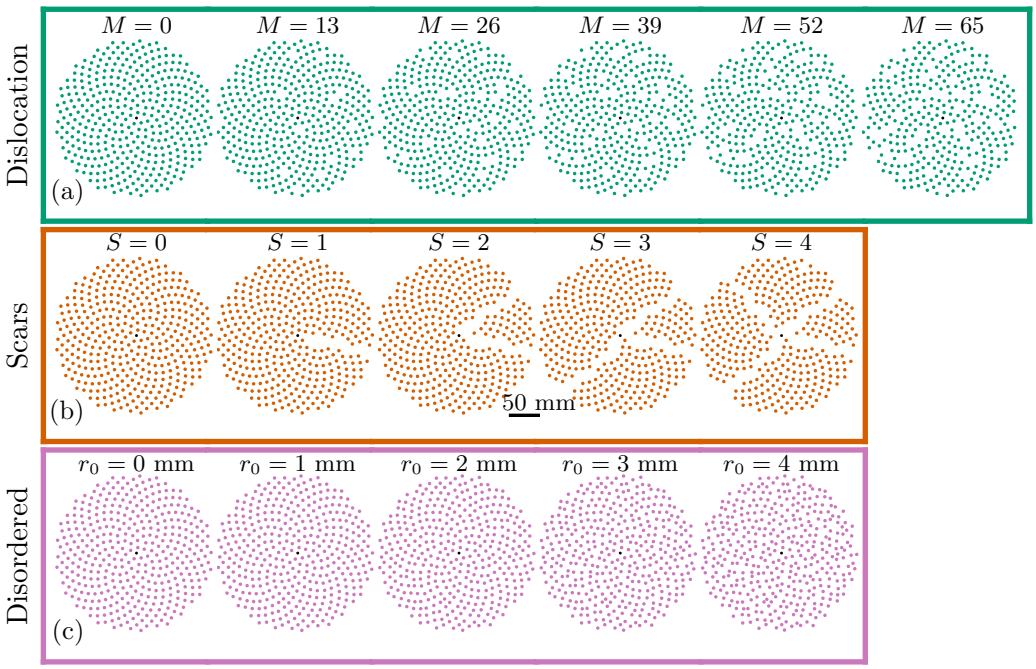

Figure 4.15: (a) Golden-angle spiral arrays consisting of $N = 390 - M$ cylinders. Cylinders are randomly removed to study the effect of dislocations. (b) Golden-angle spiral arrays consisting of $N = 390 - S \times 13$ cylinders. Cylinders are randomly removed to study the effect of scars. (c) Golden-angle spiral arrays consisting of $N = 390$ cylinders, the position of the cylinders is randomly displaced over a distance $r_{0,i}$ mm (given by a uniform random variable in the interval $[0, r_0]$) in a direction determined by the angle $\theta_{0,i}$ (which is also random) from its original position. The black dot sets the position of the fixed antenna (2) with respect to the point pattern.

is considered by randomly changing each cylinder position. The position of the cylinder i is moved by a distance $r_{0,i}$ (given by a uniform random variable in the interval $[0, r_0]$) in a direction determined by the angle $\theta_{0,i}$ (given by another random variable in $[0, 2\pi]$) from its original position [see Fig. 4.15(c)]. Note that the minimum distance between two scatterers in the most disordered case ($r_0 = 4$ mm) is 6.528 mm, and can be compared with the one corresponding to the disordered system in Section 4.2 (6.25 mm).

For all experiments performed in this section, the samples are always characterized by $a_0 = 6.93$ mm, their geometrical center is located at $(x, y) = (-5 \text{ mm}, 0)$ where the central antenna (2) sets the origin $(x, y) = (0, 0)$, and the distance between plates is fixed at $h = 13$ mm. As in the previous section, experiments are carried out with a focus on only two frequency intervals ([6.0 GHz, 7.0 GHz] and [10.5 GHz, 11.5 GHz]). Both, the reflected and transmitted signals are then measured using the same map displayed in Fig. 4.3(a). Finally, the data analysis is achieved identically to preceding experiments (see Section 4.1.3).

4.3.3.1 Dislocations

In Fig. 4.16, we plot three eigenstates characterized by different decay laws [(a) power-law, (b) exponential and (c) Gaussian] and their evolution with respect to the number of missing scatterers in the lattice M. Additionally, the quality factor average $\langle Q \rangle$, the characteristic decay time t_0, the density of states, and the mean Thouless conductance $\langle g \rangle$ are depicted as a function of the frequency and number of cylinders for both frequency intervals in Figs. 4.16[(d) and (h)], [(e) and (i)], [(f) and (j)] and [(g) and (k)], respectively.

Notably and despite the deformation of the states, the power law mode is found to survive even when $\sim 15\%$ of the scatterers have been randomly removed. Similarly, the

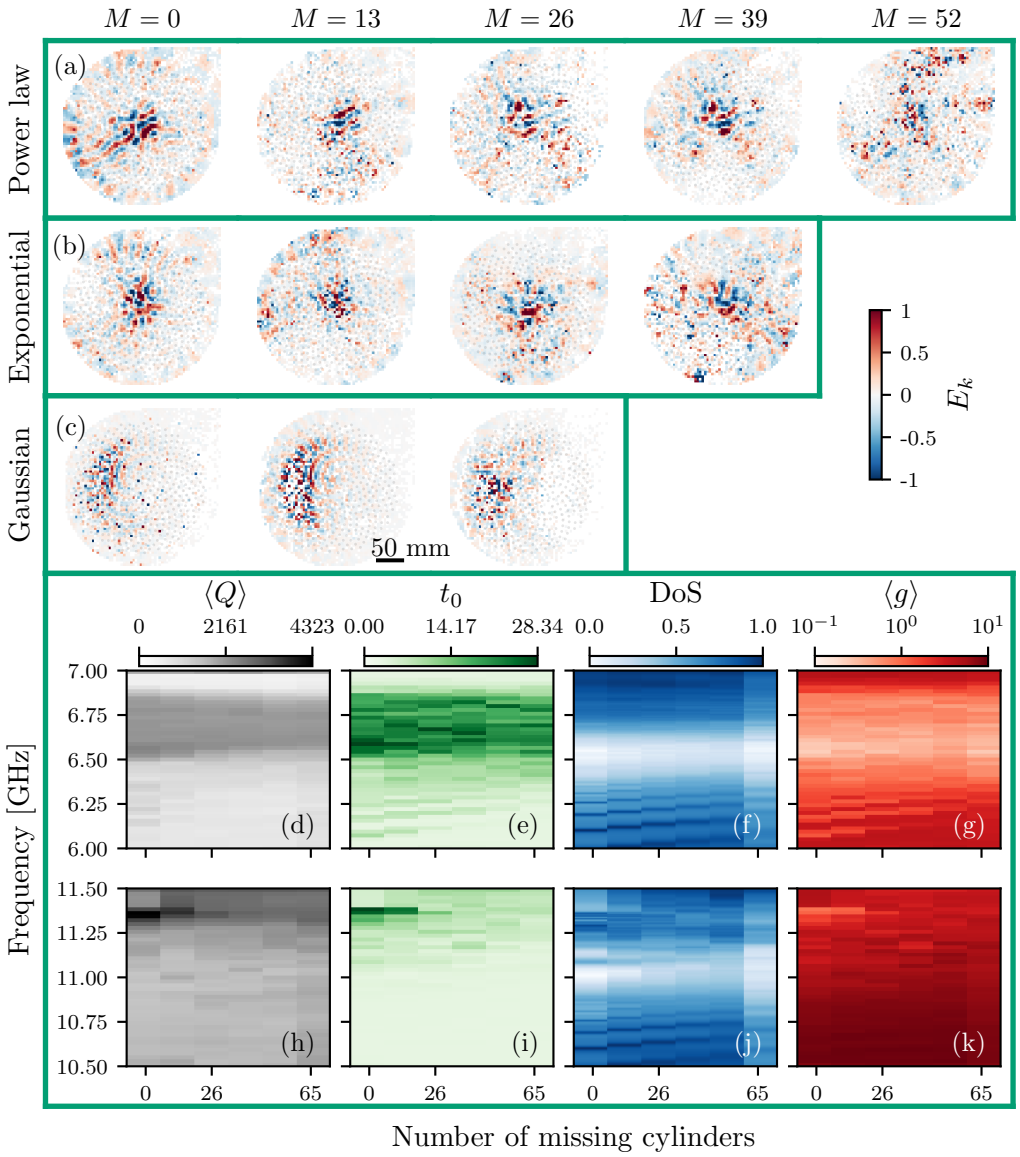

Figure 4.16: Spatial modal structure as a function of the number of dislocations of modes with (a) power-law ($\nu = 6.517$ GHz), (b) exponential ($\nu = 6.522$ GHz), and (c) Gaussian ($\nu = 11.366$ GHz) radial decay. [(d) and (h)] Mean quality factor $\langle Q \rangle_{f_0}$ computed via the harmonic inversion. [(e) and (i)] Characteristic decay time t_0 as a function of the frequency and of the number of cylinders. The total frequency range has been mapped by 47 frequency filters spaced by $\Delta f = 0.02$ GHz with $\Delta\omega = 0.01$ GHz. [(f) and (j)] Experimental normalized density of states (DoS). [(g) and (k)] Experimental Thouless conductance $\langle g \rangle$.

exponential state is still detected by the clustering algorithm for systems with $M \lesssim 39$. However, the harmonic inversion procedure faces a considerable increase in the amount of noise in both cases, making the reconstruction of the exponential state impossible when $M \gtrsim 52$. These findings are in agreement with the transport quantities [see Figs. 4.16(d)-(g)] which show localization signatures [high values of $\langle Q \rangle$ (~ 3000), and t_0 (~ 30 ns) together with low values of $\langle g \rangle (\sim 10^{-1})$] in the whole "dislocation range" studied. Note that the density of states keeps it shape for all values of M in this case. At high frequency (10.5 GHz $< \nu <$ 11.5 GHz), localization is only identified ($\langle Q \rangle \sim 4000$, $t_0 \sim 30$ ns and $\langle g \rangle \sim 10^{-1}$) for low-dislocated systems ($M \lesssim 13$). This value also coincides with the disappearance of the band gap. Nevertheless, the harmonic inversion/clustering methods are still able to find the selected Gaussian mode when $M = 26$. Remarkably, the exponential and power-law are less sensitive to the random dislocations with respect to the Gaussian mode.

4.3.3.2 Scars

The evolution of the spatial modal structure of three characteristic states, each one characterized by a different radial decay, is plotted as a function of the number of scars in Figs. 4.17(a)-(c). At low frequency (6.0 GHz $< \nu <$ 7.0 GHz), both power-law and exponential modes [see Figs. 4.17(a) and (b)] are proven to survive even when the system is affected by four scars ($S = 4$). However, the presence of the scars promotes the leakage of the states through them, thus deforming the modes and their radial decays (that are not claimed anymore to be power-law nor exponential at this point). In contrast, Fig. 4.17(c) shows a Gaussian state at high frequency ($\nu_k \approx 11.365$ GHz) whose spatial structure cannot be clustered as soon as the system is affected by four scars ($S \lesssim 4$). Despite the presence of two scars, the Gaussian mode keeps the same shape being just slightly deformed. The deformation of the state then increases, and eventually the mode disappears ($S = 3 \rightarrow S \gtrsim 4$).

Figs. 4.17{[(d), (e), (g)], [(h), (i), (k)]} depict the mean quality factor $\langle Q \rangle$, the characteristic decay time t_0, and the average Thouless conductance $\langle g \rangle$ for low and high frequencies, respectively. In agreement to previous findings, localization signatures can be observed ($\langle Q \rangle \sim 2500$, $t_0 \sim 30$ ns and $\langle g \rangle \sim 10^{-1}$) for all values of S at low frequencies (6.0 GHz $< \nu <$ 7.0 GHz). In addition, the density of states in this frequency range keeps its shape when opening each of the four scars [see Fig. 4.17(f)]. On the other hand, at high frequency (10.5 GHz $< \nu <$ 11.5 GHz), the disappearing of localization marks is seen for system with more than three scars ($S \gtrsim 3$). This coincides with the increase of short-lived modes in the band gap, making it disappear [see Fig. 4.17(j)].

4.3.3.3 Positional disorder

As in previous sections, Figs. 4.18(a), (b) and (c) show the evolution of three states with different radial decay behaviour (power law, exponential and Gaussian, respectively), but now when increasing the positional disorder in the point pattern. The three states keep their shape at low disorder strength ($r_0 = 1$ mm), however, they are highly deformed for $r_0 = 2$ mm, and in the case of the exponential mode, they cannot be found by the harmonic inversion/clustering algorithms from this point onwards. By increasing the disorder strength ($r_0 = 3$ mm) both states (power-law and Gaussian) present a huge deformation from their original shape. At this point, one can see how the Gaussian mode starts to be pushed towards the center and the edge of the lattice, abandoning the inhomogeneous region previously identified by Liew et al. [138] [see Fig. 1.19]. Analogously, the power-law mode is also displaced from the center of the spiral becoming comparable to the eigenmodes found in the Anderson case (see

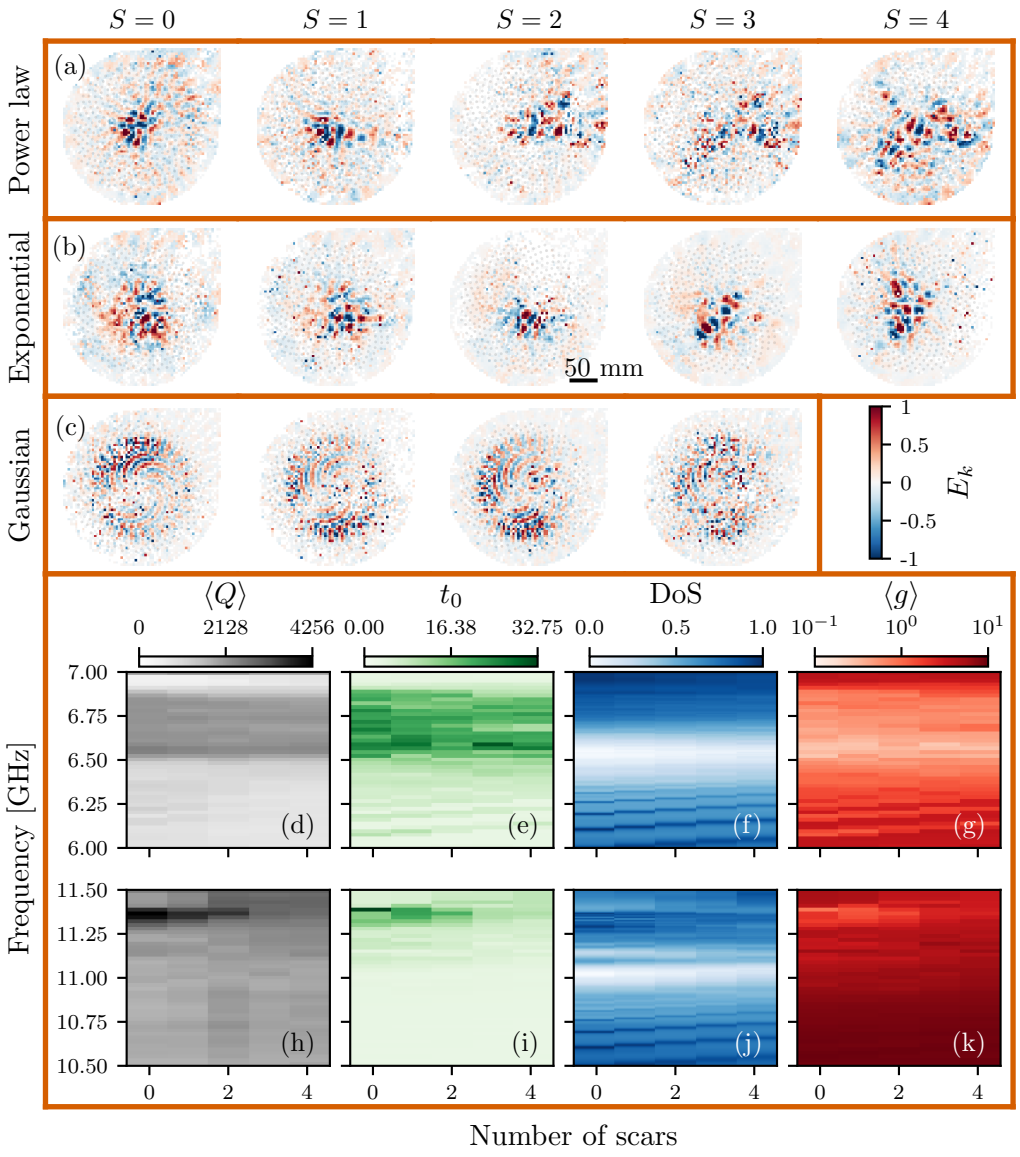

Figure 4.17: Spatial modal structure as a function of the number of scars of modes with (a) power-law ($\nu = 6.536$ GHz), (b) exponential ($\nu = 6.569$ GHz), and (c) Gaussian ($\nu = 11.365$ GHz) radial decay. [(d) and (h)] Mean quality factor $\langle Q \rangle_{f_0}$ computed via the harmonic inversion. [(e) and (i)] Characteristic decay time t_0 as a function of the frequency and of the number of cylinders. The total frequency range has been mapped by 47 frequency filters spaced by $\Delta f = 0.02$ GHz with $\Delta\omega = 0.01$ GHz. [(f) and (j)] Experimental normalized density of states (DoS). [(g) and (k)] Experimental Thouless conductance $\langle g \rangle$.

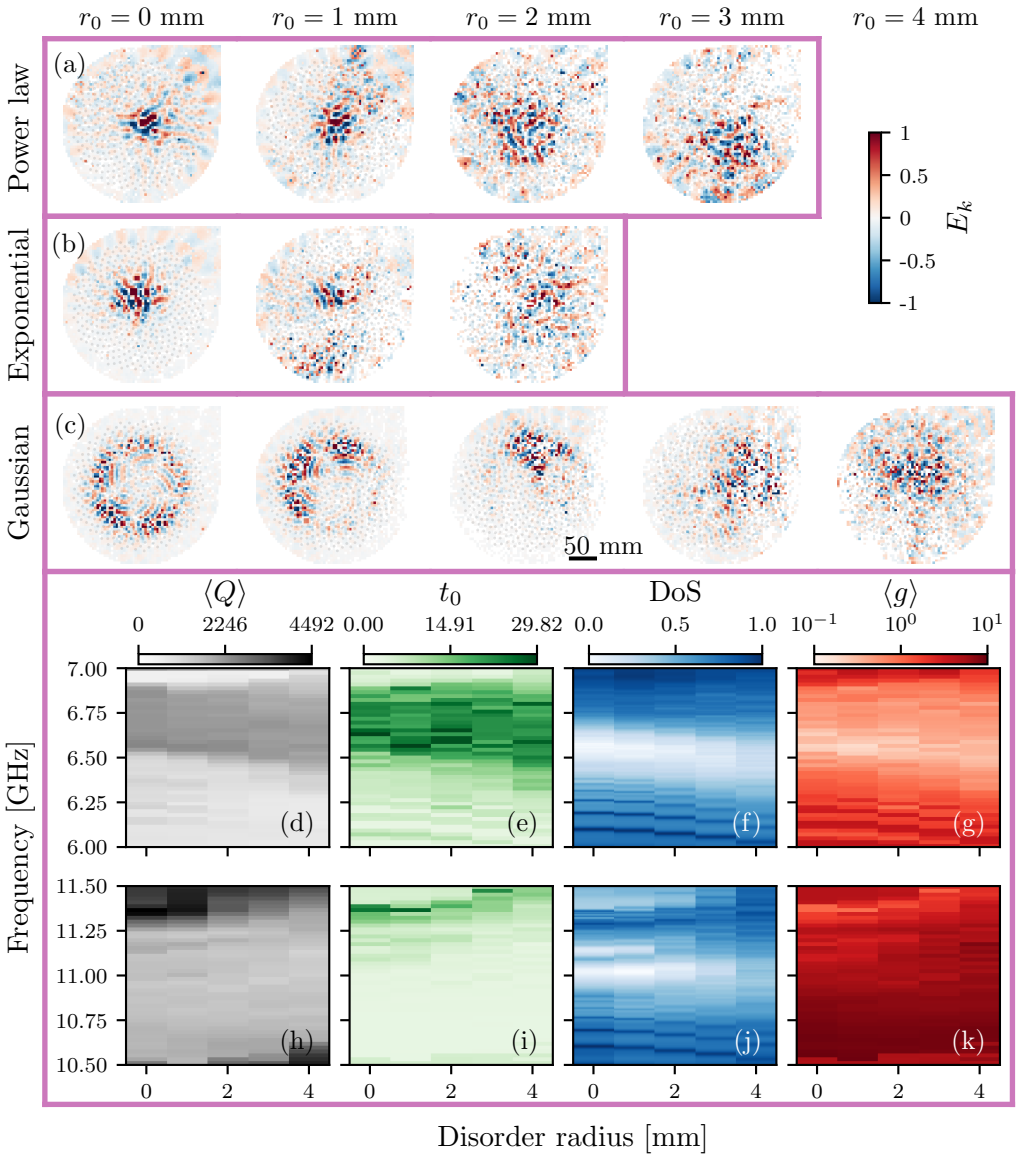

Figure 4.18: Spatial modal structure as a function of the disorder strength of modes with (a) power-law ($\nu = 6.546$ GHz), (b) exponential ($\nu = 6.570$ GHz), and (c) Gaussian ($\nu = 11.341$ GHz) radial decay. [(d) and (h)] Mean quality factor $\langle Q \rangle_{f_0}$ computed via the harmonic inversion. [(e) and (i)] Characteristic decay time t_0 as a function of the frequency and of the number of cylinders. The total frequency range has been mapped by 47 frequency filters spaced by $\Delta f = 0.02$ GHz with $\Delta\omega = 0.01$ GHz. [(f) and (j)] Experimental normalized density of states (DoS). [(g) and (k)] Experimental Thouless conductance $\langle g \rangle$.

Section 4.2). Beyond this point, the strong deformation of the power law state prevents its identification by the clustering method. Finally, for the strongest disorder ($r_0 = 4$ mm) just the "Gaussian" mode can be followed by our algorithms. Nevertheless, and identically to the power-law state, its shape seems now to correspond to the one of an Anderson disordered system instead (see Section 4.2).

Figs. 4.18(d)-(k) shows the transport quantities ($\langle Q \rangle$, t_0, the DoS, $\langle g \rangle$) for both frequency windows. At low frequency (6.0 GHz $< \nu <$ 7.0GHz), localization signs [high $\langle Q \rangle$, t_0 and low $\langle g \rangle$, see Figs. 4.17(d), (e), and (g), respectively] are present all along the disordered strength values, showing even the widening of this region going from 0.3 GHz for $r_0 = 0$ mm to 0.7 GHz for $r_0 = 4$ mm. Note that the sharp reduction in the DoS [see Fig. 4.17(f)] is slightly displaced when adding the disorder, having its center at $\sim$ 6.6 GHz for $r_0 = 0$ mm and at $\sim$ 6.4 GHz for $r_0 = 4$ mm. Nevertheless, its width seems to be robust with respect to the disorder strength, having only a small increase of the number of states for $r_0 = 4$ mm. At high frequencies (10.5 GHz $< \nu <$ 11.5GHz), localization signatures disappear for $r_0 = 3$ mm. However, the density of states keeps its shape through all disordered strengths. Figs. 4.18(d)-(k) demonstrate previous observations, where 3D localization is originated by the specific correlations of Vogel spirals and it disappears when considering random point patterns. In contrast, localization signatures below the purely 2D limit survive in the disordered system or in the golden-angle spiral.

Finally, we compute the radial decays of the "power law" and "Gaussian" states found in the disordered golden-angle spiral when $r_0 = 3$ mm and $r_0 = 4$ mm, respectively. As previously mentioned, both modes display features comparable with those of Anderson eigenstates, e.g., the separation of the center of the mode and the center of the structure (see Section 4.2). Fig. 4.19 depicts the spatial structure of the two [(a) "power law" and (b) "Gaussian"] modes and the corresponding radial decay of the corresponding spatial autocorrelation function [(c) and (d), respectively]. At this stage, the original radial characteristics of both modes have been clearly replaced by those of exponential Anderson

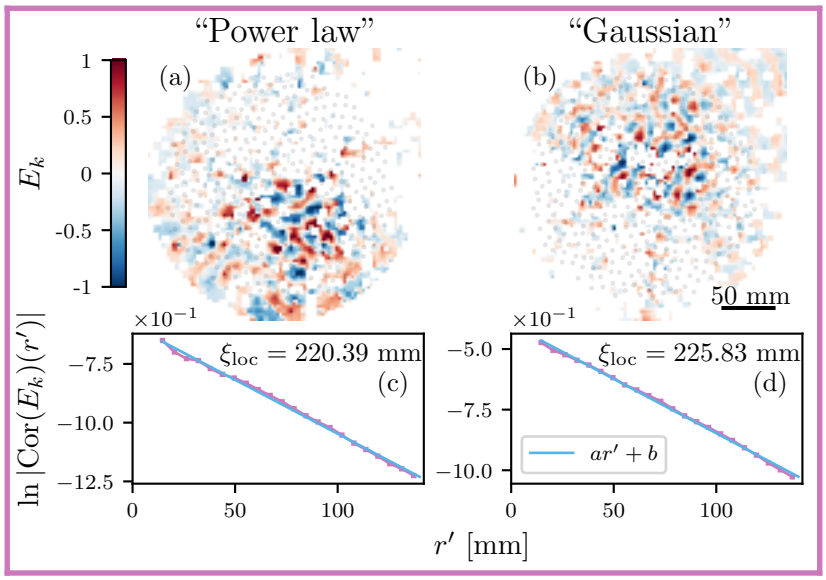

Figure 4.19: Spatial modal structure and radial profile of the spatial autocorrelation field (not shown) of the modes with [(a)-(c)] power-law, and [(b)-(d)] Gaussian radial decay depicted in Fig. 4.18 for $r_0 = 3$ mm and $r_0 = 4$ mm, respectively. Amplitude maps are normalized such that $\max(|E_k|) = 1$. Radial decays are obtained by performing an angular average in the autocorrelation space (r' is measured from the well defined autocorrelation center).

states, presenting in the two cases an exponential radial decay. However, the extraction of the localization lengths shows that both states are still delocalized [$\xi_{\text{loc}} > R_0$ ($R_0 \approx$ 140 cm)] and can leak out of the structure.

4.4 Conclusion

Microwaves experiments play an important role in the understanding of how spatial correlations can enhance or halt electromagnetic transport [87]. In this Chapter, we use the well-controlled experimental setup consisting of microwaves propagating through lattices composed of dielectric Mie scatterers, in a metallic cavity of variable height presented in Chapter 2. The simplicity of our platform allows us to efficiently study different kind of arrays such as disordered structures or aperiodic lattices with up to $\sim$ 400 scatterers. Reflected and transmitted complex fields are emitted and detected by two straight antennas at the center of the structures and at the center of the top plate constituting the cavity. The cavity is mapped in frequency and space with a high degree of accuracy thanks to the VNA and to the fact of having a movable top plate and therefore a movable antenna. Another feature of this versatile experimental setup is the ability to control the distance between the two plates, thus breaking the translation invariance in the $\hat{z}$-direction, and studying the wave propagation in the system beyond the pure 2D limit, differently to previous experiments [81]. Following the data acquisition, the features of the temporal evolution of a wave-packet as well as the properties of the resonances of the system are extracted via the Fourier transform and the harmonic inversion/clustering methods, both applied to the transmission spectra. Similarly, the density of states can be obtained directly from the reflection measurement.

The above experimental data analysis allows us to experimentally reveal the spatial modal structure supported by quasi-two-dimensional arrays of dielectric cylinders placed according to an aperiodic Vogel spirals and a traditional disordered point pattern, and its impact on wave transport. At different frequency, and by varying the distance between both plates, we investigate the behavior of the electromagnetic resonances as the system undergoes a 2D-3D crossover. Our findings show that Vogel spirals support a unique modal structure where long-lived modes with different radial decay types (exponential, power-law and Gaussian) coexist, confirming recent theoretical predictions [142]. This contrasts with disordered lattices, where eigenmodes always exhibit exponentially decreasing radial profiles. In particular, we not only disclose the huge difference in the shape of the eigenmodes corresponding to each structure and their radial decays, but also the robustness of Gaussian modes against varying the dimensionality of the cavity, while typical exponential disordered states are not spatially confined at high frequency where the cavities are not longer 2D.

We also investigate the impact of the peculiar modal structure of Vogel spirals on microwave transport properties by means of the temporal evolution of the energy as well as the characteristic decay time t_0 (related with the average resonance width $\langle \delta\nu \rangle$), the density of states, and the Thouless conductance. This analysis reveals that Vogel spirals exhibit very slow energy dynamics. Indeed, we show that in frequency windows containing long-lived modes, the values of t_0 are similar to those found in the Anderson localized regime in traditional 2D disordered systems. In these same frequency windows, the Thouless criterion for Anderson localization is shown to be fulfilled despite the lack of disorder and the presence of non-exponentially localized modes. Using this transport analysis, we confirm that long-lived modes supported by Vogel spirals are robust against the change in the dimensionality of the cavity, from 2D to 3D, so that they remain essentially unperturbed and preserve their transport features even when the homogeneity of the electric field in the $\hat{z}$-direction is broken. Finally, by taking advantage of the

versatility of our system, we explore the evolution of the unique modal structure of the golden-angle spiral and the corresponding transport quantities with respect to the size of the system, as well as to their robustness to different alterations of the point pattern. Particularly, we analyzed the behaviour of the characteristic power law, exponential and Gaussian states with respect to dislocations, scars and positional disorder.

In summary, without disorder, our results embark on the long-standing quest for Anderson localization of 3D light, which turns out to be very difficult in uncorrelated disordered systems [21, 25]. Altogether we provide a full description of the experimental details that allowed us to experimentally demonstrate the existence of robust localization of microwaves in Vogel spirals, paving the way for a broader application of such structures.

5

Helical edge states

Como cualquier divinidad:
irá al destierro quién se
atreva a negar su luz,
y será hereje él que no
quiera comulgar en su altar.
Cuarteto de Nos (Maldito show)

Contents

This Chapter is dedicated to experimentally investigate the existence of helical edge-states generated in systems with a nontrivial topological behavior and characterized by the Z_2 invariant. By using our experimental setup in the tight-binding limit, we design dielectric arrays following the Wu-Hu model [156, 157], which allows to mimic a nontrivial topological quantum system with spin. The Chapter is organized as follows: In Section 5.1, we start by introducing the details on the design of the dielectric lattices used in our experiments, as well as the technicalities of the experimental performance and the data analysis. This last one is carried out by means of the harmonic inversion/clustering methods, used to retrieve the individual eigenmodes of the system, and the computation of the circular transmission, that allows to measure directly the pseudospin channels. Results are presented in Section 5.2, where we first show how certain deformations of the dielectric arrays lead to the opening a topological gap dwelt by edge states. The last two parts of the section are devoted to demonstrate the unidirectional counterpropagative features of the helical modes that propagate along the boundary of the topological nontrivial material. It is important to point out that, despite the quality and quantity of the achieved results, this chapter is still a preamble to new topological studies and is therefore shorter than the previous chapters.

5.1 Experimental arrays and data analysis

We experimentally investigate 2D triangular lattices of lattice parameter $a_0 = 30$ mm, with a hexagonal elementary motif of radius R [see Fig. 5.1(a)]. Each honeycomb-like structure consist of $N = 384$ dielectric cylinders (see Section 2.2) placed into the experimental cavity presented in Section 2.1. The electromagnetic field is induced and measured by two loop antennas placed at the centers (1) of the movable top plate and (2) of the bottom plate. As explained in Section 2.1.2, loop antennas induce a TE polarization whose non-propagative cutoff frequency is given by $\nu_{\text{cut}} = \mathrm{c}_0/(2h)$, where c_0 is the speed of light in air and h is the distance between both plates. Our experiments are carried out by fixing the distance between plates as $h = 13$ mm, and using a frequency range [7.1 GHz, 7.7 GHz] with a frequency step of 100 kHz, corresponding to wavelengths in the range [39 mm, 42 mm]. Therefore, electromagnetic waves in the TE polarization cannot propagate and a tight-binding model is built on the first TE resonance (see Section 2.2.1.2).

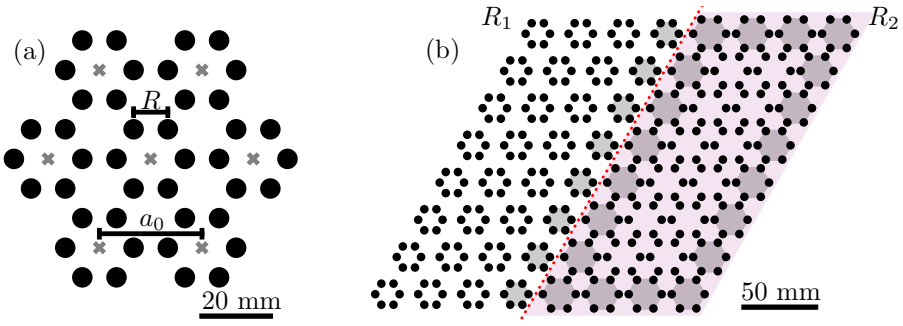

Figure 5.1: (a) 2D honeycomb array constructed from a triangular lattice with lattice parameter $a_0 = 30$ mm (grey crosses) made of artificial hexagonal atoms of radius $R = 10$ mm. (b) Honeycomb-like lattice consisting of $N = 384$ cylinders with a rhomboidal shape characterized by $a_0 = 30$ mm, $R_1 = 8.5$ mm and $R_2 = 11.5$ mm. Hexagonal cells in the edge of the nontrivial structure are highlighted in grey. The area corresponding to the nontrivial structure is highlighted in pink. The red dotted line represents the interface between both media.

5.1.1 Topological lattice design

As previously discussed in Section 1.3.2, the parameter R allows to deform the honeycomb-like lattices without altering the hexagonal clusters, thus preserving the C_6 rotational symmetry [156]. This fact allows to open a nontrivial topological gap by choosing $3R < a0$, or a trivial gap for $3R > a_0$; $a_0 = 3R$ forming the critical case of a perfect, non-gaped, honeycomb lattice. Since the pseudo time-reversal symmetry, and therefore the pseudospin channels, are based on the C_6 symmetry, deformations breaking the crystalline periodic order mix the pseudospin channels, destroying the helical states. Nevertheless, it has been shown that the topology remains valid when considering small deformations [157].

Our structures are planned to have an interface separating two different media: one of them displaying trivial features [characterized by $R_1 \lesssim 10$ mm] and the second one with a nontrivial topological character [described by $R_2 \gtrsim 10$ mm]. By considering this constraint, the dielectric arrays are designed with a regular rhomboidal shape divided into two rhomboidal substructures [see Fig. 5.1(b)]. This choice prevents the formation of edge-states in the absence of deformation [188], and maximizes the length of the interface between two sufficiently bulky structures. In Fig. 5.1(b), the nontrivial topological structure has been highlighted in pink and the hexagonal cells belonging to its edge are highlighted in grey. Note that, given the radius of the experimental cylinders (= 3 mm) and the thickness of the placing metallic tube (~ 0.25 mm), the values of the radius R_1 (R_2) are experimentally restricted to the interval [6.25 mm, 11.87 mm], allowing us to experimentally study the interplay between both trivial and nontrivial topological regimes.

5.1.2 Experimental realization

We study the behaviour of the interface states as a function of the cell radius using 11 different lattices characterized by $R_2 = 10 + i \times 10^{-1}$ mm ($i = 0, 1, \cdots, 10$) and $R_1 = 20$ mm $- R_2$. Given the mixture of the two pseudospin channels in the absence of the C_6 symmetry, and their unidirectional counterpropagation, it is possible to isolate each propagating helical state along the whole interface by changing the position of the lattice with respect to the fixed exciting antenna (2). In that way, each honeycomb-like configuration is scanned twice, where the fixed antennas are placed at the top and at the bottom of the interface between both structures [blue and golden dots in Figs. 5.2(a) and (b), respectively]. Specifically, the exciting antennas are always located at 7.5 mm from the center of the two closest cylinders on the topological side.

Due to the confinement of the electromagnetic waves inside the cylinders, each configuration is mapped by placing the movable antenna (1) over every single resonator. Therefore the scanning map identically corresponds to the map of the cylinder positions [see e.g. Figs. 5.2(a) and (b)]. At each resonator position, the VNA registers both the complex transmitted and reflected signals [$S_{21}(\nu)$ and $S_{11}(\nu)$, respectively]. For instance, Figs. 5.2[(c)-(e)] show the intensity of the two measured signals, $|S_{11}|^2$ (purple line) and $|S_{11}|^2$ (orange line), at three different positions for the "top-antenna-lattice" in Fig. 5.2(a), which is characterized by $R_1 = 9.5$ mm and $R_2 = 10.5$ mm. The three panels present measurements taken on a cylinder belonging to the nontrivial topological edge, the nontrivial topological bulk, and the trivial bulk [red, green and indigo dots in Fig. 5.2(a), respectively]. Low transmission and reflection values are due to the weak coupling regime between the antenna and the field.

According to Section 2.4.6, the orange curves in Figs. 5.2[(c)-(e)] approximate the local density of states at different positions in the weakly coupled antenna regime. Therefore, reflection values close to 1 (and fading transmission values) reveal the existence of band

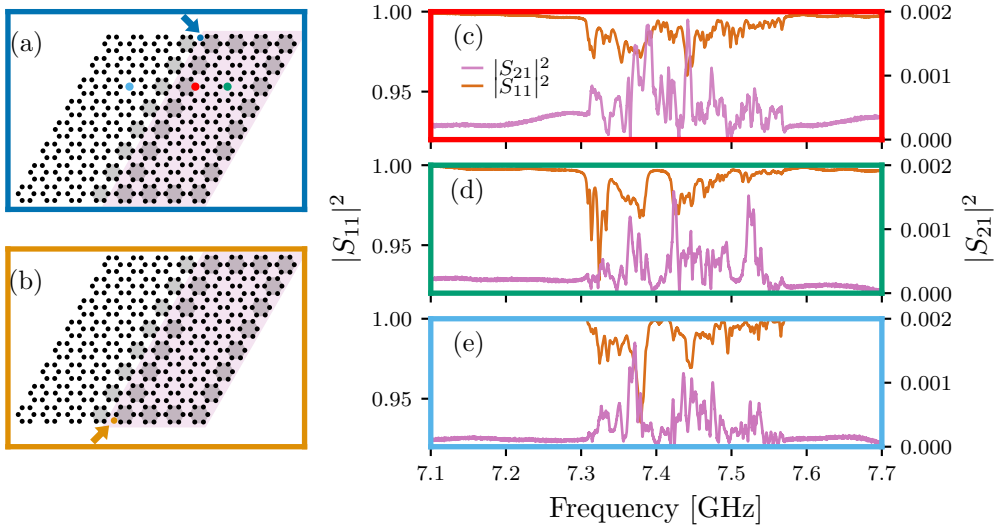

Figure 5.2: [(a)-(b)]Diagram of a honeycomb-like lattice consisting of $N = 384$ cylinders with a rhomboidal shape characterized by $a_0 = 30$ mm, $R_1 = 9.5$ mm and $R_2 = 10.5$ mm. Blue and golden dots represents the position of the fixed antenna with respect to the array. Hexagonal cells in the lattice edge are highlighted in grey. The area corresponding to the nontrivial structure is highlighted in pink. Red, green and indigo dots in (a) indicate the positions corresponding to signals in (c), (d) and (e), respectively. Reflected $|S_{11}(\nu)|^2$ (orange line) and transmitted coefficients $|S_{12}(\nu)|^2$ (purple line) in a cylinder placed at (c) the nontrivial edge, (d) the nontrivial bulk and (e) the trivial bulk.

gaps. Particularly, a frequency window with these features is observed around 7.4 GHz for measurements taken in both bulk regions [see Figs. 5.2(d) and (e)]. On the contrary, no band gap is identified for the signal registered in the edge of the nontrivial topological structure [see Fig. 5.2(c)]. According to the bulk-edge correspondence [see Section 1.3.1], the topological order of structures with not-vanishing topological invariants always leads to spatially confined edge-states with frequencies occupying the band gap.

Out of the band gaps, the transmitted signal is a superposition of peaks related to the resonances of the system, thus it can be analyzed by means of the harmonic inversion/clustering methods (see Sections 2.4.2 and 2.4.3). The harmonic inversion is implemented by dividing the complex transmission spectrum into two frequency intervals: [7.2 GHz, 7.45 GHz] and [7.4 GHz, 7.65 GHz], where the 0.5 GHz overlap prevents to be spoiled by spurious resonances generated by the filtering. Additionally, it is known from the tight-binding theory that the number of resonances carried by the system is fixed to $N = 386$, thus we choose $2K = 400$ in each interval. After the extraction of the resonance parameters by the harmonic inversion, we cluster the amplitudes of the same resonance at different positions to recover the map of the magnetic field amplitude $B_k(x, y)$ of each eigenmode in the lattice [81].

Besides to the eigenmode reconstruction, the transmitted signal $S_{21}(\nu)$ also gives access to the pseudospin channels by quantifying the circular transmission as a function of time in a hexagonal cell. This is achieved by computing the dynamics carried by a certain set of modes through the cylinder l, given as

$$S_{21}^{f_0,\Delta\omega}(l,t) = \mathcal{F}\left\{S_{21}(l,\nu) \times F^{f_0,\Delta\omega}(\nu)\right\}, \tag{5.1}$$

with $\mathcal{F}\{\cdot\}$ the Fourier transform and $F^{f_0,\Delta\omega}(\nu)$ a bandpass filter centered in f_0 and characterized by a bandwidth $\Delta\omega$ (see Section 2.4.5). Then, the energy flux between two resonators (l and m), that are separated by a distance d_{lm}, can be approximated by

discretizing the Poynting vector as [162, 189]

$$T = \mathrm{Im}\{B_{\hat{z}}^{*}\nabla_{x,y}B_{\hat{z}}\} \;\rightarrow\; T_{lm}^{f_0,\Delta\omega}(t) = \mathrm{Im}\left\{\frac{\left[S_{21}^{f_0,\Delta\omega}(l,t)\right]^{*} S_{21}^{f_0,\Delta\omega}(m,t)}{d_{lm}}\right\}, \tag{5.2}$$

where we have taken into account the TE polarization and $B_{\hat{z}} \propto S_{21}$ (see Section 2.4). Note that the Poynting vector [left hand side of Eq. (5.2)] has a one-to-one correspondence to the current density computed in Ref. [157]. Finally, for a hexagonal cell α centered in $\mathbf{r}_\alpha$, the circular transmission as a function of time is written [190]

$$C_{\alpha}^{f_0,\Delta\omega}(t) = \frac{1}{L_\alpha}\sum_{l,l+1\in\alpha} T_{l,l+1}^{f_0,\Delta\omega}(t)\mathrm{sgn}\left[(\mathbf{r}_l - \mathbf{r}_\alpha)\times(\mathbf{r}_{l+1} - \mathbf{r}_\alpha)\right], \tag{5.3}$$

where $L_\alpha = \sum_{l,l+1\in\alpha} d_{l,l+1}$, $\mathrm{sng}(\cdot)$ gives the sign of its argument, and $\mathbf{r}_l$ and $\mathbf{r}_{l+1}$ are the positions of the cylinders l and $l+1$, respectively.

To extract the circular transmission from our experimental data, we focus on the frequency interval around the gap observed in Figs. 5.2(d) and (e) [7.36 GHz, 7.46 GHz], which is mapped by 41 uniform distributed Hanning filters characterized by $\Delta\omega = 0.01$ GHz (see Section 2.4.5). Each cell is then labelled in an anti-clockwise sense as indicate in Fig. 5.3, where the arrows define the turning sense of the positive current, allowing to write Eq. (5.3) as

$$C_{\alpha}^{f_0,\Delta\omega}(t) = \frac{1}{L_\alpha}\sum_{l,l+1\in\alpha} T_{l,l+1}^{f_0,\Delta\omega}(t). \tag{5.4}$$

In the following section, we analyze the existence of nontrivial topological band gaps, and the emergence of edge states as a function of the cell deformation through the eigenfunctions and the density of states, which is directly computed from the reflected measured signal as $\mathrm{DoS} = 1 - \langle\mathrm{Re}\{S_{ii}(\mathbf{r},\nu)\}\rangle$. Later on, we use Eq. (5.4) to characterize the helical edge states as a function of time, of the frequency and of the cell radius.

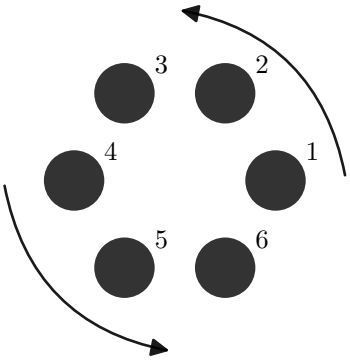

Figure 5.3: Diagram of a hexagonal cell. Arrows define the turning sense of the positive energy flow.

5.2 Helical edge states

We start our study by analyzing the behavior of the density of states as a function of the frequency and R_2, obtained using Eq. (2.60) when averaging over all the measured sites [see DoS in Fig. 5.4(a)]. For a lattice without deformation ($R_1 = R_2 = 10$ mm) around $\nu \sim 7.4$ GHz, a reduction in the number of states carried by the system is

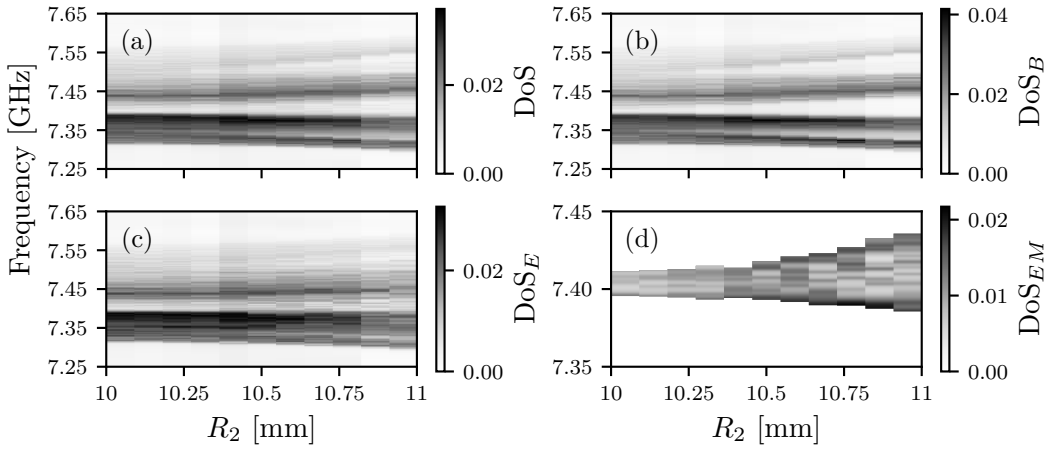

Figure 5.4: Experimental Density of States as a function of the frequency and the radius of the cell R_2 computed by averaging (a) all the measured sites, (b) only the bulk sites, and (c) only edge sites. (d) Experimental density of states computed by averaging only the edge sites, in frequency regions where $\mathrm{DoS}_B < 0.01$.

observed, indicating a Dirac point. As predicted [156, 157], increasing R_2 (and reducing R_1), removes the Dirac point and separates the bands, resulting in a wide frequency region with a poor, or even null, density of states [see Fig. 5.4(a)].

To visualize better the low density-state regime ($\nu \sim 7.4$ GHz), note that Eq. (2.60) allows to compute a "partial" density of states by averaging only over certain positions in the lattice. For instance, Figs. 5.4(b) and (c) depict the density of states carried by sites exclusively belonging to the bulk or the edge, labeled as DoS_B and DoS_E, respectively. Similar to DoS, DoS_B shows a decrement of the number of modes around $\nu \sim 7.4$ GHz, denoting the presence of a band-gap for $R_2 \gtrsim 10.2$ when excluding the structure edge. On the contrary, Fig. 5.4(c) exhibit a well populated frequency band for all frequencies and all R_2 values, showing the existence of states that live exclusively in the edge of the structure and whose eigenfrequencies are precisely in the band gap.

To validate previous findings, the spatial distribution of the eigenmodes around $\nu \sim 7.4$ GHz is recovered using the harmonic inversion/clustering methods and then plotted in

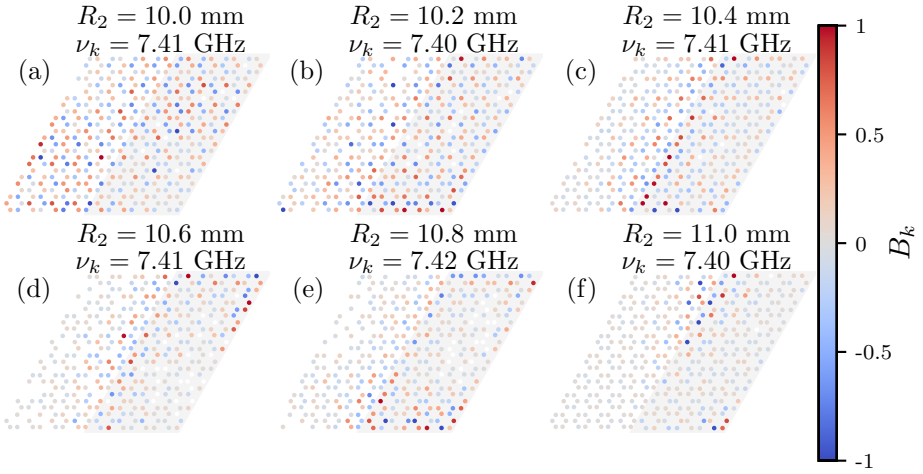

Figure 5.5: Spatial modal structure of representative modes found in our set of honeycomb-like lattices with different values of R_2. Amplitude maps are normalized such that $\max(|B_k|) = 1$. The area corresponding to the nontrivial structure is highlighted in grey.

Fig. 5.5 for different values values of R_2. Close to the honeycomb limit ($R_2 \leq 10.2$ mm), the eigenmodes recovered by our algorithms are always well extended in the whole sample [see Figs. 5.5(a) and (b)]. On the contrary, when increasing the radius of the cells ($R_2 > 10.2$ mm), the eigenstates are pushed towards the edge of the nontrivial structure, being mainly distributed along the "trivial-nontrivial" interface, with a weaker extension in "air-nontrivial" edge [see Figs. 5.5(c)-(f)]. Following the bulk-edge correspondence, the modes are exclusively confined along the edge nontrivial topological structure.

As shown in Fig. 5.5(a), non-topological modes can be spatially distributed along the edge. As a consequence, their contribution to DoS_E is still visible in Fig. 5.4(c), i.e. integrating over the sites located at the interface does not reflect exclusively the modes in the band gap. To isolate the effect of edge-states in the gap, in Fig. 5.4(d) we plot DoS_E in regions fulfilling the condition $\mathrm{DoS}_B < 0.01$, showing a gradual increment of states as well as an increase of the gap width with R_2. Complementary to Figs. 5.4(c) and 5.5, Fig. 5.4(d) validates previous the statements about the emergence of states living in the structure edge and populating the band gap when increasing the radius of the hexagonal cells.

5.2.1 Helical propagation patterns

In order to show the pseudospin polarization of the interface modes, we use Eq. (5.4) to compute the circular transmission in all hexagonal cells for a given lattice at a given frequency window f_0. The *time-integrated pattern* $\bar{C}$ of a lattice is calculated by integrating the circular transmission of every hexagonal cell in the time domain. For instance, Fig. 5.6 displays eight different patterns of $\bar{C}$ obtained by changing the position of the fixed antenna, the radius of the cells, and the frequency of the exciting pulse f_0 (see Section 2.4.5). Due to the strong coupling between the two antennas when they are close together, the signals measured at the two hexagons closest to the fixed antenna is strongly perturbed, and therefore they have been removed from our analysis.

As one can observe, for both values of R_2, Figs. 5.6(a), (c), (e) and (g) demonstrate the existence of well defined unidirectional circular energy flows which are extended along the whole trivial-nontrivial interface. More surprising are the patterns displayed in Fig. 5.6(b) and (d), which show circular currents along the air-nontrivial edge. As previously stated by Wu and Hu [156, 157], since the time-reversal symmetry rely on the C_6 rotational symmetry, the breaking of the crystalline structure, and therefore of the time-reversal symmetry, mixes the two pseudospin channels hampering helical propagation. Nevertheless, as observed in Figs. 5.6(b) and (d), our tight-binding experimental system seems to be robust and efficient with respect to the abrupt crystalline breaking, allowing the helical propagation in the air-nontrivial edge.

By increasing the cell radius, one can observe that the propagation in the air-nontrivial edge tends to disappear [see Figs. 5.6(f) and (h)]. Differently, helical modes in the trivial-nontrivial interface keep their shape even for the largest hexagonal radius studied ($R_2 = 11$ mm). Note that the disparity in the boundary conditions of the nontrivial structure leads to a frequency difference between both unidirectional patterns for the same sample [see e.g. Figs. 5.6(a) and (b)]. In consequence, counterpropagative helical states can be isolated in frequency, or in space by changing the antenna position with respect to the dielectric structure [see e.g. Figs. 5.6(a) and (c)].

As observed from Fig. 5.6, thanks to the versatility of our experimental platform, propagating helical states can be properly isolated and therefore, controlled. To gain more intuition about this phenomenon, in Fig. 5.7 we plot the global polarization of the system $\langle \bar{C} \rangle$, which is computed by averaging the pattern $\bar{C}$ over all the hexagonal cells in the structure. Particularly, Fig. 5.7 shows $\langle \bar{C} \rangle$ in a lattice with the exciting loop antenna in its bottom part, however an analogous result is obtained by changing the antenna

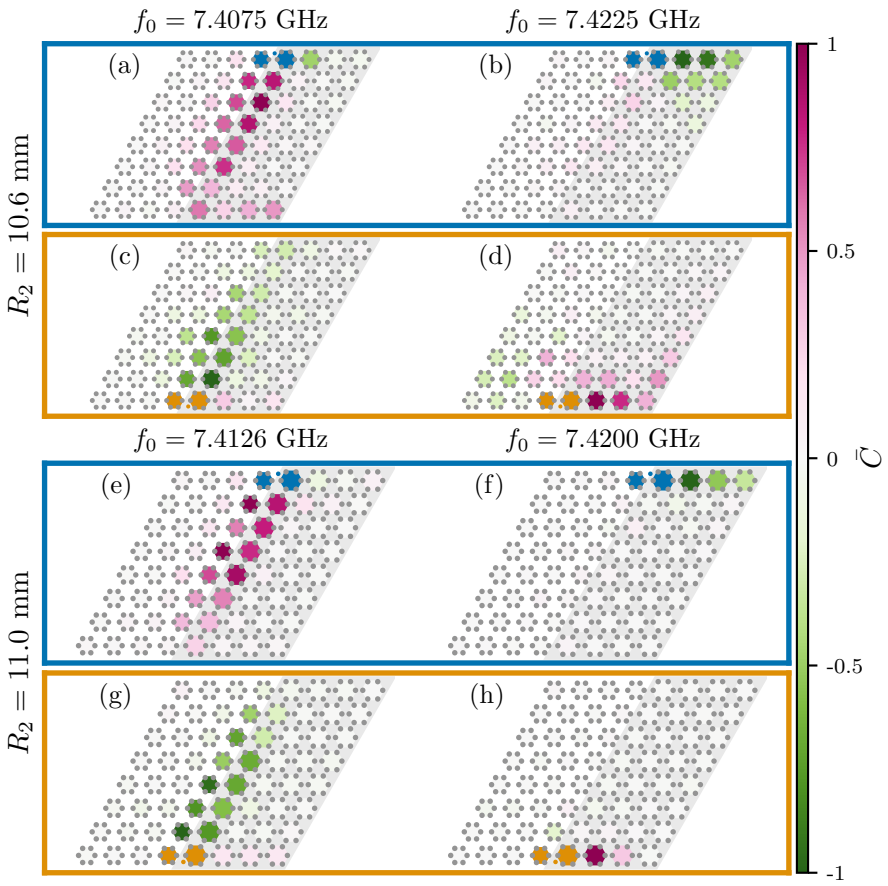

Figure 5.6: Time integrated pattern $\bar{C}$ for honeycomb-like structures characterized by [(a)-(d)] $R_2 = 10.6$ mm and [(e)-(h)] $R_2 = 11$ mm. Structures enclosed in blue or orange boxes are distinguished by the position of the exciting loop antenna. The integrated pattern are computed by integrating in time Eq. (5.4), which in turn are obtained using Hanning filters centered at f_0 with $\Delta = 0.01$ GHz. The area corresponding to the nontrivial structure is highlighted in grey.

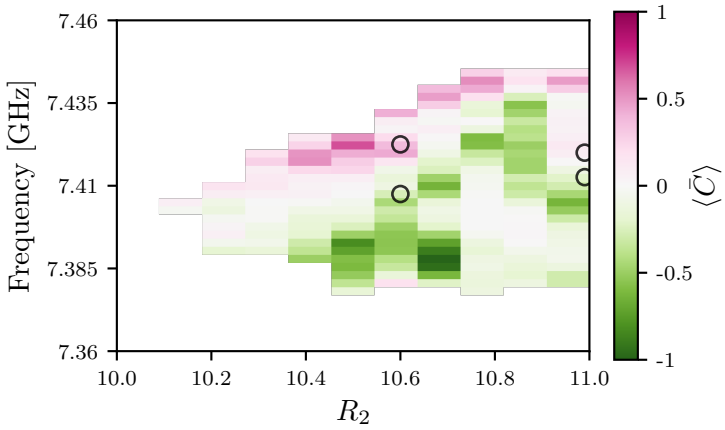

Figure 5.7: Global polarization $\langle \bar{C} \rangle$ computed by averaging the pattern $\bar{C}$ over all cell in a lattice with the fixed loop antenna in its bottom part. Black circles indicate the integrated patterns presented in Fig. 5.6.

position. Similarly to DoS_{EM} in Fig. 5.4, the frequency window is reduced to encompass only the propagating helical states.

As we can expect, the honeycomb limit ($R_1 = R_2 = 10$ mm) is characterized by the absence of helical modes and in consequence the effective polarization goes to zero.

Nevertheless, even small deformations of the lattice ($R_2 \sim 10.1$ mm) start leading to the emergence of helical modes. Note that the intensity of the helical mode propagating on the air-nontrivial edge (pink regions in Fig. 5.7) is always weaker than the one in the trivial-nontrivial interface (green regions in Fig. 5.7)[1].

5.2.2 Helical transfer rate

To complete the characterization of the helical states with our experimental platform, we measure the transfer rate τ^{-1} of the patterns $\bar{C}$. This is done by considering the temporal evolution of circular transmission $C(t)$ through certain paths at the boundary of the nontrivial structure. For instance, Fig. 5.8(a) depicts one of our experimental arrays ($R_2 = 11$ mm) which is characterized by having the exciting antenna in its upper part, and where the hexagonal cells supporting helical states in the trivial-topological interface have been highlighted and ordered according to their distance to the antenna. As in the previous section, the signal of the closest cell to the antenna is strongly perturbed by the coupling between both antennas, therefore it is not taken into account.

Fig. 5.8(b) presents the circular transmission $C_\alpha(t)$ as a function of time for every single hexagonal highlighted cell in Fig. 5.8(a) at a frequency $f_0 = 7.410$ GHz. In each cell, the circular transmission is a positive bump whose maxima monotonically advance in time from one cell to another. In that way, the time corresponding to each bump maximum is plotted in Fig. 5.8(c) with respect to cell number. A linear proportionality between the two quantities is observed. Note that, up to a length scale constant, the transfer rate τ^{-1} is equivalent to a propagation velocity v[2], that can be extracted by performing a linear fit.

In contrast to the tight-binding model studied in Ref. [157], the cylinder-cylinder interaction in our experimental setup is not restricted to first nearest neighbour coupling only, but second and even third nearest neighbour couplings also contribute [165]. To understand the implications of this fact, in Fig. 5.9(a) we show the band dispersion of a 2D topological ribbon considering up to third nearest neighbour coupling. As previously mentioned in Refs. [156, 157], the appearance of two degenerate modes within the gap

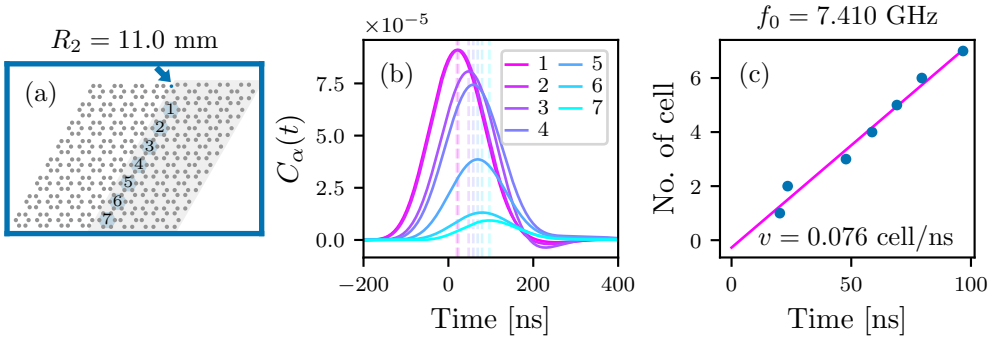

Figure 5.8: (a) Diagram of a honeycomb-like lattice characterized by $R_2 = 11$ mm. The blue dot represents the position of the fixed antenna with respect to the array. Hexagonal cells in the lattice edge defining a path are highlighted in blue and labeled with respect to the distance to the emitting antenna. The area corresponding to the nontrivial structure is highlighted in grey. (b) Circular transmission $C_\alpha(t)$ as a function time for each of the labeled cells in (a). $C_\alpha(t)$ is computed according to Eq. (5.4). Dashed lines indicate the position of the maxima in time for each bump. (c) The corresponding time of the bump maxima in (b) with respect to the number of cell. Pink solid line is a liner fit to find the propagation velocity v.

[1] As can be seen in Fig. 5.6, the edge states trivial-nontrivial or air-nontrivial are separated in frequency, and therefore can be discriminated in Fig. 5.7.

[2] For convenience, we keep this terminology.

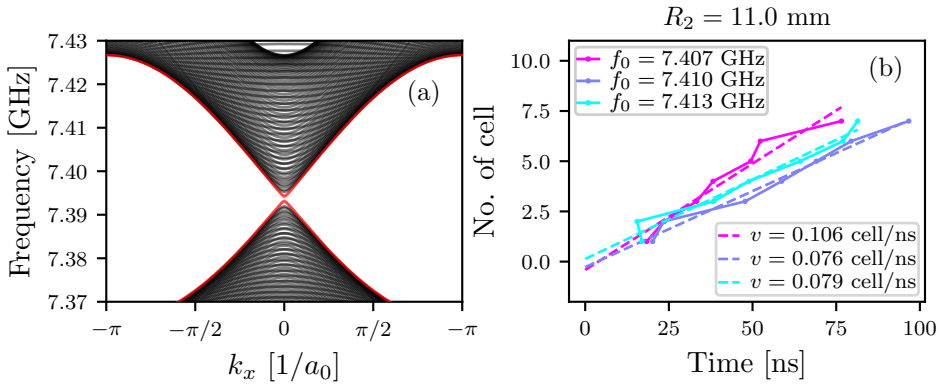

Figure 5.9: Band dispersion of a 2D ribbon system of 50 hexagonal cells with third neighbour coupling computed using the PythTB Python package. To map the experiments, we use the experimental coupling values [see Fig. 2.8(d) and Eq. (2.34)] of a system characterized by $R = 10.025$ mm. Red curves correspond to the helical states. (b) The corresponding time of the bump maxima with respect to the number of cell for the system in Fig. 5.8(a). Dashed lines are linear fit to find the propagation velocity v.

indicates the presence of helical states. However and differently to Fig. 1.25(a), the higher order nearest-neighbor coupling breaks the linear relation between k_x and the frequency around the gap. Consequently, helical states are not expected to conserve the same velocity for all frequencies. This is exemplified in Fig. 5.9(b), where the propagation velocity of the same helical state is extracted and plotted at three different frequencies f_0, leading to a different value in each case.

Finally, the change of the propagation velocity $\langle v \rangle$ with respect to the radius of the hexagonal cells R_2 can be measured by averaging v over all propagating frequencies. Note that considering the two antenna positions leads to four different propagating paths in the boundary of the nontrivial structure (see. Fig. 5.6). In Figs. 5.10[(a)-(d)], we show one lattice configuration where these four paths are highlighted in different colors. As in Fig. 5.8(a), the hexagonal cells in a given path have been ordered according to their distance to the emitting antenna, and consequently labeled.

The average propagation velocity $\langle v \rangle$ of the helical states as a function of the radius R_2 for the four different path in Figs. 5.10[(a)-(d)] are plotted in Figs. 5.10(e). One

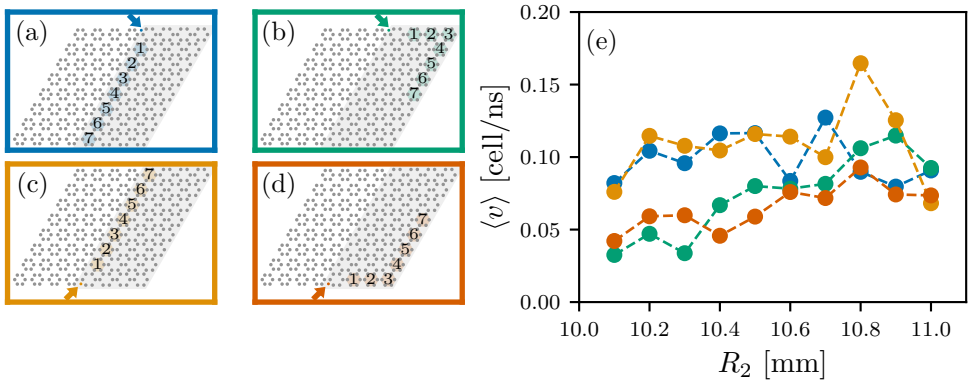

Figure 5.10: [(a)-(d)] Diagrams of the honeycomb-like lattices characterized by $R_2 = 11$ mm. The blue, green, golden, and orange dots represent the position of the fixed antenna with respect to the array. Hexagonal cells in the lattice edge defining a path are highlighted and labeled with respect to the distance to the emitting antenna. The area corresponding to the nontrivial structure is highlighted in grey. (e) Average velocity $\langle v \rangle$ as function of R_2 for the helical states propagating along the different paths in [(a)-(d)].

can observe that for a given edge of the nontrivial structure, the average time $\langle v \rangle$ stay unchanged with respect to the antenna position (see blue and golden dots, or green and orange dots). However, when comparing the same antenna configuration, a clear difference can be seen: the velocity of the helical mode in the air-nontrivial edge is slower for small deformations (see blue and green dots, or golden and orange dots). As previously discussed, this difference is due to the distinct boundary condition of the nontrivial structure where the helical states propagates. Note that helical modes traveling through trivial-nontrivial interface keep the same value for all deformations. Differently, helical states propagating in air-nontrivial edge present a consistent velocity increase with respect to R_2, being almost equal to the trivial-nontrivial helical velocity for $R_2 = 11$ mm.

5.3 Conclusion

In this Chapter, we experimentally identify and characterize the propagation of topological helical states in a set of microwave honeycomb-like lattices. Our experimental samples are made of dielectric cylinders that are placed into a metallic cavity made of two parallel aluminum plates separated by a distance $h = 13$ mm. The versatility of our setup allows us to efficiently control different spatial features of the samples such as the radius of the hexagonal cells that composed the honeycomb-like arrays, i.e. the topological characteristics of the array. The electromagnetic field inside the cavity is excited and measured by loop antennas placed at the center of the top and bottom plates that impose a TE polarization, in which our cylinders behave as resonators, then mimicking a tight-binding system with up to third nearest neighbour coupling contributions. The reflected and transmitted complex fields in the cavity are scanned in space and frequency with a high degree of accuracy thanks to the VNA and to the movable top antenna, which is attached to the movable top plate. Additionally, each sample is measured twice after changing the location of the fixed antenna with respect to the dielectric lattice. Following to the data acquisition, the parameters of the resonances of the system are extracted thanks to the harmonic inversion/clustering methods applied to the transmitted signal. Similarly, the features of the temporal evolution of a wave-packet are studied by means of the Fourier transform. On the other hand, the density of states is obtained from the reflection measurement.

Using the above data analysis, we are able to experimentally demonstrate the opening of a nontrivial topological band gap when increasing the radius of the hexagonal cells that composed the honeycomb-like lattices. We show that the deformation of the honeycomb-like lattices also leads to the emergence of topological states that dwell in the edge of the structure and whose frequencies appear inside the topological band-gap. Our findings reveal that the gap size as well as the confinement of this peculiar modes in the edge structure directly depends on the radius of the cell, confirming previous theoretical predictions [156, 157].

We also investigate the impact of the edge states in wave transport by performing the Fourier transform of the filtered transmission signal. Particularly, we focus on analyzing the circular transmission which is directly derived from the Poynting vector and has a one-by-one correspondence with the current density studied in Ref [157]. By integrating in time the circular transmission, we are able to disclose the wave patterns of the helical modes. We show the unidirectional counterpropagative behaviour of the helical modes around the boundary of the topological material. Differently to previous theoretical predictions [156, 157], we prove our system to be robust against the abrupt crystalline structure breaking, allowing the helical states to propagate even in the edge of the dielectric structure with the air. Thanks to the experimental design of our samples, helical modes can be easily isolated from one another, thus opening the door to wave-guiding applications.

Finally, by evaluating the spatial evolution of the helical states along the edge of the nontrivial topological structure, we extract the propagating helical velocity. By taking into account the second- and third-nearest-neighbour tight-binding coupling between resonators, we show that the helical velocities are frequency dependent.

Conclusion & perspectives

Combien de temps encore à te voir revenir
Dans des rêves brumeux imbibés de plaisir?
Exhibant tes amants me proposant maîtresses
Qu'importe le flacon pourvu qu'il y ait l'ivresse

Je ne veux plus te voir, je ne veux plus t'entendre
Je n'veux plus rien savoir, je ne veux plus comprendre
Je ne peux plus te croire, je veux juste t'oublier
Quand tu te fais prendre arrête de crier

Zoufris Maracas (Et ta mère)

Throughout this manuscript, we have investigated the spatial localization of electromagnetic waves generated by different physical and geometrical mechanisms. Specifically, we have successfully extended the localization landscape approach to a wide class of 1D and 2D tight-binding lattices with uncorrelated random on-site energies. Uncorrelated disorder leads to the phenomenon known as Anderson localization, characterized by exponentially localized eigenstates, which, in the discrete case, lie on both edges of the band. We have also experimentally explored the impact of correlated potentials in wave transport by performing microwaves scattering experiments in aperiodic systems (Vogel spirals) and correlated disordered media. We have confirmed that correlated Vogel spiral support a unique modal structure where long-lived modes with different radial decay types (exponential, power-law and Gaussian) coexist. Remarkably, such long-lived modes are robust against the change of dimensionality of the cavity, from 2D to 3D. Finally, we have experimentally identified and characterized the emergence of topological helical states in a set of microwave honeycomb-like lattices. We have shown that the interface between two topologically distinct lattices (or outer edges) supports two contrapropagative states of opposite helicity. Taken together, our results demonstrate that it is possible to model, control and localize electromagnetic waves not only within, but beyond Anderson's conception. As mentioned in the introduction, our main goal was not solve the problem of Anderson localization of 3D light, but to improve the general understanding on the different mechanisms that allow electromagnetic wave localization to take place. We humbly believe that the challenge has been met. Throughout this manuscript, experimental evidence and physical interpretations have combined to provide the building blocks of a scaffold of new knowledge upon which others can climb to construct the ultimate understanding of Anderson localization of electromagnetic waves. Progress has been made, but much remains to be done...

One of the objectives of Chapter 3 was to extend the scope of the localization landscape formalism to disordered electromagnetic wave systems, which are governed by the vector Maxwell's equations. However, to the best of our knowledge, a vector definition of the

localization landscape is still missing, making impossible the direct application of this powerful tool to 3D light. Later on, by imposing suitable spatial condition to the electric and magnetic fields, we were able to investigate the scalar character of the fields, showing that spatial localization of waves is achieved only at high frequencies. Unfortunately, in its current form, the continuous localization landscape is not capable to predict the behavior of such high-frequency localized states, and it is therefore necessary to improve the approach. As also mentioned in Chapter 3, multiple interesting effects take place at the center of the band of a tight-binding system (see e.g. Chapter 5). However this frequency range is still completely unreachable to our approach. Additionally, despite the robustness of our method to compute the dual localization landscape, it is not completely universal: for instance in the case of the Kagome lattice, where the definition of $\mathbf{k}_{\max}$ remains a challenge given the presence of a flat band.

As highlighted in Chapter 4, we have remarkably exhibited localization of 3D electromagnetic waves using 2D planar aperiodic arrays. This fact can be contrasted with the case of correlated disordered structures, where localization was found to be always restricted to frequencies in the purely 2D limit regime. Therefore, a better understanding on the precise "ingredients" required to achieve 3D localization of electromagnetic waves in correlated systems is needed. A similar analysis may be also developed for different transport regimes, for instance to explain the origin of band gaps that have been demonstrated to be closely related with the localized eigenmodes [78, 79, 138].

In Chapter 5, we have reported the unambiguous observation of helical counterpropagative edge modes in a dielectric structure with nontrivial topological behaviour, characterized by a Z_2 invariant. It turns out that recently, Li et al. [191] have investigated the effect of disorder in this type of topological insulators. The authors have shown that, additionally to the expected metal-insulator transition, the disorder induces a new nontrivial topological phase in the material—namely a *topological Anderson insulator* [192–196]. Given the versatility and robustness of our setup, as well as the new findings, we believe it is possible to demonstrate this topological transition experimentally. Besides this, it is important to remark that all our tight-binding experiments were carried out using only the fundamental TE resonance of the cylinder and the rotational symmetry C_6 generated by the specific array. As exhibited by Reisner [164], higher resonant modes can be easily achieved in our experimental platform. Moreover, Reisner et al. [197] also demonstrated that is possible induce non-linear losses by coupling short-circuited Schotky diodes to the cylinders. By doing that, the authors were able to design a topological reflective power limiter [197, 198]. These two examples illustrate how new different symmetries can be induced in our system, opening the door to different topological phenomena.

At this point, it is important for me to point out that this Thesis has approached the study of wave systems from several different angles, all using the same experimental platform. The significant results presented in this manuscript are based on precise, quantitative experimental access to various physical observables. For instance, we have demonstrated how the local density of states (and therefore the density of states), the Thouless conductance, the spatial structure of the eigenmodes and even the time evolution of a wave-packet can be precisely obtained from our experimental processes. And not only that, but we have also showed that by playing with the polarization of the excited field, we can change the constitutive equations of our problem, going from a tight-binding Hamiltonian to fully vector propagating problem governed by Maxwell's equations. It is also true that our systems are limited by the number of cylinders, or the physical size of the platform. Nevertheless, I would like to remark that, to the best of my knowledge, there is no other platform that alone provides access to this variety of

observables with the same quantitative quality. In addition, let me now draw your attention to the moderate resources with which this platform operates. Personally, in the last three years conducting this research, I'm truly convinced that all the scientific community ought to be more concerned about the resources spent (and sometimes wasted) in research and how we can reduce them. As we have demonstrated in this Thesis, meaningful and beautiful physics can be achieved taking this new constraint into account.

Appendix A

The tight-binding formalism

Traigo ante ti
la lucha de un hombre
suplico a mi Dios
que ampare su ausencia,
causa de mi demencia,
¿Dónde estás santa inocencia?
Delalma (Acto de fé)

This Appendix is devoted to present the tight-binding method. Tight-binding Hamiltonians are pertinent to model many different wave problems in physics and do not depend on the nature of the considered waves. This formalism is introduced by considering atomic structures in which atoms are weakly coupled with their neighbours, however, it is also useful to describe several physical systems as a classical chain of harmonic oscillators. Tight-binding models are also commonly used to study perfect [165] as well as disordered lattices [1, 199–201]. Similarly, Tight-binding Hamiltonians are used to model our experimental system of dielectric cylinder (considering TE polarized waves) introduced in Chapter 2.

General formulation

To show the formalism of the tight-binding approximation, we start considering a crystalline periodic lattice whose potential fulfils $V(\mathbf{r}) = V(\mathbf{r}+\mathbf{R})$, with $|\mathbf{r}-\mathbf{R}| = a_0$ the lattice parameter [see Fig. A.1]. We assume that in this lattice, the Hamiltonian $\hat{H}$ can be locally approximated by the Hamiltonian of a single atomic site $\hat{H}_s$ at a given position. The isolated atomic state $\psi_n(\mathbf{r})$ is then described by the Schrödinger equation as

$$\hat{H}_s\psi_n(\mathbf{r}) = E_n\psi_n(\mathbf{r}), \tag{A.1}$$

where E_n is the atomic energy of $\psi_n(\mathbf{r})$, which is infinite degenerated in the crystal. Additionally, the Bloch theorem in the periodic lattice requires

$$\psi_n(\mathbf{r}+\mathbf{R}_j) = \mathrm{e}^{\mathbf{i}\mathbf{k}\cdot\mathbf{R}_j}\psi_n(\mathbf{r}) \tag{A.2}$$

with $\mathbf{k}$ the wave vector of the wavefunction, and $\mathbf{R}_j$ denoting the position of the atom j in the crystal.

Given the overlap of the atomic wavefunction with the adjacent atomic sites, $\psi_n(\mathbf{r})$ is not an eigenstate of $\hat{H}$. In this case, the Hamiltonian is written as

$$\hat{H} = \hat{H}_s + \Delta U, \tag{A.3}$$

where the potential ΔU contains all corrections between the potential of the single atom and the full periodic potential. Then, $\hat{H}$ can be expressed in the crystalline base by projecting it on the isolated atomic states as

$$\begin{aligned} H_{ij} &= \int \psi_n^*(\mathbf{r}+\mathbf{R}_i)\hat{H}\psi_n(\mathbf{r}+\mathbf{R}_j)\mathrm{d}\mathbf{r}, \\ &= \int \psi_n^*(\mathbf{r}+\mathbf{R}_i)\hat{H}_s\psi_n(\mathbf{r}+\mathbf{R}_j)\mathrm{d}\mathbf{r} + \int \psi_n^*(\mathbf{r}+\mathbf{R}_i)\Delta U\psi_n(\mathbf{r}+\mathbf{R}_j)\mathrm{d}\mathbf{r}, \\ &= E_n\mathrm{e}^{\mathbf{i}\mathbf{k}\cdot(\mathbf{R}_j-\mathbf{R}_i)} + \int \psi_n^*(\mathbf{r}+\mathbf{R}_i)\Delta U\psi_n(\mathbf{r}+\mathbf{R}_j)\mathrm{d}\mathbf{r}. \end{aligned} \tag{A.4}$$

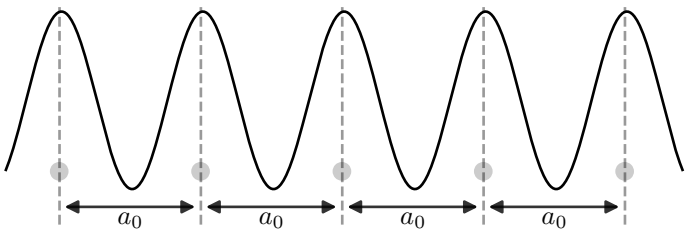

Figure A.1: Simplified diagram of a periodic potential in 1D with periodicity a_0.

In Eq. (A.4), we have discretized the Hamiltonian of the crystalline lattice on the atomic position base. Note that the elements H_{ij} only depend on the self-energy of the isolated atomic functions and the overlap between neighbouring sites. In consequence, the crystal can be interpreted as a discrete lattice of interacting sites, where the diagonal terms H_{ii} are called as the *self energies* and the non diagonal terms H_{ij} are the *couplings*. Since the matrix elements H_{ij} depends on the specificities of the problem, they are not typically computed, but measured experimentally instead (see Section 2.2.1.2).

Appendix B

Energy prediction from the $\mathcal{L}^2$ landscape

Forzas do ar, terra, mar e lume, a vós fago esta chamada:
se é verdade que tendes máis poder que a humana xente,
eiquí e agora, facede que os espíritos dos amigos que están fóra,
participen con nós desta Queimada.
Esconxuro

Contents

This appendix present complementary results to Chapter 3. Here, we propose an algorithm to find the eigenenergies of a tight-binding Hamiltonian using the $\mathcal{L}^2$-localization landscape. The scope of the Appendix is as follows: In Section B.1, we introduce the $\mathcal{L}^2$-landscape formalism. Later, in Section B.2 the details of the algorithm that allows to find the energies of the system are given.

B.1 The $\mathcal{L}^2$ landscape approach

In Chapter 3, a new tool that allows to extract important information about the low-energy states of a quantum particle in a disordered potential is study. The localization landscape approach, firstly introduce by Filoche and Mayboroda [26], is defined via the Green function of the Hamiltonian [Eq. (1.7)] and is capable to predict the energies and positions of the localized functions. Despite the landscape has been extrapolated to other wave system such as mechanical waves [65] or cold atoms [74], the lack of high-energy predictions makes it unfeasible to describe electromagnetic waves in disordered media, where localization occurs only at high-frequencies (see Section 3.1). In tight-binding disordered structures, localization is also present at high energies, however, the discrete character of the system allows to successfully extend the landscape theory for a broad class of 2D lattices (see Section 3.2) at both, low- and high-energy, band edges. Unfortunately, the center of the band where many interesting properties appear for many new topological materials is still inaccessible to this formalism. Nevertheless, it exists another variant of the localization landscape, called the $\mathcal{L}^2$-localization landscape and introduced by Herviou and Bardarson [186], which is presented as a tool capable to predict the position of any mode around an energy E_T in a generic physical model, claiming to be efficiently applied to topological modes and many body Hamiltonians as well.

In the tight-binding framework, the $\mathcal{L}^2$-landscape is defined as

$$u_n^{(2)} = \sqrt{(\mathcal{H}^\dagger \mathcal{H})^{-1}_{nn}}, \tag{B.1}$$

where $\mathcal{H} = \hat{H} - (E_T + \mathrm{i}\epsilon)\,\mathbb{1}$ with $\hat{H}$ defined as in Eq. (3.20). Note that the parameter ϵ assures existence of the $\mathcal{H}^{-1}$ if E_T is an eigenvalue of $\hat{H}$, allowing as well to resolve between different states close in energy. The election of ϵ is then restricted to be smaller that the mean level spacing of the system. Even though Eq. (B.1) is defined for tight-binding systems, this formalism can be numerically extended to continuous setting. Equation (B.1) is derived by applying the Cauchy-Schwartz inequality to Eq. (1.6), leading to

$$|\psi_n| \leq |E| \|\psi\|_2 \sqrt{\sum_m (\mathcal{H}^{-1})_{n,m} (\mathcal{H}^{-1})^*_{n,m}}. \tag{B.2}$$

Since the $\mathcal{L}^2$-landscape uses a different normalization condition over the eigenfunctions $\|\psi\|_2 = \sqrt{\sum_n |\psi_n|^2} = 1$, the localization subregions definition [Eq. (1.10)] is not valid anymore. Therefore, it is not possible to predict the energies of the system.

Considering a Hermitian Hamiltonian allows to write the $\mathcal{L}^2$-localization landscape in terms of the eigenfunctions and eigenvalues as

$$\left(u_n^{(2)}\right)^2 = \sum_i \frac{\left|\psi_n^i\right|^2}{\left(E^i - E_T\right)^2 + \epsilon^2}, \tag{B.3}$$

where each site is determined by the contribution of all states weighted by the corresponding energy after being shifted by $E_T + \mathrm{i}\epsilon$. Thus, states with closest energies to

E_T have greater contributions to the landscape even near to spectral quasidegenerancies. To gain some intuition about $\mathcal{L}^2$-landscape, Figs. B.1(a), (b), and (c) show the $\mathcal{L}^2$-landspace computed using Eq. (B.1) for the same 1D disordered chain by considering three different values of E_T. Similar to the original localization landscape, each $\mathcal{L}^2$-landscape is a complex relief of peaks and valleys and all of them are different from each other. In Fig. B.1(d), six different eigenmodes in the bottom band edge (ψ^1, ψ^2), in the middle of the band (ψ^{100}, ψ^{101}), and in the top band edge (ψ^{199}, ψ^{200}) are also depicted. Notably, all states are well predicted by the $\mathcal{L}^2$-landscape peaks even in the middle of the band. Such new advantage allows to explore the complete spectrum of a disorder system without solving the eigenvalue problem.

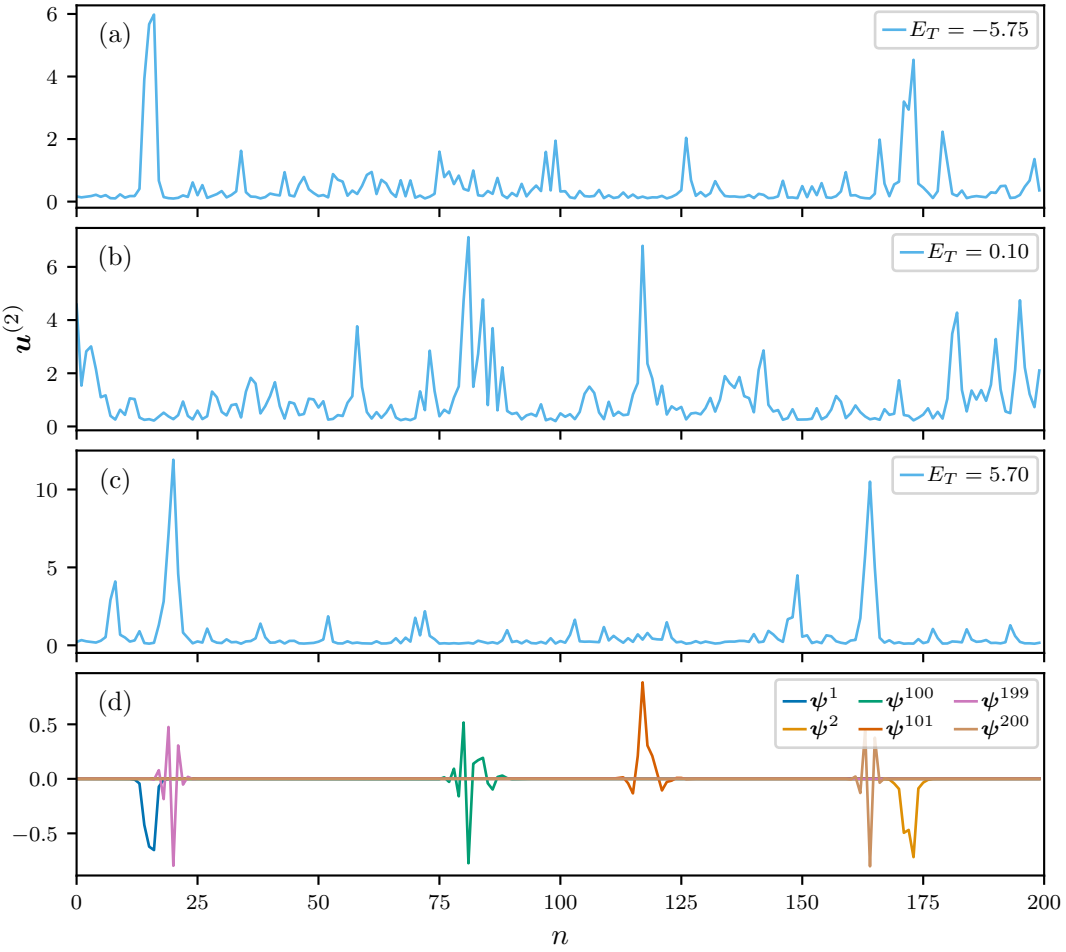

Figure B.1: The $\mathcal{L}^2$-localization landscape with (a) $E_T = -5.75$, (b) E_T=0.1, (c) $E_T = 5.7$ and $\epsilon = (4+V_{\max})/(N \times 100)$, computed using Eq. (B.1). (d) The two states with: the lowest energies, the highest energies and in the middle of the band of a 1D chain with on-site disorder, $N = 200$ and $V_{\max} = 10$. Each random value is taken from a uniform random variable in the interval $[-V_{\max}/2, V_{\max}/2]$ and $t = 1$.

B.2 Energy prediction

As we have observed, the $\mathcal{L}^2$-localization landscape is able to improve the precision of the conventional landscape which usually fails for spatial or spectral quasidegeneracies (see Sections 1.1.3.4 and 3.2.5). Unfortunately, this new landscape does not extract information about the energies of the modes. In this section, we will introduce an algorithm that allows to access to the eigenenergies by means of the $\mathcal{L}^2$-localization landscape.

We start considering a discrete structure with constant coupling $t = 1$ and on-site disorder given by an i.i.d. random variable in $[-V_{\max}/2, V_{\max}/2]$. Therefore, the spectrum of possible energies is bound in the interval $[-\min(\mathcal{E}) - V_{\max}/2, \max(\mathcal{E}) + V_{\max}/2]$ with $\mathcal{E}$ depending of spatial structure of the discrete array (see, e.g., Table 3.1). The algorithm then consists on dividing the total energy band into a set of K different energies $\{E_1, \cdots, E_k, \cdots, E_K\}$ separated by a step $E_k - E_{k-1} = \delta > 0$. Later, one can compute the $\mathcal{L}^2$-landscape using each energy in the set as an energy shift with a constant value of ϵ. Finally, by comparing the changes in the position of the maxima values of two distinct landscapes, successive in energy, we fix the bounds of each eigenenergy.

For instance, Fig. B.2 shows three $\mathcal{L}^2$-localization landscapes with slightly different values of E_T. The first and second landscape maxima are label with their actual values. As we can observe, the maximum of $\boldsymbol{u}^{(2)}(E_T = -2.96)$ is placed at different position that the maxima of the previous and followed landscapes. Thus, according to Eq. (B.3), there is at least one eigenmode $\boldsymbol{\psi}^i$ whose energy E^i is bound by $E_k - \delta/2 < E^i < E_k + \delta/2$. Since the construction of the landscape in Eq. (B.3) only depends on the energy distance to E_T, one can have a state whose signature is never dominant [see in Fig. B.2(b) the second maxima with value ~ 50.08]. To handle this, the algorithm not only look for the maximum of each landscape, rather it follows the behavior of the 2 highest local maxima.

To show the accuracy of the algorithm, numerical simulations have been performed to find the complete spectrum of honeycomb and hexagonal lattices with weak disorder $V_{\max} = 3$ and $V_{\max} = 6$, respectively. Values of N are chosen as shown in Table 3.2, and $\epsilon = [\min(\mathcal{E}) + \max(\mathcal{E}) + V_{\max}]/(N \times 100)$ with $\mathcal{E}$ as in Table 3.1. Figure B.3 shows a comparison between the actual counting function obtained by diagonalizing Eq. (3.20), and the prediction made by the algorithm previously described for two values of K. As

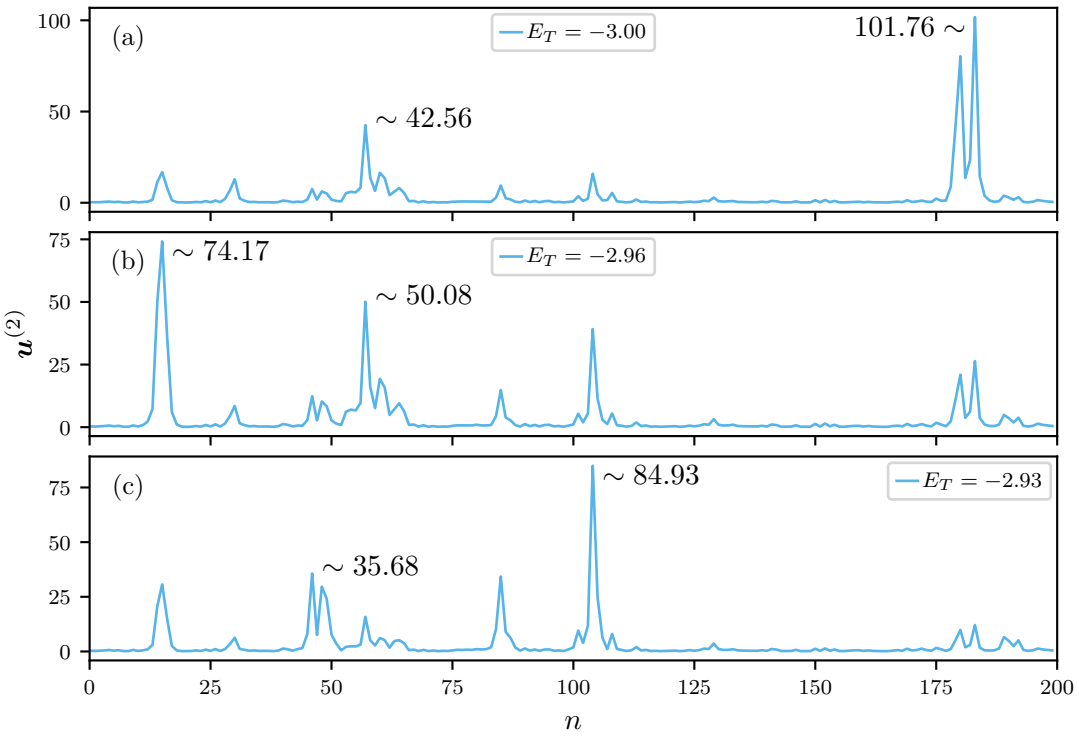

Figure B.2: The $\mathcal{L}^2$-localization landscape with (a) $E_T = -3$, (b) $E_T = -2.96$ and (c) $E_T = -2.93$ and $\epsilon = (4 + V_{\max})/(N \times 100)$. We consider a 1D disordered chain with on-site disorder, $N = 200$ and $V_{\max} = 10$. Each random value is taken from a uniform random variable in the interval $[-V_{\max}/2, V_{\max}/2]$ and $t = 1$. Local maxima are label with their actual values.

we can observe, the accuracy of the algorithm strongly depends on the election of K. For $K = N$, the algorithm is just able to find approximately half of the eigenvalues of the spectrum. This problem comes from the existence of eigenenergy clusters with an energy scale smaller than δ. We have to stress that this problem affects the order of the states with respect to the real solution, but not the total accuracy of the algorithm. However, an increment of K leads to the algorithm to guess successfully almost the complete spectrum of the system, i.e., $> 97\%$ of the energies. Here, the prediction follows closely the actual IDOS for both lattices.

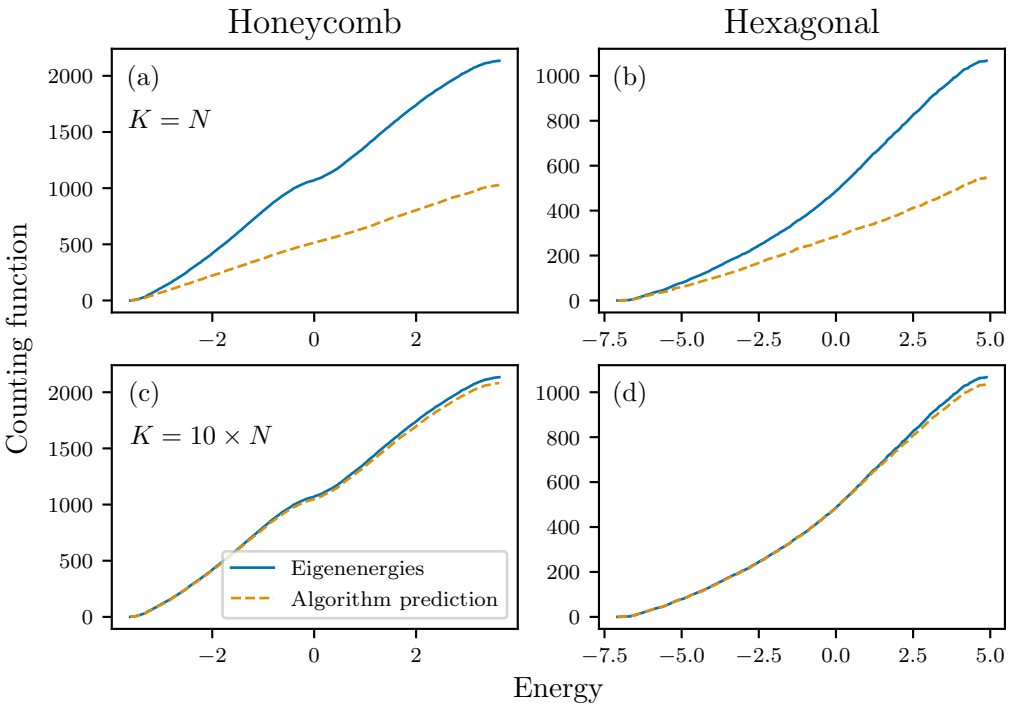

Figure B.3: Counting function computed by the $\mathcal{L}^2$-localization landscape algorithm (dotted line) with [(a) and (b)] $K = N$ and [(c) and (d)] $K = 10 \times N$. Here, the weakest disorder (see Table 3.2) was chosen for the [(a) and (c)] Honeycomb and [(b) and (d)] Hexagonal lattices.

B.3 Conclusions

Introduced as an alternative method to the localization landscape presented in Section 1.1.3, the $\mathcal{L}^2$-localization landscape is a remarkable tool capable to predict the position of localized eigenstates all along the spectrum without solving the eigenvalue equation [186]. Despite it is defined for tight-binding Hamiltonians, the $\mathcal{L}^2$-landscape is easily applicable to any other wave phenomena description. In this appendix, we present a numerical algorithm that allows to guess the eigenenergies of the states using the $\mathcal{L}^2$-landscape approach. Despite of the big accuracy of our algorithm, the computation time needed to calculate the complete $\mathcal{H}^{-1}$ for a large number of energies overcomes the time spent by solving the original problem Eq. (3.20). Thus, its implementation is not recommended to find the complete spectrum, rather just to extract some information in a small energy windows.

Appendix C

Wave scattering through a regular lattice

No veo nada nuevo,
sólo bebo cuando debo hacer lo que debo,
y acabo ciego sin poder ser
el hombre que prometí sacar adelante
como cantante se ha cansado de correr
así que antes de que me despida de esta mierda mátame,
acaba con las alas de este ángel desátame,
devuélveme los años perdidos que ya no sé
si se recuperarán altera'os por las pivas y el caché...
Hard GZ (Experimento)

Contents

This appendix complements the results presented in Chapter 4. In it, we explore electromagnetic scattering in a planar regular triangular array. The Appendix is organized as follows: Section C.1 presents the construction of the dielectric lattice and details of the experimental procedure and data analysis. Then, Section C.2 analyzes the behavior of the eigenstates, as well as of different transport quantities.

C.1 Experimental array and analysis details

Analogous to the lattices investigated in Chapter 4, our regular array is made of $N = 396$ dielectric cylinders (see Section 2.2) arranged into our experimental cavity introduced in Section 2.1. The electromagnetic field is induced and measured by two straight antennas (each of them in the center of each plate), then producing a TM polarization (see Section 2.1.2).

C.1.1 The regular array

Our regular lattice is a triangular array characterized by a lattice parameter $a_0 = 13.1$ mm, i.e. the distance between two neighbouring sites is always given by a_0. For the sake of comparison with the golden-angle spiral and the disordered system studied in Chapter 4, just the sites enclosed within a circular area of radius $R_0 = 140$ mm are considered into the experimental array, leading to a planar (2D) density $\rho \approx 0.65$ cm^{-2}. The diagram of the regular map used to arrange the scatterers together of a picture of the real system can be observed in Fig. C.1

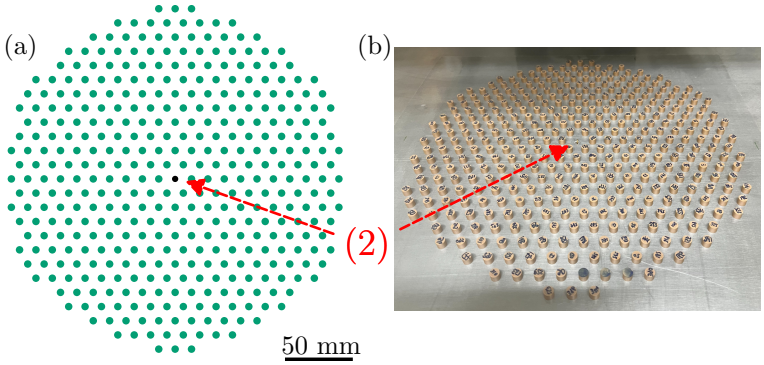

Figure C.1: (a) Regular array consisting of $N = 396$ cylinder created with $a_0 = 13.1$ mm. The black dot indicates the position of the fixed antenna (2), which determines the origin of the reference system. (b) Image of the 2D regular array of dielectric cylinders. The top plate has been removed to reveal the details of the sample.

C.1.2 Experimental and data analysis performance

Differently to the experiments performed in Chapter 4, here we focus only in the case $h = 13$ mm. Nevertheless, we consider the same frequency range [5.5 GHz, 15 GHz] with the same frequency step of 250 kHz, corresponding to wavelengths in the range [20 mm, 54 mm] and the cutoff frequency $\nu_{\text{cut}} \approx 11.53$ GHz. Using the movable antenna (1), the cavity is once again mapped according to Fig. 4.3(a), i.e. over 3675 points where the geometrical center of the lattice is located at $(x, y) = (0, 0)$ [see blue circle in Fig. 4.3(a)]. At each position (x, y), both complex reflected and transmitted signals are registered [$S_{11}(\nu)$ and $S_{21}(\nu)$, respectively] by the VNA.

Identically to Chapter 4, the analysis of the transmitted signal is carried out via the harmonic inversion/clustering methods (see Sections 2.4.2 and 2.4.3), by dividing the complete spectrum at each position into 19 intervals with bandwidth 0.6 GHz and an overlap of 0.05 GHz. The value of $2K$ provided to the harmonic inversion method is identify identically as in Sections 4.1.3 and 2.4.2 for each interval. In addition, analysis of the wave dynamics is performed thanks to the Fourier-transform using Gaussian filters with $\Delta\omega = 0.01$ GHz (see Section 2.4.5) over all positions to compute the total energy carried by a certain superposition of modes [see Eq. (4.3)]. Energy dynamics as a functions of the frequency is obtain by mapping the frequency internal [5.54 GHz, 14.96 GHz] via 472 Gaussian band-pass filters. The supposition of an exponential temporal decay of the energy allows us to access to the characteristic decay time t_0 as $E \sim \exp(-t/t_0)$. Next, the DoS is calculated from the reflected signal as $\text{DoS} = \left[1 - \left\langle |S_{ii}(\mathbf{r}, \nu)|^2 \right\rangle\right]$ (see Section 2.4.6). Finally, using the DoS and the characteriztic times t_0, we the average Thouless conductance is extracted experimentally as in Eq. (4.4).

C.2 Transport and modes in a regular lattice

In Figs. C.2(a), the density of quality factors Q_k is plotted as a function of ν_k for the regular lattice in the case $h = 13$ mm. Green arrows are added to indicate the frequency of the states in Fig. C.3. Additionally, the characteristic decay time t_0, recovered from the temporal evolution of the energy, is presented in Fig. C.2(b), while the corresponding DoS is also depicted in Fig. C.2(c). Finally, using the two previously introduced quantities (DoS and t_0), the average Thouless conductance is computed and presented in Fig. C.2(d). As discussed in Chapter 4, Figs. 4.6(a) and (b) presents strong similarities between the density of Q_k and t_0, showing in both cases a complex relief of sharp peaks and valleys.

Regular lattice results can be directly compared with those found in Vogel spirals (see Fig. 4.8). For instance, Fig. C.2(c) revels the existence of two band gaps at exactly the same position that those in aperiodic systems, where regular structure gaps are just slightly wider. Similar findings have been already discussed when comparing a regular system and a stealthy hyperuniform disordered lattice in the 2D limit ($h = 5$ mm) [81]. Equivalently, our results support preceding proposals about importance of short-range spatial correlations for the opening of band gaps in non-regular materials [99].

For frequencies below the first band gap ($\nu < 8$ GHz), Fig. C.2(a) shows small Q_k-values ($Q_k \to 0$) along all the interval except for two bumps. First, the frequency interval (6 GHz, 7 GHz), where $Q_k \sim 2000$, is characterized by a huge decrease of the DoS with decay times of $t_0 \sim 10$ ns, giving rise to a soft decrease of the Thouless conductance [see Fig. C.2(b)-(d)]. Extended states as the one in Fig. C.3(a) are found in this frequency range. The second frequency window ($\nu_k \sim 7.3$ GHz) is denoted by huge quality factors ($Q_k \sim 6000$). However, a DoS completely flat together with short characteristic decay times $t_0 \to 0$ produce a flat Thouless conductance ($\langle g \rangle > 1$). In this frequency region, the harmonic inversion/clustering algorithms are just able to decode the spatial structure of one extended eigenmode, shown in Fig. C.3(b).

According to Fig. C.2, the lower edge of the first gap (8.2 GHz $< \nu <$ 8.4 GHz) is populated by states with high quality factors ($Q_k \sim 4000$) and long characteristic times ($t_0 \sim 40$ ns), having both the order of localized modes in the golden-angle spiral and the disordered array. Subsequently, the Thouless conductance sharply drops by around one order of magnitude, indicating the possible presence of long-lived states. However, the harmonic inversion/clustering methods are only able to prove the existence of extended states as those observed in Figs. C.3(c) and (d). As on the Vogel spiral, the peaks at the center of the first band gap ($\nu \sim 9.1$ GHz) in all transport quantities (see Fig. C.2) correspond to the signature of defect modes caused by scatterers imperfections. These

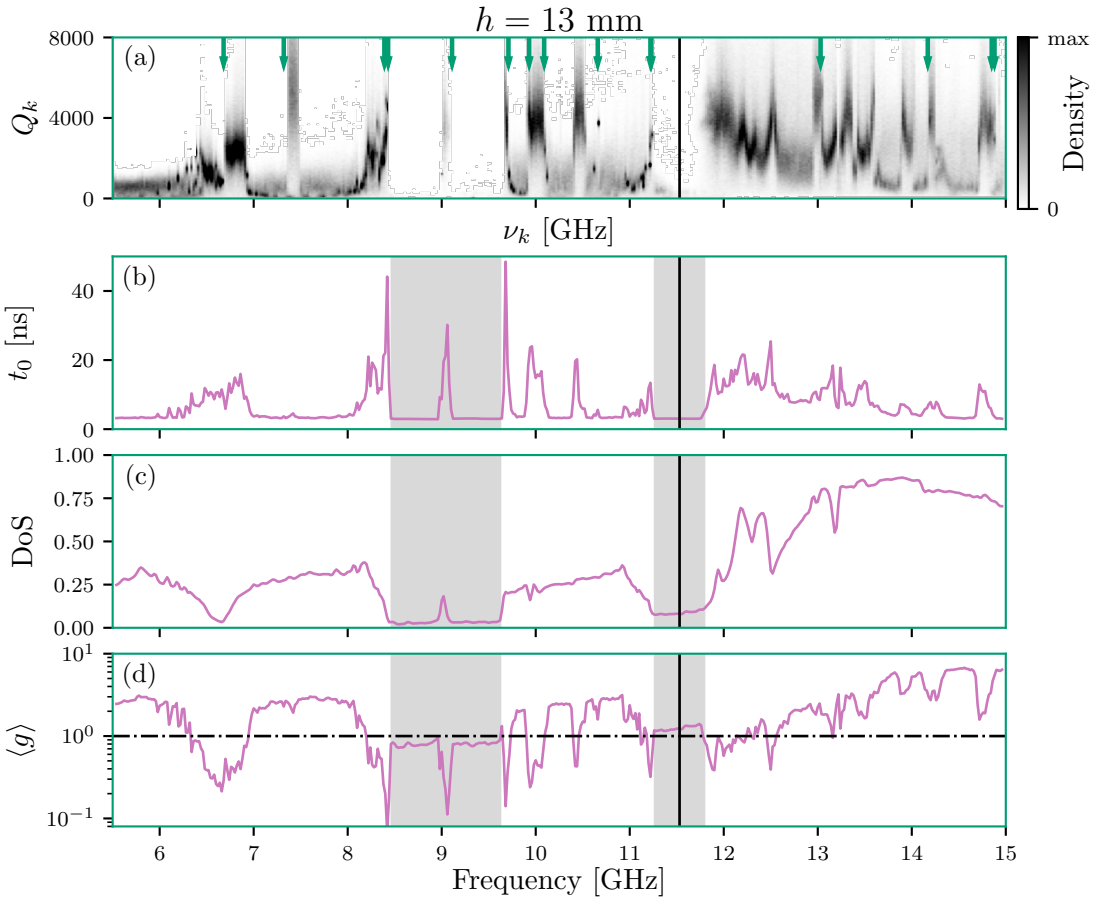

Figure C.2: Density plots of the quality factors Q_k as a function of the resonant frequencies ν_k extracted via the harmonic inversion with a distance between plates $h = 13$ mm for the regular lattice. Arrows indicate the frequencies of the states presented in Fig. C.3. (b) Characteristic decay time t_0 as a function of the frequency. The total frequency range have been mapped by 472 frequency filters spaced by $\Delta f = 0.02$ GHz with $\Delta\omega = 0.01$ GHz. (c) Experimental DoS as a function of the frequency. (d) Experimental Thouless conductance $\langle g \rangle$ as a function of the frequency. The dash-dotted line indicates $\langle g \rangle = 1$. Black vertical lines indicate the cut-off frequency ν_{cut}.

states have large quality factors ($Q_k \sim 4000$) and are strongly localized in a restricted number of cylinders (< 10) as shown in Fig. C.3(e).

The upper edge of the first band gap ($\nu \sim 9.9$ GHz) displays similar features than the ones observed in the lower band edge [huge quality factors ($Q_k \sim 5000$), huge characteristic times ($t_0 \sim 45$ ns), and a sharp drop in $\langle g \rangle$ ($\langle g \rangle \sim 10^{-1}$)]. However and identically to the lower edge, the posterior analysis of the populating states still shows well extended modes [see Figs. C.3(f) and (g)]. The upper band edge is followed by a frequency band (9.95 GHz $< \nu <$ 11 GHz) denoted by low quality factors ($Q_k \to 0$), except from two strips located around 10 GHz and 10.5 GHz where $Q_k \sim 4000$. Here, the DoS present a constant value all along this range [see Fig. C.2(c)]. Likewise that for the density of Q_k, two sharp peaks are observed for the characteristic times where $t_0 \sim 20$ ns, producing the fast decrease of $\langle g \rangle$ in both windows. The spatial reconstruction of two representative states found in at $\nu \sim 10$ GHz and $\nu \sim 10.6$ GHz can be seen in Figs. C.3(h) and (i), respectively. These two modes can be compared with those found in Vogel spirals in similar frequency windows [see Figs. 4.8 and 4.11(a) and (d)], being also centered around "defect positions" and occupying the whole measured space. In Chapter 4, a relation between the nature of such states and the imperfections of the cylinders was proposed.

Contrary to the Vogel spiral, just a small increase of the characteristic times and quality

factors is observed in the lower edge of the second gap ($t_0 \sim 10$ ns and $Q_k \sim 2000$), leading to a small change in $\langle g \rangle$. Nevertheless, the spatial structure of populating modes in this frequency range [see Figs. C.3(j) and (k)], together to those of states in the lower edge of the first gap [see Figs. C.3(c) and (d)], can be compared with band edge Gaussian modes in the GA spiral (see Fig. 4.10). As in Vogel spiral, band edge wave patterns in regular systems result from Bragg scattering [40, 99], however the homogeneity of the array prevents spatial confinement in this case.

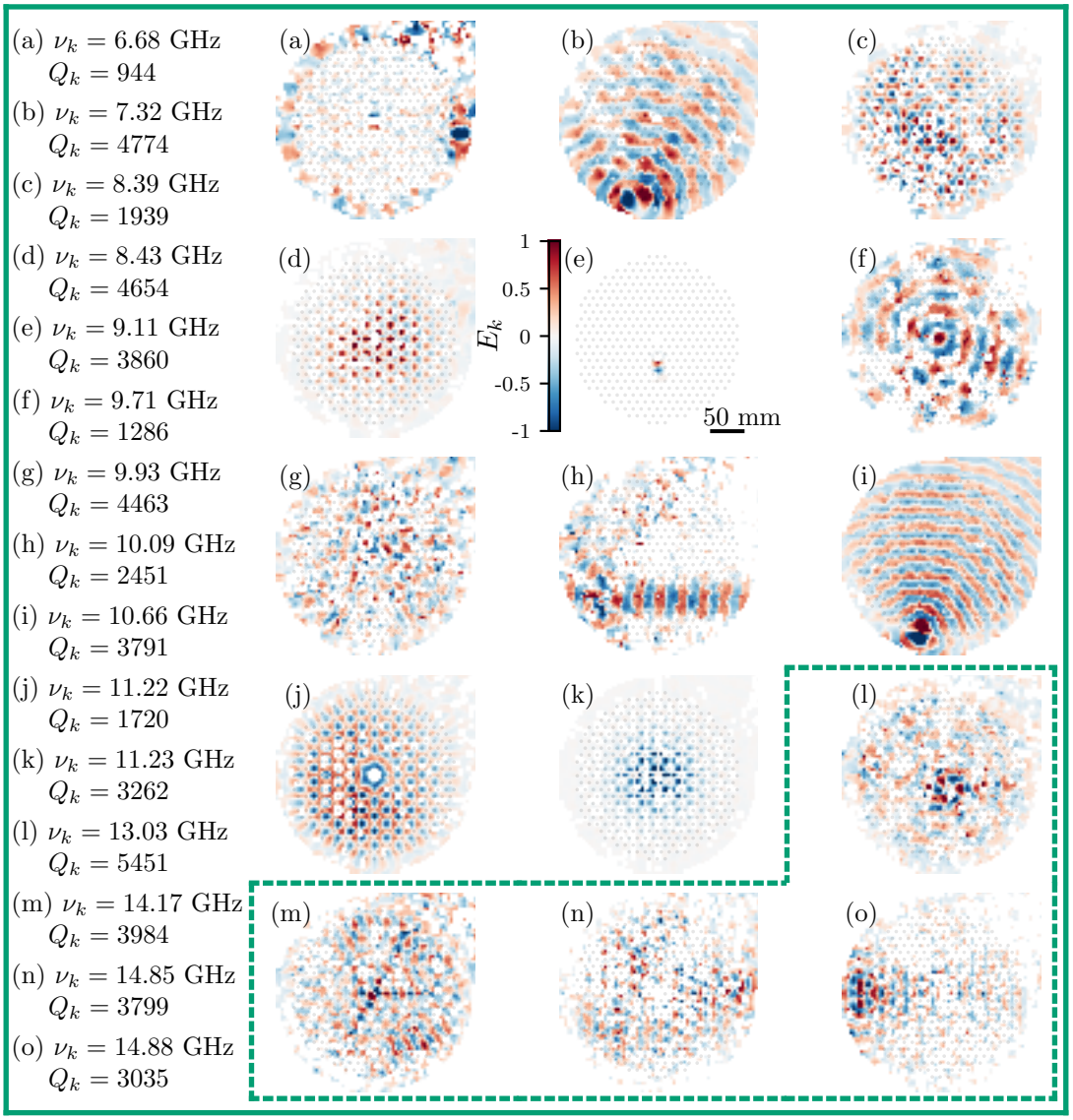

Figure C.3: [(a)-(o)] Spatial modal structure of representative modes found in the same regular lattice. Amplitude maps are normalized such that $\max(|E_k|) = 1$. Green dotted box contains the states with frequencies beyond the 2D limit.

Finally, for frequency region beyond the 2D threshold ($\nu > 12$ GHz), a progression of peaks with quality factors $0 < Q_k < 4000$ is recovered by the harmonic inversion. This band is characterized by a progressive continuous increment of the DoS, confirming the emergence of new 3D modes. The characteristic time shows different peaks with poor values ($t_0 \sim 15$ ns), giving rise to values of $\langle g \rangle$ around 1. Opposite to the cases studied in Chapter 4 and despite the high modal overlap regime, some eigenstates are recovered by the harmonic inversion/clustering algorithms. Figs. C.3(l)-(o) depict four different modes

found in the 3D regime in the regular lattice. Note that all modes all well extended along all the measured space.

C.3 Conclusion

Similar to the experiments described in Chapter 4, in this Appendix we perform scattering microwave experiments to analyse different transport regimes, as well as the properties of eigenmodes in a triangular lattice. The experimental array is composed by dielectric Mie cylinders placed into a metallic cavity made up by two aluminum plates separated by a distance $h = 13$ mm. Using a VNA, the transmitted and reflected signal are emitted and detected by two straight antennas located in the center of the bottom and the movable top plate. Part of the analysis of the transmitted signal is carried out by the harmonic inversion and clustering methods introduced in Chapter 2, allowing to extract the spatial structure of certain modes in the system, as well as other important quantities such as the quality factor. Additionally, thanks to the Fourier transform, the features of the temporal evolution of a wave packet can be obtained from the transmission signal. On the other hand, the density of states directly calculated from the reflection measurement given the intrinsic connection between the local density of states and the Green function.

Or experimental results show a strong similarity in transport quantities obtained through regular lattices and aperiodic systems, such as the presence of two well defined band gaps driven by Bragg scattering, thus confirming the key role of short-range correlations to opening band gaps in non-regular materials. However, the regular lattice is characterized by the absence of confined states, which in the case of the golden-angle spiral are caused for the inhomogeneity distribution of spacing between neighbouring cylinders [138].

Bibliography

[1] P. W. Anderson. "Absence of Diffusion in Certain Random Lattices". *Phys. Rev.* **109**, 1492 (1958).

[2] P. W. Anderson. "The question of classical localization A theory of white paint?" *Philosophical Magazine B* **52**, 505 (1985).

[3] R. Weaver. "Anderson localization of ultrasound". *Wave Motion* **12**, 129 (1990).

[4] R. A. Méndez-Sánchez, L. Gutiérrez, A. Morales, J. Flores, A. Díaz-de-Anda, and G. Monsivais. "Anderson Localization Phenomenon in One-dimensional Elastic Systems". *Acta Physica Polonica A* **124**, 1063 (2013).

[5] J. C. Ángel, J. C. T. Guzmán, and A. D. de Anda. "Anderson localization of flexural waves in disordered elastic beams". *Scientific Reports* **9**, 3572 (2019).

[6] H. Hu, A. Strybulevych, J. H. Page, S. E. Skipetrov, and B. A. van Tiggelen. "Localization of ultrasound in a three-dimensional elastic network". *Nature Physics* **4**, 945 (2008).

[7] S. Karbasi, C. R. Mirr, P. G. Yarandi, R. J. Frazier, K. W. Koch, and A. Mafi. "Observation of transverse Anderson localization in an optical fiber". *Opt. Lett.* **37**, 2304 (2012).

[8] S. Karbasi, R. J. Frazier, K. W. Koch, T. Hawkins, J. Ballato, and A. Mafi. "Image transport through a disordered optical fibre mediated by transverse Anderson localization". *Nature Communications* **5**, 3362 (2014).

[9] B. A. Van Tiggelen. "Localization of Waves". In: *Diffuse Waves in Complex Media*. Ed. by J.-P. Fouque. Dordrecht: Springer Netherlands, (1999).

[10] S. E. Skipetrov and J. H. Page. "Red light for Anderson localization". *New Journal of Physics* **18**, 021001 (2016).

[11] S. John. "Electromagnetic Absorption in a Disordered Medium near a Photon Mobility Edge". *Phys. Rev. Lett.* **53**, 2169 (1984).

[12] Y. Lahini, A. Avidan, F. Pozzi, M. Sorel, R. Morandotti, D. N. Christodoulides, and Y. Silberberg. "Anderson Localization and Nonlinearity in One-Dimensional Disordered Photonic Lattices". *Phys. Rev. Lett.* **100**, 013906 (2008).

[13] T. Schwartz, G. Bartal, S. Fishman, and M. Segev. "Transport and Anderson localization in disordered two-dimensional photonic lattices". *Nature* **446**, 52 (2007).

[14] M. Segev, Y. Silberberg, and D. N. Christodoulides. "Anderson localization of light". *Nature Photonics* **7**, 197 (2013).

[15] R. Dalichaouch, J. P. Armstrong, S. Schultz, P. M. Platzman, and S. L. McCall. "Microwave localization by two-dimensional random scattering". *Nature* **354**, 53 (1991).

[16] D. Laurent, O. Legrand, P. Sebbah, C. Vanneste, and F. Mortessagne. "Localized Modes in a Finite-Size Open Disordered Microwave Cavity". *Phys. Rev. Lett.* **99**, 253902 (2007).

[17] D. S. Wiersma, P. Bartolini, A. Lagendijk, and R. Righini. "Localization of light in a disordered medium". *Nature* **390**, 671 (1997).

[18] M. Störzer, P. Gross, C. M. Aegerter, and G. Maret. "Observation of the Critical Regime Near Anderson Localization of Light". *Phys. Rev. Lett.* **96**, 063904 (2006).

[19] T. Sperling, W. Bührer, C. M. Aegerter, and G. Maret. "Direct determination of the transition to localization of light in three dimensions". *Nature Photonics* **7**, 48 (2013).

[20] T. van der Beek, P. Barthelemy, P. M. Johnson, D. S. Wiersma, and A. Lagendijk. "Light transport through disordered layers of dense gallium arsenide submicron particles". *Phys. Rev. B* **85**, 115401 (2012).

[21] T. Sperling, L. Schertel, M. Ackermann, G. J. Aubry, C. M. Aegerter, and G. Maret. "Can 3D light localization be reached in 'white paint'?" *New Journal of Physics* **18**, 013039 (2016).

[22] S. E. Skipetrov and I. M. Sokolov. "Absence of Anderson Localization of Light in a Random Ensemble of Point Scatterers". *Phys. Rev. Lett.* **112**, 023905 (2014).

[23] R. Rezvani Naraghi, S. Sukhov, J. J. Sáenz, and A. Dogariu. "Near-Field Effects in Mesoscopic Light Transport". *Phys. Rev. Lett.* **115**, 203903 (2015).

[24] B. A. van Tiggelen and S. E. Skipetrov. "Longitudinal modes in diffusion and localization of light". *Phys. Rev. B* **103**, 174204 (2021).

[25] A. Yamilov, S. E. Skipetrov, T. W. Hughes, M. Minkov, Z. Yu, and H. Cao. "Anderson localization of electromagnetic waves in three dimensions". *Nature Physics* **19**, 1308 (2023).

[26] M. Filoche and S. Mayboroda. "Universal mechanism for Anderson and weak localization". *Proceedings of the National Academy of Sciences* **109**, 14761 (2012).

[27] L. A. Razo-López, G. J. Aubry, M. Filoche, and F. Mortessagne. "Low- and high-energy localization landscapes for tight-binding Hamiltonians in two-dimensional lattices". *Phys. Rev. Res.* **5**, 023102 (2023).

[28] L. A. Razo-López, G. J. Aubry, F. A. Pinheiro, and F. Mortessagne. "Strong localization of microwaves beyond two dimensions in aperiodic Vogel spirals". *Phys. Rev. B* **109**, 014205 (2024).

[29] L. A. Razo-López, G. J. Aubry, F. A. Pinheiro, and F. Mortessagne. "Aperiodicity is more effective than disorder in localizing electromagnetic waves [Invited]". *Opt. Mater. Express* **14**, 816 (2024).

[30] P. Drude. "Zur Elektronentheorie der Metalle". *Annalen der Physik* **306**, 566 (1900).

[31] N. W. Ashcroft and N. D. Mermin. "Solid State Physics". Holt-Saunders, (1976).

[32] N. Mott and W. Twose. "The theory of impurity conduction". *Advances in Physics* **10**, 107 (1961).

[33] S. N. Mott. "Metal–insulator transitions". *Physics Today* **31**, 42 (1978).

[34] J. T. Edwards and D. J. Thouless. "Numerical studies of localization in disordered systems". *Journal of Physics C: Solid State Physics* **5**, 807 (1972).

[35] D. Thouless. "Electrons in disordered systems and the theory of localization". *Physics Reports* **13**, 93 (1974).

[36] D. J. Thouless. "Maximum Metallic Resistance in Thin Wires". *Phys. Rev. Lett.* **39**, 1167 (1977).

[37] J. Wang and A. Z. Genack. "Transport through modes in random media". *Nature* **471**, 345 (2011).

[38] S. Mondal, R. Kumar, M. Kamp, and S. Mujumdar. "Optical Thouless conductance and level-spacing statistics in two-dimensional Anderson localizing systems". *Phys. Rev. B* **100**, 060201 (2019).

[39] E. Abrahams, P. W. Anderson, D. C. Licciardello, and T. V. Ramakrishnan. "Scaling Theory of Localization: Absence of Quantum Diffusion in Two Dimensions". *Phys. Rev. Lett.* **42**, 673 (1979).

[40] R. Monsarrat. "Propagation of light waves in correlated disordered media: density of states, transport, localisation". PhD Thesis. Université PSL (2022).

[41] D. Vollhardt and P. Wölfle. "Scaling Equations from a Self-Consistent Theory of Anderson Localization". *Phys. Rev. Lett.* **48**, 699 (1982).

[42] A. Lagendijk, B. v. Tiggelen, and D. S. Wiersma. "Fifty years of Anderson localization". *Physics Today* **62**, 24 (2009).

[43] J. Kroha, T. Kopp, and P. Wölfle. "Self-consistent theory of Anderson localization for the tight-binding model with site-diagonal disorder". *Phys. Rev. B* **41**, 888 (1990).

[44] J. Billy, V. Josse, Z. Zuo, A. Bernard, B. Hambrecht, P. Lugan, D. Clément, L. Sanchez-Palencia, P. Bouyer, and A. Aspect. "Direct observation of Anderson localization of matter waves in a controlled disorder". *Nature* **453**, 891 (2008).

[45] G. Roati, C. D'Errico, L. Fallani, M. Fattori, C. Fort, M. Zaccanti, G. Modugno, M. Modugno, and M. Inguscio. "Anderson localization of a non-interacting Bose–Einstein condensate". *Nature* **453**, 895 (2008).

[46] J. Chabé, G. Lemarié, B. Grémaud, D. Delande, P. Szriftgiser, and J. C. Garreau. "Experimental Observation of the Anderson Metal-Insulator Transition with Atomic Matter Waves". *Phys. Rev. Lett.* **101**, 255702 (2008).

[47] A. Aspect and M. Inguscio. "Anderson localization of ultracold atoms". *Physics Today* **62**, 30 (2009).

[48] F. Jendrzejewski, A. Bernard, K. Müller, P. Cheinet, V. Josse, M. Piraud, L. Pezzé, L. Sanchez-Palencia, A. Aspect, and P. Bouyer. "Three-dimensional localization of ultracold atoms in an optical disordered potential". *Nature Physics* **8**, 398 (2012).

[49] P. Sheng and Z.-Q. Zhang. "Scalar-Wave Localization in a Two-Component Composite". *Phys. Rev. Lett.* **57**, 1879 (1986).

[50] E. N. Economou and C. M. Soukoulis. "Calculation of optical transport and localization quantities". *Phys. Rev. B* **40**, 7977 (1989).

[51] S. H. Choi, S.-W. Kim, Z. Ku, M. A. Visbal-Onufrak, S.-R. Kim, K.-H. Choi, H. Ko, W. Choi, A. M. Urbas, T.-W. Goo, and Y. L. Kim. "Anderson light localization in biological nanostructures of native silk". *Nature Communications* **9**, 452 (2018).

[52] F. Scheffold, R. Lenke, R. Tweer, and G. Maret. "Localization or classical diffusion of light?" *Nature* **398**, 206 (1999).

[53] A. A. Chabanov, M. Stoytchev, and A. Z. Genack. "Statistical signatures of photon localization". *Nature* **404**, 850 (2000).

[54] F. Scheffold and D. Wiersma. "Inelastic scattering puts in question recent claims of Anderson localization of light". *Nature Photonics* **7**, 934 (2013).

[55] M. Rusek, J. Mostowski, and A. Orłowski. "Random Green matrices: From proximity resonances to Anderson localization". *Phys. Rev. A* **61**, 022704 (2000).

[56] J. Haberko, L. S. Froufe-Pérez, and F. Scheffold. "Transition from light diffusion to localization in three-dimensional amorphous dielectric networks near the band edge". *Nature Communications* **11**, 4867 (2020).

[57] F. Scheffold, J. Haberko, S. Magkiriadou, and L. S. Froufe-Pérez. "Transport through Amorphous Photonic Materials with Localization and Bandgap Regimes". *Phys. Rev. Lett.* **129**, 157402 (2022).

[58] D. N. Arnold, G. David, D. Jerison, S. Mayboroda, and M. Filoche. "Effective Confining Potential of Quantum States in Disordered Media". *Phys. Rev. Lett.* **116**, 056602 (2016).

[59] D. N. Arnold, G. David, M. Filoche, D. Jerison, and S. Mayboroda. "Computing Spectra without Solving Eigenvalue Problems". *SIAM Journal on Scientific Computing* **41**, B69 (2019).

[60] Y. Chalopin, F. Piazza, S. Mayboroda, C. Weisbuch, and M. Filoche. "Universality of fold-encoded localized vibrations in enzymes". *Scientific Reports* **9**, 12835 (2019).

[61] G. Lemut, M. J. Pacholski, O. Ovdat, A. Grabsch, J. Tworzydło, and C. W. J. Beenakker. "Localization landscape for Dirac fermions". *Phys. Rev. B* **101**, 081405 (2020).

[62] A. Ostrowski. "Über die determinanten mit überwiegender Hauptdiagonale". *Commentarii Mathematici Helvetici* **10**, 69 (1937).

[63] A. Ostrowski. "Determinanten mit überwiegender Hauptdiagonale und die absolute Konvergenz von linearen Iterationsprozessen". *Commentarii Mathematici Helvetici* **30**, 175 (1956).

[64] E. M. Harrell and A. V. Maltsev. "Localization and landscape functions on quantum graphs". *Trans. Amer. Math. Soc.* **373**, 1701 (2020).

[65] G. Lefebvre, A. Gondel, M. Dubois, M. Atlan, F. Feppon, A. Labbé, C. Gillot, A. Garelli, M. Ernoult, S. Mayboroda, M. Filoche, and P. Sebbah. "One Single Static Measurement Predicts Wave Localization in Complex Structures". *Phys. Rev. Lett.* **117**, 074301 (2016).

[66] D. N. Arnold, G. David, M. Filoche, D. Jerison, and S. Mayboroda. "Localization of eigenfunctions via an effective potential". *Communications in Partial Differential Equations* **44**, 1186 (2019).

[67] S. Balasubramanian, Y. Liao, and V. Galitski. "Many-body localization landscape". *Phys. Rev. B* **101**, 014201 (2020).

[68] M. Filoche, S. Mayboroda, and T. Tao. "The effective potential of an M-matrix". *Journal of Mathematical Physics* **62**, 041902 (2021).

[69] R. A. Horn and C. R. Johnson. "Matrix analysis". Cambridge University Press Cambridge, England, (1985).

[70] M. Filoche, M. Piccardo, Y.-R. Wu, C.-K. Li, C. Weisbuch, and S. Mayboroda. "Localization landscape theory of disorder in semiconductors. I. Theory and modeling". *Phys. Rev. B* **95**, 144204 (2017).

[71] M. Piccardo, C.-K. Li, Y.-R. Wu, J. S. Speck, B. Bonef, R. M. Farrell, M. Filoche, L. Martinelli, J. Peretti, and C. Weisbuch. "Localization landscape theory of disorder in semiconductors. II. Urbach tails of disordered quantum well layers". *Phys. Rev. B* **95**, 144205 (2017).

[72] C.-K. Li, M. Piccardo, L.-S. Lu, S. Mayboroda, L. Martinelli, J. Peretti, J. S. Speck, C. Weisbuch, M. Filoche, and Y.-R. Wu. "Localization landscape theory of disorder in semiconductors. III. Application to carrier transport and recombination in light emitting diodes". *Phys. Rev. B* **95**, 144206 (2017).

[73] J.-P. Banon, P. Pelletier, C. Weisbuch, S. Mayboroda, and M. Filoche. "Wigner-Weyl description of light absorption in disordered semiconductor alloys using the localization landscape theory". *Phys. Rev. B* **105**, 125422 (2022).

[74] P. Pelletier, D. Delande, V. Josse, A. Aspect, S. Mayboroda, D. N. Arnold, and M. Filoche. "Spectral functions and localization-landscape theory in speckle potentials". *Phys. Rev. A* **105**, 023314 (2022).

[75] M. Filoche, P. Pelletier, D. Delande, and S. Mayboroda. *The Anderson mobility edge as a percolation transition.* (2023). arXiv: `2309.03813 [cond-mat.dis-nn]`.

[76] M. M. Sigalas, C. M. Soukoulis, C.-T. Chan, and D. Turner. "Localization of electromagnetic waves in two-dimensional disordered systems". *Phys. Rev. B* **53**, 8340 (1996).

[77] M. Florescu, S. Torquato, and P. J. Steinhardt. "Designer disordered materials with large, complete photonic band gaps". *Proceedings of the National Academy of Sciences* **106**, 20658 (2009).

[78] L. S. Froufe-Pérez, M. Engel, J. J. Sáenz, and F. Scheffold. "Band gap formation and Anderson localization in disordered photonic materials with structural correlations". *Proceedings of the National Academy of Sciences* **114**, 9570 (2017).

[79] R. Monsarrat, R. Pierrat, A. Tourin, and A. Goetschy. "Pseudogap and Anderson localization of light in correlated disordered media". *Phys. Rev. Res.* **4**, 033246 (2022).

[80] F. Sgrignuoli, S. Torquato, and L. Dal Negro. "Subdiffusive wave transport and weak localization transition in three-dimensional stealthy hyperuniform disordered systems". *Phys. Rev. B* **105**, 064204 (2022).

[81] G. J. Aubry, L. S. Froufe-Pérez, U. Kuhl, O. Legrand, F. Scheffold, and F. Mortessagne. "Experimental Tuning of Transport Regimes in Hyperuniform Disordered Photonic Materials". *Phys. Rev. Lett.* **125**, 127402 (2020).

[82] Lord Rayleigh. "XXXIV. On the transmission of light through an atmosphere containing small particles in suspension, and on the origin of the blue of the sky". *The London, Edinburgh, and Dublin Philosophical Magazine and Journal of Science* **47**, 375 (1899).

[83] R. W. Hart and R. A. Farrell. "Light Scattering in the Cornea*". *J. Opt. Soc. Am.* **59**, 766 (1969).

[84] G. B. Benedek. "Theory of Transparency of the Eye". *Appl. Opt.* **10**, 459 (1971).

[85] V. Twersky. "Transparency of pair-correlated, random distributions of small scatterers, with applications to the cornea*". *J. Opt. Soc. Am.* **65**, 524 (1975).

[86] R. O. Prum and R. H. Torres. "Structural colouration of mammalian skin: convergent evolution of coherently scattering dermal collagen arrays". *Journal of Experimental Biology* **207**, 2157 (2004).

[87] K. Vynck, R. Pierrat, R. Carminati, L. S. Froufe-Pérez, F. Scheffold, R. Sapienza, S. Vignolini, and J. J. Sáenz. "Light in correlated disordered media". *Rev. Mod. Phys.* **95**, 045003 (2023).

[88] S. Torquato. "Random Heterogeneous Materials: Microstructure and Macroscopic Properties". Springer New York, (2002).

[89] S. Torquato and F. H. Stillinger. "Local density fluctuations, hyperuniformity, and order metrics". *Phys. Rev. E* **68**, 041113 (2003).

[90] J.-P. Hansen and I. R. McDonald, eds. "Theory of Simple Liquids". Fourth Edition. Oxford: Academic Press, (2013).

[91] S. Torquato. "Hyperuniform states of matter". *Physics Reports* **745**, 1 (2018). Hyperuniform States of Matter.

[92] C. Kittel. "Introduction to Solid State Physics". 8th ed. Wiley, (2004).

[93] J. D. Joannopoulos, S. G. Johnson, J. N. Winn, and R. D. Meade. "Photonic Crystals: Molding the Flow of Light - Second Edition". Princeton University Press, (2008).

[94] P. N. Pusey and W. van Megen. "Phase behaviour of concentrated suspensions of nearly hard colloidal spheres". *Nature* **320**, 340 (1986).

[95] J. Zhu, M. Li, R. Rogers, W. Meyer, R. H. Ottewill, W. B. Russel, P. M. Chaikin, and S.-7. S. S. Crew. "Crystallization of hard-sphere colloids in microgravity". *Nature* **387**, 883 (1997).

[96] A. P. Gast and W. B. Russel. "Simple Ordering in Complex Fluids". *Physics Today* **51**, 24 (1998).

[97] P. Meakin. "Fractal aggregates". *Advances in Colloid and Interface Science* **28**, 249 (1987).

[98] R. Hosemann. "Crystalline and Paracrystalline Order in High Polymers". *Journal of Applied Physics* **34**, 25 (1963).

[99] L. S. Froufe-Pérez, M. Engel, P. F. Damasceno, N. Muller, J. Haberko, S. C. Glotzer, and F. Scheffold. "Role of Short-Range Order and Hyperuniformity in the Formation of Band Gaps in Disordered Photonic Materials". *Phys. Rev. Lett.* **117**, 053902 (2016).

[100] V. Saranathan, J. D. Forster, H. Noh, S.-F. Liew, S. G. J. Mochrie, H. Cao, E. R. Dufresne, and R. O. Prum. "Structure and optical function of amorphous photonic nanostructures from avian feather barbs: a comparative small angle X-ray scattering (SAXS) analysis of 230 bird species". *Journal of The Royal Society Interface* **9**, 2563 (2012).

[101] M. A. Klatt, J. Kim, and S. Torquato. "Cloaking the underlying long-range order of randomly perturbed lattices". *Phys. Rev. E* **101**, 032118 (2020).

[102] R. D. Batten, F. H. Stillinger, and S. Torquato. "Classical disordered ground states: Super-ideal gases and stealth and equi-luminous materials". *Journal of Applied Physics* **104**, 033504 (2008).

[103] S. Torquato, G. Zhang, and F. H. Stillinger. "Ensemble Theory for Stealthy Hyperuniform Disordered Ground States". *Phys. Rev. X* **5**, 021020 (2015).

[104] O. Leseur, R. Pierrat, and R. Carminati. "High-density hyperuniform materials can be transparent". *Optica* **3**, 763 (2016).

[105] A. Donev, F. H. Stillinger, and S. Torquato. "Unexpected Density Fluctuations in Jammed Disordered Sphere Packings". *Phys. Rev. Lett.* **95**, 090604 (2005).

[106] N. Granchi, R. Spalding, M. Lodde, M. Petruzzella, F. W. Otten, A. Fiore, F. Intonti, R. Sapienza, M. Florescu, and M. Gurioli. "Near-Field Investigation of Luminescent Hyperuniform Disordered Materials". *Advanced Optical Materials* **10**, 2102565 (2022).

[107] N. Granchi, M. Lodde, K. Stokkereit, R. Spalding, P. J. van Veldhoven, R. Sapienza, A. Fiore, M. Gurioli, M. Florescu, and F. Intonti. "Near-field imaging of optical nanocavities in hyperuniform disordered materials". *Phys. Rev. B* **107**, 064204 (2023).

[108] L. Dal Negro, R. Wang, and F. A. Pinheiro. "Structural and Spectral Properties of Deterministic Aperiodic Optical Structures". *Crystals* **6**, (2016).

[109] E. Maciá. "The role of aperiodic order in science and technology". *Reports on Progress in Physics* **69**, 397 (2005).

[110] E. Maciá. "Aperiodic Structures in Condensed Matter: Fundamentals and Applications". Condensed Matter Physics. Taylor & Francis, (2008).

[111] E. Maciá. "Exploiting aperiodic designs in nanophotonic devices". *Reports on Progress in Physics* **75**, 036502 (2012).

[112] F. Sgrignuoli, S. Gorsky, W. A. Britton, R. Zhang, F. Riboli, and L. Dal Negro. "Multifractality of light in photonic arrays based on algebraic number theory". *Communications Physics* **3**, 106 (2020).

[113] M. Reisner, Y. Tahmi, F. Piéchon, U. Kuhl, and F. Mortessagne. "Experimental observation of multifractality in Fibonacci chains". *Phys. Rev. B* **108**, 064210 (2023).

[114] F. Sgrignuoli and L. Dal Negro. "Subdiffusive light transport in three-dimensional subrandom arrays". *Phys. Rev. B* **101**, 214204 (2020).

[115] M. Kohmoto, B. Sutherland, and K. Iguchi. "Localization of optics: Quasiperiodic media". *Phys. Rev. Lett.* **58**, 2436 (1987).

[116] M. Kohmoto, B. Sutherland, and C. Tang. "Critical wave functions and a Cantor-set spectrum of a one-dimensional quasicrystal model". *Phys. Rev. B* **35**, 1020 (1987).

[117] S. V. Boriskina, A. Gopinath, and L. D. Negro. "Optical gap formation and localization properties of optical modes in deterministic aperiodic photonic structures". *Opt. Express* **16**, 18813 (2008).

[118] S. V. Boriskina and L. D. Negro. "Sensitive label-free biosensing using critical modes in aperiodic photonic structures". *Opt. Express* **16**, 12511 (2008).

[119] Z. V. Vardeny, A. Nahata, and A. Agrawal. "Optics of photonic quasicrystals". *Nature Photonics* **7**, 177 (2013).

[120] M. Razi, R. Wang, Y. He, R. M. Kirby, and L. Dal Negro. "Optimization of Large-Scale Vogel Spiral Arrays of Plasmonic Nanoparticles". *Plasmonics* **14**, 253 (2019).

[121] A. Gopinath, S. V. Boriskina, B. M. Reinhard, and L. D. Negro. "Deterministic aperiodic arrays of metal nanoparticles for surface-enhanced Raman scattering (SERS)". *Opt. Express* **17**, 3741 (2009).

[122] S. Y. Lee, J. J. Amsden, S. V. Boriskina, A. Gopinath, A. Mitropolous, D. L. Kaplan, F. G. Omenetto, and L. D. Negro. "Spatial and spectral detection of protein monolayers with deterministic aperiodic arrays of metal nanoparticles". *Proceedings of the National Academy of Sciences* **107**, 12086 (2010).

[123] J. Trevino, H. Cao, and L. Dal Negro. "Circularly Symmetric Light Scattering from Nanoplasmonic Spirals". *Nano Letters* **11**, 2008 (2011).

[124] F. M. Huang, Y. Chen, F. J. G. de Abajo, and N. I. Zheludev. "Optical super-resolution through super-oscillations". *Journal of Optics A: Pure and Applied Optics* **9**, S285 (2007).

[125] L. Negro. "Optics of Aperiodic Structures: Fundamentals and Device Applications". Jenny Stanford Publishing, (2013).

[126] L. D. Negro, N. Lawrence, and J. Trevino. "Analytical light scattering and orbital angular momentum spectra of arbitrary Vogel spirals". *Opt. Express* **20**, 18209 (2012).

[127] A. Christofi, F. A. Pinheiro, and L. D. Negro. "Probing scattering resonances of Vogel's spirals with the Green's matrix spectral method". *Opt. Lett.* **41**, 1933 (2016).

[128] M. E. Pollard and G. J. Parker. "Low-contrast bandgaps of a planar parabolic spiral lattice". *Opt. Lett.* **34**, 2805 (2009).

[129] O. J. Trojak, S. Gorsky, F. Sgrignuoli, F. A. Pinheiro, S.-I. Park, J. D. Song, L. Dal Negro, and L. Sapienza. "Cavity quantum electro-dynamics with solid-state emitters in aperiodic nano-photonic spiral devices". *Applied Physics Letters* **117**, 124006 (2020).

[130] O. J. Trojak, S. Gorsky, C. Murray, F. Sgrignuoli, F. A. Pinheiro, L. Dal Negro, and L. Sapienza. "Cavity-enhanced light–matter interaction in Vogel-spiral devices as a platform for quantum photonics". *Applied Physics Letters* **118**, 011103 (2021).

[131] A. Bravais and L. Bravais. "Essai sur la disposition des feuilles curvisériées". *Annales des sciences naturelles (Botanique)* **7**, 42 (1837).

[132] A. H. Church. "The Principles of Phyllotaxis". *Annals of Botany* **18**, 227 (1904).

[133] T. Cook. "The Curves of Life: Being an Account of Spiral Formations and Their Application to Growth in Nature, to Science, and to Art: with Special Reference to the Manuscripts of Leonardo Da Vinci". Dover Books Explaining Science. Dover Publications, (1979).

[134] D. W. Thompson. "On Growth and Form". Ed. by J. T. Bonner. Canto. Cambridge University Press, (1992).

[135] R. V. Jean. "Phyllotaxis: The status of the field". *Mathematical Biosciences* **127**, 181 (1995).

[136] P. Ball. "Shapes: Nature's Patterns: A Tapestry in Three Parts". Oxford University Press, (2011).

[137] H. Vogel. "A better way to construct the sunflower head". *Mathematical Biosciences* **44**, 179 (1979).

[138] S. F. Liew, H. Noh, J. Trevino, L. D. Negro, and H. Cao. "Localized photonic band edge modes and orbital angular momenta of light in a golden-angle spiral". *Opt. Express* **19**, 23631 (2011).

[139] J. Trevino, S. F. Liew, H. Noh, H. Cao, and L. D. Negro. "Geometrical structure, multifractal spectra and localized optical modes of aperiodic Vogel spirals". *Opt. Express* **20**, 3015 (2012).

[140] M. Naylor. "Golden, $\sqrt{2}$, and π Flowers: A Spiral Story". *Mathematics Magazine* **75**, 163 (2002).

[141] F. Sgrignuoli, R. Wang, F. A. Pinheiro, and L. Dal Negro. "Localization of scattering resonances in aperiodic Vogel spirals". *Phys. Rev. B* **99**, 104202 (2019).

[142] M. Prado, F. Sgrignuoli, Y. Chen, L. Dal Negro, and F. A. Pinheiro. "Structural entropy and spatial decay of quasimodes in Vogel spirals". *Phys. Rev. B* **104**, 184204 (2021).

[143] M. Z. Hasan and C. L. Kane. "Colloquium: Topological insulators". *Rev. Mod. Phys.* **82**, 3045 (2010).

[144] K. v. Klitzing, G. Dorda, and M. Pepper. "New Method for High-Accuracy Determination of the Fine-Structure Constant Based on Quantized Hall Resistance". *Phys. Rev. Lett.* **45**, 494 (1980).

[145] E. H. Hall. "On a New Action of the Magnet on Electric Currents". *American Journal of Mathematics* **2**, 287 (1879).

[146] D. J. Thouless, M. Kohmoto, M. P. Nightingale, and M. den Nijs. "Quantized Hall Conductance in a Two-Dimensional Periodic Potential". *Phys. Rev. Lett.* **49**, 405 (1982).

[147] B. Simon. "Holonomy, the Quantum Adiabatic Theorem, and Berry's Phase". *Phys. Rev. Lett.* **51**, 2167 (1983).

[148] M. V. Berry. "Quantal phase factors accompanying adiabatic changes". *Proceedings of the Royal Society of London. A. Mathematical and Physical Sciences* **392**, 45 (1984).

[149] S.-s. Chern. "On the Curvatura Integra in a Riemannian Manifold". *Annals of Mathematics* **46**, 674 (1945).

[150] Y. Hatsugai. "Chern number and edge states in the integer quantum Hall effect". *Phys. Rev. Lett.* **71**, 3697 (1993).

[151] Y. Hatsugai. "Edge states in the integer quantum Hall effect and the Riemann surface of the Bloch function". *Phys. Rev. B* **48**, 11851 (1993).

[152] X.-L. Qi, Y.-S. Wu, and S.-C. Zhang. "General theorem relating the bulk topological number to edge states in two-dimensional insulators". *Phys. Rev. B* **74**, 045125 (2006).

[153] T. Ozawa, H. M. Price, A. Amo, N. Goldman, M. Hafezi, L. Lu, M. C. Rechtsman, D. Schuster, J. Simon, O. Zilberberg, and I. Carusotto. "Topological photonics". *Rev. Mod. Phys.* **91**, 015006 (2019).

[154] F. D. M. Haldane. "Model for a Quantum Hall Effect without Landau Levels: Condensed-Matter Realization of the "Parity Anomaly"". *Phys. Rev. Lett.* **61**, 2015 (1988).

[155] C. L. Kane and E. J. Mele. "Z_2 Topological Order and the Quantum Spin Hall Effect". *Phys. Rev. Lett.* **95**, 146802 (2005).

[156] L.-H. Wu and X. Hu. "Scheme for Achieving a Topological Photonic Crystal by Using Dielectric Material". *Phys. Rev. Lett.* **114**, 223901 (2015).

[157] L.-H. Wu and X. Hu. "Topological Properties of Electrons in Honeycomb Lattice with Detuned Hopping Energy". *Scientific Reports* **6**, 24347 (2016).

[158] M. Dresselhaus, G. Dresselhaus, and A. Jorio. "Group Theory: Application to the Physics of Condensed Matter". Springer Berlin Heidelberg, (2007).

[159] J. J. Sakurai and J. Napolitano. "Modern Quantum Mechanics". 2nd ed. Cambridge University Press, (2017).

[160] Z. Zhu, Y. Cheng, and U. Schwingenschlögl. "Band inversion mechanism in topological insulators: A guideline for materials design". *Phys. Rev. B* **85**, 235401 (2012).

[161] P. Markoš and C. M. Soukoulis. "Wave Propagation: From Electrons to Photonic Crystals and Left-Handed Materials". Student edition. Princeton University Press, (2008).

[162] J. D. Jackson. "Classical electrodynamics". 3rd ed. New York: Wiley New York, (1999).

[163] C. F. Bohren and D. R. Huffman. "Absorption and Scattering by a Sphere". In: *Absorption and Scattering of Light by Small Particles*. John Wiley & Sons, Ltd, (1998).

[164] M. Reisner. "Experimental studies of multifractality and topological phase transitions in microwave resonator lattices". PhD Thesis. Université Côte d'Azur (2023).

[165] M. Bellec, U. Kuhl, G. Montambaux, and F. Mortessagne. "Tight-binding couplings in microwave artificial graphene". *Phys. Rev. B* **88**, 115437 (2013).

[166] M. Reisner, M. Bellec, U. Kuhl, and F. Mortessagne. "Microwave resonator lattices for topological photonics [Invited]". *Opt. Mater. Express* **11**, 629 (2021).

[167] J. Barthélemy, O. Legrand, and F. Mortessagne. "Complete S matrix in a microwave cavity at room temperature". *Phys. Rev. E* **71**, 016205 (2005).

[168] M. R. Wall and D. Neuhauser. "Extraction, through filter-diagonalization, of general quantum eigenvalues or classical normal mode frequencies from a small number of residues or a short-time segment of a signal. I. Theory and application to a quantum-dynamics model". *The Journal of Chemical Physics* **102**, 8011 (1995).

[169] V. A. Mandelshtam and H. S. Taylor. "Spectral Analysis of Time Correlation Function for a Dissipative Dynamical System Using Filter Diagonalization: Application to Calculation of Unimolecular Decay Rates". *Phys. Rev. Lett.* **78**, 3274 (1997).

[170] V. A. Mandelshtam and H. S. Taylor. "Harmonic inversion of time signals and its applications". *The Journal of Chemical Physics* **107**, 6756 (1997).

[171] J. Maier L. C. and J. C. Slater. "Field Strength Measurements in Resonant Cavities". *Journal of Applied Physics* **23**, 68 (2004).

[172] C. Ruiz, M. Spiliopoulou, and E. Menasalvas. "C-DBSCAN: Density-Based Clustering with Constraints". In: *Rough Sets, Fuzzy Sets, Data Mining and Granular Computing*. Ed. by A. An, J. Stefanowski, S. Ramanna, C. J. Butz, W. Pedrycz, and G. Wang. Berlin, Heidelberg: Springer Berlin Heidelberg, (2007).

[173] H. Ishio, A. I. Saichev, A. F. Sadreev, and K.-F. Berggren. "Wave function statistics for ballistic quantum transport through chaotic open billiards: Statistical crossover and coexistence of regular and chaotic waves". *Phys. Rev. E* **64**, 056208 (2001).

[174] E. Akkermans and G. Montambaux. "Mesoscopic Physics of Electrons and Photons". Cambridge University Press, (2007).

[175] S. Rotter and S. Gigan. "Light fields in complex media: Mesoscopic scattering meets wave control". *Rev. Mod. Phys.* **89**, 015005 (2017).

[176] M. L. Lyra, S. Mayboroda, and M. Filoche. "Dual landscapes in Anderson localization on discrete lattices". *Europhysics Letters* **109**, 47001 (2015).

[177] P. Desforges, S. Mayboroda, S. Zhang, G. David, D. N. Arnold, W. Wang, and M. Filoche. "Sharp estimates for the integrated density of states in Anderson tight-binding models". *Phys. Rev. A* **104**, 012207 (2021).

[178] G. David, M. Filoche, and S. Mayboroda. "The landscape law for the integrated density of states". *Advances in Mathematics* **390**, 107946 (2021).

[179] W. Wang and S. Zhang. "The exponential decay of eigenfunctions for tight-binding Hamiltonians via landscape and dual landscape functions". *Annales Henri Poincaré* **22**, 1429 (2021).

[180] K. S. Novoselov, A. Mishchenko, A. Carvalho, and A. H. C. Neto. "2D materials and van der Waals heterostructures". *Science* **353**, aac9439 (2016).

[181] D. Tománek. "Editorial: Collection on Two-dimensional Materials and Devices". *Phys. Rev. Appl.* **13**, 030001 (2020).

[182] M. A. Springer, T.-J. Liu, A. Kuc, and T. Heine. "Topological two-dimensional polymers". *Chem. Soc. Rev.* **49**, 2007 (2020).

[183] C. R. Johnson. "Positive Definite Matrices". *The American Mathematical Monthly* **77**, 259 (1970).

[184] S. S. Shamailov, D. J. Brown, T. A. Haase, and M. D. Hoogerland. *Anderson localisation in two dimensions: insights from Localisation Landscape Theory, exact diagonalisation, and time-dependent simulations.* (2020). arXiv: `2003.00149 [cond-mat.quant-gas]`.

[185] D. Arnold, M. Filoche, S. Mayboroda, W. Wang, and S. Zhang. "The Landscape Law for Tight Binding Hamiltonians". *Communications in Mathematical Physics* **396**, 1339 (2022).

[186] L. Herviou and J. H. Bardarson. "$\mathcal{L}^2$ localization landscape for highly excited states". *Phys. Rev. B* **101**, 220201 (2020).

[187] M. Kakoi and K. Slevin. "A Stochastic Method to Compute the L^2 Localisation Landscape". *Journal of the Physical Society of Japan* **92**, 054707 (2023).

[188] M. Bellec, U. Kuhl, G. Montambaux, and F. Mortessagne. "Manipulation of edge states in microwave artificial graphene". *New Journal of Physics* **16**, 113023 (2014).

[189] T. Stegmann, J. A. Franco-Villafañe, Y. P. Ortiz, M. Deffner, C. Herrmann, U. Kuhl, F. Mortessagne, F. Leyvraz, and T. H. Seligman. "Current vortices in aromatic carbon molecules". *Phys. Rev. B* **102**, 075405 (2020).

[190] U. Dhakal and D. Rai. "Circular current and induced force in a molecular ring junction". *Journal of Physics: Condensed Matter* **31**, 125302 (2019).

[191] J. Li, R.-L. Chu, J. K. Jain, and S.-Q. Shen. "Topological Anderson Insulator". *Phys. Rev. Lett.* **102**, 136806 (2009).

[192] C. W. Groth, M. Wimmer, A. R. Akhmerov, J. Tworzydło, and C. W. J. Beenakker. "Theory of the Topological Anderson Insulator". *Phys. Rev. Lett.* **103**, 196805 (2009).

[193] H. Jiang, L. Wang, Q.-f. Sun, and X. C. Xie. "Numerical study of the topological Anderson insulator in HgTe/CdTe quantum wells". *Phys. Rev. B* **80**, 165316 (2009).

[194] L.-Z. Tang, L.-F. Zhang, G.-Q. Zhang, and D.-W. Zhang. "Topological Anderson insulators in two-dimensional non-Hermitian disordered systems". *Phys. Rev. A* **101**, 063612 (2020).

[195] S. E. Skipetrov and P. Wulles. "Topological transitions and Anderson localization of light in disordered atomic arrays". *Phys. Rev. A* **105**, 043514 (2022).

[196] S. E. Skipetrov and P. Wulles. "Photonic topological Anderson insulator in a two-dimensional atomic lattice". *Comptes Rendus. Physique* (2023). Online first.

[197] M. Reisner, D. H. Jeon, C. Schindler, H. Schomerus, F. Mortessagne, U. Kuhl, and T. Kottos. "Self-Shielded Topological Receiver Protectors". *Phys. Rev. Appl.* **13**, 034067 (2020).

[198] M. Reisner, F. Mortessagne, E. Makri, T. Kottos, and U. Kuhl. "Microwave Limiters Implemented by Coupled Dielectric Resonators Based on a Topological Defect Mode and CT-Symmetry Breaking". *Acta Physica Polonica A* (2019).

[199] A. H. Karamlou, J. Braumüller, Y. Yanay, A. Di Paolo, P. M. Harrington, B. Kannan, D. Kim, M. Kjaergaard, A. Melville, S. Muschinske, B. M. Niedzielski, A. Vepsäläinen, R. Winik, J. L. Yoder, M. Schwartz, C. Tahan, T. P. Orlando, S. Gustavsson, and W. D. Oliver. "Quantum transport and localization in 1d and 2d tight-binding lattices". *npj Quantum Information* **8**, 35 (2022).

[200] X. Mao, J. Liu, J. Zhong, and R. A. Römer. "Disorder effects in the two-dimensional Lieb lattice and its extensions". *Physica E: Low-dimensional Systems and Nanostructures* **124**, 114340 (2020).

[201] J. Liu, X. Mao, J. Zhong, and R. A. Römer. "Localization, phases, and transitions in three-dimensional extended Lieb lattices". *Phys. Rev. B* **102**, 174207 (2020).